# Design and Construction of a Mobile Air Conditioning Test Facility for Transient Studies

P. G. Weston, W. E. Dunn, and N. R. Miller

ACRC TR-97 May 1996

*For additional information:*

Air Conditioning and Refrigeration Center
University of Illinois
Mechanical & Industrial Engineering Dept.
1206 West Green Street
Urbana, IL 61801

(217) 333-3115

*Prepared as part of ACRC Project 51*
*Design and Control of Mobile Air-conditioning Systems*
*N. R. Miller and W. E. Dunn, Principal Investigators*

*The Air Conditioning and Refrigeration Center was founded in 1988 with a grant from the estate of Richard W. Kritzer, the founder of Peerless of America Inc. A State of Illinois Technology Challenge Grant helped build the laboratory facilities. The ACRC receives continuing support from the Richard W. Kritzer Endowment and the National Science Foundation. The following organizations have also become sponsors of the Center.*

Amana Refrigeration, Inc.
Brazeway, Inc.
Carrier Corporation
Caterpillar, Inc.
Dayton Thermal Products
Delphi Harrison Thermal Systems
Eaton Corporation
Electric Power Research Institute
Ford Motor Company
Frigidaire Company
General Electric Company
Lennox International, Inc.
Modine Manufacturing Co.
Peerless of America, Inc.
Redwood Microsystems, Inc.
U. S. Army CERL
U. S. Environmental Protection Agency
Whirlpool Corporation

*For additional information:*

*Air Conditioning & Refrigeration Center*
*Mechanical & Industrial Engineering Dept.*
*University of Illinois*
*1206 West Green Street*
*Urbana IL 61801*

*217 333 3115*

# DESIGN AND CONSTRUCTION OF A MOBILE AIR CONDITIONING TEST FACILITY FOR TRANSIENT STUDIES

Pete G. Weston, M.S.
Department of Mechanical and Industrial Engineering
University of Illinois at Urbana-Champaign, 1996
W.E. Dunn and N.R. Miller, Advisors

Compared to other air-conditioning and refrigeration systems, mobile air-conditioning systems are unique in the respect that they operate almost entirely under transient conditions. The major operating transients include: (i) changes in compressor speed due to variations in vehicle engine speed, (ii) changes in condenser air flow due to ram-air effects at the front of the vehicle, (iii) changes in the passenger compartment air temperature during a pulldown mode, and (iv) cycling of the compressor clutch to prevent evaporator frosting. A versatile experimental facility has been developed to permit testing of mobile a/c systems under a wide variety of both transient and steady-state operating conditions. The facility serves as a flexible test bed for the development and validation of transient system models, advanced mobile a/c control techniques, and on-board diagnostic tools for mobile applications. The air- and refrigerant-side loops of the facility are thoroughly instrumented and can accommodate the stock or prototype components of nearly any mobile a/c system. The facility makes extensive use of controlled system-input devices which allow the researcher to simulate the majority of the transient operating conditions encountered by mobile a/c systems in field usage. Transient demonstration tests show that the facility is an excellent tool for conducting modeling, control, and diagnostic studies. Steady-state validation tests show that the evaporator- and condenser-side energy balances are in need of improvement. Sources of error have been identified, and an appropriate plan of corrective action has been established.

# TABLE OF CONTENTS

# LIST OF TABLES

# LIST OF FIGURES

# 1. INTRODUCTION

This paper discusses the design, construction, and performance of a versatile experimental facility for testing mobile air-conditioning systems under a variety of transient and steady-state operating conditions. The facility is part of the Air Conditioning and Refrigeration Center (ACRC) of the University of Illinois at Urbana-Champaign. The ACRC constitutes a joint effort between industry, government, and our university to make continuing advancements in air-conditioning and refrigeration technologies. The facility is located in Room 115K of Mechanical Engineering Laboratory.

## 1.1 Basic Attributes of Mobile A/C Systems

Compared to household and commercial air-conditioning and refrigeration systems, mobile a/c systems (i.e., the a/c systems of automotive and heavy-equipment vehicles such as cars, trucks, vans, tractors and excavation machines) are unique in several respects. For example, a mobile a/c system must cool a moderately sized cabin volume in as short a time as possible, and then maintain a moderate, more comfortable level of cooling in this volume for a longer period of time. The vehicle cabin is typically heavily laden with heat due to pronounced amounts of heat transfer through the engine firewall, the vehicle floorpan, and, most markedly, the glass windows of the cabin. In order to facilitate the rapid cooling of a heat-soaked vehicle cabin, mobile a/c systems typically have cooling capacities which rival those of household room air conditioners. Mobile a/c components must be efficient enough to provide this capacity while remaining small enough in size and weight to be practical for vehicle applications. In addition, the input power to the system must be low in order to minimize the load on the vehicle's engine so as to promote better fuel economy and fewer drivability concerns. Most importantly, the system must be able to efficiently deliver its capacity and maintain a steady level of cooling while operating in an ever-transient environment. The fact that mobile a/c systems operate almost entirely under transient conditions is what truly sets these systems apart from others. The major operating transients include: (i) changes in compressor speed due to the variations in vehicle engine speed, (ii) changes in condenser air flow due to ram-air effects at the front of the vehicle, (iii) changes in the passenger compartment air temperature during a pulldown mode, and (iv) cycling of the compressor clutch to prevent evaporator frosting.

## 1.2 Project Description

### 1.2.1 Project Motivations

Most current mobile a/c systems utilize an orifice tube, as opposed to a thermostatic expansion valve, to throttle the refrigerant stream from the high-pressure condensing conditions

to the low-pressure evaporating conditions. Orifice tubes are advantageous in the respect that they are inexpensive to produce and have no moving parts, and, thus, generate fewer reliability concerns. However, unlike a thermostatic expansion valve, an orifice tube does not actively control the system capacity. Instead, the capacity is typically controlled by cycling the compressor clutch off and on. Unfortunately, the cycling action introduces efficiency losses to the system and promotes increased clutch wear. In addition, the cycling action often generates noticeable swings in the evaporator outlet air temperature and objectionable surges in the vehicle engine load. Load surges are particularly noticeable in vehicles which utilize optimized drive trains and downsized engines to achieve better fuel economy. Hence, mobile system designers are in need of alternative control techniques which (i) improve the energy efficiency of the system, (ii) minimize abusive transients, (iii) minimize the effects on drivability, and (iv) maintain a smooth and steady evaporator outlet air temperature during transient modes of operation. Modern advances in microprocessor technologies and variable-displacement compressor designs make advanced control strategies an increasingly attractive option for achieving these performance goals.

In addition to the need for improved control strategies, mobile system manufacturers are also in need of methods by which to improve the reliability of their systems so as to reduce warranty costs and increase customer satisfaction. On-board diagnostic tools which can detect and predict potential system failures are of particular interest. Such tools are especially beneficial in heavy-equipment system applications because a/c system failures can lead to expensive downtimes in these applications due to the fact that safety regulations require the a/c system to be in working order if the machine is to be used in hot working environments.

Finally, in compliance with recent governmental legislation designed to eliminate the use of ozone-depleting refrigerants such as R-12, all new mobile a/c systems introduced to the marketplace must use a refrigerant which is environmentally safe. The current fluid of choice is refrigerant R-134a. The phaseout of R-12 necessarily prompted manufacturers to redesign existing systems for use with the new refrigerant. As a result, a renewed emphasis was placed upon the general need for a flexible mobile a/c system integration and design tool. In particular, mobile system manufacturers have expressed a desire for a model-based design package which can be used to accurately predict both the transient and steady-state performance characteristics of prototype and existing systems.

### 1.2.2 Project Goals

In response to the above motivations, we focused our research around three central project goals. They are:

(1) To thoroughly document the transient behavior and performance characteristics of mobile a/c systems, and to use this knowledge to develop transient system models which aid in the design, simulation, control, and diagnosis of mobile a/c systems.
(2) To develop microprocessor-based advanced control algorithms which optimize the performance of a given mobile a/c system through efficient use of devices such as variable-displacement compressors, electronic expansion valves, and variable-speed fans.
(3) To develop real-time diagnostic tools which predict faults and failures within the a/c system and then store the information in on-board memory which can be accessed by a service technician to help facilitate the troubleshooting and repair process.

The first and foremost step toward achieving these objectives was to design and construct a suitable test facility. In particular, the proposed facility had to be flexible enough to accommodate the complete system of any given manufacturer with a reasonable amount of installation time, as well as be able to accommodate emerging technologies such as variable-displacement compressors and electronic expansion valves. In addition, the facility had to be designed in a manner which enables the researcher to simulate the wide range of transient operating conditions experienced by mobile a/c systems in field usage. Finally, the facility had to be thoroughly instrumented on a full-scale system level to allow the researcher to be able to collect both the quantitative and qualitative data necessary to develop and validate transient system models. Our test facility meets each of these requirements.

## 1.3 Overview of the Test Facility

The conceptual structure of our test facility is illustrated in the form of a block diagram in Figure 1.1. As is shown in the diagram, the facility is comprised of five main subsystems: (1) an air flow system, (2) the test refrigeration system, (3) a data acquisition system, (4) an environment controller, and (5) a system controller. This document focuses on the design, construction, and performance of the air flow system, the refrigerant loop, and the data acquisition system. The environment controller is under current development and will be detailed in a future publication. Likewise, the system controller will be developed and documented in future research. The two controllers are discussed briefly at the end of this chapter.

### 1.3.1 Air- and Refrigerant-Side Loops

Figure 1.2 shows the general layout of the air- and refrigerant-side loops, as well as the layout of the test facility instrumentation. The air flow system is seen to be comprised of separate evaporator- and condenser-side air loops. Each air loop is equipped with a controlled

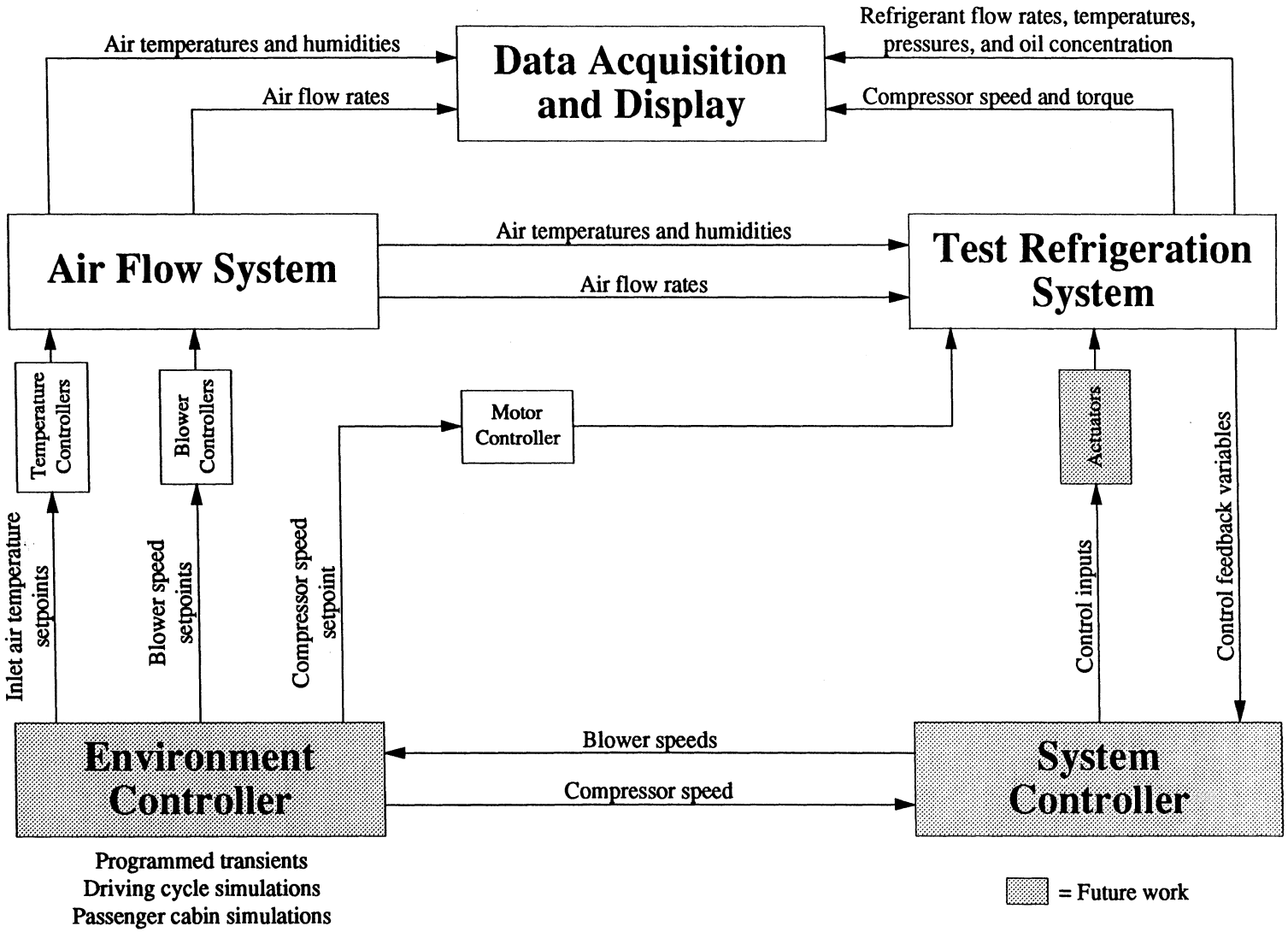


Figure 1.1 The major subsystems of the test facility.

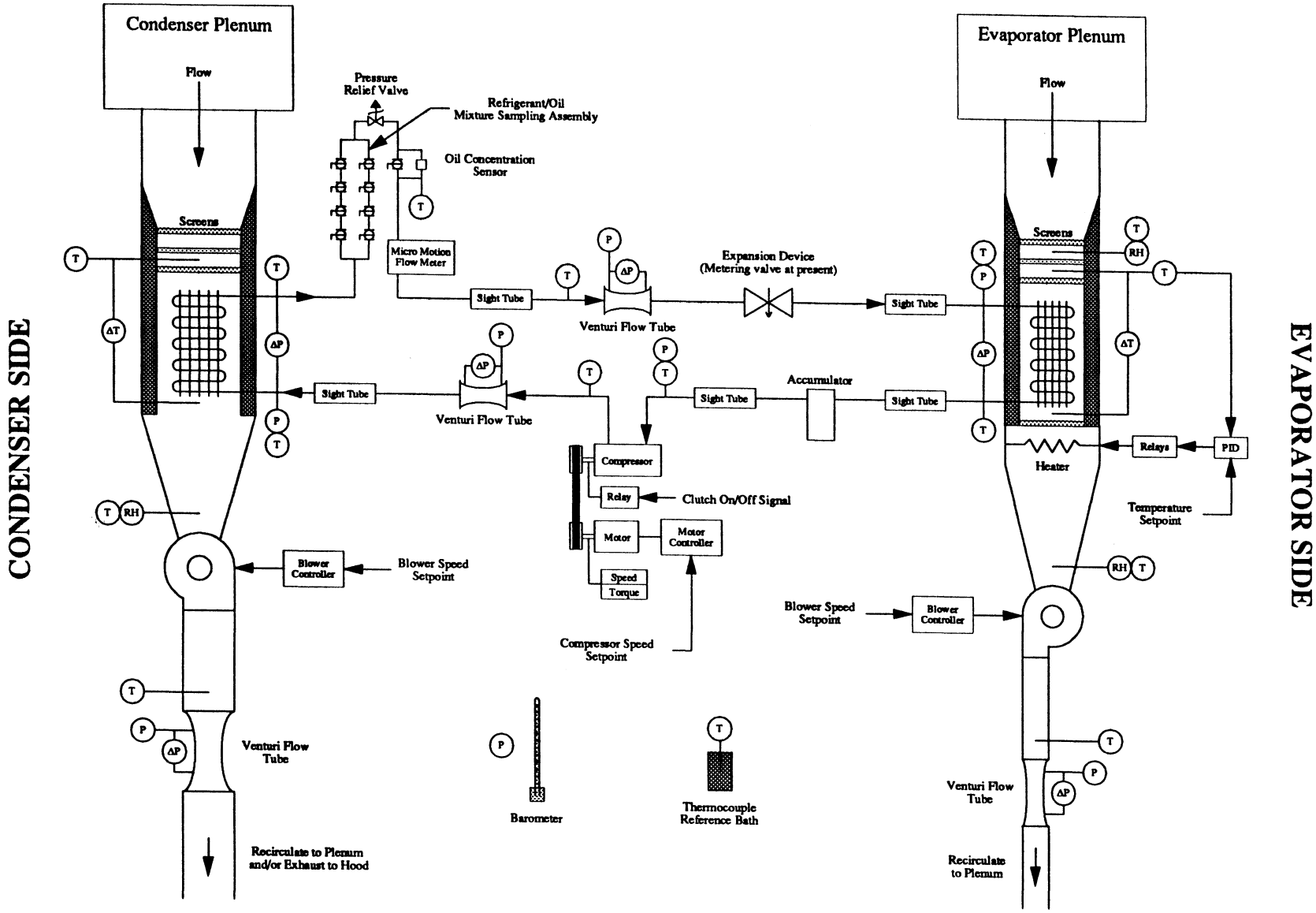


Figure 1.2 The general layout of the test facility components and instrumentation.

blower which establishes the air flow rate across the heat exchanger. The air flow rates are measured with calibrated Venturi Flow Tubes (VFT's). Furthermore, each air loop is thoroughly instrumented with electronic pressure, temperature, and humidity sensors which enable the researcher to record transient air-side performance data in addition to steady-state air-side calorimetry data. The evaporator air loop is equipped with a controlled heater which allows the researcher to vary the evaporator inlet air temperature in a wide variety of steady or dynamic patterns. A similar heater will be installed in the condenser-side air loop in the future. The individual loop controllers receive their command setpoints from the environment controller of Figure 1.1. The air loops can accommodate the heat exchangers of both automotive and heavy-equipment systems. Space to accommodate a second test section tunnel has been reserved in the evaporator air loop to facilitate future testing of two-evaporator mobile a/c systems, such as those of vans, buses, and other large-cabin vehicles.

Like the air loops, the refrigerant loop can accommodate the stock or prototype components of nearly any mobile a/c system. In accordance with new mobile a/c system designs, the loop uses refrigerant R-134a. The refrigerant loop is thoroughly instrumented with pressure and temperature sensors which enable the researcher to record a variety of transient and steady-state data over a broad range of operating conditions. Mass flow meters are installed in both the discharge line and the liquid line of the loop to allow for quantitative analysis of the storage and distribution of the refrigerant charge during transient modes of operation. The refrigerant loop is also extensively instrumented with cylindrical sight tubes which permit visual identification of the refrigerant state, distribution, and flow regime in any part of the system. Furthermore, the liquid line of the loop is fitted with a prototype sensor which measures the circulating compressor oil concentration in real time. The compressor speed is regulated by a controlled drive motor, and the compressor clutch can be activated either manually or with a computer-controlled relay. The compressor drive assembly is also equipped with speed and torque sensors. In short, both the air- and refrigerant-side loops of the facility are well equipped to conduct transient modeling studies, as well as diagnostic and control studies.

### 1.3.2 Environment Controller

The environment controller is a PC-based real-time controller which regulates the test conditions seen by the evaporator, condenser, and compressor. We are presently in the process of implementing this controller. On its most basic level, the environment controller acts as an automated user interface which allows the researcher to remotely set the values of the compressor speed, the compressor clutch cycling rate, the condenser air flow rate, the evaporator air flow rate, and the evaporator inlet air temperature. The environment controller also allows the researcher to run preprogrammed routines which change the system inputs in a prescribed

manner. This latter property of the environment controller allows us to simulate the wide variety of transient operating conditions encountered by mobile a/c systems in field usage. For example, via remote setpoint control of the compressor motor controller, we can vary the compressor speed in a manner which mimics the engine speed fluctuations of a city or highway driving cycle. Likewise, the condenser air flow rate can be simultaneously changed along with the compressor speed to simulate ram-air effects at the front of the vehicle. Furthermore, by supplying the evaporator-side heater controller with an evaporator inlet air temperature setpoint which decays over time, we can simulate the initial pulldown of a heat-soaked passenger cabin. In general, the environment controller is a versatile tool for generating a wide, repeatable range of system dynamics for the development and validation of transient models and advanced control algorithms.

### 1.3.3 System Controller

As was previously discussed, the system controller will be a microprocessor-based device which utilizes advanced control algorithms to optimize the performance of a given mobile a/c system. Because advanced control techniques often utilize predictive-type system models, the system controller is also likely to serve as a diagnostics device capable of detecting system faults such as refrigerant charge loss or expansion valve failure. Future and/or existing sensors on the air- and refrigerant-side loops will be used to sense the inputs to the system controller. However, as is shown in Figure 1.1, the compressor speed will most likely be passed to the system controller by the environment controller to simulate the process of reading an engine speed from the Electronic Control Module (ECM) of a vehicle. The most effective combination of sensors, actuators, and control algorithms will be determined through future research.

# 2. DESIGN AND CONSTRUCTION OF THE TEST FACILITY

## 2.1 Air Flow System

### 2.1.1 Air Loop Design Criteria

The air loops are designed to meet the specifications shown in Table 2.1. At the time we designed our facility, the mobile a/c market was undergoing the change from systems which use refrigerant R-12 to those which use R-134a. The R-134a designs had not yet been released in the marketplace, and any information concerning these new designs was either tentative or proprietary. Hence, the maximum air flow rates specified in Table 2.1 were based upon those of typical R-12 systems and past sponsor recommendations. R-134a systems tend to use higher air flow rates, but we intentionally oversized our blowers in anticipation of this fact, and our facility is capable of delivering air flow rates which are typical of R-134a systems. Similarly, the maximum heat exchanger sizes specified in Table 2.1 were based upon the overall dimensions of R-12 mobile a/c evaporators and condensers existing in the market at the time we formed our design. The maximum evaporator inlet air temperature specified in Table 2.1 approximates the temperature of a heat-soaked vehicle cabin on a hot summer day. The maximum condenser inlet air temperature specified in Table 2.1 approximates the temperature of desert air entering the front grille of a vehicle.

Table 2.1 The basic design specifications of the evaporator and condenser air loops.

| Design Variable | Evaporator Air Loop | Condenser Air Loop |
|---|---|---|
| Heat Exchanger Size (max.) | 16 in. x 16 in. | 40 in. x 24 in. |
| Inlet Air Temperature (max.) | 120 °F | 120 °F |
| Air Flow Rate | 40–240 scfm | 400–1600 scfm |

### 2.1.2 Air Loop Configurations

Figure 2.1 shows a pictorial view of the evaporator air loop. The evaporator air loop is a closed loop in which chilled air exiting the evaporator is heated and recirculated to the inlet. We chose this configuration because it easily facilitates the simulation of a vehicle cabin pulldown process. During a cabin pulldown process, chilled air from the evaporator enters the passenger compartment of the vehicle and receives heat from the thermal loads of the cabin. The air stream then recirculates to the evaporator inlet and transfers the heat to the refrigerant. This is exactly the case in Figure 2.1, in which our controlled duct heater acts as the variable heat load of the cabin.

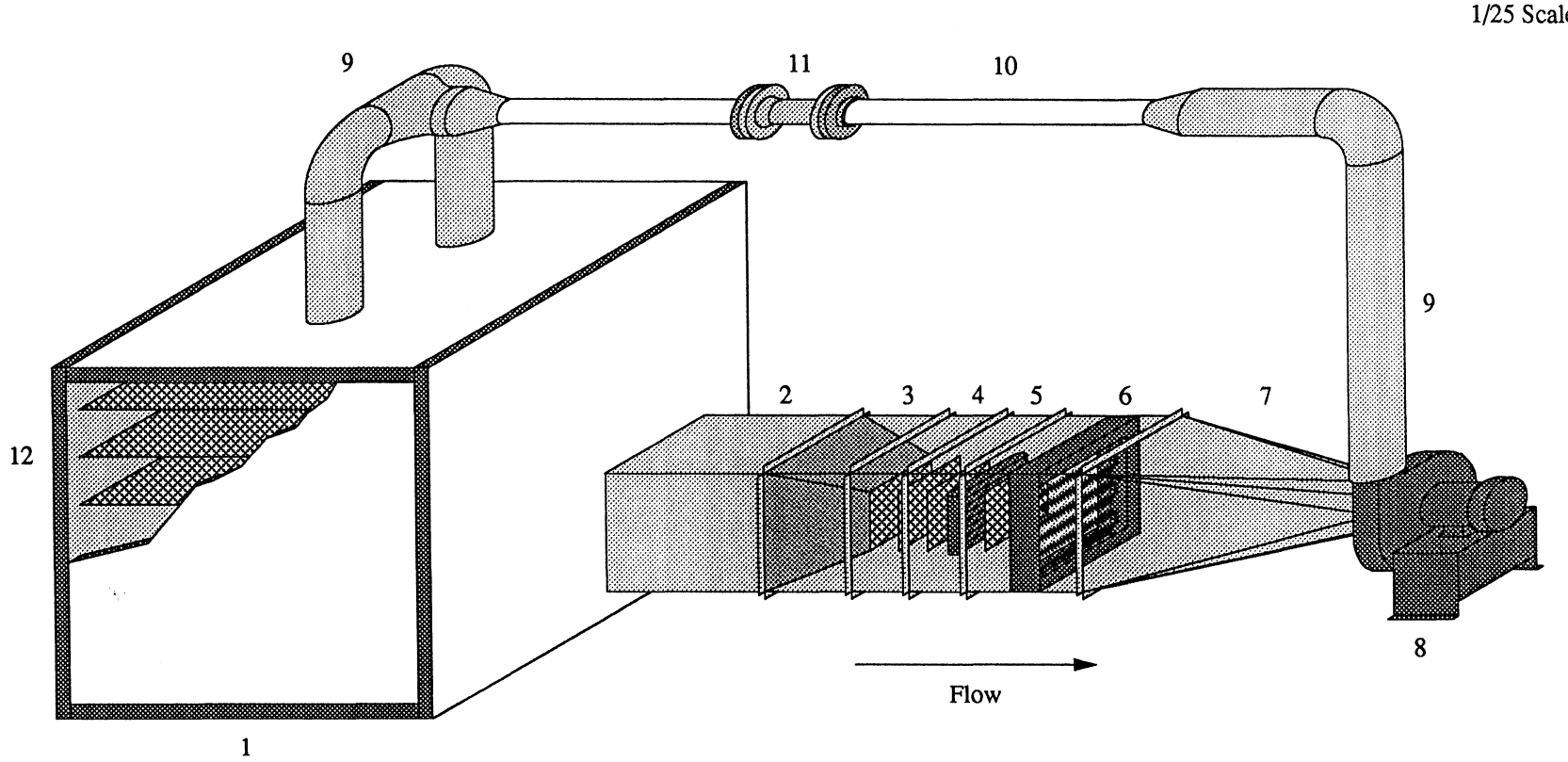


1. Plenum
2. Entrance Section
3. Converging Section
4. Measurement Section
5. Heat Exchanger Section
6. Heater Section
7. Rectangular-to-Round Transition
8. Blower
9. Sheet Metal Pipe (6-in. Dia.)
10. PVC Pipe (3-in. I.D.)
11. Venturi Flow Tube
12. Plenum Screens

Figure 2.1 The evaporator air loop.

Figure 2.2 shows a pictorial view of the condenser air loop. The condenser air loop is a semiclosed loop capable of 0–100 % recirculation. Supply air is drawn in from the room through an intake port cut into the top of the plenum, and hot condenser outlet air is either expelled out of the room through our laboratory's fume hood exhaust pipe or recirculated to the plenum to adjust the temperature of the condenser inlet air stream. In the future, a heater will be added upstream of the condenser to improve the inlet air temperature control capability and to permit us to establish above-ambient initial temperature conditions at the condenser inlet.

### 2.1.3 Air Loop Components

#### 2.1.3.1 Plenums

The plenum of each loop dampens turbulence in the air stream to promote a smooth, repeatable flow at inlet of the test section tunnel. Each plenum is constructed of 2-in. thick panels of foam insulation board (Celotex® Model No. 604). The panels are fastened to an internal skeletal frame made of Unistrut™ steel channels. The insulation board provides structural rigidity while limiting the heat transfer between the air stream and the ambient environment. The interior board surfaces have a light-gage aluminum foil facer which prevents moisture absorption from the air stream. The exterior board surfaces have a heavy-gage aluminum foil facer which protects the brittle insulation material from accidental dents and punctures. The joints formed by adjacent boards are sealed with aluminum foil tape to prevent air and moisture leakage.

Turbulence reduction is accomplished by expanding the air flow into the large plenum volume so as to greatly reduce the flow velocity. The plenums were made as large as possible within the spatial constraints of our lab to allow the greatest possible velocity reduction. The interior dimensions of the plenums measure 3 ft 11 in. (W) x 3 ft 8 in. (H) x 4 ft (D) (evaporator side) and 3 ft 5 in. (W) x 3 ft 8 in. (H) x 4 ft (D) (condenser side). In addition, each plenum contains three fine-mesh polypropylene flow conditioning screens (100 x 100 mesh per inch, 0.0042-in. wire diameter, 34 % open area) which further dampen turbulence and promote uniform filling of the chamber. Polypropylene screen is used because it is inexpensive (i.e., compared to wire screens of the same mesh size) and resistant to moisture. The screens are framed in aluminum channels commonly used for making household storm door windows. The frames are equally spaced between the top of the plenum and the top of the test section tunnel and are held in place by brackets bolted to the interior Unistrut frame.

The evaporator plenum has two 6-in. diameter return ports which equally distribute the recirculated air stream in the chamber when testing a single-evaporator system. Space is reserved on the front face of the plenum to accommodate a second tunnel for testing two-

1/25 Scale

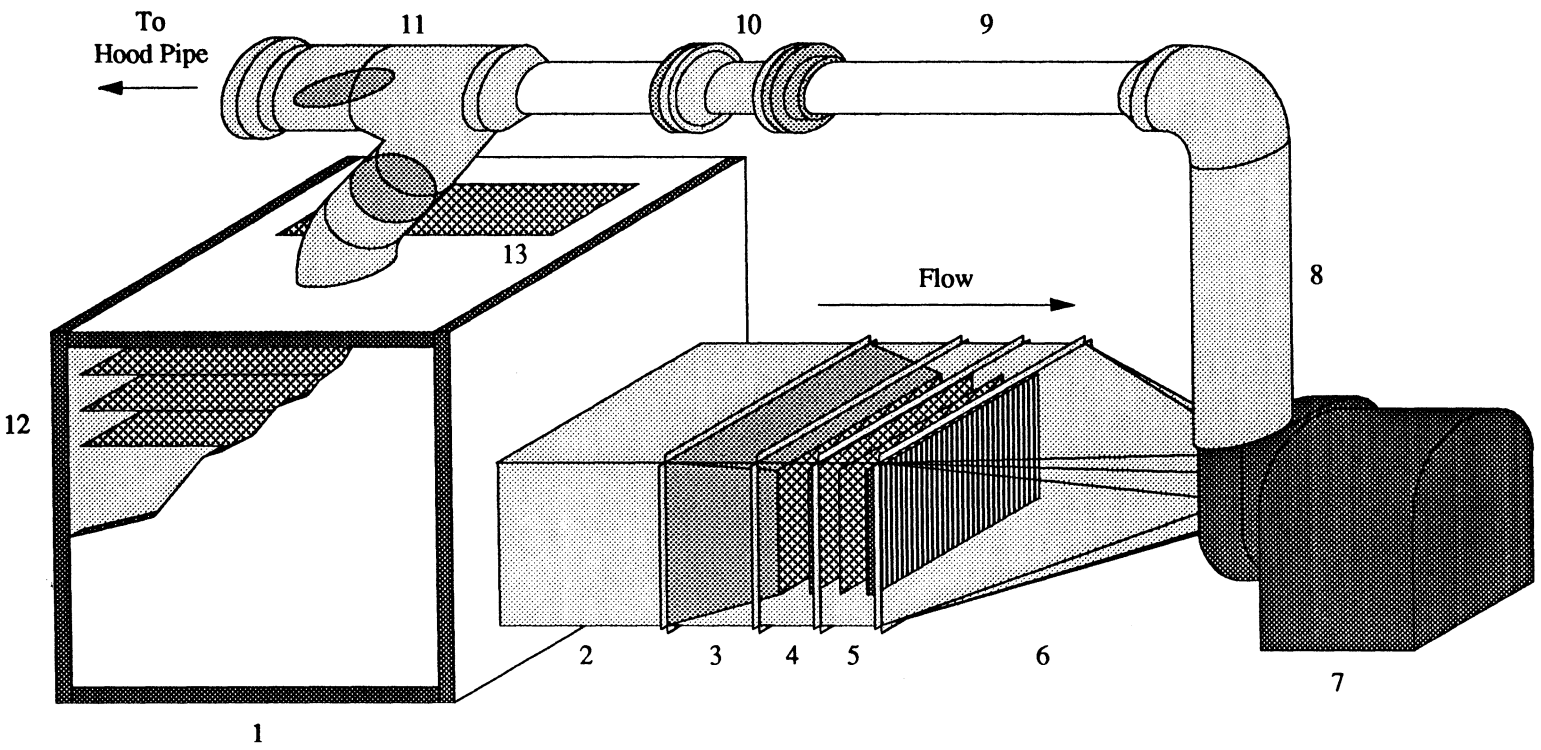


1. Plenum
2. Entrance Section
3. Converging Section
4. Measurement Section
5. Heat Exchanger Section
6. Rectangular-to-Round Transition
7. Blower
8. Sheet Metal Pipe (10-in. Dia.)
9. PVC Pipe (6-in. I.D)
10. Venturi Flow Tube
11. Recirculation Section (10-in. Dia.)
12. Plenum Screens
13. Air Intake Port

Figure 2.2 The condenser air loop.

evaporator systems. In such tests, the second return port is assigned to the second evaporator loop. The condenser plenum has a 13-in. x 36-in. ambient-air intake port covered with a medium-mesh screen which traps dust and prevents foreign objects from entering the chamber. Recirculated air enters through an adjacent 10-in. diameter port and mixes with the ambient intake air in the turbulent area above the first polypropylene flow conditioning screen.

#### 2.1.3.2 Test Section Ducts

Figure 2.3 shows the duct pieces which comprise the test section tunnel of each air loop. The pieces were fabricated from 22-gage galvanized sheet metal at the University of Illinois Physical Plant sheet metal shop. The galvanized material helps ensure that the ducts do not corrode after being repeatedly exposed to high-humidity test conditions. The tunnel pieces connect with 1-in. folded flanges lined with adhesive-backed strips of 1/8-in. thick closed-cell blended-rubber gasketing material (McMaster-Carr Stock No. 8694K67). The flanges are held together with #8-32 zinc-coated (i.e., corrosion-resistant) round head machine screws and nuts, and the corner joints are sealed with Panduit® duct seal putty to prevent air and moisture leakage. Each tunnel is supported by a Unistrut framework. Several of the tunnel pieces shown in Figure 2.3 are packed with removable plywood inserts which support the air-side temperature and humidity instrumentation and tailor the flow to the size of the specific heat exchanger being tested. Instructions for packing and assembling the tunnel pieces are given in Weston (1996). The tunnel pieces are further described below.

Entrance Section

The entrance section simply joins the plenum to the remaining pieces of test section tunnel. The entrance section of the evaporator air loop is presently empty, but may be used in the future to house humidity injection ports and/or temperature and humidity mixing vanes. The entrance section of the condenser air loop is also presently empty, but will house a heater in the future. Selection of a condenser air loop heater was postponed until the performance of the recirculation damper scheme could be evaluated and experience had been gained from the evaporator-side heater installation. The evaporator-side heater was initially installed in the entrance section of the evaporator air loop, and subsequent tests revealed the evaporator inlet air temperature profile was severely stratified with the heater installed in this location (as much as 20 °F for a 90–100 °F inlet air temperature setting). The severe stratification was caused by the following facts:

(1) The coils of the duct heater are unevenly spaced by the manufacturer, resulting in uneven heating of the air stream.

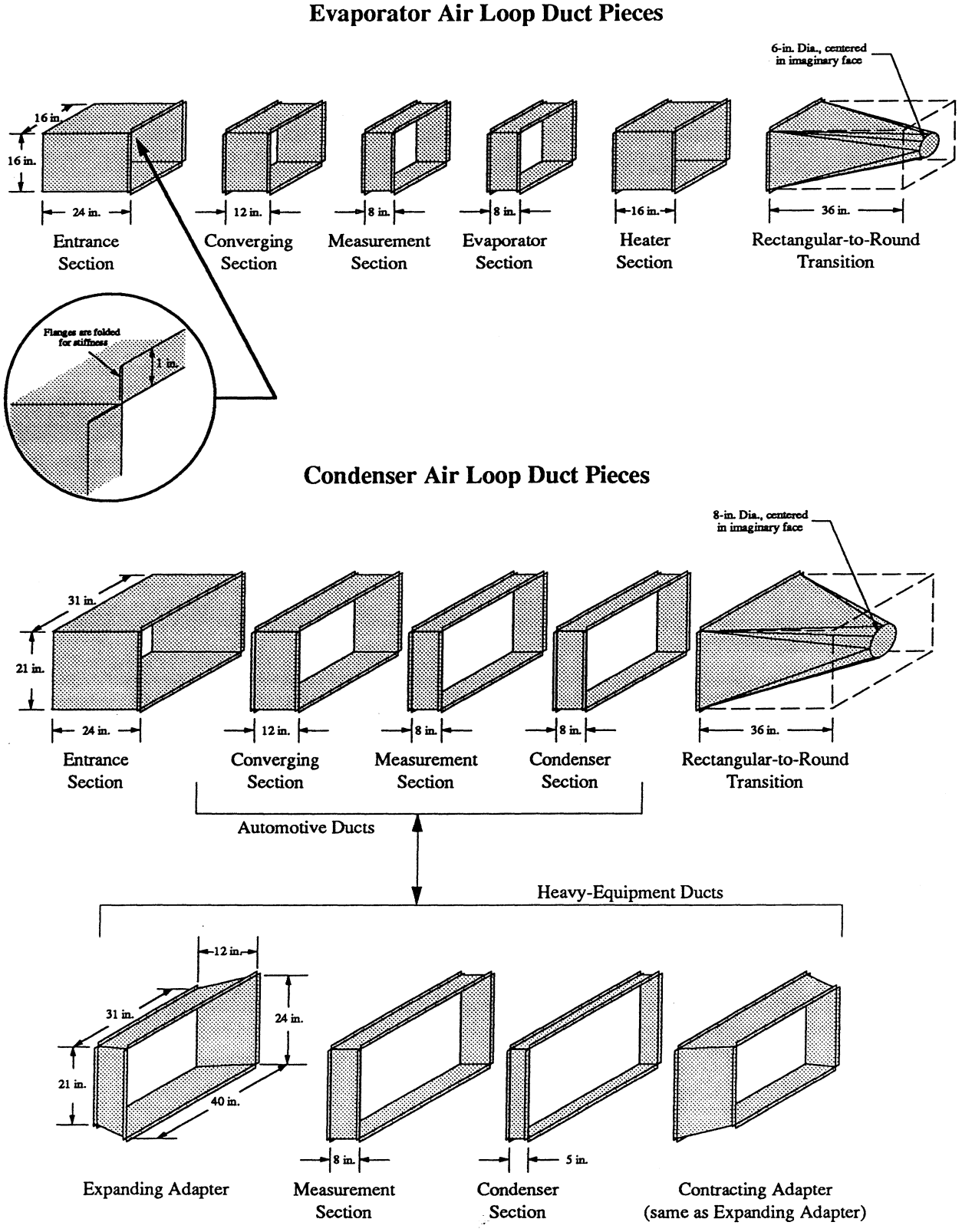


Figure 2.3 The duct pieces which comprise the test section tunnels of the air loops.

(2) Flow conditioning screens mounted in tunnel sections downstream of the entrance section inherently suppress turbulent mixing of the air stream.
(3) The velocity profile at the heater inlet was underdeveloped due to the relatively short distance between the exit of the plenum and inlet of the heater, thereby causing some of the coils to run hotter than others and unevenly heat the air stream.

We resolved the stratification problem by moving the heater to the location shown in Figure 2.1 (i.e., downstream of the evaporator) so as to allow the heated air stream to be judiciously mixed by the blower before recirculating to the evaporator inlet. Unlike the evaporator air loop, the condenser air loop is not a closed flow system, so the heater must be located upstream of the condenser (i.e., in the entrance section) in order to control the condenser inlet air temperature in situations where recirculation cannot be used (such as during a test in which the condenser outlet air temperature varies transiently). Experience gained from the evaporator-side heater installation dictates that a section of mixing vanes must be installed downstream of the future condenser-side heater, and that a fine-mesh screen must be located upstream of the heater to ensure a well-developed velocity profile at the heater inlet. Unfortunately, the spatial constraints of our lab prevent us from extending the length of the entrance section significantly past its present length of 24 in. to help correct the latter flow development problem.

Converging Section

The converging section contracts the cross-sectional area of the tunnel to the size of the heat exchanger being tested, thereby creating a more uniform and repeatable velocity profile at the heat exchanger inlet. Figure 2.4 shows an exploded view of a typical evaporator-side converging section. The convergent is formed from panels of 1/4-in. thick plywood which are held together by wood glue and/or zinc corner braces. The plywood is covered with aluminum foil tape to provide a smooth flow surface and to prevent the wood from absorbing moisture during high-humidity tests. The convergent mounts in the duct with an interference fit, and the side cavities between the convergent and the duct are filled with foam insulation to limit heat transfer between the air stream and the ambient environment. The insulation also helps to further secure the convergent in the duct. A condenser-side converging section is constructed in the same manner shown in Figure 2.4. However, the condenser-side section is replaced with the expanding adapter piece shown in Figure 2.3 when testing condensers larger than 31 in. x 21 in. All of the condensers we have tested to date have essentially filled the entire cross-sectional area of the duct, so condenser-side convergents have not yet been used.

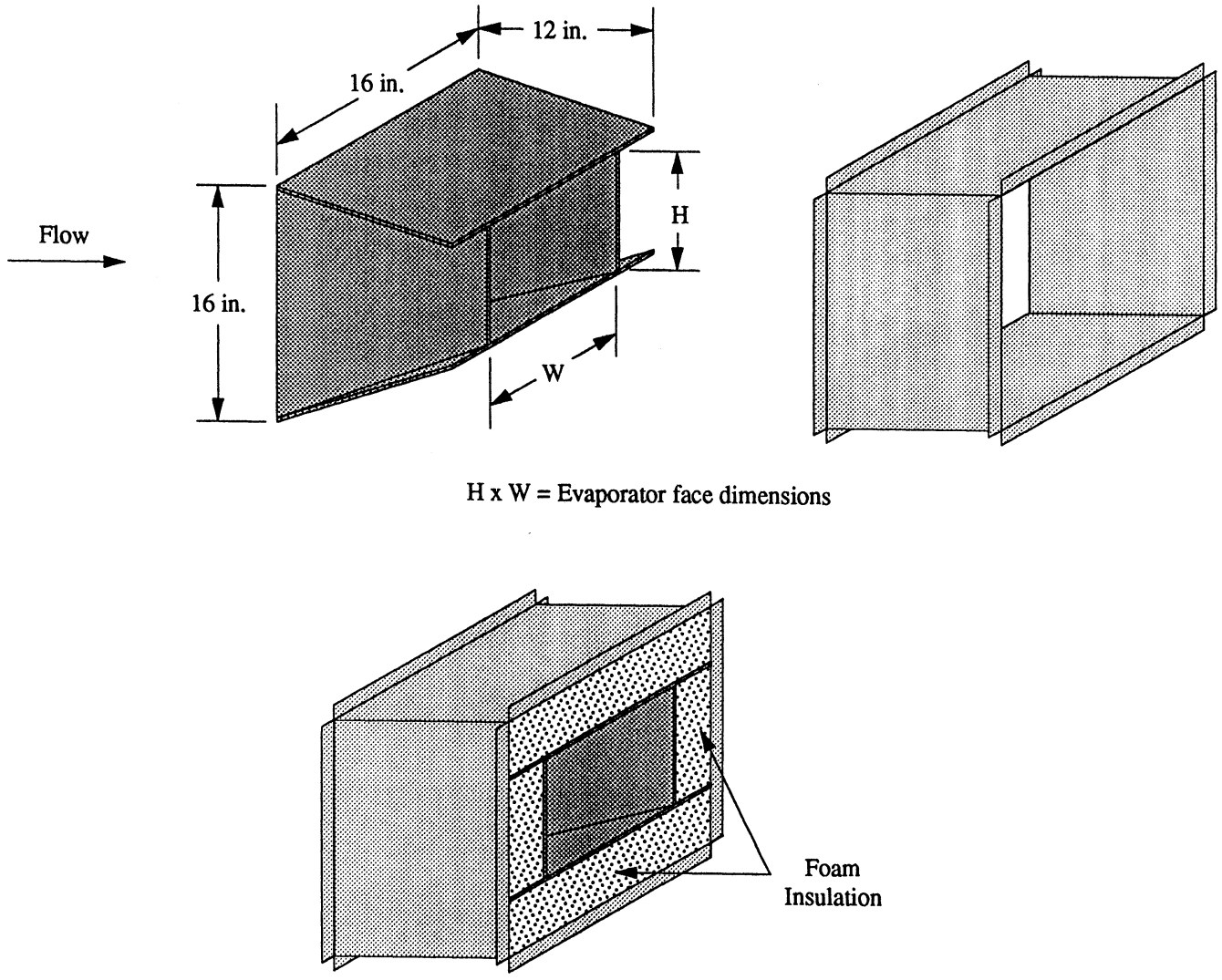


Figure 2.4 A typical evaporator-side converging section.

Measurement Section

The measurement section houses air-side temperature and humidity instrumentation, as well as three fine-mesh polypropylene screens which help create a uniform velocity profile at the heat exchanger inlet. The screens have the same specifications as those used in the plenums. Figure 2.5 shows an exploded view of a typical evaporator-side measurement section. A condenser-side section is constructed in the same manner but excludes the humidity probe. As is shown in the figure, the screens are held by 3/4-in. thick plywood frames which preserve the cross-sectional area established by the upstream convergent. The screen at the inlet of the section reduces turbulence, destroys developing boundary layers, and flattens the velocity profile of the incoming air stream. A humidity probe located 2.25 in. behind the inlet screen senses the relative humidity upstream of the heat exchanger. The spacing between the probe and the screen was chosen to be slightly larger than the distance over which eddies shed by the screen should decay, which is approximately 500 times the screen wire diameter of 0.0042 in., or 2.1 in. in this case (Gavin, 1983). A second screen located 1.75 in. downstream of the humidity probe further flattens the velocity profile and removes the nonuniformities introduced to the profile by the obtrusive body of the probe.

A bank of smaller probe ports is located 2.5 in. downstream of the second screen. The ports allow the researcher to traverse the flow area with a thermocouple probe or an anemometer probe so as to verify the uniformity of the temperature and velocity profiles of the flow (uniform temperature and velocity profiles indicate a uniform mass flow across the face of the heat exchanger). The temperature probe tube shown in Figure 2.5 is generally kept positioned in the center of the duct to sense the inlet air temperature of the heat exchanger. As is shown in Figure 2.5, guide tubes pilot the probe through the cavity between the duct wall and the plywood frame. Like before, all of the side cavities are filled with foam insulation to limit heat transfer between the air stream and the ambient environment.

A nine-point grid formed by intersecting strands of heavy-gage (30-$lb_f$ test) fishing line is located 1 in. downstream of the probe ports. Fishing line is used to form the grid because it is resistant to moisture, unobtrusive to the flow, and does not conduct electricity. The intersections occur at the centroids of an imaginary 3 x 3 grid of equal areas, and a thermocouple is glued to each intersection with the bead pointing upstream. The nine thermocouples comprise the reference junctions of a thermopile used to measure the average outlet air temperature of the heat exchanger. A screen at the exit of the measurement section removes the nonuniformities introduced to the velocity profile by the temperature probe and the thermopile grid.

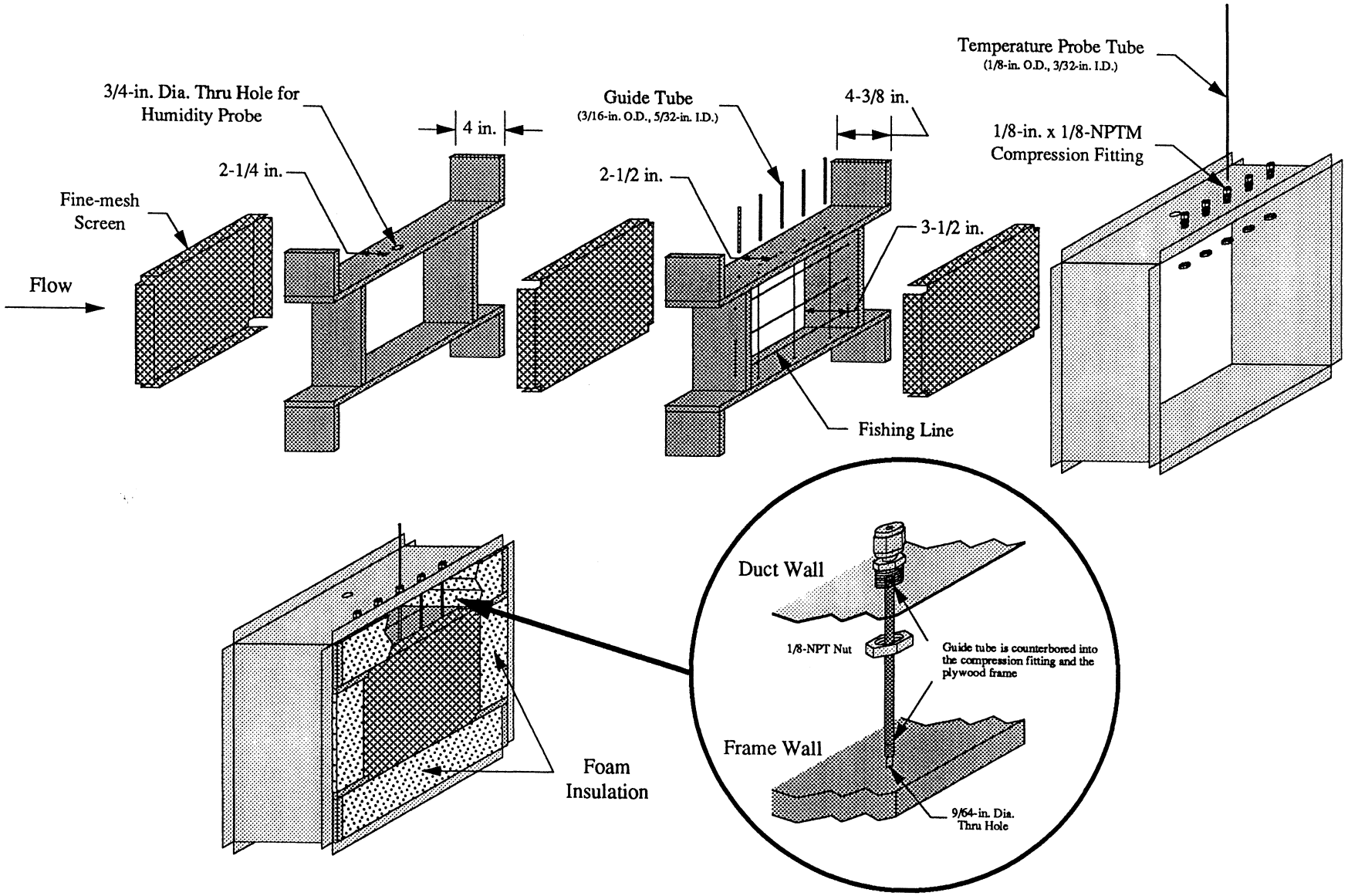


Figure 2.5 A typical evaporator-side measurement section.

Heat Exchanger Section

The heat exchanger section supports and insulates the evaporator or condenser coil being tested. Figure 2.6 shows an exploded view of a typical evaporator-side heat exchanger section. A condenser-side section is constructed in the same manner but excludes the drain pan (a drain is provided at the bottom of the evaporator-side section to guide condensate out of the duct). The plywood frame encasing the heat exchanger exposes only the finned face area of the coil to the air stream so as to permit a smooth, repeatable flow across the coil. Once again, the cavities between the frame and duct walls are filled with foam insulation to limit heat transfer with the ambient environment. Nine thermocouples which constitute the measuring junctions of the thermopile used to measure the average outlet air temperature of the heat exchanger are mounted on a sheet of galvanized wire cloth at the exit of the section. Wire cloth is used instead of fishing line because the cloth can be easily removed to access the heat exchanger coil. In the evaporator air loop, a fine-mesh polypropylene screen covers the downstream side the grid to shield the thermocouples from heater coil radiation.

### 2.1.3.3 Evaporator Air Loop Heater

The evaporator air loop heater is a 7-kW, slip-in style open-coil duct heater (Brasch Electroduct® Model No. S-93-00396) which operates on 240-VAC 3-phase power. When we installed the heater, gaps measuring approximately 3/4 in. existed between the perimeter of the stock heater frame and the interior walls of our duct. The gaps were blocked off with strips of galvanized sheet metal to prevent air from bypassing the heater. A Proportional-Integral-Derivative (PID) controller modulates the heater power to maintain a steady or dynamic evaporator inlet air temperature setpoint. The control circuit is discussed in Chapter 3. In a steady-state test, the heater simply replaces the energy removed from the air stream by the evaporator so as to raise the evaporator inlet air temperature back to its initial value. In a dynamic test, the heater either (i) adds less energy to the air stream than is removed by the evaporator, thereby simulating a cabin cooling process, or (ii) adds more energy to the air stream than is removed by the evaporator, thereby raising the evaporator inlet air temperature in a dynamic fashion for transient modeling purposes.

The heater power rating of 7 kW was selected based upon maximum evaporator cooling capacities observed in past ACRC research (5 kW) plus the additional amount of power (2 kW) used to produce dynamic temperature changes. Applying the First Law of Thermodynamics to a control volume placed around both the evaporator and the heater shows that the net temperature change of the air stream between the inlet of the evaporator and the outlet of the heater (assuming negligible heat transfer with the ambient environment) is given by

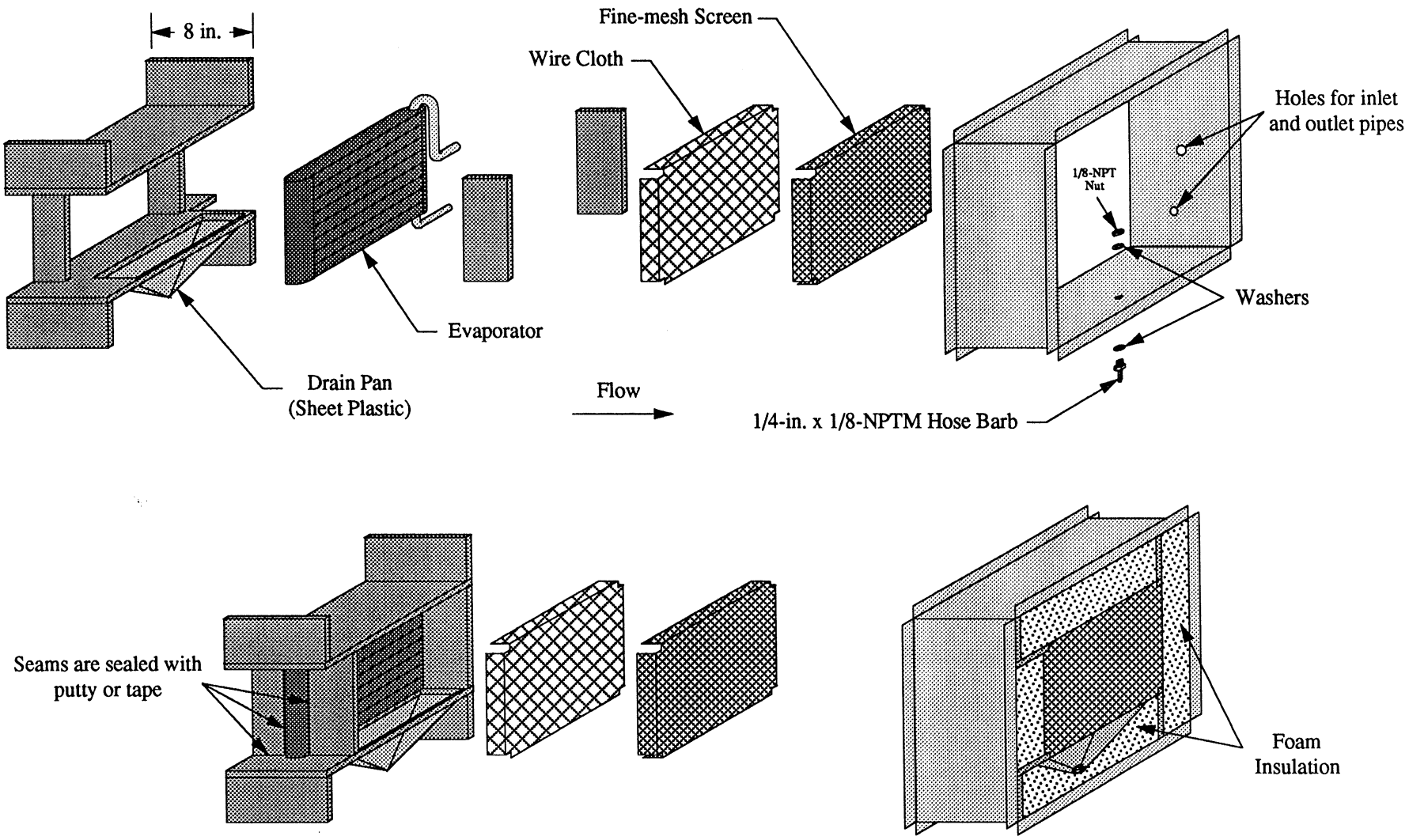


Figure 2.6 A typical evaporator-side heat exchanger section.

$$\Delta T = \frac{\dot{Q}_{heat} - \dot{Q}_{evap}}{\dot{m}_a c_p} \tag{2.1}$$

Assuming a constant specific heat for air of $c_p = 1.007$ kJ/kg-K, the heater can theoretically produce a maximum dynamic temperature change of $\Delta T = 14.6$ °C (26.3 °F) given the maximum heater output of $\dot{Q}_{heat} = 7$ kW, an evaporator cooling load of $\dot{Q}_{evap} = 5$ kW, and an air flow rate of 240 scfm ($\dot{m}_a = 0.136$ kg/s).

2.1.3.4 Blowers

Each air loop utilizes a radial-blade centrifugal blower and a variable-speed drive to achieve a wide, repeatable range of air flow rates. The blowers are sized to produce the air flow rates given in Table 2.1, plus a factor of safety which accounts for the increased flow rates used in R-134a systems and allows future equipment to be added to the loops without causing a significant loss of air flow. The blower sizing process is detailed in Weston (1996). In short, the process involves estimating the pressure losses caused by the proposed flow system at a given flow rate and density, and then selecting a blower which can provide an equivalent pressure rise at that flow rate and density. In order to calculate worst-case estimates of the system pressure losses, face dimensions of 7-1/2 in. x 8 in. and 22-3/8 in. x 15 in. were respectively chosen to represent the smallest evaporator and condenser sizes to be tested in our facility, and the condenser air loop was assumed to be operating in an open-loop fashion (i.e., with the exhaust flow discharging to the atmosphere as opposed to being recirculated to the plenum or vented into the suction pipe of our laboratory's fume hood). Other trial component dimensions and specifications (i.e., blower sizes, screen mesh sizes, flow meter sizes, pipe sizes, etc.) were then selected for each air loop until a blower/system combination was found which could theoretically provide the desired air flow rate (plus a factor of safety) at a reasonable size and cost. Table 2.2 summarizes the specifications of the chosen blowers. A direct-drive blower with a Totally Enclosed Fan-Cooled (TEFC) motor rated 1 hp at 3450 rpm is used in the evaporator air loop (Dayton Model No. 4C108), and a belt-driven blower with a TEFC motor rated 5 hp at 3450 rpm is used in the condenser air loop (Dayton Model No. 4C131). Each blower is mounted on four rubber vibration isolator feet (Grainger Stock No. 4C950) which reduce noise and minimize the vibrations transmitted to adjoining components of the facility.

Evaporator Air Loop Blower Performance

Figure 2.7 shows the predicted worst-case static pressure loss curve for flow through our evaporator air loop (i.e., with a small evaporator installed in the loop) for air flow at standard density ($\rho_{std} = 0.075$ $lb_m/ft^3$). The curve was generated from the results of pressure loss

Table 2.2 Summary of the air loop blower specifications.

| Blower Model No. | Inlet Diameter | Wheel Diameter | Outlet Dimensions | Motor Nameplate Rating | Drive Type |
|---|---|---|---|---|---|
| 4C108 | 6 in. | $10\frac{9}{16}$ in. | $3\frac{1}{2}$ in. x 4 in. | 1 hp at 3450 rpm | Direct |
| 4C131 | 8 in. | $13\frac{1}{2}$ in. | $5\frac{3}{4}$ in. x $7\frac{1}{8}$ in. | 5 hp at 3450 rpm | Belt |

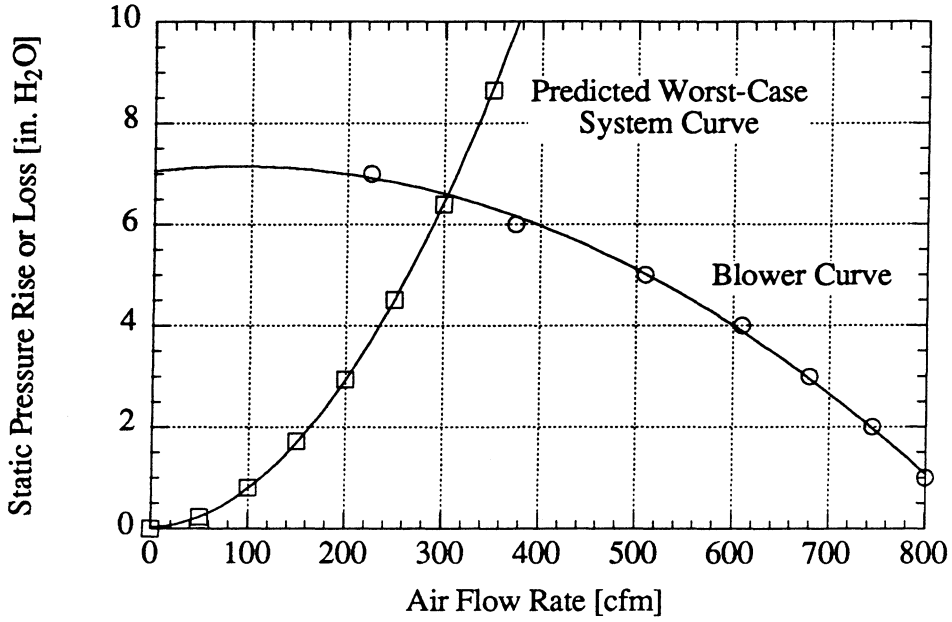


Figure 2.7 The Dayton 4C108 blower curve and the predicted worst-case static pressure loss curve for standard-density flow through the evaporator air loop.

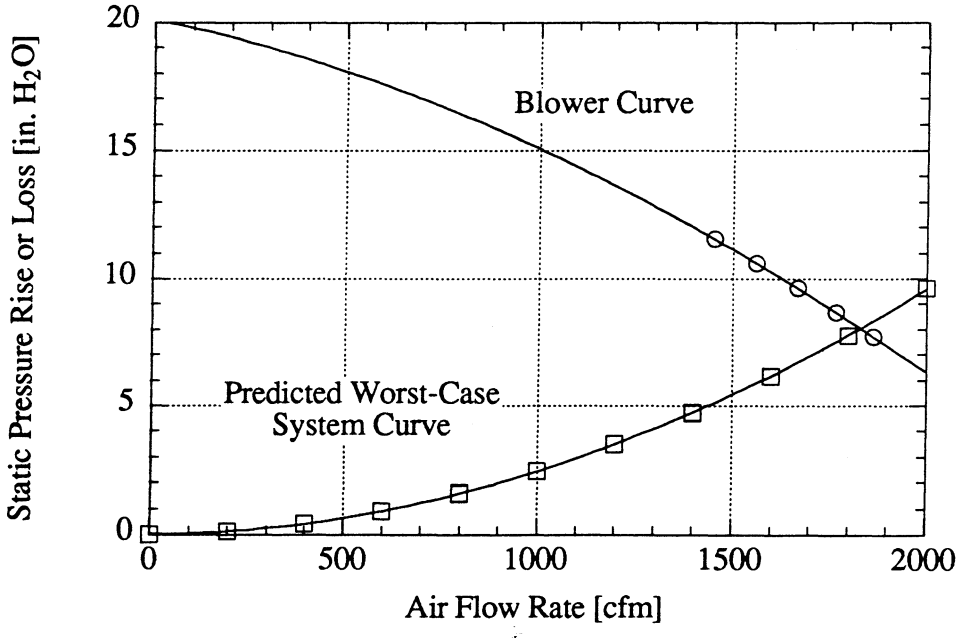


Figure 2.8 The Dayton 4C131 blower curve and the predicted worst-case static pressure loss curve for standard-density flow through the condenser air loop.

calculations given in Weston (1996). The predicted static pressure loss is 4.17 in. $H_2O$ at the maximum design flow rate of 240 scfm. Figure 2.7 also shows a plot of the Dayton 4C108 blower rating data for a blower speed of 3450 rpm. A second-order polynomial curve fit of the rating data shows that the blower can produce a static pressure rise of 6.87 in. $H_2O$ when delivering 240 scfm, yielding a comfortable safety factor of 1.65 (65 % excess) between the rated and required static pressure specifications. The intersection of the blower rating curve and the predicted system pressure loss curve indicates the blower should actually be able to generate an air flow rate of 305 scfm under the worst-case conditions. We presently measure a maximum air flow rate of 302–306 scfm with (i) a larger evaporator coil installed in the loop (10-1/4 in. x 7-1/2 in. face dimensions), (ii) an additional screen installed in the loop not accounted for in the original design calculations (i.e., the screen shielding the evaporator outlet thermocouple grid from heater radiation), and (iii) the motor running at its natural speed (i.e., with the motor speed controller inputting a 60-Hz line frequency to the motor). The measured flow is in excellent agreement with the design flow. By running the motor overspeed up to a line frequency 77 Hz, we are able to generate air flow rates up to 365 scfm. For frequencies greater than 77 Hz, the motor current exceeds the maximum rated current of the speed controller.

Condenser Air Loop Blower Performance

Figure 2.8 shows the predicted worst-case static pressure loss curve for flow through our condenser air loop (i.e., with a small condenser installed in the loop and with no recirculation or assistive hood suction) for air flow at standard density. The curve was also generated from the results of pressure loss calculations given in Weston (1996). The predicted static pressure loss is 6.14 in. $H_2O$ at the maximum design flow rate of 1600 scfm. Figure 2.8 also shows a plot of the Dayton 4C131 blower rating data for a drive motor speed of 3450 rpm (i.e., a blower shaft speed of 3848 rpm). A second-order polynomial curve fit of the rating data shows that the blower can produce a static pressure rise of 10.25 in. $H_2O$ when delivering 1600 scfm, yielding a comfortable safety factor of 1.67 (67 % excess) between the rated and required static pressure specifications. The intersection of the blower rating curve and the predicted system pressure loss curve indicates the blower should actually be able to generate an air flow rate of 1830 scfm under the worst-case conditions. We presently measure a maximum air flow rate of 1600–1645 scfm with (i) a larger condenser coil installed in the loop (28 in. x 16-1/2 in. face dimensions), (ii) no recirculation, (iii) an assistive pull of approximately 300 scfm by the fume hood, (iv) the variable-pitch belt drive adjusted to give the highest possible flow rate, and (v) the motor running slightly under its natural speed (i.e., with the motor speed controller inputting a 56.5-Hz line frequency to the motor). We are unable to run the drive above 56.5 Hz without exceeding the maximum output current of the speed controller. At this line frequency, the motor draws 16.5 A

of current, which significantly exceeds the motor nameplate rating of 12 A at 60 Hz. The motor is clearly overloaded. Apparently, the pressure losses in the system are much higher than we had predicted. The problem warrants future investigation.

#### 2.1.3.5 Return Piping

As is shown in Figure 2.1, the evaporator-side blower discharges into a straight length of 6-in. diameter sheet metal pipe which reduces to a 3-in. I.D. run of polyvinyl chloride (PVC) pipe. A Venturi Flow Tube mounted in the PVC pipe is used to measure the air flow rate. The VFT outlet pipe expands into a 6-in. diameter sheet metal tee which splits the flow into the two branches which return to the plenum. The expansion slows the velocity of the air so as to decrease pressure losses in the return fittings and to reduce turbulence at the plenum inlets.

As is shown in Figure 2.2, the condenser-side blower discharges into a straight length of 10-in. diameter sheet metal pipe which reduces to a 6-in. I.D. run of PVC pipe. A VFT mounted in the PVC pipe is used to measure the air flow rate. The VFT outlet pipe expands into a 10-in. diameter 45° wye equipped with a butterfly damper at each outlet. Again, the expansion slows the velocity of the air so as to decrease pressure losses in the return fittings and to reduce turbulence at the plenum inlet. As was previously discussed, by adjusting the dampers, hot condenser outlet air can either be exhausted out of the room through the hood pipe or recirculated to the plenum to raise the temperature of the condenser inlet air stream.

## 2.2 Refrigerant Loop

### 2.2.1 General Components and Connections

A basic mobile a/c refrigerant loop consists of a compressor, a condenser, an expansion device, and an evaporator. Depending upon the type of expansion device used, the system will also have either an accumulator mounted in the suction line or a receiver/drier mounted in the liquid line. The types of inlet and outlet fittings used to connect the components vary widely among manufacturers, and stock refrigerant lines are always bent to fit the routing of a particular vehicle. Hence, the practice of using stock refrigerant lines to connect components in our facility proves to be extremely impractical, and often impossible. Instead, we braze modular pipe assemblies from standard-sized copper pipes and fittings, and we connect these modular assemblies with reusable compression fittings to form general-purpose refrigerant lines which can be easily reconfigured to form a different routing. Although compression fittings have a higher potential for leaks compared to nonpermanent solder-type joints, they are advantageous in the respect that the fittings can be easily disassembled and reconfigured without having to heat

the refrigerant lines. This reduces the chance of contaminating the loop with soldering fluxes and burnt compressor oil residue.

The sizes of our general-purpose lines were selected based upon the typical hose and pipe sizes used in stock mobile a/c systems. These typical sizes are listed in Table 2.3. The hose size designation indicates the nominal hose diameter in sixteenths of an inch (i.e., a #6 hose has a nominal diameter of 6/16 = 3/8 in.). In most stock refrigerant hose assemblies, the hose is crimped to a pipe whose outer diameter matches the hose nominal diameter. However, #12 hoses are often crimped to 5/8-in. O.D. pipe fittings in addition to 3/4-in. O.D. fittings. We join stock mobile a/c components to our general-purpose lines by slightly modifying the original parts or lines. For example, if the stock component is equipped with a manifold block, we usually cut the block from the component and connect the severed pipe ends to our general-purpose lines with compression unions. Figure 2.9 shows an example of an evaporator installed in this manner. Similarly, if the stock component is equipped with a hose fitting, we cut the mating hose at an appropriate distance away from the fitting and crimp a hose-to-pipe compression adapter to the severed end to join the hose our general-purpose line.

Table 2.3 The typical hose and pipe sizes used in stock mobile a/c systems.

| Hose Size | Hose Diameter | | | Pipe Size | Typical Usage |
|---|---|---|---|---|---|
| | I.D. | O.D. | Nominal | | |
| #6 | $\frac{5}{16}$ in. | $\frac{3}{4}$ in. | $\frac{3}{8}$ in. | $\frac{3}{8}$ in. O.D. | Liquid Line |
| #8 | $\frac{13}{32}$ in. | $\frac{29}{32}$ in. | $\frac{1}{2}$ in. | $\frac{1}{2}$ in. O.D. | Discharge Line<br>Liquid Line |
| #10 | $\frac{1}{2}$ in. | 1 in. | $\frac{5}{8}$ in. | $\frac{5}{8}$ in. O.D. | Suction Line |
| #12 | $\frac{5}{8}$ in. | $1\frac{3}{32}$ in. | $\frac{3}{4}$ in. | $\frac{3}{4}$ in. O.D. | Suction Line |

### 2.2.2 Pressure and Temperature (P/T) Taps

Figure 2.10 shows the two modular P/T tap configurations we designed for use in our facility. Assembly instructions are given in Weston (1996). At present, our suction-line taps are constructed from 5/8-in. O.D. copper pipe, and our discharge- and liquid-line taps are constructed from 1/2-in. O.D. copper pipe. In all cases, the refrigerant pressure is sensed by a 1/16-in. diameter static pressure tap drilled through the wall of the pipe (Benedict, 1977). The inner wall of the pipe is filed to remove burrs and to square the edges of the hole. A 1/4-in. x 1/8-NPTF copper fitting brazed to the exterior of the pipe encompasses the hole and seats a 1/8-in. x 1/8-NPTM brass compression fitting. The latter fitting provides a seal around a length

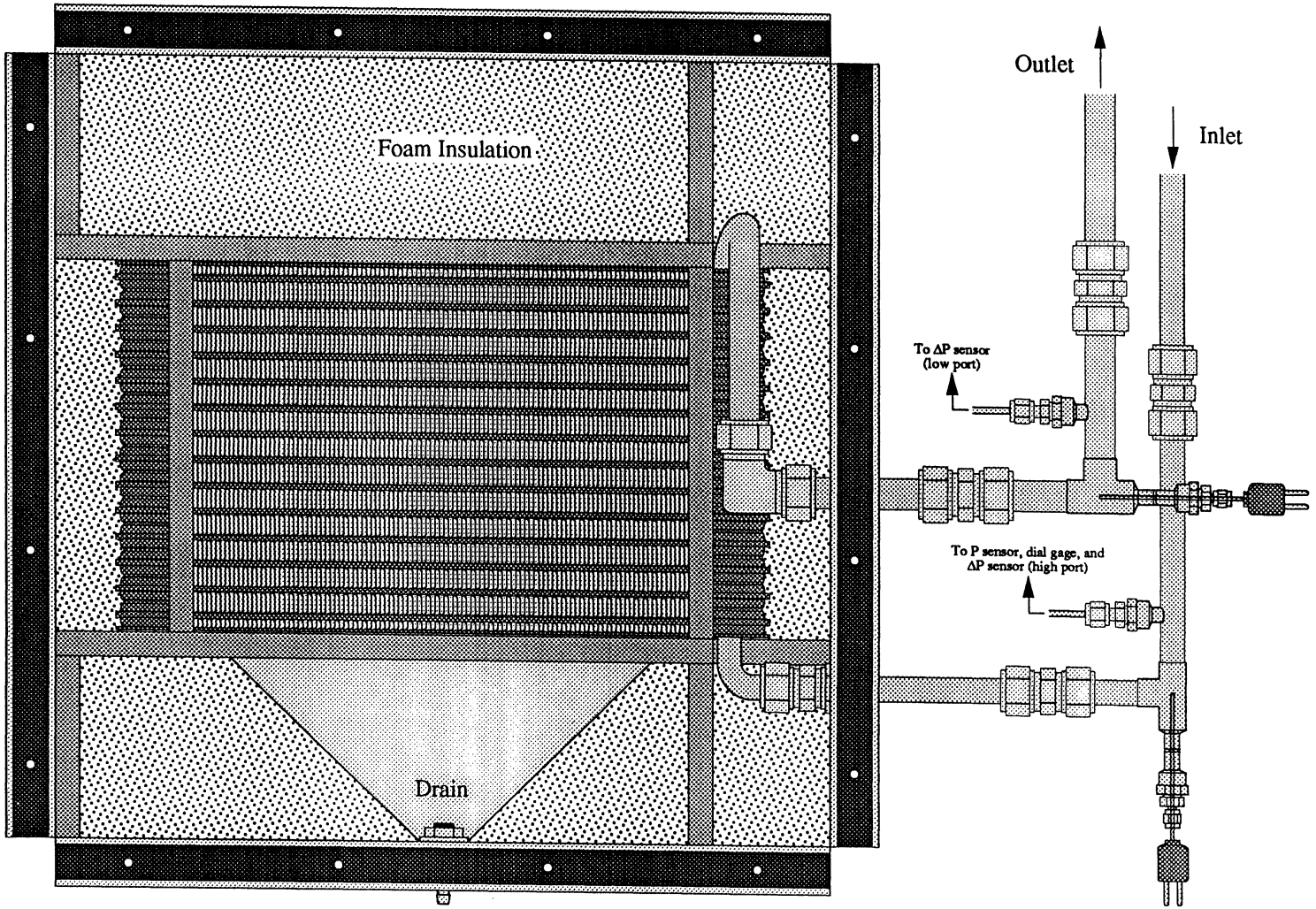


Figure 2.9 A view looking upstream at a typical evaporator installation.

(a)

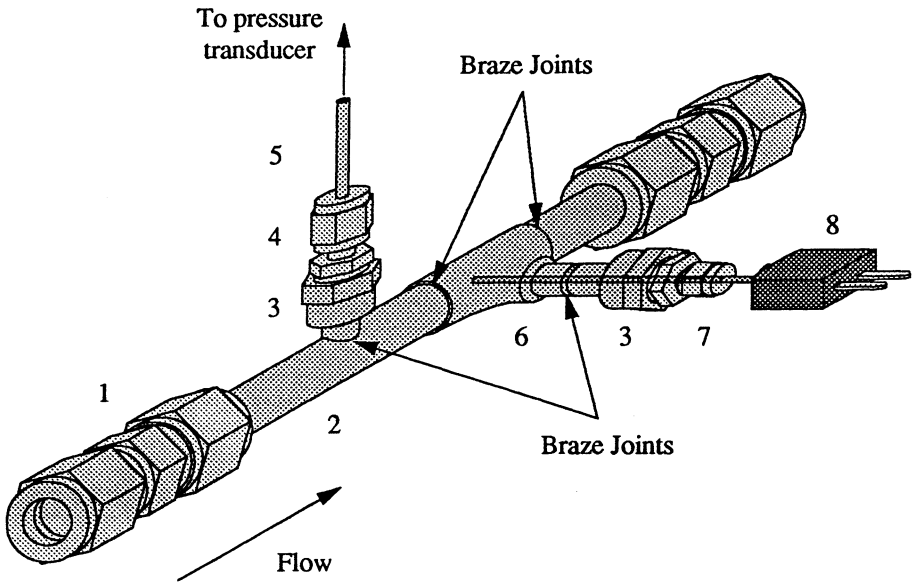


1. 1/2 x 1/2-in. Compression Union
2. 1/2-in. O.D. Copper Pipe
3. 1/4-in. x 1/8-NPTF Copper Fitting
4. 1/8-in. x 1/8-NPTM Compression Fitting
5. 1/8-in. O.D. Copper Tubing
6. 1/2 x 1/2 x 1/4-in. Copper Tee
7. 1/16-in. x 1/8-NPTM Compression Fitting
8. Thermocouple Probe
9. 1/2 x 1/4 x 1/2-in. Copper Tee

(b)

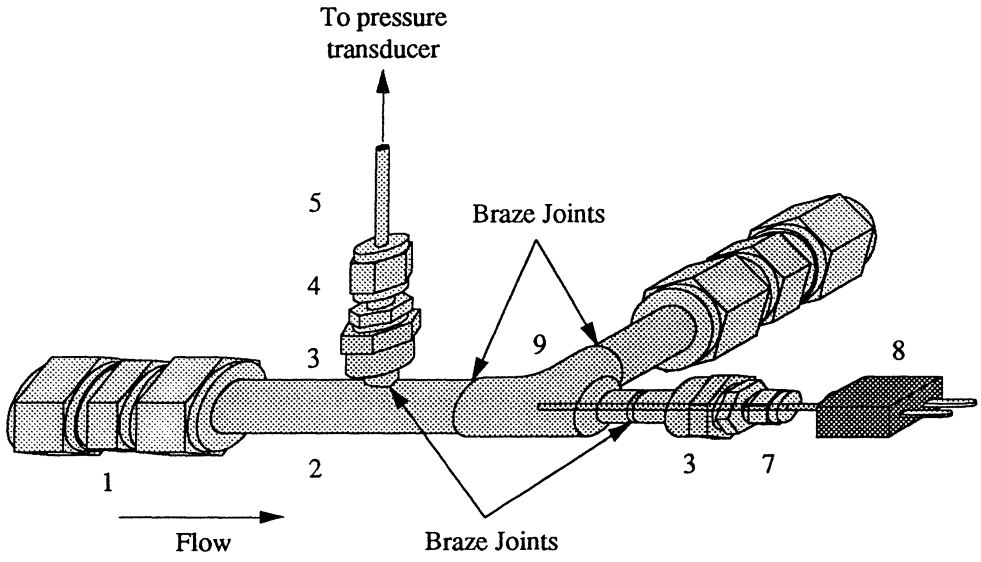


Figure 2.10 The two P/T tap configurations used in the facility: (a) a straight tap, and (b) an angled tap (1/2-in. O.D. line size shown).

of 1/8-in. O.D. (0.065-in. I.D.) soft copper tubing which transmits the fluid pressure from the tap to a pressure transducer. As a side note, when stating fitting sizes such as "1/4-in. x 1/8-NPTF," the "1/4-in." dimension refers to the O.D. pipe size which inserts into one end of the fitting (the compression end, or the end that is to be brazed or soldered), and the "1/8-NPTF" dimension refers to the size of the NPTF (National Pipe Taper–Female) threads cut into the opposite end of the fitting.

Continuing, the refrigerant temperature is sensed by a thermocouple probe sealed in the line with a 1/16-in. x 1/8-NPTM compression fitting. The probe is located downstream of the pressure tap so as not to disturb the flow across the tap. The angled mounting configuration of Figure 2.10b is used wherever possible because this configuration encourages the refrigerant flow to enter the well surrounding the probe and thereby minimize the temperature gradient (i.e., heat conduction) along the length of the probe. The temperature measurements are discussed in greater detail in Chapter 3. As is shown in Figure 2.9, we locate each P/T tap as close as possible to the inlet or outlet of the component being instrumented so as to help prevent the refrigerant properties from changing between the point where the pressure and temperature measurements are taken and the point where the refrigerant stream actually enters or leaves the component.

### 2.2.3 Sight Tubes

Cylindrical sight tubes are used throughout our refrigerant lines so that the researcher can visually identify of the state, distribution, and flow regime of the refrigerant/oil mixture in any given part of the loop. The sight tubes also permit visual detection of low charge levels, loop contaminants, and compressor slugging phenomena. Figure 2.11 shows an exploded view of our sight tube design. Assembly instructions are given in Weston (1996). The glass tube is a stock length of borosilicate gage glass having the specifications shown in Table 2.4. We chose borosilicate gage glass because it has low thermal expansion coefficient and a high resistance to physical and thermal shock. 5/8-in. O.D. glass is used in the suction line, and 1/2-in. O.D. glass is used in the discharge and liquid lines. Teflon® compression ferrules and a bead of refrigerant-safe epoxy provide a permanent, leakproof seal around the glass. A transparent Lexan™ polycarbonate shield encases the glass for safety and forces the assembly to vibrate as one rigid piece, thereby ensuring that line vibrations do not fatigue and break the glass.

### 2.2.4 Compressor and Compressor Drive Assembly

Figure 2.12 shows a schematic of the compressor drive assembly. The assembly consists of a drive motor, a speed and torque sensor, a jackshaft, a drive pulley, a drive belt, a compressor, and a compressor mounting plate. All of the components are mounted on a vertical aluminum backplate supported by Unistrut steel channels. Although not shown in the figure, steel-mesh

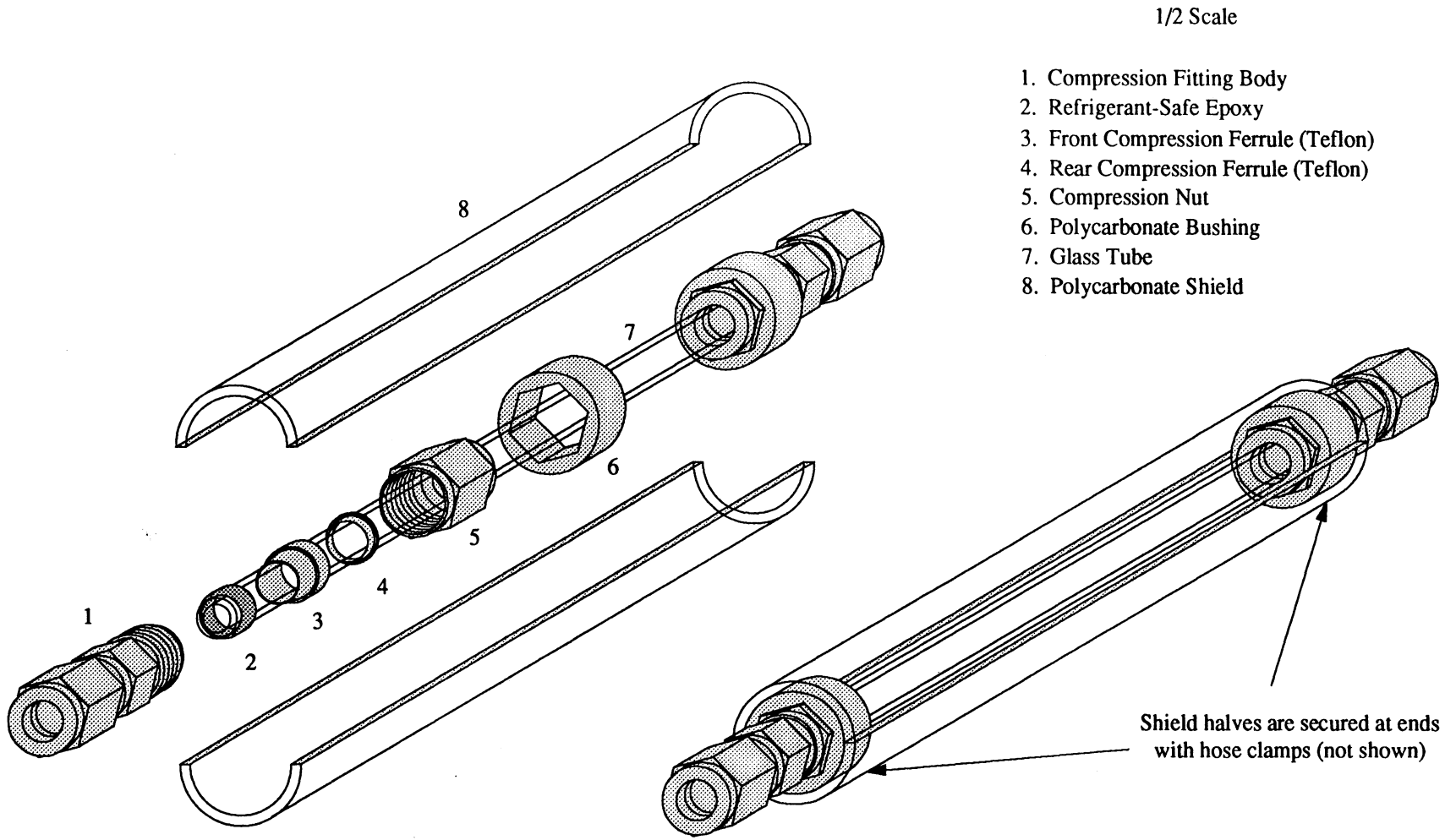


Figure 2.11 A typical sight tube assembly (1/2-in. O.D. line size shown).

Table 2.4 The specifications of the gauge glass used to construct the sight tubes.

| Vendor and Stock No. | Outer Diameter | Wall Thickness | Length | Pressure Rating |
|---|---|---|---|---|
| McMaster-Carr 3723K11 | $\frac{1}{2}$ in. | $\frac{5}{64}$ in. | 8 in. | 460 psi (T < 150 °F)<br>340 psi (T < 425 °F) |
| McMaster-Carr 3724K11 | $\frac{5}{8}$ in. | $\frac{3}{32}$ in. | 8 in. | 435 psi (T < 150 °F)<br>320 psi (T < 425 °F) |

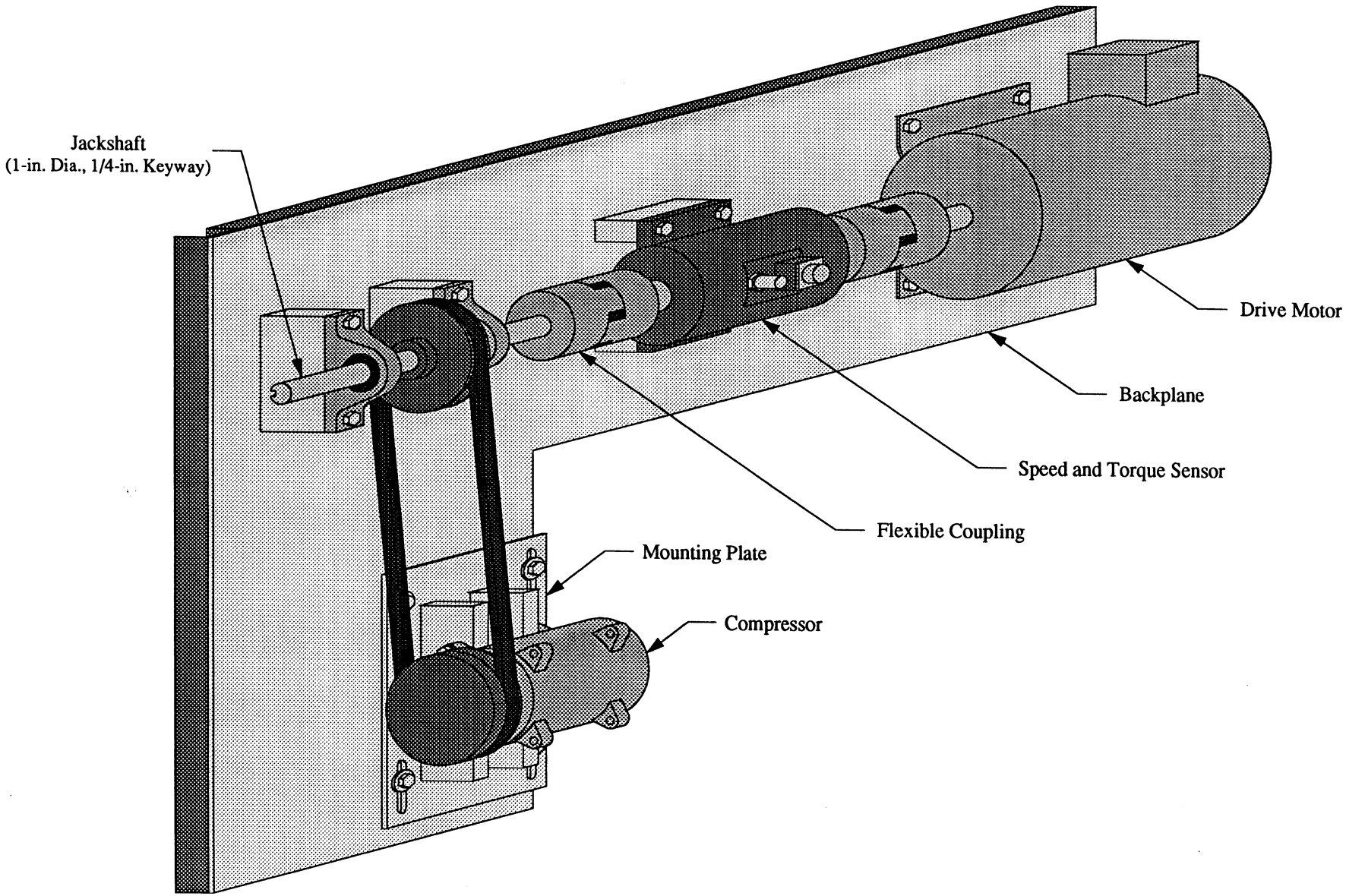


Figure 2.12 The compressor drive assembly.

safety guards cover all of the moving parts. The assembly was originally designed by T.A. Michael for use in a preliminary mobile a/c test stand and was salvaged for use in the present facility (Michael, 1989). The drive motor (Baldor Model No. M3219T) is a 230-VAC, 3-phase, Open Drip-Proof (ODP) electric motor rated 7-1/2 hp at 3450 rpm. The motor speed is regulated by an AC motor speed controller (PoWrMaster Model No. CIMR-7.5G2-E-10). Because an ODP motor can overheat if run significantly below its rated speed for an extended period of time, we added a 5-in. diameter household clip-on fan near the motor casing to assist in cooling the motor during low-speed runs. The motor drives a 1-in. diameter steel jackshaft supported by two ball bearing pillow blocks. The speed and torque of the jackshaft are measured by a rotary sensor spliced between the motor and jackshaft with flexible couplings. The compressor is driven by a belt looping between the compressor pulley and a drive pulley mounted on the jackshaft. The compressor pulley "free wheels" with the drive until the electromagnetic clutch on the compressor is engaged, which causes a disc fixed to the compressor shaft to turn with the pulley and operate the compressor. The compressor is supported by mounting brackets fabricated from aluminum or mild-steel stock. The brackets attach to a flat aluminum mounting plate bolted to the backplate of the compressor stand. Slotted holes in the mounting plate permit the drive belt to be tensioned. Weston (1996) contains an ongoing list of compressors we have acquired for testing. Weston (1996) also contains sample drawings of several mounting brackets and a diagram of the general mounting plate.

### 2.2.5 Discharge-Line Assembly

The discharge line carries hot, superheated, high-pressure refrigerant vapor from the outlet of the compressor to the inlet of the condenser. As shown in Figure 1.2, our general-purpose discharge line consists of a compressor outlet T tap (Figure 2.10b without the P tap), a VFT assembly, a condenser inlet sight tube, and a condenser inlet P/T tap (Figure 2.10a). All of the components are connected with 1/2-in. O.D. copper pipe, which is the typical discharge-line size used in stock mobile a/c systems. To date, we have excluded stock compressor discharge mufflers from our laboratory installations because muffler dynamics are not of initial interest to our research. Mufflers can be easily patched into the lines in future tests if desired.

### 2.2.6 Condenser

Mobile a/c condensers are usually a plate/fin or tube/fin construction which mounts in cross flow with the air stream. Automotive condensers are most often made entirely of aluminum. Heavy-equipment condensers are often made of steel for durability and usually have a relatively wide fin spacing to prevent excessive fouling from dirt and debris. Because steel has a lower thermal conductivity than aluminum, and because the fin spacing is wider, heavy-equipment

condensers are larger in size and require higher air flow rates than their automotive counterparts to achieve the same rate of heat transfer. As was previously discussed, we use the larger sized ducts of Figure 2.3 to mount these coils in our facility. We mount any given condenser in our facility in the same orientation as in the field unless otherwise requested by the manufacturer.

### 2.2.7 Liquid-Line Assembly

The liquid line carries warm, subcooled, high-pressure liquid refrigerant from the outlet of the condenser to the inlet of the expansion device. The portion of line carrying cold, two-phase, low-pressure refrigerant from the outlet of the expansion device to the inlet of the evaporator is also considered to be part of the liquid line. As shown in Figure 1.2, our general-purpose liquid line consists of a condenser outlet P/T tap (Figure 2.10a), a condenser outlet sight tube, a Coriolis-type mass flow meter, a VFT inlet T tap (Figure 2.10a without the P tap), a VFT assembly, an evaporator inlet sight tube, and an evaporator inlet P/T tap (Figure 2.10b). The line also contains two assemblies for measuring the concentration of compressor oil circulating with the refrigerant, a pressure relief valve, an expansion device, and (depending upon the type expansion device used) a receiver/drier. These latter components are further discussed below. All of the components are connected with 1/2-in. O.D. copper pipe, which is a typical liquid-line size used in stock mobile a/c systems.

#### 2.2.7.1 Oil Concentration Sensor

Our liquid line features a prototype sensor which measures the percent-by-mass concentration of compressor oil mixed in with the refrigerant flow without the need to extract a sample. The sensor records real-time measurements of the speed of sound in the flowing liquid refrigerant/oil mixture and correlates these measurements to the circulating oil concentration through an empirical relation. Because the measurements are performed in real time, the migration of compressor oil can be tracked throughout a transient mode of system operation. The reader is referred to the work of Meyer and Jabardo (1994) for a more thorough description of the measurement technique and for details concerning the initial design of the sensor. At present, fellow researcher R.G. Cowie is developing a refined, packaged version of the sensor used by Meyer and Jabardo. The packaged version is the version used in our facility.

The sensor package presently consists of two acoustic transducers, a mounting block, a thermistor, and a microprocessor-based regulator circuit. Figure 2.13 shows how the sensor is mounted in our facility. The mounting block is a 1-1/2-in. stainless steel cube which bolts around a 6-in. length of 1/2-in. O.D. thin-walled (0.010-in. thick) stainless steel tubing. We used thin-walled stainless steel tubing because its acoustic transmission properties are better than those of standard copper pipe. The two acoustic transducers thread into opposite sides of the

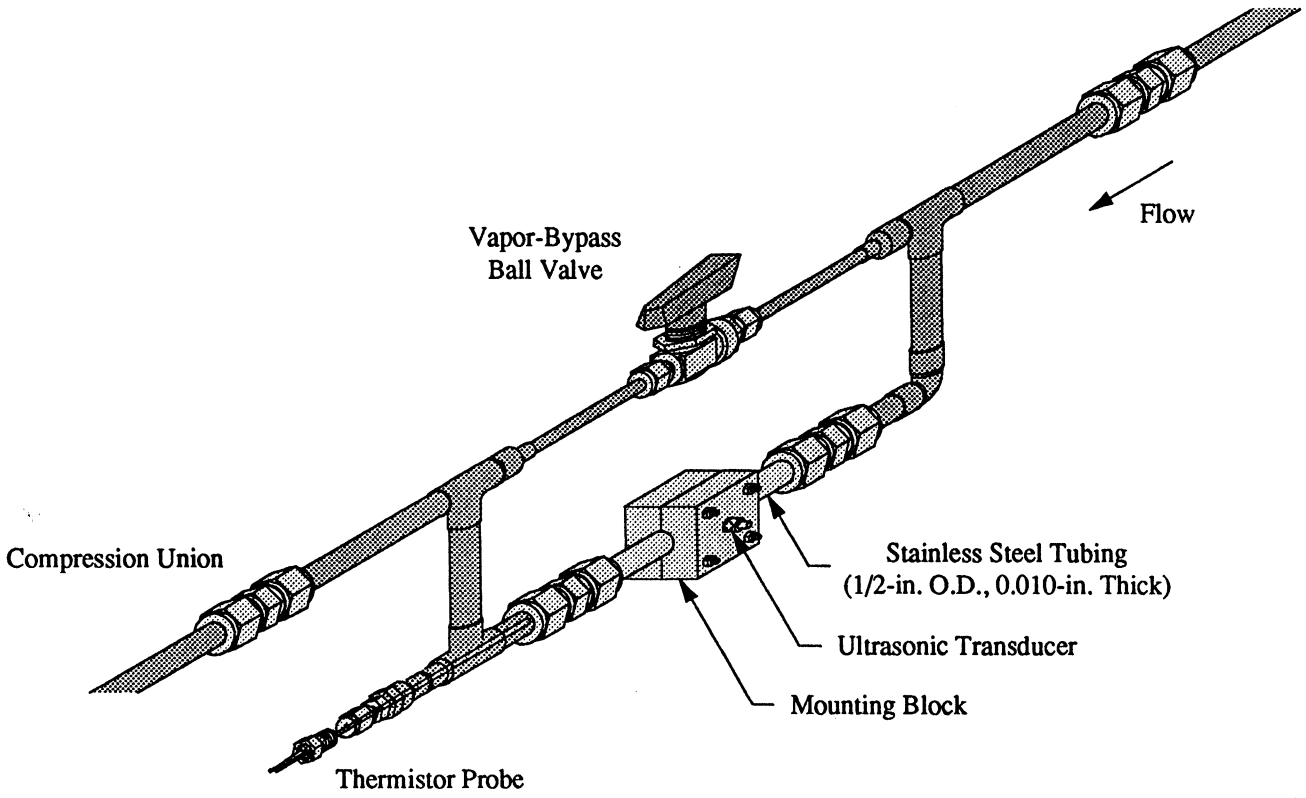


Figure 2.13 The assembly used to mount the oil concentration sensor.

mounting block and bottom against the walls of the stainless steel tube. The first transducer transmits an ultrasonic pulse across the flowing liquid refrigerant/oil mixture, and the second transducer receives the pulse on the opposite side of the tube. Because two-phase flow patterns tend to severely attenuate the amplitude of the acoustic pulse, we located the sensor at the bottom of a "U"-type arrangement which encourages the mounting tube to fill only with liquid during times in which vapor is present in the liquid line. The temperature of the flowing refrigerant/oil mixture is sensed by a thermistor probe (OMEGA Model No. ON-970-44032) which is sealed in the line with a 1/8-in. x 1/8-NPTM compression fitting. The sensor's microprocessor-based regulator circuit operates the transducers, computes the thermistor temperature, and calculates the time of flight of the acoustic pulse. The circuit then uses the temperature and time-of-flight measurements in conjunction with the known path length between the transducers (measured with a pair of calipers) to compute the speed of sound (and, hence, the concentration of oil) in the flowing refrigerant/oil mixture. The microprocessor can store the data in onboard memory and/or transmit the values to our facility's DAS via two 0–5 VDC analog outputs. Final and more complete details concerning the sensor will be presented in future publications.

#### 2.2.7.2 Mixture Sampling Assembly

The mixture sampling assembly is used to trap a sample of the flowing liquid refrigerant/oil mixture for manual off-line determination of the circulating oil concentration. The sampling assembly was installed to validate the readings of the prototype sensor. When development of the latter sensor is complete, the rather long 34-in. sampling assembly will either be removed from the liquid line or placed on a bypass to reduce the overall system pressure drop, line length, and refrigerant charge. Figure 2.14 shows a schematic of the sampling assembly. The assembly consists of two parallel branches of ball valves (Hoke® Model No. 7122G4B). The valves have Teflon seats compatible with refrigerant R-134a (DuPont, 1993) and are suitably rated for 1500 psig of pressure over a temperature range of 0 to 350 °F. The identical geometry of the two branches helps to ensure that the flow distributes equally between the two pathways. When all four valves of a branch are closed, a sample of the refrigerant/oil flow becomes trapped between the two middle valves of the branch. As is shown in Figure 2.14, the trapped section can then removed from the loop for analysis. All remaining flow diverts to the second pathway to allow the refrigerant loop to remain in operation. When the analysis of the withdrawn sample is complete, the section is reattached to the loop and evacuated via a Schrader valve before restoring flow to the branch.

To determine the oil concentration, the section removed from the loop is placed on an analytical balance, and the balance is tared. The section is then removed from the balance and blown down through a cascade impactor. The cascade impactor contains a series of seven brass

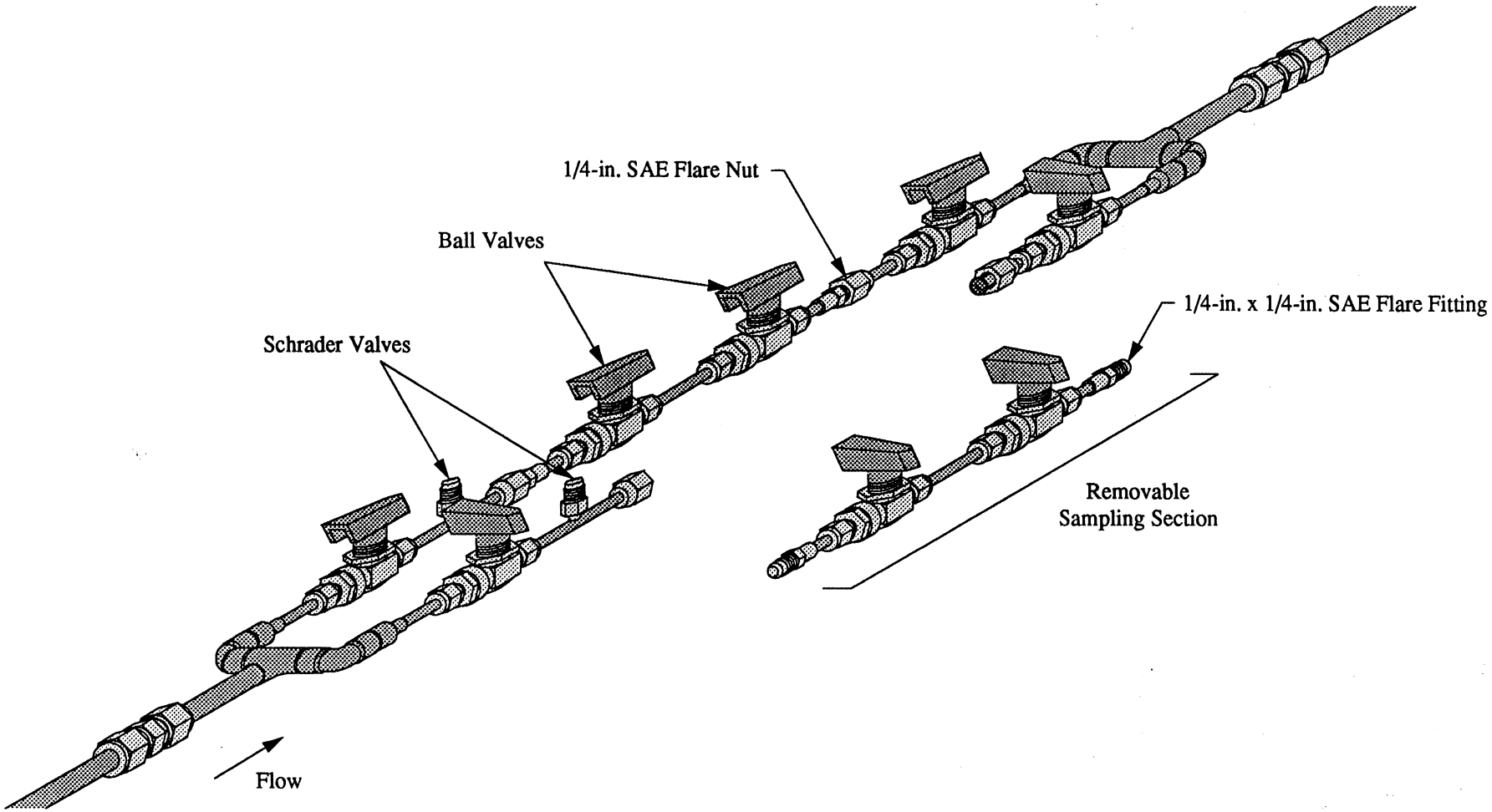


Figure 2.14 The mixture sampling assembly.

disks, each of which holds a glass-fiber filter pad. The liquid refrigerant flashes into vapor and proceeds out of the impactor through a series of small orifices located under the discs, whereas the oil "impacts out" onto the filter pads and the walls of the impactor. After the sample has been flashed through the impactor, the walls of both the impactor and the emptied section are swabbed with the filter pads to collect any residual oil, and the emptied section is placed back on the tared balance to obtain the total sample mass (typically about 3 grams). The filter pads are also weighed on the analytical balance before and after being exposed to the oil to determine the mass of oil contained in the sample. The latter mass measurement is then divided by the total sample mass to compute the oil concentration. The method described above was developed through a concurrent ACRC project and was found to be much faster than the standard ASHRAE method (ASHRAE Standard 41.1-1984) for determining oil concentration. The ASHRAE method can take up to 24 hours to complete and requires a much larger sample size. With the procedure outlined above, the circulating oil concentration can be accurately measured in less than 30 minutes with a much more reasonable sample size.

#### 2.2.7.3 Pressure Relief Valve

Most mobile a/c systems have a pressure relief valve mounted somewhere on the high-pressure side of the system, typically on either the discharge side of the compressor cylinder head or on the discharge side of the compressor inlet/outlet manifold block. We installed a 450-psig pressure relief valve (Mueller Model No. A-15502-R) in our liquid line to guard against cases in which the original-equipment valve is mounted on a stock fitting excluded from our laboratory installation, or against cases in which the release pressure of the original-equipment valve exceeds the rated pressure of the 1/2-in. O.D. gage glass used in our high-pressure lines. An evacuated, large-capacity (30-$lb_m$) refrigerant cylinder is attached to the release side of our pressure relief valve to capture escaping refrigerant if the valve should happen to vent.

#### 2.2.7.4 Expansion Device

The expansion device throttles the refrigerant from the high-pressure, high-temperature condensing conditions to the low-pressure, low-temperature evaporating conditions. Stock mobile a/c systems use either a thermostatic expansion valve or an orifice tube as the expansion device. Our facility can accommodate both of these devices, as well as a needle-type metering valve. The expansion devices are further discussed below.

Thermostatic Expansion Valve (TEV or TXV)

A TEV is an active control device which modulates the refrigerant flow to maintain a constant level of superheat at the evaporator outlet. Figure 2.15 shows a typical TEV design.

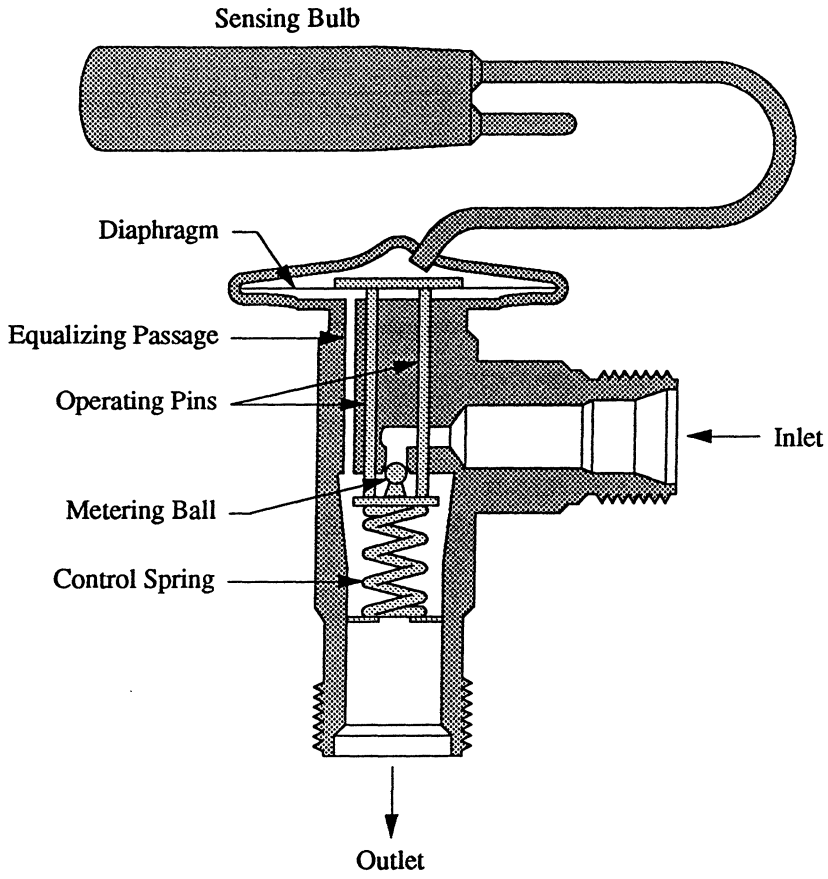


Figure 2.15 A typical mobile a/c TEV design.

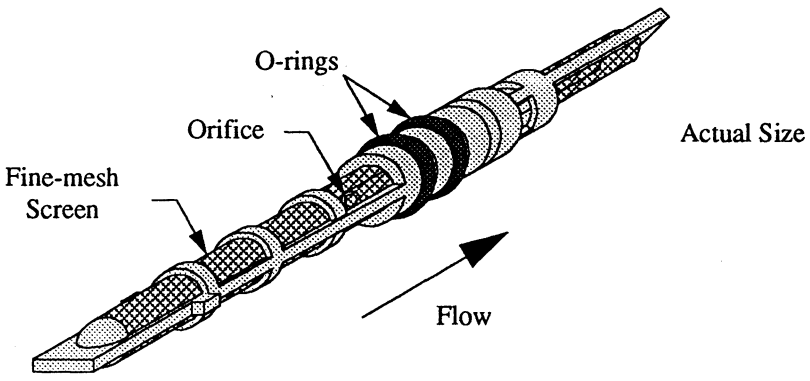


Figure 2.16 A typical mobile a/c orifice tube design.

The sensing bulb shown in the figure fastens to the exterior of the evaporator outlet pipe with insulating tape. The bulb is charged with refrigerant and forms a closed-volume system with a chamber above a diaphragm in the valve head. The diaphragm, in turn, moves a metering ball via a set of operating pins. If the evaporator outlet superheat falls below a preset level, then the pressure within the sensing bulb decreases, and the diaphragm is forced upward by (i) a control spring situated beneath the metering ball and (ii) the evaporator pressure transmitted to the underside of the diaphragm by an equalizing passage. As the diaphragm is forced upward, the metering ball moves toward the valve seat and decreases the refrigerant flow to the evaporator, thereby "starving" the evaporator of refrigerant. The evaporator remains starved for refrigerant until the outlet superheat increases, whereupon the pressure in the sensing bulb increases and moves the diaphragm in the opposite direction. Movement of the diaphragm continues until the preset level of superheat is restored. The superheat level is preset by adjusting the initial compression of the control spring.

Orifice Tube

An orifice tube is a passive throttling device which has a fixed-diameter opening. Figure 2.16 shows a typical orifice tube design. The design consists of a short length of tubing encased in a polymer housing. O-rings provide a seal around the housing, and fine-mesh screens on the housing prevent foreign particles from clogging the orifice. The assembly inserts into the liquid line with an interference fit and is generally held in place by shoulders, crimps, or detents in the pipe wall. Unlike a TEV, an orifice tube does not actively control the refrigerant mass flow rate (or, accordingly, the system capacity). Instead, the system capacity is controlled either through the use of a variable-displacement compressor or by cycling the clutch of a fixed-displacement compressor. Also, because there is no guarantee that the refrigerant exiting the evaporator will be superheated when using an orifice tube, the suction line will contain an accumulator to prevent unevaporated liquid from reaching the compressor.

Metering Valve

A Hoke 2300 Series metering valve (Model No. 2311F4B-2300K1) is used as the throttling device in our facility when operating conditions unobtainable with the stock TEV or orifice tube are desired. The valve is equipped with a 20-turn vernier micrometer handle for precise establishment of flow settings. The valve is rated for a temperature range of -40 to 200 °F and a maximum pressure of 3000 psig. The valve packing material (Buna-N) is reportedly compatible with R-134a (DuPont, 1993). A mating actuator package (Hoke Model No. 0121F2E) is available from the manufacturer for implementing electronic valve control schemes in future research.

#### 2.2.7.5 Receiver/Drier

Systems which use a TEV will also have a receiver/drier located upstream of the TEV in the liquid line. A receiver/drier is essentially a canister which stores excess refrigerant charge during low-load conditions. The receiver/drier also contains a desiccant which absorbs moisture from the refrigerant. Moisture can freeze in the TEV and adversely effect the valve performance. Moisture can also react with the refrigerant and oil to form acids which damage seals throughout the refrigerant loop.

### 2.2.8 Evaporator

Mobile a/c evaporators are usually a plate/fin or tube/fin compact heat exchanger design mounted in cross flow with the air stream. Plate/fin evaporators are commonly constructed entirely of aluminum, and tube/fin evaporators are commonly constructed of aluminum or copper tubes with aluminum fins. We install any given evaporator in our facility in the same orientation as in the field unless otherwise requested by the manufacturer. Larger vehicles such as vans may employ a two-evaporator system in which one evaporator cools the rear of the cabin. Our facility can accommodate a second evaporator loop.

### 2.2.9 Suction-Line Assembly

The suction line carries cool, low-pressure refrigerant from the outlet of the evaporator to the inlet of the compressor. As shown in Figure 1.2, our general-purpose suction line consists of an evaporator outlet P/T tap (Figure 2.10b), an evaporator outlet sight tube, a compressor inlet sight tube, and a compressor inlet P/T tap (Figure 2.10b). All of the components are connected with 5/8-in. O.D. copper pipe, which is a typical suction-line size used in stock mobile a/c systems. A Schrader valve is brazed into a tee in our suction line for charging purposes, and we install an accumulator in the suction line if an orifice tube or the Hoke metering valve is being used as the expansion device.

#### 2.2.9.1 Accumulator

Much like a receiver/drier, an accumulator is essentially a canister which stores excess refrigerant charge during low-load conditions and contains a desiccant which removes moisture from the refrigerant. The accumulator also has the important job of preventing large quantities of unevaporated liquid refrigerant from slugging to the compressor. Figure 2.17 shows a typical accumulator design. The refrigerant stream enters the side of the accumulator canister and expands into the chamber volume. The vapor portion of the flow migrates to the top of the canister and becomes drawn into the mouth of the outlet pipe, whereas the liquid portion of the

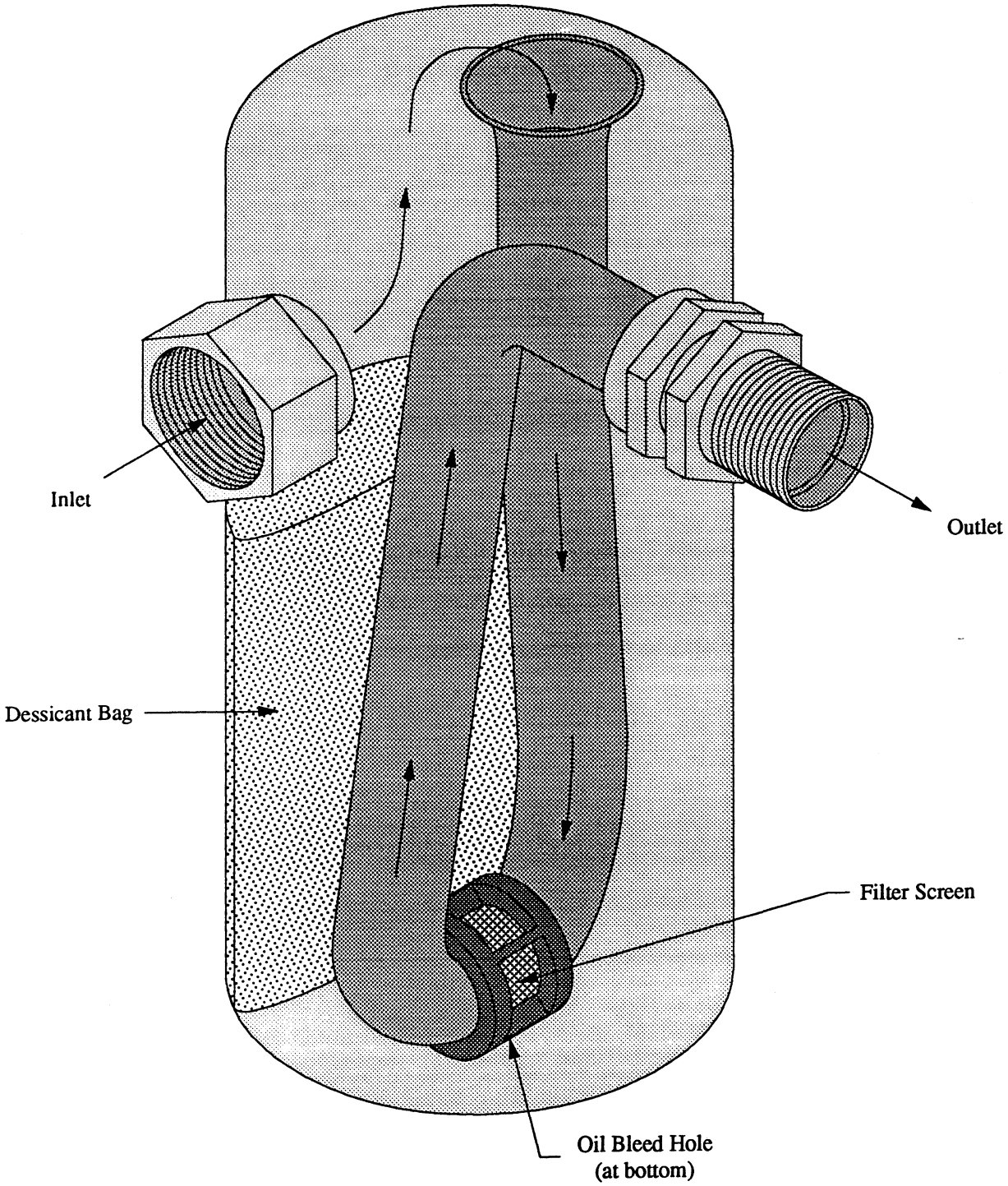


Figure 2.17 A typical mobile a/c accumulator design.

flow splashes against the chamber walls and falls to the bottom of the canister. In many accumulator designs, the mouth of the outlet pipe is additionally located beneath a dome-shaped umbrella which shields the pipe opening from the liquid-laden inlet refrigerant stream. The liquid refrigerant eventually evaporates and proceeds into the outlet pipe as vapor, whereas a bleed hole at the bottom of the pipe allows the nonvolatile oil (and, unavoidably, a small amount of liquid refrigerant) to be drawn into the pipe and return to the compressor.

# 3. THE MEASUREMENT AND CONTROL DEVICES OF THE TEST FACILITY

## 3.1 Data Acquisition System (DAS)

The DAS hardware salvaged for temporary use in our facility consists of three Strawberry Tree Incorporated (STI) 12-bit Analog Connection™ cards (Model No. ACM2-12-8A) and one 16-bit Analog Connection card (Model No. ACM2-16-16) mounted in a Macintosh II™ computer. Each 12-bit card has eight differential analog inputs, two analog outputs, and eight digital input/output lines. The 16-bit card has 16 differential analog inputs and 16 digital input/output lines. All of the cards are equipped with integrating analog-to-digital (A/D) converters (one converter per card) which achieve superior rejection of 60-Hz noise. The three 12-bit cards link to three STI Model No. T51 terminal panels, and the single 16-bit card links to two STI Model No. T21 terminal panels. The terminal panels are mounted in aluminum chassis boxes located near the Macintosh II computer. The panels connect to the Analog Connection cards with 28-AWG (American Wire Gage) ribbon cables. The DAS hardware is regulated by STI WorkBench™ Version 3.0.2 software which also serves as the user interface. The panel coding and channel numbering schemes are summarized in Table 3.1.

### 3.1.1 DAS Specifications and Features

#### 3.1.1.1 Scan Rate

The WorkBench software allows the user to set a different scan rate and resolution for each individual channel. The 24 analog inputs of the three 12-bit cards can each be scanned at a maximum rate of 133 Hz with full 12-bit resolution. The 16 analog inputs of the single 16-bit card can each be scanned at a maximum rate of 14 Hz with full 16-bit resolution. Faster scan rates are possible if lower resolutions are selected. The channels can also be scanned in "Low Noise Mode," in which case the integrating A/D converter rejects 60-Hz noise. When scanning in Low Noise Mode, resolutions are set to their maximums by default, and the 40 channels can each be scanned at a maximum rate of 1.5 Hz. At present, all of the channels are configured to be scanned at a rate of 1 Hz in Low Noise Mode.

#### 3.1.1.2 Accuracy and Input Impedance

The STI A/D cards can measure voltages on three unipolar range settings (50 mV, 500 mV, and 10 V) and three bipolar range settings (± 25 mV, ± 250 mV, and ± 5 V). Tables 3.2 and 3.3 show the rated accuracies of the 12- and 16-bit cards for each of the given ranges assuming the full 12- and 16-bit resolutions are selected. The accuracy specifications include linearity, drift, offset, resolution, and factory calibration errors. The tables also show the input impedance of the

Table 3.1 A chart for converting our DAS panel code designations to the channel numbering scheme used by the STI WorkBench software (e.g. Analog Input 4 of Panel C is Channel 20).

| Card Model No. | Card Serial No. | Panel Model No. | Panel Letter Code | Panel Analog Input No. 1 | 2 | 3 | 4 | 5 | 6 | 7 | 8 |
|---|---|---|---|---|---|---|---|---|---|---|---|
| ACM2-12-8A | 10361 | T51 | A | 33 | 34 | 35 | 36 | 37 | 38 | 39 | 40 |
| ACM2-16-16 | 20332-J1/ | T21 | B | 25 | 26 | 27 | 28 | 29 | 30 | 31 | 32 |
| | 20331-J2 | T21 | C | 17 | 18 | 19 | 20 | 21 | 22 | 23 | 24 |
| ACM2-12-8A | 10187 | T51 | D | 9 | 10 | 11 | 12 | 13 | 14 | 15 | 16 |
| ACM2-12-8A | 10364 | T51 | E | 1 | 2 | 3 | 4 | 5 | 6 | 7 | 8 |

Table 3.2 The rated accuracy and input impedance specifications of a 12-bit ACM2-12-8A STI DAS card.

| Input Voltage Range | Full Scale Resolution | Input Impedance | Accuracy: the larger of ± % of Range | ± % of Reading |
|---|---|---|---|---|
| -5 to +50 mV | 12 μV | > 1000 MΩ | 0.08 | — |
| -25 to +25 mV | 12 μV | > 1000 MΩ | 0.16 | — |
| -50 to +500 mV | 120 μV | 200 kΩ | 0.05 | 0.2 |
| -250 to +250 mV | 120 μV | 200 kΩ | 0.05 | 0.2 |
| -1 to +10 V | 2.4 mV | 200 kΩ | 0.05 | 0.2 |
| -5 to +5 V | 2.4 mV | 200 kΩ | 0.05 | 0.3 |

Table 3.3 The rated accuracy and input impedance specifications of a 16-bit ACM2-16-16 STI DAS card.

| Input Voltage Range | Full Scale Resolution | Input Impedance | Accuracy: the larger of ± % of Range | ± % of Reading |
|---|---|---|---|---|
| -5 to +50 mV | 0.8 μV | > 1000 MΩ | 0.04 | — |
| -25 to +25 mV | 0.8 μV | > 1000 MΩ | 0.08 | — |
| -50 to +500 mV | 8 μV | 200 kΩ | 0.01 | 0.05 |
| -250 to +250 mV | 8 μV | 200 kΩ | 0.01 | 0.05 |
| -1 to +10 V | 150 μV | 200 kΩ | 0.01 | 0.05 |
| -5 to +5 V | 150 μV | 200 kΩ | 0.01 | 0.10 |

cards for each range. For each card, the input impedance is large (> 1000 MΩ) for the 50 mV and ± 25 mV ranges only. Later discussions will show that the implementation of an accurate measurement technique involves careful consideration of both the input impedance and the accuracy specifications.

#### 3.1.1.3 Analog and Digital Outputs

Pending the design and installation of our environment controller, we had intended to use the analog outputs of the three 12-bit cards to generate transient remote setpoint signals to be tracked by the motor and heater controllers used in our facility. However, the analog outputs on two of the three 12-bit cards were found to be damaged at the time this salvaged equipment was installed, and the WorkBench software does not allow the outputs of the third card to be used if the outputs of the other two cards are inoperable. Thus, we presently use the digital outputs of the cards and standard benchtop function generators to generate all remote setpoint signals. Figure 3.1 shows an example of how a control device is wired to a digital output of the STI system. The 5-VDC supply shown in the figure is an auxiliary source provided by the STI A/D card, but an external source may also be used provided that one attaches the ground of the external source to the digital ground terminal of the DAS input panel. Each digital output is an open-collector transistor switch regulated by either a built-in or user-programmed logic routine executing under the WorkBench software. When the logic routine produces a "0," the switch saturates, and the source voltage is applied across the input terminals of the control device. When the logic routine produces a "1," the switch unsaturates, and no voltage is applied to the device. The resulting input to the device is a 5-VDC square wave.

### 3.1.2 General Signal Measurement Techniques

We are presently replacing the STI DAS with a PC-based system which has a greater number of channels, better voltage resolution, a higher input impedance, a higher common-mode voltage rating, faster scan rates, and better communications capability with both present and future control devices. To more easily facilitate the changeover to the new system, the measurement techniques employed with the STI system are described below in as general terms as possible. Specific comments about the STI arrangements are made where appropriate.

#### 3.1.2.1 Voltage Measurements

Most of the instruments used in our facility produce a voltage output. To measure a voltage signal, the positive and negative output leads of the sensor are connected to the positive and negative input terminals of a DAS channel as is shown in Figure 3.1. A multiplexer (MUX) successively attaches the channels to an amplifier preceding the A/D converter. Care is taken to

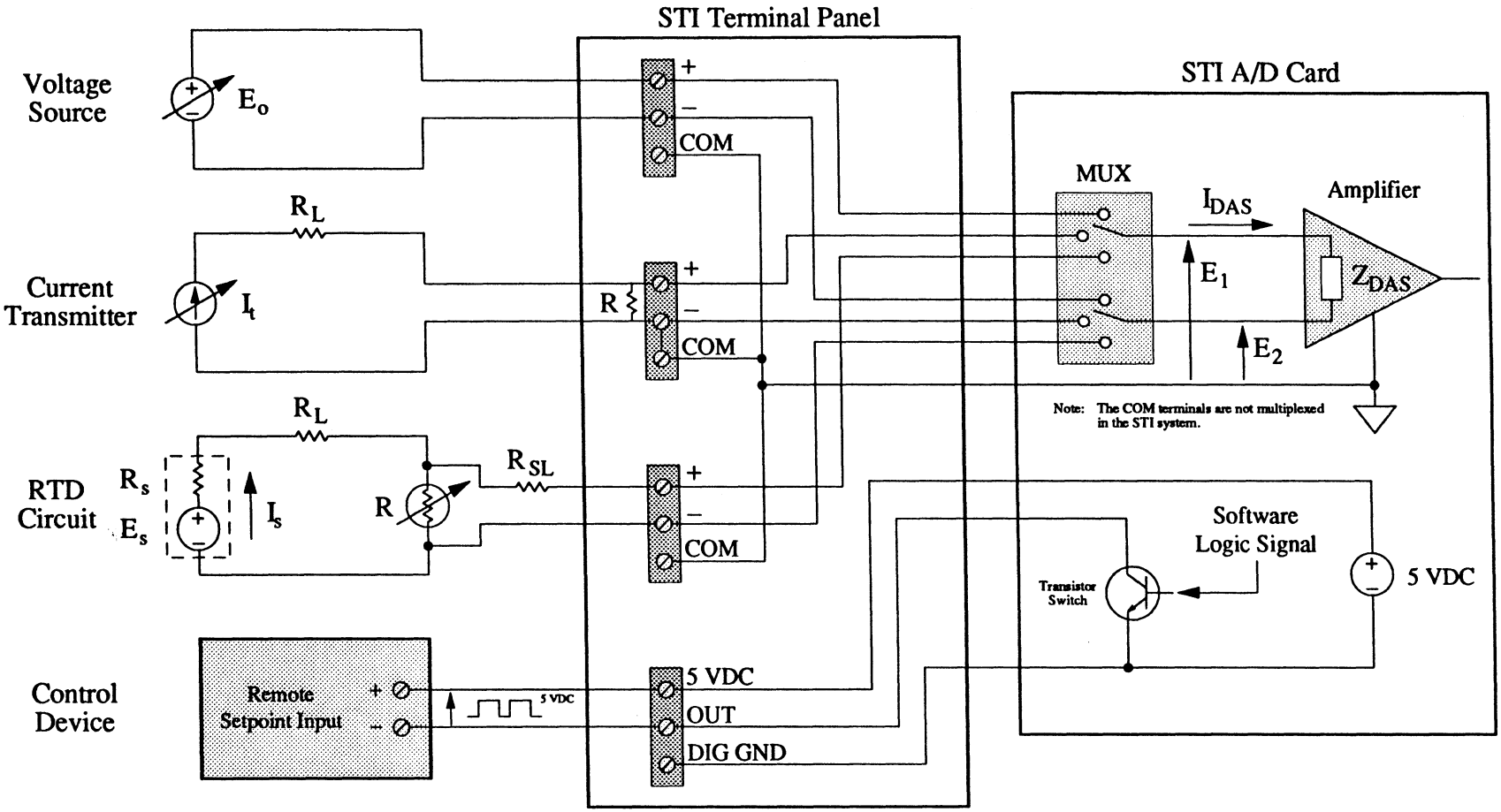


Figure 3.1 The typical setups used to measure voltages, currents, and resistances with the STI DAS, and an example of how a control device is wired to a digital output of the STI DAS.

ensure that the differential voltage signal applied to the input terminals of the DAS does not exceed the common-mode voltage rating of the amplifier. The common-mode voltage $E_{CM}$ is defined as the average voltage applied to the input terminals of the amplifier relative to the ground reference of the amplifier. From Figure 3.1, the common-mode voltage applied to the inputs of the DAS amplifier is seen to be

$$E_{CM} = \frac{1}{2}(E_1 + E_2) \qquad (3.1)$$
$$= E_2 + \frac{1}{2}E_o$$

where $E_1$ and $E_2$ are the potentials between the amplifier ground (COM) and the positive and negative input terminals, respectively, and $E_o$ ($= E_1 - E_2$) is the voltage signal being sensed. If $E_{CM}$ exceeds a specified limit, then the measurement of $E_o$ becomes erroneous, and the amplifier may suffer damage. For the STI DAS cards, $E_{CM}$ cannot exceed 8 V.

The majority of the voltage-output instruments used in our facility produce an output signal $E_o$ in the range of 0–5 VDC. Hence, from Equation 3.1, the voltage $E_2$ must be less than 5.5 V in order for $E_{CM}$ to stay within the specified limit when measuring signals in this range. For many of the instruments, the negative output lead is commoned to the negative excitation lead. The negative excitation lead, in turn, is tied to earth ground. Earth ground potential measures within $E_2 = \pm 0.02$ V of the COM potential, so the common-mode specification is met in these installations. For other instruments (namely, our Setra Model 228-1 and Model 239 pressure transducers), the negative output lead is ungrounded and nominally measures 4.7 VDC above the earth-grounded negative excitation lead. Hence, $E_2$ is at most 4.7 + 0.02 = 4.72 VDC for these sensors, and the common-mode specification is again satisfied. The remaining voltage-output instruments used in our facility are thermocouples. All of the thermocouples used in our facility have an ungrounded-type construction (i.e., the thermocouple bead is electrically isolated from the metal sheath of the probe in which it is mounted, and, hence, from whatever electrical ground the probe touches), so the positive and negative output leads of these circuits are normally floating relative to both earth ground and COM. Although the differential output voltage $E_o$ of a thermocouple circuit is small (on the order of millivolts), the potential $E_2$ can be large due to noise voltages superimposed on the positive and negative leads. Hence, shorting bars are installed between the negative and COM terminals of the thermocouple circuits to force $E_2 = 0$ and thereby ensure that the common-mode specification is met.

#### 3.1.2.2 Current Measurements

Three of the instruments used in our facility transmit 4–20 mA current signals. To measure a signal of this sort, the transmitted current $I_t$ is passed through a shunt resistance R installed

across the positive and negative terminals of a DAS channel as is shown in Figure 3.1. Ohm's Law is then used to calculate the value of $I_t$ from the voltage drop $E_o$ measured across the shunt:

$$I_t = \frac{E_o}{R} \tag{3.2}$$

We now pause to note the importance of the DAS input impedance specification. When the MUX of Figure 3.1 attaches the DAS amplifier to the positive and negative ends of the shunt, the DAS acts like a resistor in parallel with the shunt (at least, it does when measuring a DC signal). Basic circuit analysis shows that the current drawn by the DAS-side branch of the parallel combination is

$$I_{DAS} = \left(\frac{R}{Z_{DAS} + R_{SL} + R}\right) I_t \tag{3.3}$$

where $Z_{DAS}$ is the input impedance (i.e., the apparent DC resistance) of the DAS, and $R_{SL}$ is the combined resistance of the two sensing leads (if any) which connect the shunt to the DAS. Hence, the current passing through the shunt is not truly the transmitted current $I_t$, but is instead the difference $I_t - I_{DAS}$. Stated another way, the value of $I_t$ calculated from Equation 3.2 has a bias error of

$$\delta I_{t,\,bias} = I_{DAS} \tag{3.4}$$

Furthermore, the voltage signal measured at the inputs of the DAS is not truly the voltage drop $E_o$ across the shunt, but is instead the difference $E_o - R_{SL} I_{DAS}$. Alternatively stated, the measurement of $E_o$ has a bias error of

$$\delta E_{o,\,bias} = R_{SL} I_{DAS} \tag{3.5}$$

Equation 3.3 shows that as $Z_{DAS}$ becomes large, $I_{DAS}$ becomes small, and the associated bias errors become negligible. In addition, if the shunt is installed directly across the positive and negative input terminals of the DAS (as is done in our facility), then $R_{SL}$ becomes zero, and $\delta E_{o,\,bias}$ is forced equal to zero regardless of the value of $Z_{DAS}$.

Choosing a Shunt Resistor

The shunt resistance R is selected to minimize the total uncertainty in the value of $I_t$ calculated from Equation 3.2. In general, if a variable X is a function of several other measured quantities $(x_1, x_2, \ldots, x_n)$, then the total uncertainty in the value of X is given by

$$\delta X = \sqrt{(\delta X_{bias})^2 + \left(\frac{\partial X}{\partial x_1}\delta x_1\right)^2 + \left(\frac{\partial X}{\partial x_2}\delta x_2\right)^2 + \ldots + \left(\frac{\partial X}{\partial x_n}\delta x_n\right)^2} \tag{3.6}$$

where $\delta X_{bias}$ is the root sum square (RSS) of all known bias errors in X, and $\delta x_n$ is the total uncertainty in the measurement of $x_n$ (Moffat, 1988). Often times, $\delta X$ is more conveniently expressed as a fraction or percent of reading. The fractional form of the uncertainty can always found by dividing both sides of Equation 3.6 by X. For the special but common case in which X is purely a product of the $x_n$, the fractional uncertainty takes on a direct and convenient form. That is, if

$$X = x_1^a\, x_2^b \ldots x_n^m \tag{3.7}$$

then

$$\frac{\delta X}{X} = \sqrt{\left(\frac{\delta X_{bias}}{X}\right)^2 + \left(a\frac{\delta x_1}{x_1}\right)^2 + \left(b\frac{\delta x_2}{x_2}\right)^2 + \ldots + \left(m\frac{\delta x_n}{x_n}\right)^2} \tag{3.8}$$

Applying the latter equation to Equation 3.2 yields the total fractional uncertainty in the calculated value of $I_t$. That is,

$$\frac{\delta I_t}{I_t} = \sqrt{\left(\frac{\delta I_{t,\,bias}}{I_t}\right)^2 + \left(\frac{\delta E_o}{E_o}\right)^2 + \left(\frac{\delta R}{R}\right)^2} \tag{3.9}$$

where $\delta E_o$ is the total uncertainty in the measurement of $E_o$, and $\delta R$ is the total uncertainty in the value of R. The total uncertainty in the measurement of $E_o$ is given by

$$\delta E_o = \sqrt{(\delta E_{o,\,bias})^2 + (\delta E_{o,\,m})^2} \tag{3.10}$$

where $\delta E_{o,\,m}$ is the accuracy of the DAS measurement of $E_o$ (as is given by Table 3.2 or Table 3.3), and $\delta E_{o,\,bias}$ is the bias error given by Equation 3.5. The total uncertainty in the value of R is

$$\delta R = \sqrt{(\delta R_m)^2 + (\delta R_T)^2} \tag{3.11}$$

where $\delta R_m$ is the total uncertainty in the measured value of R (or, if R is not measured, $\delta R_m$ is the manufactured tolerance of the resistor), and $\delta R_T$ is the drift in the value of R due to changes in the resistor temperature.

Concerning the uncertainty $\delta R_m$, we measure each shunt resistance with a Hewlett Packard Model No. HP 34401A digital multimeter before installing each shunt in our facility. The HP 34401A utilizes a highly accurate four-wire resistance measurement technique, the principle

of which is discussed later in this chapter. Table 3.4 summarizes the accuracy specifications of the HP 34401A. In general, the accuracy of a resistance measurement made with the HP 34401A is typically much better than the manufactured tolerance of the resistor. Concerning the uncertainty $\delta R_T$, we specifically use resistors which have low temperature drift characteristics. The temperature drift characteristic of a resistor is quantified in terms of a temperature coefficient $k_T$ which is most often expressed in units of parts per million per degree Celsius (ppm/°C). That is, $k_T$ equals $10^6$ times the fractional change in R per degree Celsius. Hence, if the resistor temperature drifts by an amount $\delta T$ away from the temperature at which the value of R was initially measured, then the resistor value changes by the amount

$$\delta R_T = \frac{k_T}{10^6} R \, \delta T \tag{3.12}$$

Substituting Equations 3.10–3.12 into Equation 3.9 gives the most convenient form of the total fractional uncertainty in the calculated value of $I_t$:

$$\frac{\delta I_t}{I_t} = \sqrt{\left(\frac{\delta I_{t,\,bias}}{I_t}\right)^2 + \left(\frac{\delta E_{o,\,bias}}{E_o}\right)^2 + \left(\frac{\delta E_{o,\,m}}{E_o}\right)^2 + \left(\frac{\delta R_m}{R}\right)^2 + \left(\frac{k_T}{10^6}\,\delta T\right)^2} \tag{3.13}$$

The latter form is convenient because the individual terms beneath the radical can be directly compared to each other to reveal which measurements contribute the greatest errors to the overall result. The best accuracy in the measurement of $I_t$ is typically achieved if $E_o$ is sensed on a unipolar voltage range of the DAS (i.e., assuming a DC current is being sensed), and if the value of R is chosen such that $E_o$ equals the upper limit of the chosen range when the maximum current is being sensed. For a general case, the transmitter specification sheet must then be checked to verify that the device can drive the prospective load of R plus any line resistance $R_L$ (total loads are limited to 1000 Ω for the transmitters used in our facility). In addition, if the transmitter uses an external power supply, the specification sheet must be checked again to determine the minimum supply voltage needed to drive the load.

The Selected Choice of Shunts

The outputs of the three 4–20 mA current transmitters used in our facility are sensed with the 12-bit DAS cards. As is shown in Table 3.2, the unipolar voltage range settings offered by the cards have upper limits of 50 mV, 500 mV, and 10 V. Shunt values of R = 2.5, 25, and 500 Ω respectively match $E_o$ to these upper limit values when sensing the maximum current of 20 mA. Figure 3.2 shows a plot of the total fractional uncertainty in the measurement of $I_t$ over a 4–20 mA range for setups which use the stated values of R. In each case, the temperature coefficient of the shunt was fixed at $k_T = \pm 20$ ppm/°C (an available catalogue value), and the

Table 3.4 The rated accuracy specifications of the HP 34401A digital multimeter for (a) four-wire resistance measurements and (b) DC voltage measurements.

(a)

| Range | Resolution | Accuracy ± (% of Reading + % of Range) |
|---|---|---|
| 100 Ω | 100 μΩ | 0.010 + 0.004 |
| 1 kΩ | 1 mΩ | 0.010 + 0.001 |
| 10 kΩ | 10 mΩ | 0.010 + 0.001 |
| 100 kΩ | 100 mΩ | 0.010 + 0.001 |
| 1 MΩ | 1 Ω | 0.010 + 0.001 |
| 10 MΩ | 10 Ω | 0.040 + 0.001 |
| 100 MΩ | 100 Ω | 0.800 + 0.010 |

(b)

| Range | Resolution | Accuracy ± (% of Reading + % of Range) |
|---|---|---|
| 100 mV | 100 nV | 0.0050 + 0.0035 |
| 1 V | 1 μV | 0.0040 + 0.0007 |
| 10 V | 10 μV | 0.0035 + 0.0005 |
| 100 V | 100 μV | 0.0045 + 0.0006 |
| 1000 V | 1 mV | 0.0045 + 0.0010 |

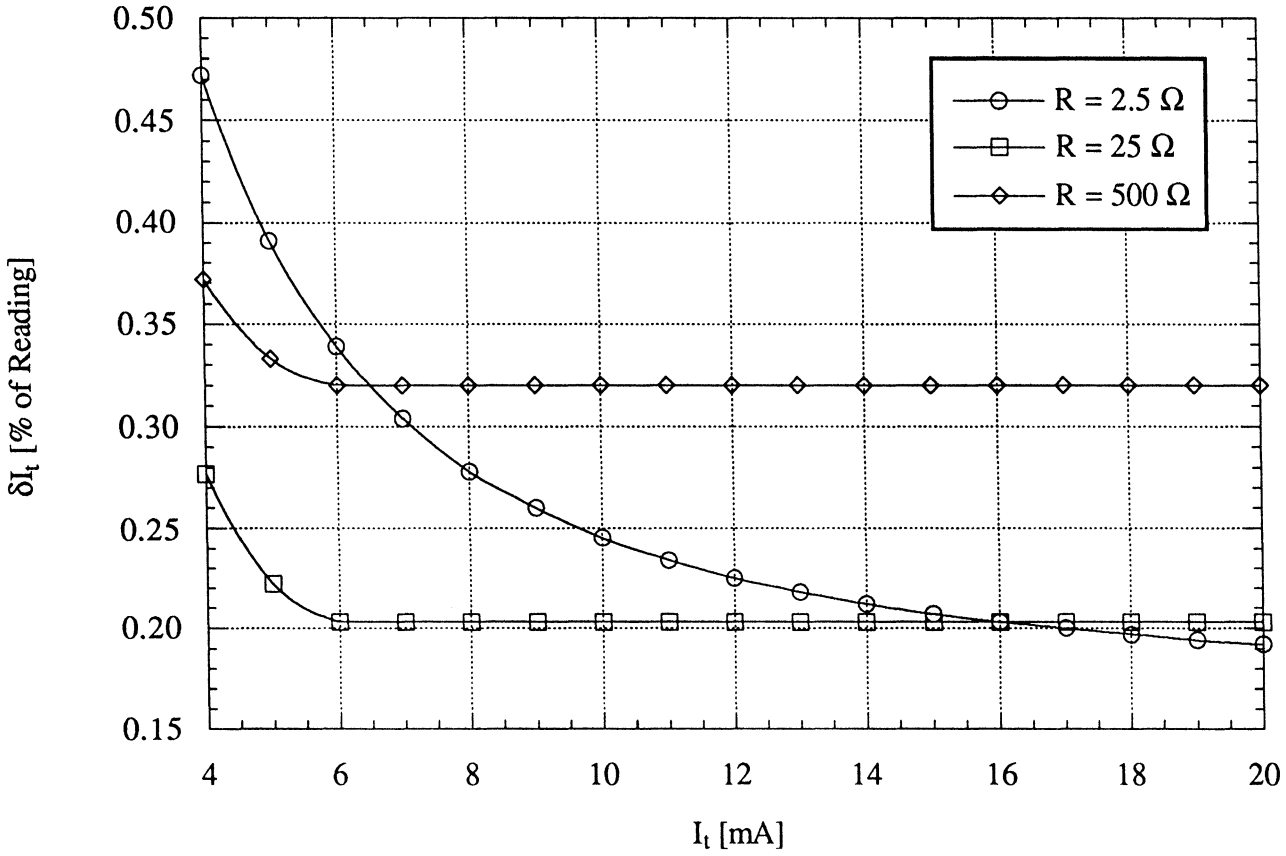


Figure 3.2 The total fractional uncertainty in the measurement of a transmitted current $I_t$ for several choices of shunt resistances R.

temperature drift was fixed at $\delta T = \pm 8$ °C (a reasonable value considering the shunts used in our facility are located in a stable ambient environment and dissipate under 1/4 W of power).

When using the combination of the 2.5-Ω shunt and the 50-mV range, the input impedance of the DAS is very large (> 1000 MΩ), so the contribution of $\delta I_{t,\,bias}$ to the total fractional uncertainty in $I_t$ is negligibly small (± 0.00000025 %). However, the fractional uncertainty in the measurement of R (± 0.17 %) and the fractional uncertainty in the measurement of $E_o$ for low currents (± 0.44 % for $I_t$ = 4 mA or $E_o$ = 10 mV) are both relatively high compared to the other cases. As a result, the total fractional uncertainty in $I_t$ is relatively high over the lower third of the 4–20 mA range as is shown in Figure 3.2. When using the combination of the 500-Ω shunt and the 10-V range, the input impedance of the DAS is relatively low (200 kΩ), so the contribution of $\delta I_{t,\,bias}$ to the total fractional uncertainty in $I_t$ is relatively high (± 0.25 %). Consequently, the total fractional uncertainty in $I_t$ is poor over the entire 4–20 mA range. The combination of the 25-Ω shunt and the 500-mV range provides the best compromise between the individual error contributions and results in the lowest overall uncertainty in $I_t$ as is shown in Figure 3.2. Each shunt presently used in our facility is a nominal 2.5-Ω, 1-W precision resistor (Newark Stock No. 96F3608) having a temperature coefficient of ± 20 ppm/°C and a manufactured tolerance of ± 1 %. In light of the previous analysis, we will use 25-Ω shunts with the STI DAS in future experiments.

### 3.1.2.3 Resistance Measurements

Real-time resistance measurements are required for three Resistance Temperature Detectors (RTD's) used in our facility. We measure the RTD resistances via the four-wire technique depicted in Figure 3.1. The technique involves passing a known source current through the RTD with one pair of leads and sensing the voltage drop across the RTD with the second pair of leads. The value R of the resistance is then calculated from Ohm's Law as

$$R = \frac{E_o}{I_s} \tag{3.14}$$

where $I_s$ is the known source current, and $E_o$ is the measured voltage drop. The method is directly analogous to the technique used to measure a transmitted current $I_t$, but only now the shunt resistance (i.e., the RTD resistance R) is the varying quantity, and the transmitted current (i.e., the source current $I_s$) is the known and constant quantity. Constant-current sources with sufficiently small drift characteristics are relatively expensive and difficult to find, so we approximate a constant-current source in the lab by connecting a voltage source $E_s$ in series with a set resistance $R_s$ as is shown in Figure 3.1. The value of the source voltage is measured on another DAS channel to account for drift. If $R_s$ is chosen to be sufficiently large, then changes in

the source current caused by the temperature-induced changes in the RTD resistance R become negligible, and the current through R can be assumed to be

$$I_s = \frac{E_s}{R_s + R_o} \tag{3.15}$$

where $R_o$ is the nominal resistance of the RTD at 0 °C. The actual source current produced by the combination of $E_s$ and $R_s$ is

$$I_s' = \left[ R_s + R_L + \frac{R\,(Z_{DAS} + R_{SL})}{Z_{DAS} + R_{SL} + R} \right]^{-1} E_s \tag{3.16}$$

where $R_L$ is the combined resistance of the leads connecting R to the source combination.

As before, the DAS acts like a resistor in parallel with R. The current drawn by the DAS-side branch of the parallel combination is

$$I_{DAS} = \left( \frac{R}{Z_{DAS} + R_{SL} + R} \right) I_s' \tag{3.17}$$

and the actual current through R is the difference $I_s' - I_{DAS}$. Thus, the value of $I_s$ calculated from Equation 3.15 has a bias error of

$$\delta I_{s,\,bias} = I_s - (I_s' - I_{DAS}) \tag{3.18}$$

and the output voltage measurement has a bias error of

$$\delta E_{o,\,bias} = R_{SL} I_{DAS} \tag{3.19}$$

Again, as $Z_{DAS}$ becomes large, $I_{DAS}$ becomes small, and the associated bias errors become negligible. However, unlike the previous problem in which the shunt resistance could be located directly at the inputs of the DAS to force $R_{SL} = 0$ (and, thus, force $\delta E_{o,\,bias} = 0$), the RTD is generally located far from the DAS, so $R_{SL}$ and the corresponding bias error $\delta E_{o,\,bias}$ are not likely to be negligibly small relative to the values of R and $E_o$. As a result, a high DAS input impedance (i.e., a negligibly small $I_{DAS}$) is generally required to achieve an accurate resistance measurement.

Choosing a Set Resistor

The set resistance $R_s$ is chosen to minimize the total fractional uncertainty in the value of R calculated from Equation 3.14 for a given choice of $E_s$. The total fractional uncertainty in the calculated value of R is found by applying Equation 3.8 to Equation 3.14, which gives

$$\frac{\delta R}{R} = \sqrt{\left(\frac{\delta E_o}{E_o}\right)^2 + \left(\frac{\delta I_s}{I_s}\right)^2} \tag{3.20}$$

where $\delta E_o$ is the total uncertainty in the measurement of $E_o$, and $\delta I_s$ is the total uncertainty in the value of $I_s$ calculated from Equation 3.15. The total uncertainty in the measurement of $E_o$ is given by

$$\delta E_o = \sqrt{(\delta E_{o,\,bias})^2 + (\delta E_{o,\,m})^2} \tag{3.21}$$

where $\delta E_{o,\,m}$ is the accuracy of the DAS measurement of $E_o$, and $\delta E_{o,\,bias}$ is the bias error given by Equation 3.19. The total uncertainty in the calculated value of $I_s$ is (in fractional form)

$$\frac{\delta I_s}{I_s} = \sqrt{\left(\frac{\delta I_{s,\,bias}}{I_s}\right)^2 + \left(\frac{\delta E_s}{E_s}\right)^2 + \left(\frac{\delta R_s}{R_s + R_o}\right)^2} \tag{3.22}$$

where $\delta E_s$ is the total uncertainty in the measurement of $E_s$, and $\delta R_s$ is the total uncertainty in the value of $R_s$. The total uncertainty in the measurement of $E_s$ is just the accuracy of the DAS voltage measurement $\delta E_{s,\,m}$. The total uncertainty in the value of $R_s$ is (from Equations 3.11 and 3.12)

$$\delta R_s = \sqrt{(\delta R_{s,\,m})^2 + \left(\frac{k_T}{10^6} R_s\, \delta T\right)^2} \tag{3.23}$$

where $\delta R_{s,\,m}$ is the total uncertainty in the measured value of $R_s$. Substituting Equations 3.21–3.23 into Equation 3.20 gives the most convenient form of the total fractional uncertainty in the calculated value of R:

$$\frac{\delta R}{R} = \left[\left(\frac{\delta E_{o,\,bias}}{E_o}\right)^2 + \left(\frac{\delta E_{o,\,m}}{E_o}\right)^2 + \left(\frac{\delta I_{s,\,bias}}{I_s}\right)^2 + \left(\frac{\delta E_{s,\,m}}{E_s}\right)^2 + \left(\frac{\delta R_{s,\,m}}{R_s + R_o}\right)^2 + \left(\frac{R_s}{R_s + R_o}\,\frac{k_T}{10^6}\,\delta T\right)^2\right]^{1/2} \tag{3.24}$$

The value of $R_s$ is chosen to minimize Equation 3.24 given an available source voltage $E_s$.

The Selected Choice of Set Resistors

The resistances of the three RTD's used in our facility are sensed with the 12-bit DAS cards. Each RTD has a nominal resistance of $R_o = 100\ \Omega$ at 0 °C. The RTD's are used over a temperature range of -20 to 60 °C, which corresponds to a resistance range of approximately 90 to 125 Ω. The source voltage $E_s$ is an auxiliary 6.9-VDC supply provided by one of the 12-bit cards. Figure 3.3 shows plots of the total fractional uncertainty in the measurement of R over a

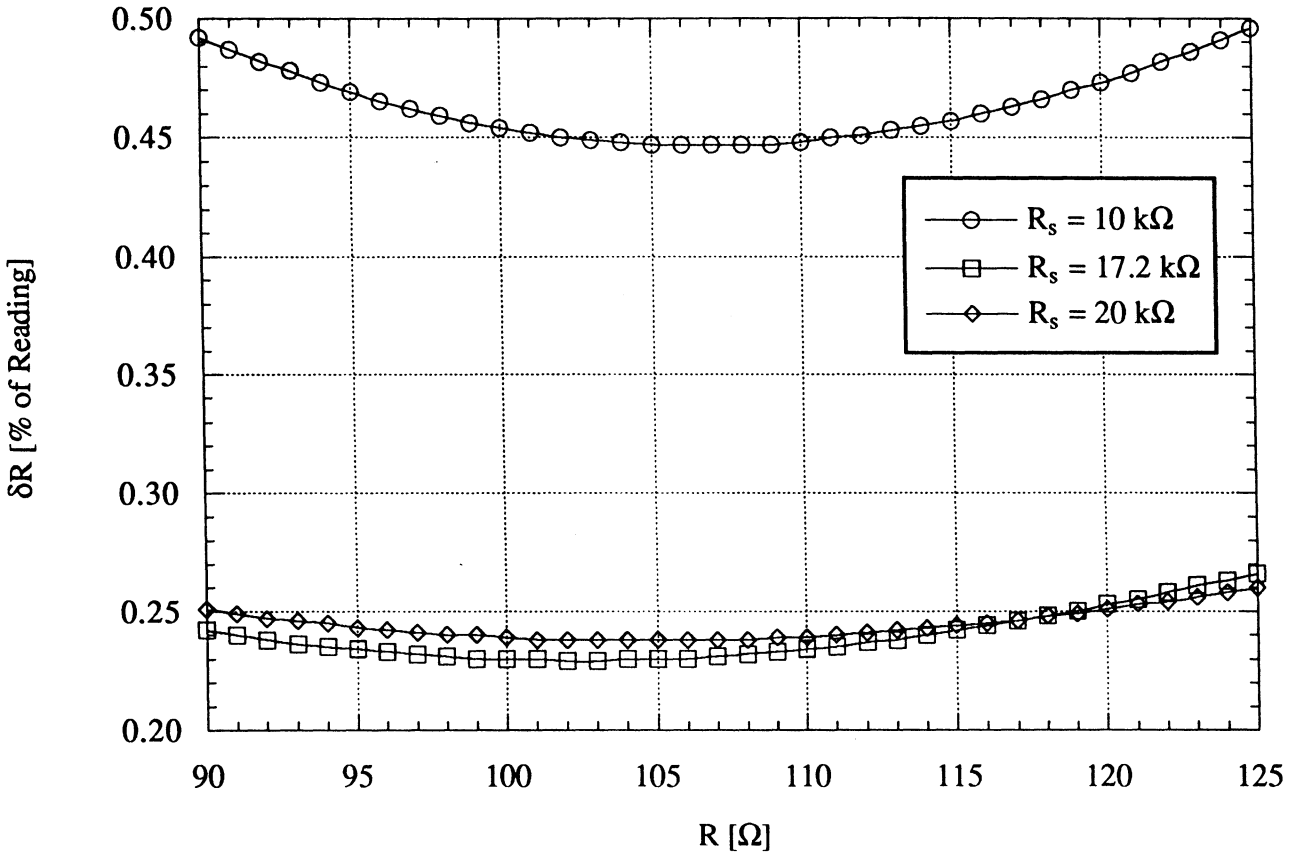


Figure 3.3 The total fractional uncertainty in the measurement of a resistance R for several choices of set resistances $R_s$.

range of 90 to 125 Ω for set resistances of $R_s$ = 10 kΩ, 17.2 kΩ, and 20 kΩ. For each case, the temperature coefficient of $R_s$ was fixed at $k_T = \pm 25$ ppm/°C, and the temperature drift was fixed at $\delta T = \pm 8$ °C. The line resistances $R_{SL}$ and $R_L$ were each fixed at 1 Ω.

The 17.2-kΩ curve of Figure 3.3 represents the lowest possible uncertainty in the measurement of R which can be obtained with the 12-bit cards and the 6.9-VDC source voltage. For this case, the maximum voltage drop across the RTD is $E_o$ = 50 mV for the maximum expected value of R = 125 Ω, so $E_o$ is correspondingly measured on the 50-mV unipolar range setting. As is shown in Table 3.2, $Z_{DAS}$ is very large for this range setting (> 1000 MΩ), so the corresponding bias errors are negligible. If the set resistance is made less than 17.2 kΩ, then a larger source current is generated in the loop, resulting in a larger voltage drop across the RTD. As a result, $E_o$ must be measured on a range for which $Z_{DAS}$ is relatively low (200 kΩ), and the corresponding bias errors become increasingly significant. More importantly, as $R_s$ is made smaller, the assumed source current $I_s$ becomes a poorer approximation of the true source current $I_s'$, causing the bias error $\delta I_{s,\,bias}$ to become large. Thus, for any choice of $R_s$ less than 17.2 kΩ, the total fractional uncertainty in the measurement of R increases significantly as is illustrated by the 10-kΩ curve of Figure 3.3 (the 10-kΩ value was chosen somewhat arbitrarily, but one will find that the uncertainty is even larger for values closer to, but still less than, 17.2 kΩ). If the set resistance is made greater than 17.2 kΩ, then $I_s$ better approximates $I_s'$, and the bias error $\delta I_{s,\,bias}$ decreases. However, the decrease in the bias error is offset by a larger increase in the uncertainty in the measurement of $E_o$ because $E_o$ then spans less of the 50-mV range. As a result, the total fractional uncertainty in R slightly increases as is illustrated by the 20-kΩ curve of Figure 3.3. Each set resistor presently used in our facility consists of two adjacent 10-kΩ resistors of a dual in-line package resistor network chip (RESNET Model No. 668-A-1002 D) soldered in series. Each combination forms a nominal 20-kΩ resistor having a temperature coefficient of ± 25 ppm/°C, so the 20-kΩ curve of Figure 3.3 applies to our facility installations.

### 3.1.3 General Wiring Scheme

#### 3.1.3.1 Zone Boxes

The wiring between each instrument and the DAS is routed through one of three aluminum-chassis junction boxes mounted on the Unistrut framework supporting the evaporator- and condenser-side air loops. Each box contains terminal strips mounted on rectangular bars of aluminum stock measuring 2 in. (W) x 12 in. (H) x 3/8 in. (D). The bars, in turn, are bolted to the interior surface of the chassis. A thermally conductive heat sink compound is spread between the bar/chassis interfaces, and the outer surfaces of the chassis are covered with 1/4-in. thick foam insulation board. The entire construction is designed to prevent temperature gradients from

forming along the lengths of the terminal strips because temperature gradients introduce error voltages to the thermocouple circuits routed through the boxes. A junction box having such isothermal connection zones is termed a "zone box" in standard thermocouple literature. The junction boxes used in our facility are hereafter referred to as zone boxes.

Wiring diagrams showing the circuit connections made within the zone boxes are given in Figures 3.4–3.6. Three cables (Belden/Cooper Model No. 1225A) carry signals between the zone boxes and the DAS input panels located on the opposite side of the room. Each cable contains 20 individually shielded, twisted pairs of 22-AWG tinned-copper wire. As is shown in Figures 3.4–3.6, the shields form continuous paths between the instruments and the DAS, and each shield is properly grounded at the end nearest the signal source. Figures 3.4–3.6 also show that many of the installations utilize a multipin connector which allows the instrument to be easily disconnected and removed for calibration, maintenance, or repair. The soldered pin-to-wire joints within each connector are insulated with heat-shrink tubing to strengthen the connections and to prevent accidental short-circuits. Although not labeled in Figures 3.4–3.6, the pinout sequence for each connector is alphabetical from top to bottom (i.e., the top pin of the connector is pin A; the next pin down is pin B; etc.).

#### 3.1.3.2 Power Supplies

A 24-VDC, 2.4-A power supply (International Power Model No. IHC24-2.4) and a 5-VDC, 1.2-A power supply (International Power Model No. IHA5-1.2/OVP) provide input power to the instruments. Each power supply is located in a separate chassis box, and each is wired as shown in Figure 3.7. The negative lead of each supply is tied to earth ground to provide a single, convenient ground reference for all of the instrumentation, and to prevent common-mode voltage problems at the inlets of the amplifiers of the pressure transducers (discussed later). The positive and negative output leads of the supplies are tapped to jumpered terminal strips at the bottom of each zone box as is shown in Figures 3.4–3.6. The latter strips serve as the supply rails for all of the instruments requiring power. The power supplies and the instruments remain energized 24 hours per day to prevent warm-up shifts in the sensor output readings.

## 3.2 Temperature Instrumentation

Temperature measurements are made in our facility with thermocouples, resistance temperature detectors (RTD's), and thermistors. Table 3.5 summarizes the location and type of each instrument and gives the variable name associated with each measurement. The measurement techniques are discussed in the next several sections. The thermistor regulated by the circuitry of the oil concentration sensor is not discussed in this document.

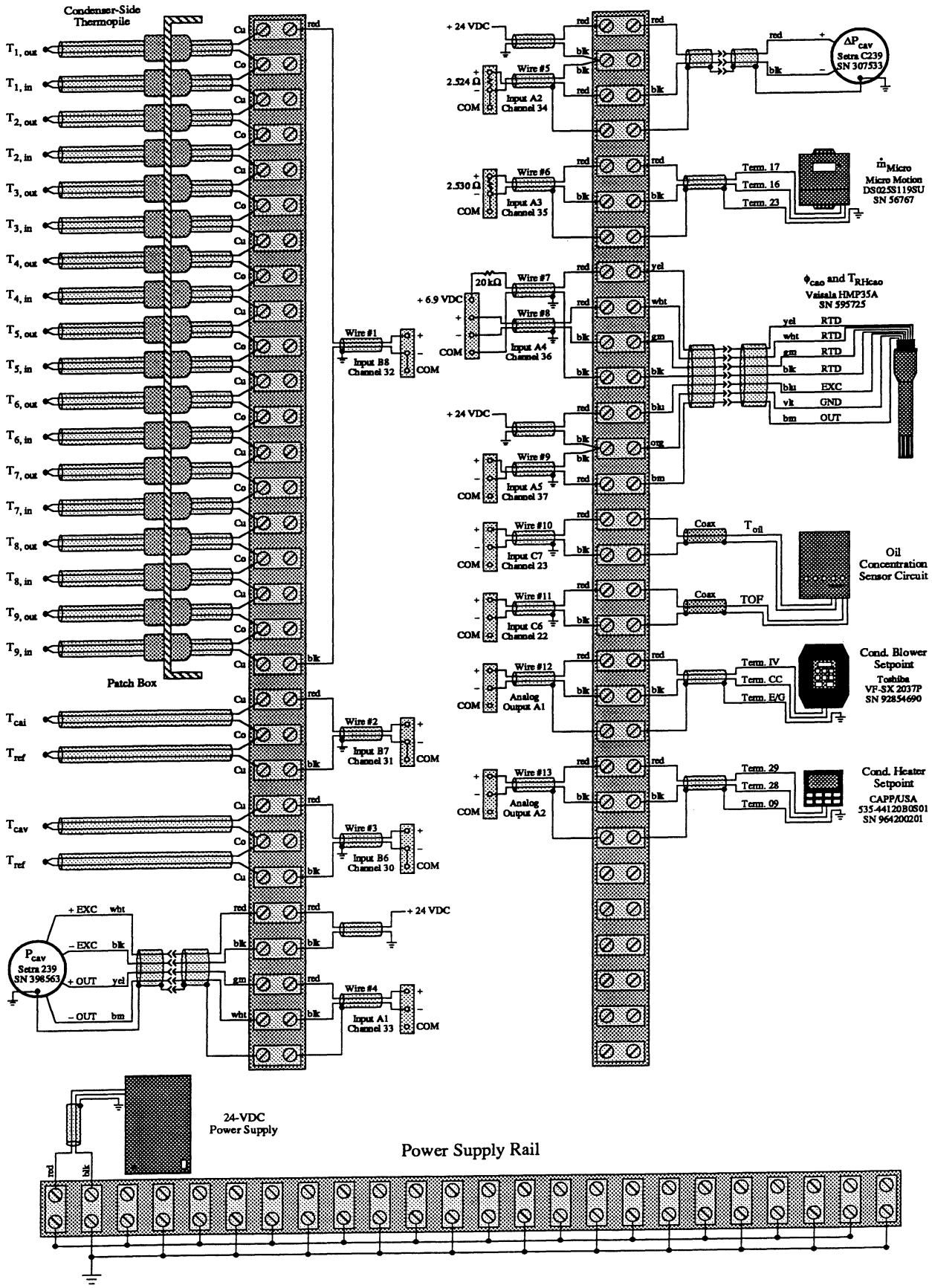


Figure 3.4 The wiring connections of Zone Box 1.

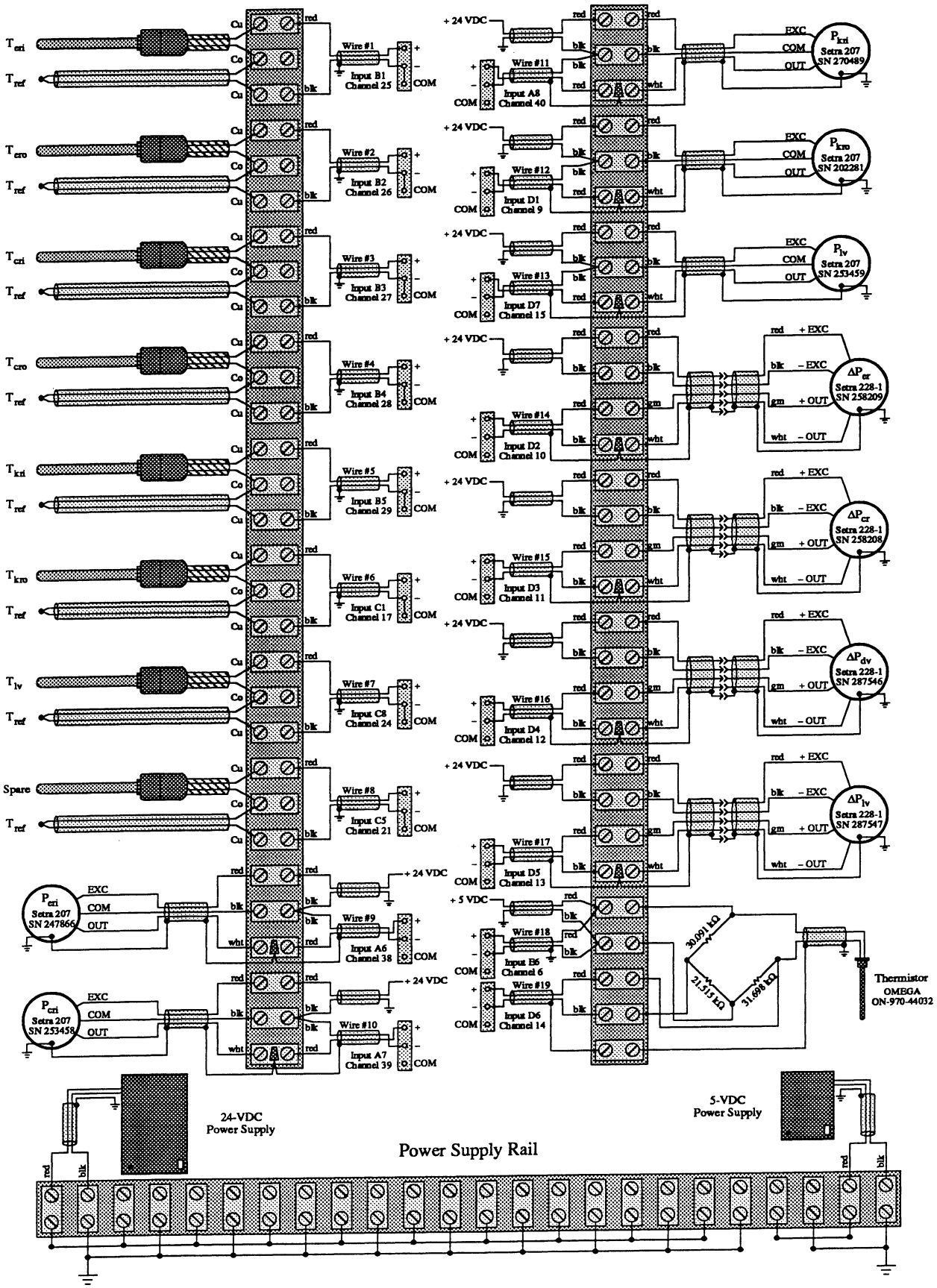


Figure 3.5 The wiring connections of Zone Box 2.

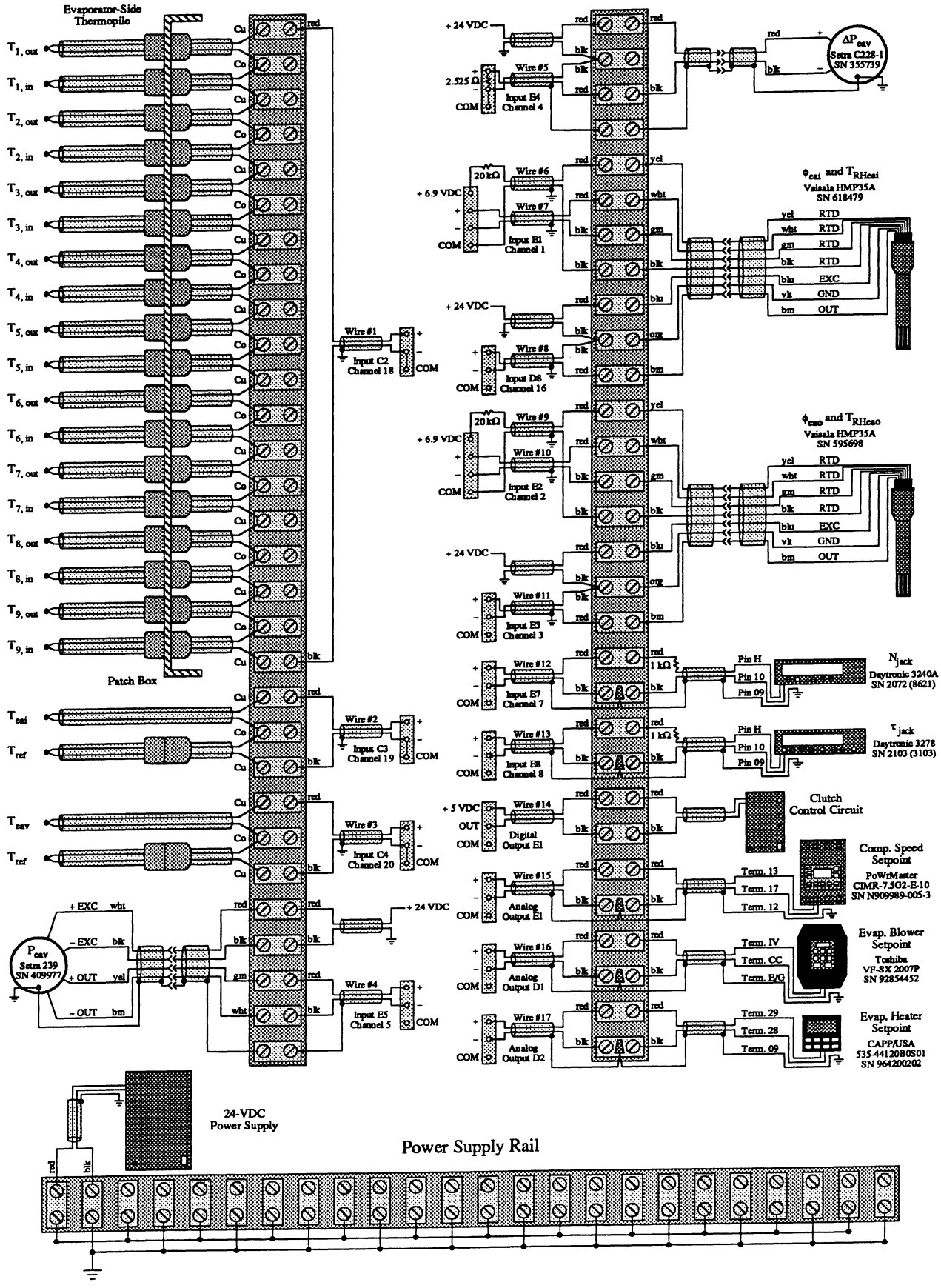


Figure 3.6 The wiring connections of Zone Box 3.

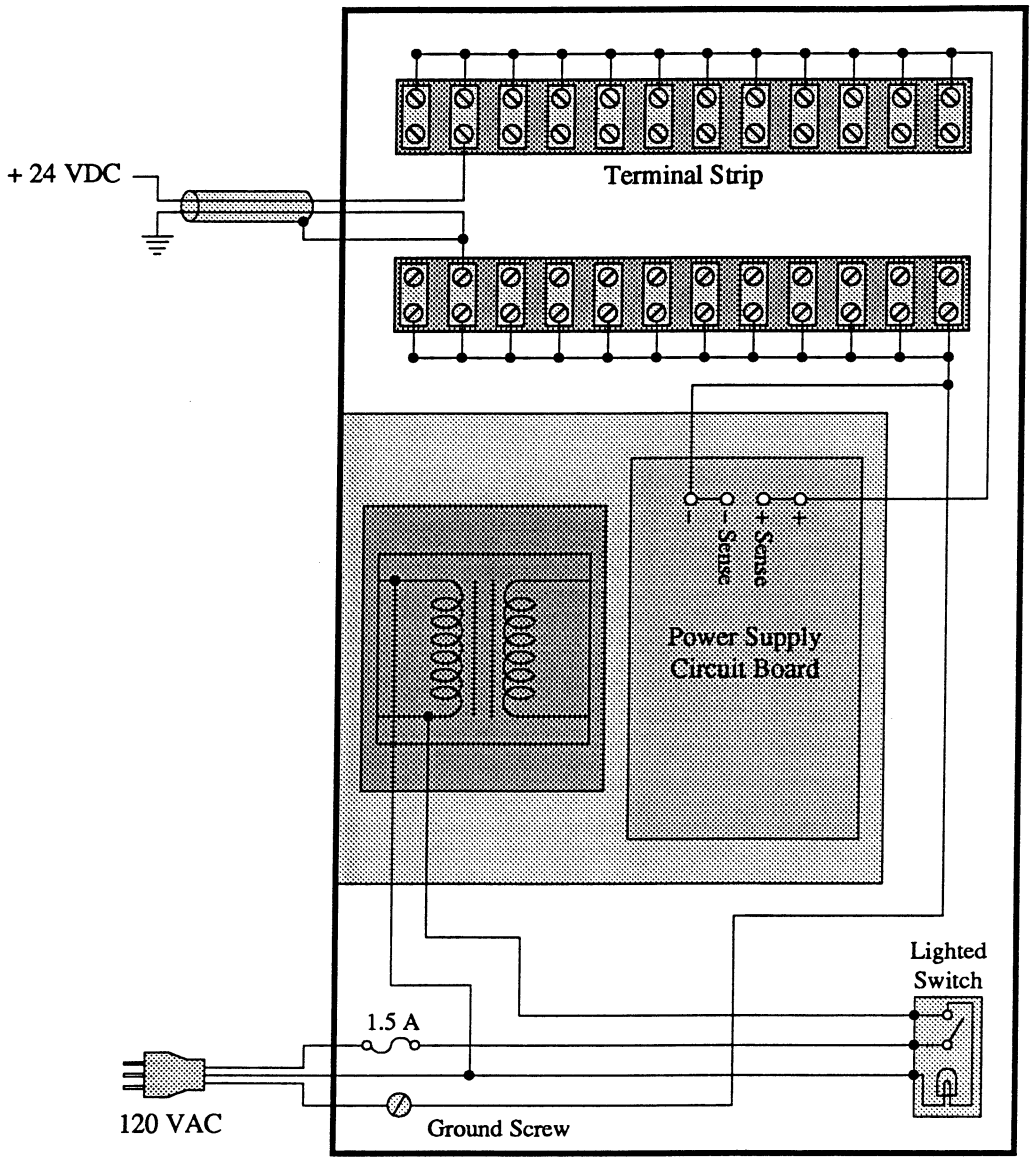


Figure 3.7 The typical wiring of the power supplies used in the facility.

Table 3.5 Summary of the temperature signals measured in the facility.

| Variable Name and Description | | Temperature-Sensing Instrument | |
|---|---|---|---|
| | | Type | Model No. |
| $T_{eai}$ | Evaporator inlet air temperature | Type-T wire junction (30-AWG) | Gordon T30-2-506 |
| $T_{eao}$ | Evaporator outlet air temperature | Type-T thermopile (30-AWG) | Gordon T30-2-506 |
| $T_{eav}$ | Evaporator air loop VFT inlet air temperature | Type-T wire junction (30-AWG) | Gordon T30-2-506 |
| $T_{cai}$ | Condenser inlet air temperature | Type-T wire junction (30-AWG) | Gordon T30-2-506 |
| $T_{cao}$ | Condenser outlet air temperature | Type-T thermopile (30-AWG) | Gordon T30-2-506 |
| $T_{cav}$ | Condenser air loop VFT inlet air temperature | Type-T wire junction (30-AWG) | Gordon T30-2-506 |
| $T_{eri}$ | Evaporator inlet refrigerant temperature | Type-T immersion probe | OMEGA TMQSS-062U-3 |
| $T_{ero}$ | Evaporator outlet refrigerant temperature | Type-T immersion probe | OMEGA TMQSS-062U-3 |
| $T_{kri}$ | Compressor inlet refrigerant temperature | Type-T immersion probe | OMEGA TMQSS-062U-3 |
| $T_{kro}$<br>$T_{dv}$ | Compressor outlet refrigerant temperature, same as Discharge-line VFT inlet refrigerant temperature | Type-T immersion probe | OMEGA TMQSS-062U-3 |
| $T_{cri}$ | Condenser inlet refrigerant temperature | Type-T immersion probe | OMEGA TMQSS-062U-3 |
| $T_{cro}$ | Condenser outlet refrigerant temperature | Type-T immersion probe | OMEGA TMQSS-062U-3 |
| $T_{lv}$ | Liquid-line VFT inlet refrigerant temperature | Type-T immersion probe | OMEGA TMQSS-062U-3 |
| $T_{RHeai}$ | Temperature at evaporator inlet humidity probe | Four-wire RTD (Pt 100) of humidity probe | Vaisala HMP 35A |
| $T_{RHeao}$ | Temperature at evaporator outlet humidity probe | Four-wire RTD (Pt 100) of humidity probe | Vaisala HMP 35A |
| $T_{RHcao}$ | Temperature at condenser outlet humidity probe | Four-wire RTD (Pt 100) of humidity probe | Vaisala HMP 35A |
| $T_{ref}$ | Thermocouple reference bath temperature | Thermistor probe<br>Wheatstone bridge | OMEGA ON-970-44032<br>N/A |
| $T_{oil}$ | Refrigerant/oil temperature at oil concentration sensor | Thermistor probe<br>Regulator circuit of oil concentration sensor | OMEGA ON-970-44032<br>N/A |
| $T_b$ | Barometer fluid/scale temperature | Mercury-in-glass thermometer on barometer housing | PRINCO Nova™ 469 |

### 3.2.1 Thermocouples

Copper-constantan (Type-T) thermocouples are used to measure the majority of the air- and refrigerant-side temperatures in our facility. Thermocouples provide the fast response time needed for transient studies while requiring only a minimum amount of circuitry. Figure 3.8 shows the classical thermocouple circuit used in our facility. The circuit consists of a measuring junction wired in series with a reference junction. The reference junction is located in an isothermal bath whose temperature $T_{ref}$ is accurately sensed by a thermistor. The output voltage of the circuit is

$$E_o = V(T) - V(T_{ref}) \tag{3.25}$$

where the function V(T) describes the emf produced by a thermocouple junction at a temperature T. The value of V(T) is commonly referred to as the Seebeck voltage. The Seebeck voltage is a nonlinear function of T and cannot be physically measured without error because the act of connecting voltmeter leads (usually made of a copper alloy) to the thermocouple introduces two unknown thermoelectric voltages to the circuit. However, the difference between two Seebeck voltages (i.e., $E_o$) can be physically measured without error by using the circuit of Figure 3.8 provided that the two voltmeter-to-thermocouple connections are at the same temperature. We shall return to this point later.

The relationship between $E_o$ and T is determined by calibrating the circuit over the desired range of T with the reference junction held at a constant temperature. By holding the reference temperature fixed, $V(T_{ref})$ remains fixed, and $E_o$ is then only a function of T. The calibration is typically performed with the reference junction held in an ice bath because an ice bath can be precisely maintained at a constant temperature of 0 °C and can be reproduced from test to test. A polynomial curve fit of the form

$$E_o^{ice}(T) = c_0 + c_1 T + c_2 T^2 + c_3 T^3 + \ldots + c_n T^n \tag{3.26}$$

will generally fit the data well, where the "ice" superscript on $E_o^{ice}(T)$ is included to enforce the fact that the equation is valid only if the reference junction is in an ice bath at 0 °C. We have not yet calibrated our circuits to determine the coefficients $c_n$, so we must presently use standard coefficients established by the National Institute of Standards and Technology (NIST). The NIST values of $c_n$ for Type-T thermocouples are given in Weston (1996). In general, for any given thermocouple type, the NIST equation (i.e., Equation 3.26 with the appropriate NIST $c_n$) represents the nominal temperature-voltage characteristics of the given type. Thermocouple wires are manufactured to conform to the NIST-established behavior within prescribed limits. Figure 3.9 shows a plot of the NIST equation for Type-T thermocouples over the entire range of

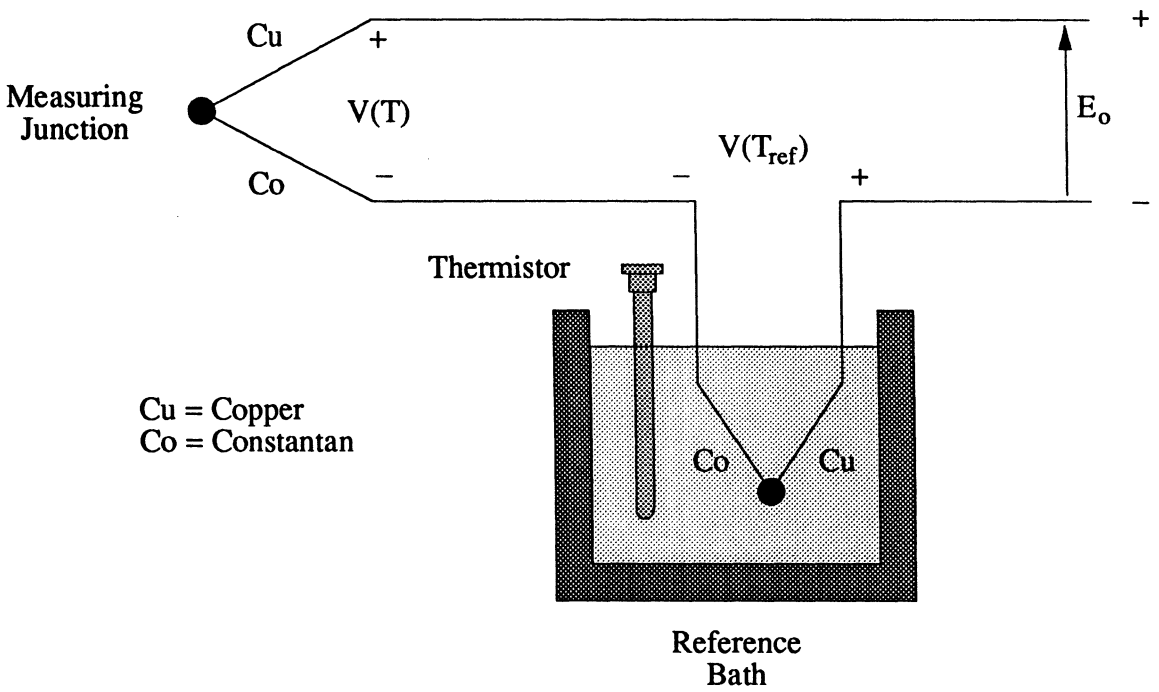


Figure 3.8 The classical two-junction thermocouple circuit used to make the majority of the temperature measurements in our facility.

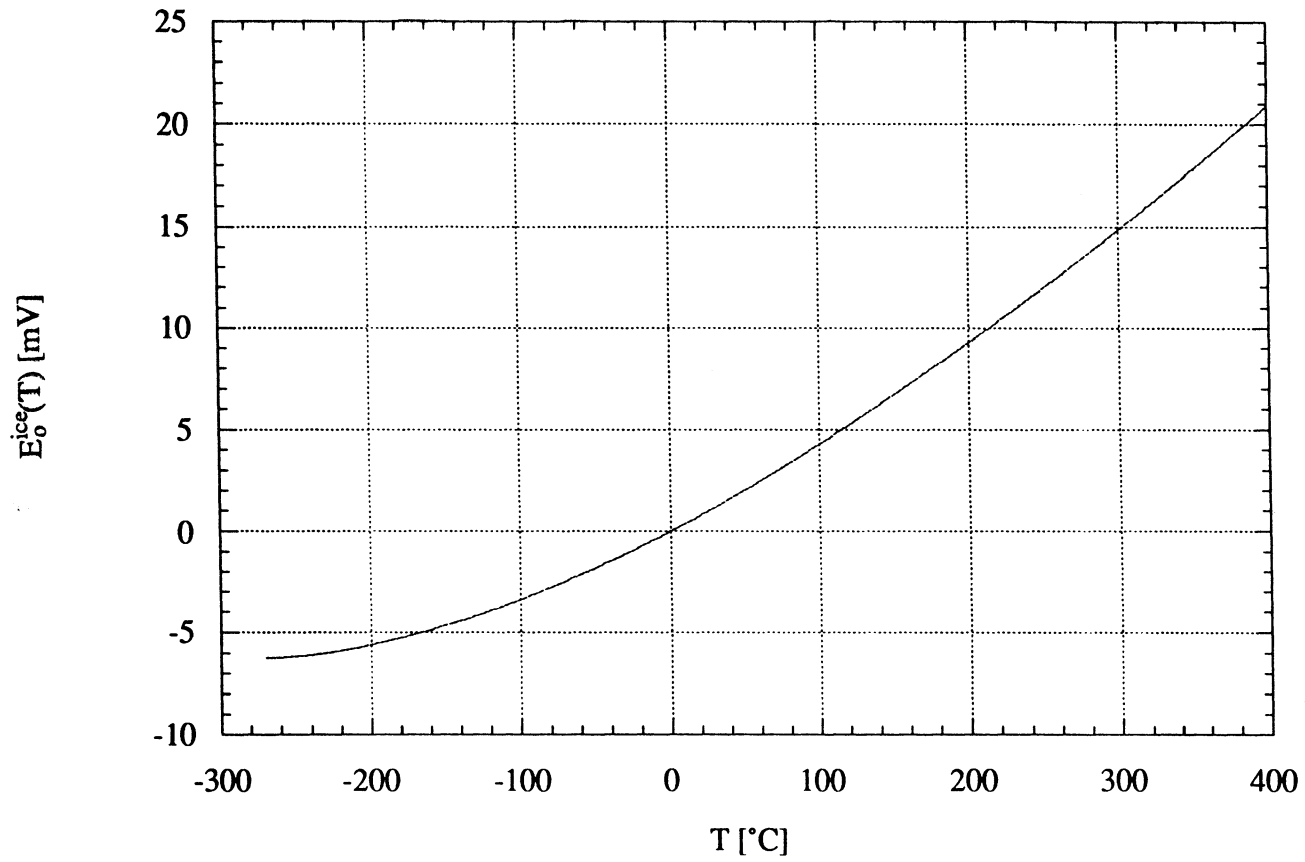


Figure 3.9 The nominal temperature-voltage characteristics of Type-T thermocouples as established by NIST.

usage documented by NIST (-270 to 400 °C). An eighth-order polynomial is used to describe the temperature-voltage relationship above 0 °C, and a fourteenth-order polynomial is used to describe the relationship below 0 °C.

In practice, if the reference junction is not at the exact same temperature as it was during the calibration run, then the measured output voltage $E_o$ must be converted to an equivalent calibration-referenced output voltage to determine T. We do not use an ice bath in our facility, so the output voltages measured from our circuits must be converted to equivalent ice-referenced voltages before T can be calculated from the NIST equation. To perform the conversion, we first note from Equation 3.25 that $E_o^{ice}(T)$ can be equivalently expressed as

$$E_o^{ice}(T) = V(T) - V(0\ °C) \tag{3.27}$$

Evaluating the latter equation at $T_{ref}$ and rearranging gives

$$V(T_{ref}) = E_o^{ice}(T_{ref}) + V(0\ °C) \tag{3.28}$$

Substituting Equation 3.28 into Equation 3.25 gives

$$\begin{aligned} E_o &= V(T) - [E_o^{ice}(T_{ref}) + V(0\ °C)] \\ &= [V(T) - V(0\ °C)] - E_o^{ice}(T_{ref}) \\ &= E_o^{ice}(T) - E_o^{ice}(T_{ref}) \end{aligned} \tag{3.29}$$

Rearranging the last expression gives the equivalent ice-referenced output voltage needed to determine T:

$$E_o^{ice}(T) = E_o + E_o^{ice}(T_{ref}) \tag{3.30}$$

In summary, the temperature of the measuring junction is calculated as follows:

1. Equation 3.26 is evaluated at the reference bath temperature $T_{ref}$ (as is measured by the thermistor of Figure 3.8) to give $E_o^{ice}(T_{ref})$.
2. The calculated value of $E_o^{ice}(T_{ref})$ is added to the measured output voltage $E_o$ (as is dictated by Equation 3.30) to determine $E_o^{ice}(T)$.
3. Equation 3.26 is solved implicitly for T given the value of $E_o^{ice}(T)$ calculated in Step 2.

Step 3 involves the use of iterative equation solving techniques which can be time consuming when reducing thousands of transient data points and are impractical for computing temperatures in real time, such as for display on a DAS monitor. Hence, NIST also provides

coefficients for an inverse relation giving temperature directly as a function of voltage. The inverse relation is

$$T = a_0 + a_1 E_o^{ice} + a_2 (E_o^{ice})^2 + a_3 (E_o^{ice})^3 + \ldots + a_n (E_o^{ice})^n \qquad (3.31)$$

where the coefficients $a_n$ are given in Weston (1996). Sixth- and seventh-order polynomials are respectively used to calculate temperatures above and below 0 °C. Values of T calculated from Equation 3.31 fall within ± 0.04 °C of the values which exactly satisfy the established reference equation (Equation 3.26) (Burns, 1993). We presently use Equation 3.31 to calculate T as opposed to an iterative process.

The three-step calculation procedure described above is programmed into the WorkBench software so that the system temperatures can be monitored in real time on the DAS display monitor. Reduced-order forms of Equations 3.26 and 3.31 are used in the WorkBench implementation because the software only allows polynomials of order three or less to be directly entered in its menu blocks. The reduced-order polynomials are given in Weston (1996). The latter polynomials are least-squares curve fits of data generated from the NIST equation over the range of temperatures expected to be measured in our air- and refrigerant-side loops. At present, the values of T calculated by the WorkBench software via the reduced-order polynomials are the values logged in the data files and subsequently used in all data reduction calculations. To achieve better accuracy in future experiments, we will configure the DAS to directly log the output voltage $E_o$ of each circuit as opposed to the displayed value of T, and all official temperature calculations will be performed off line using either the higher-order NIST polynomials or in-house calibration polynomials.

#### 3.2.1.1 Thermocouple Measuring Junctions

Each air-side measuring junction consists of a bead welded at the end of a length of duplex-insulated, 30-AWG, Type-T thermocouple wire (Gordon Model No. T30-2-506). We used a thermocouple welder (Dynatech Model No. 116) to form the beads. The fine gage of the wire allows a small (~ 1/32-in. diameter) bead to be welded, thereby resulting in a faster temperature response time compared to couples formed from larger gage wires. Unfortunately, the copper-constantan wire pair is neither twisted nor shielded. The integrating A/D converters of the STI DAS adequately attenuate 60-Hz noise, but the thermocouple signals are still susceptible to the effects of high-frequency noise signals generated by our variable-speed motor drives. This latter problem (if, in fact, it is a problem) warrants future investigation. Continuing, the thermocouple wire is rated ANSI Special Limits of Error, meaning that the temperature-voltage characteristics of an ice-referenced circuit constructed from the wire will conform to the NIST equation to

within ± 0.5 °C or ± 0.4 % of reading (whichever is greater) when sensing temperatures in the range of -200 to 350 °C (OMEGA, 1992). At the heat exchanger inlets, the wire is supported in the air flow by a 1/8-in. O.D. (3/32-in. I.D.) brass tube which inserts into the probe ports of the measurement section as is shown in Figure 2.5. The wire is positioned such that the thermocouple bead hangs in the flow approximately 3/16 in. from the end of the support tube. Care is taken to ensure that the exposed lengths of wire leading to the bead do not touch the walls of tube because the tube is earth-grounded via its contact with the ductwork. A similar thermocouple/tube combination is located at the upstream end of each VFT inlet pipe to measure the inlet temperature to the VFT.

Each refrigerant-side measuring junction consists of a Type-T thermocouple bead housed in a 3-in. long, 1/16-in. O.D. stainless steel probe (OMEGA Model No. TMQSS-062U-3). The probe construction is ungrounded in type (i.e., the thermocouple junction within the probe is electrically isolated from the sheath). The probes are supported in the refrigerant lines by the tap arrangements shown in Figure 2.10. In each installation, a length of 26-AWG Type-T thermocouple extension wire is used to connect the probe to its respective zone box. The extension wire is cut extra long so that the probe can be easily relocated when installing different systems. Any excess length of wire is tightly bundled with cable ties to reduce magnetic noise pickup. Extension-grade wire is used to make the connections because finer gage wires become kinked, broken, or excessively cold-worked if repeatedly bundled. The probes and extension wires are rated ANSI Limits of Error, meaning that the temperature-voltage characteristics of an ice-referenced circuit constructed from these components will conform to the NIST equation to within ± 1 °C or ± 1.5 % of reading (whichever is greater) when sensing temperatures in the range of -200 to 0 °C, and to within ± 1 °C or ± 0.75 % of reading (whichever is greater) when sensing temperatures in the range of 0 to 350 °C (OMEGA, 1992).

#### 3.2.1.2 Thermocouple Reference Bath

Our isothermal reference bath is a plastic coffee thermos filled with tap water. The thermos is clamped to the Unistrut framework supporting the condenser air loop and is located far from any sources of heat. Each reference junction consists of a bead welded at the end of a length of 30-AWG Type-T wire rated ANSI Special Limits of Error. The length of wire submerged in the bath is coated with Plasti Dip® to prevent galvanic action between the reference junctions (Benedict, 1977), and to prevent the bath fluid from migrating up the duplex insulation of the wire by capillary action. For future experiments, we will use a silicone oil for the bath fluid because silicone oil is nonvolatile and has a higher thermal conductivity than water.

Reference Bath Thermistor

The temperature of the reference bath fluid is sensed by a thermistor probe (OMEGA Model No. ON-970-44032) wired in a Wheatstone bridge circuit as is shown in Figure 3.5. The bridge excitation is provided by the 5-VDC power supply. A 5-VDC supply is used because (i) a 5-VDC signal is directly measurable by the DAS (recall $E_{CM}$ cannot exceed 8 V for the STI DAS cards) and (ii) a 5-VDC supply creates a smaller current through the thermistor, thereby resulting in a lower self-heating error. A thermistor is used to measure the bath temperature because, unlike an RTD, a thermistor is highly sensitive to small changes in temperature. However, the increased sensitivity comes at the expense of decreased linearity, particularly if the thermistor is used over a wide range of temperatures (fortunately, ours is not). We calibrated our thermistor circuit against a calibrated, ASTM-certified (American Society of Testing and Materials) mercury-in-glass thermometer in a constant-temperature bath (NESLAB Model No. RTE-220) over a safely expected range of facility reference bath temperatures (14.7 to 26.7 °C). Proper stem corrections were applied to the thermometer readings (Benedict, 1977), and the highly accurate HP 34401A multimeter was used to read the input and output voltages of the Wheatstone bridge. The voltage-measurement accuracy specifications of the HP 34401A are given in Table 3.4b. Figure 3.10 shows a plot of the calibration data. The following linear least-squares curve fit describes the data well:

$$T_{ref} = 91.691 \frac{E_{bo}}{E_{bi}} + 16.088 \tag{3.32}$$

where
$T_{ref}$ = reference bath (i.e., thermistor) temperature [°C]
$E_{bo}$ = bridge output voltage [VDC]
$E_{bi}$ = bridge input voltage [VDC]

The equation fits the calibration data to within ± 0.07 °C with 95 % confidence.

In practice, the STI DAS is used to sense the bridge voltages, so the accuracy achieved in measuring $T_{ref}$ in the lab is slightly worse than the stated accuracy of the calibration. The total uncertainty in the STI DAS measurement of $T_{ref}$ is found by applying Equation 3.6 to Equation 3.32, which gives

$$\delta T_{ref} = \sqrt{(\delta T_{ref,\,cal})^2 + \left(\frac{m}{E_{bi}}\,\delta E_{bo}\right)^2 + \left(m\frac{E_{bo}}{E_{bi}^2}\,\delta E_{bi}\right)^2} \tag{3.33}$$

where $\delta T_{ref,\,cal}$ is the accuracy of the calibration, and m = 91.691 °C-V/V is the slope of Equation 3.32. The calibration uncertainty $\delta T_{ref,\,cal}$ is assumed to include the self-heating errors of the thermistor. $E_{bo}$ and $E_{bi}$ are measured with the 12-bit DAS cards. $E_{bo}$ is measured on the

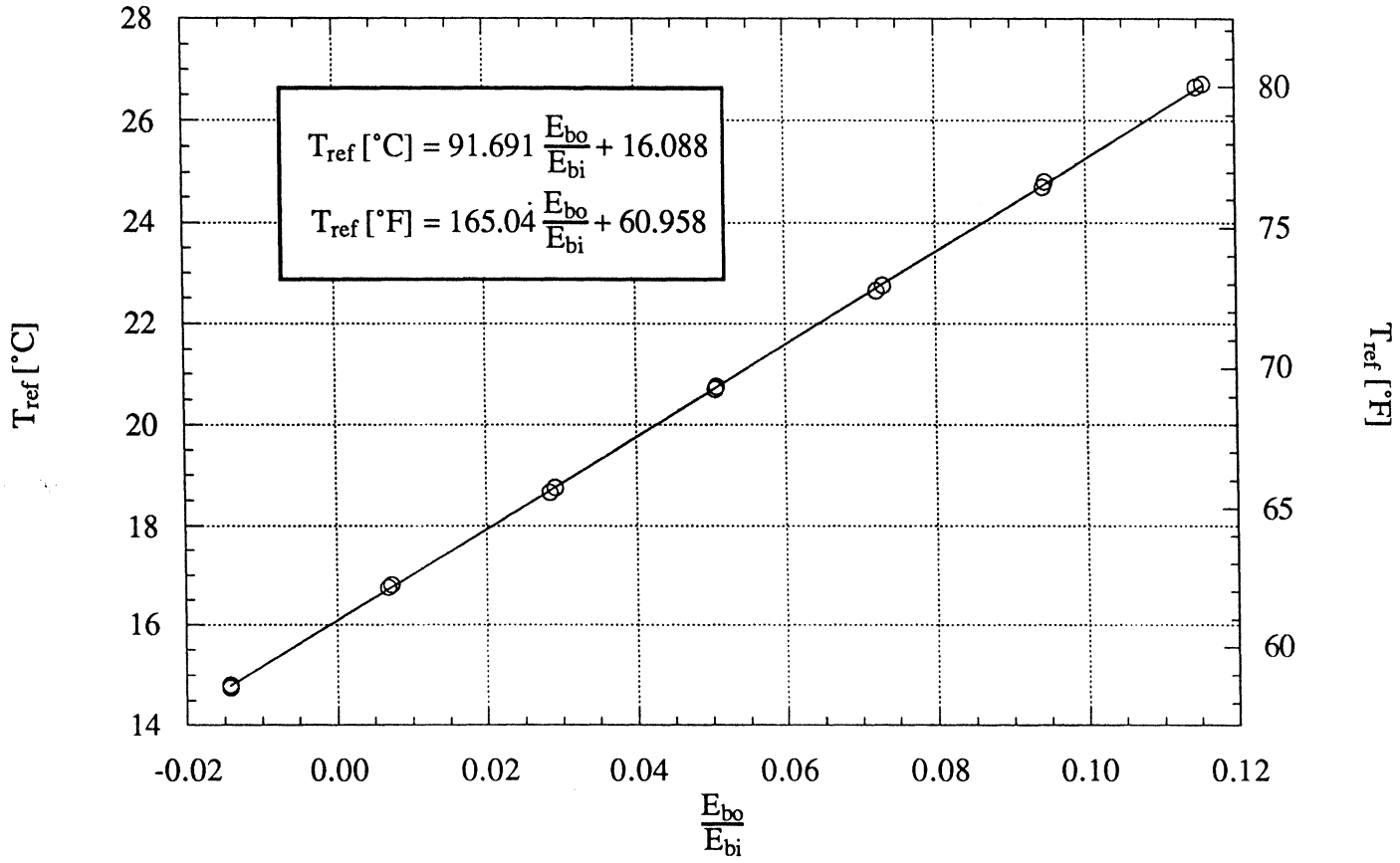


Figure 3.10 The thermistor calibration curve.

$\pm$ 5-V bipolar range, and $E_{bi}$ is measured on the 10-V unipolar range. Table 3.2 gives the corresponding measurement uncertainties $\delta E_{bo}$ and $\delta E_{bi}$. For a nominal bridge excitation voltage of $E_{bi}$ = 5 VDC, Equation 3.33 yields (to two significant figures) a total uncertainty of $\delta T_{ref} = \pm 0.12$ °C over the entire calibrated range of thermistor temperatures.

3.2.1.3 Accuracy of the Thermocouple Temperature Measurements

The total uncertainty in the value of T sensed by each thermocouple circuit is found by applying Equation 3.6 to Equation 3.31, which gives

$$\delta T = \sqrt{(\delta T_{ANSI})^2 + (\delta T_{eqn})^2 + \left(\frac{\partial T}{\partial E_o^{ice}} \delta E_o^{ice}\right)^2} \tag{3.34}$$

where $\delta T_{ANSI}$ is the manufactured tolerance of the Type-T wire (i.e., the ANSI error limit specification), and $\delta T_{eqn}$ is the accuracy of the curve fit of Equation 3.31 ($\delta T_{eqn} = \pm 0.04$ °C). The uncertainty $\delta E_o^{ice}$ in Equation 3.34 is found by applying Equation 3.6 to Equation 3.30, which gives

$$\delta E_o^{ice} = \sqrt{(\delta E_o)^2 + \left(\frac{\partial E_o^{ice}}{\partial T} \delta T_{ref}\right)^2} \tag{3.35}$$

where $\delta E_o$ is the accuracy of the DAS measurement of $E_o$, and $\delta T_{ref}$ is given by Equation 3.33. Substituting Equation 3.35 into Equation 3.34 gives the most convenient form of the total uncertainty in the calculated value of T:

$$\delta T = \sqrt{(\delta T_{ANSI})^2 + (\delta T_{eqn})^2 + (\delta T_{ref})^2 + \left(\frac{\partial T}{\partial E_o^{ice}} \delta E_o\right)^2} \tag{3.36}$$

The output voltage $E_o$ of each thermocouple circuit is measured with the 16-bit DAS card on the 50-mV unipolar range. Table 3.3 shows the range actually spans from -5 to 50 mV, thereby encompassing the negative output voltages produced when the measuring junction temperature is below the reference bath temperature. Table 3.3 also shows that the measurement accuracy $\delta E_o$ is $\pm$ 0.04 % of this range, or $\delta E_o = \pm 0.022$ mV. The partial derivative appearing in front of $\delta E_o$ in Equation 3.36 is the inverse of the Seebeck coefficient. The Seebeck coefficient describes the change in emf produced by a thermocouple junction per degree change of temperature at the junction. The Seebeck coefficient is calculated by taking the derivative of the established reference equation (Equation 3.26) with respect to T. Figure 3.11 shows a plot of the uncertainty $\delta T$ calculated from Equation 3.36 over the approximate range of temperatures measured with thermocouples in our facility (-30 to 125 °C) for the two different ANSI wire

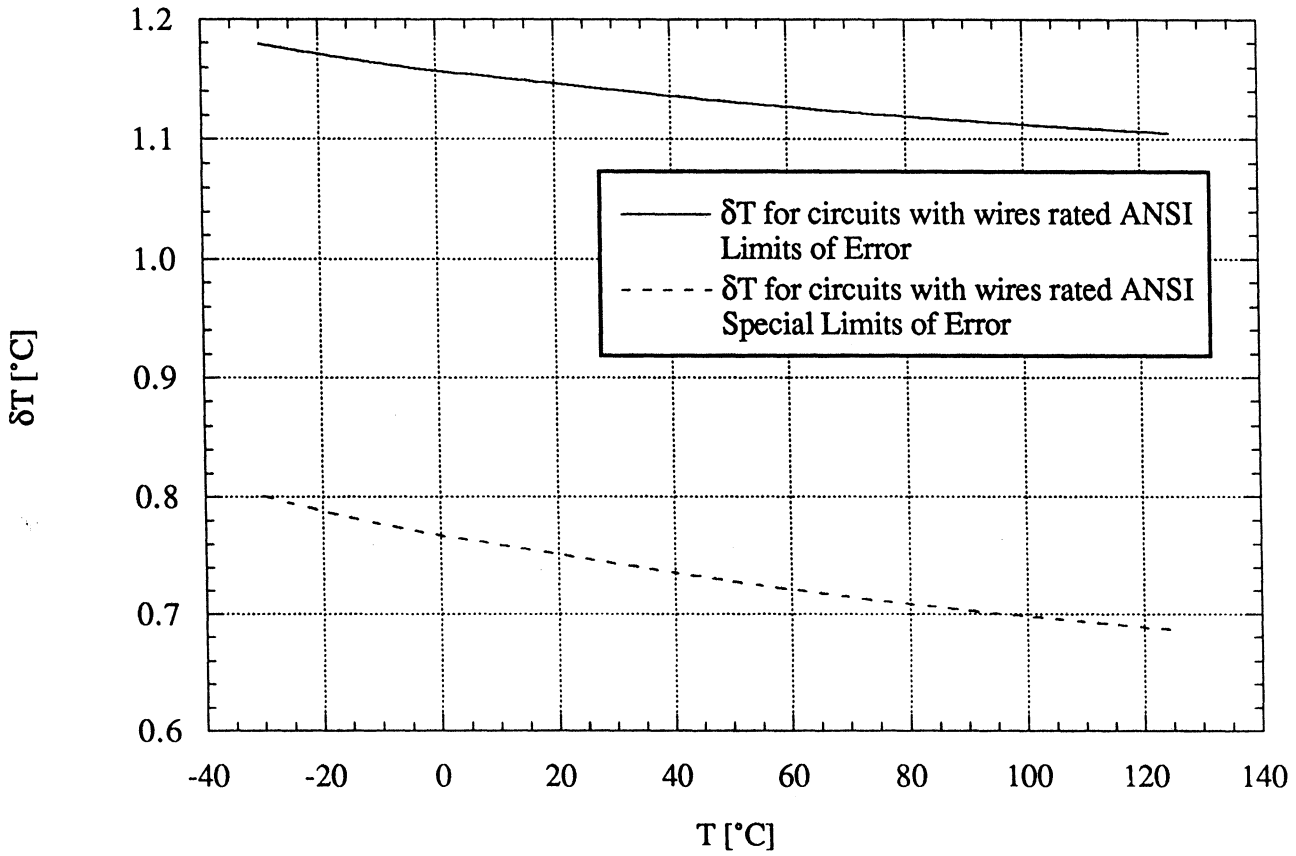


Figure 3.11 The total uncertainty in the measurement of a thermocouple junction temperature for circuits constructed of wires which conform to standard or special ANSI error limits, and whose reference junctions are placed in a room-temperature reference bath.

grades. The results are based upon the assumption that the reference junction temperature falls within the calibrated range of our thermistor. The measurement accuracy is seen to vary from 0.69 to 0.80 °C for circuits constructed with wires rated ANSI Special Limits of Error (i.e., our air-side circuits), and from 1.1 to 1.2 °C for circuits constructed with wires rated ANSI Limits of Error. Each of our refrigerant-side circuits uses both grades of wire, so the error curve for these circuits lies somewhere between the two curves plotted in Figure 3.11. The measurement accuracies of both the air- and refrigerant-side circuits can likely be improved to ± 0.3 °C or better through direct calibration of the circuits.

#### 3.2.1.4 Thermocouple Installation Effects

In an actual installation, a thermocouple exchanges heat with its surrounding environment through conduction, radiation, and convection, and each of these modes of heat transfer can undesirably effect the temperature sensed by the junction. The reader is referred to the work of Benedict (1977) for discussion of these effects. Uncertainties caused by these effects are not accounted for in Equation 3.36 because they are difficult to quantify. However, we do take steps to minimize these effects in our facility installations. For example, wherever possible, a refrigerant-side probe is mounted in an angled tap configuration (Figure 2.10b) to encourage the refrigerant flow to enter the well surrounding the probe and thereby minimize the temperature gradient (i.e., heat conduction) between the tip and the base of the probe. Also, the pipe walls encompassing each probe are insulated to bring the wall temperature closer to the fluid temperature and thereby minimize the radiative heat transfer between the probe and the surrounding walls.

One should also be aware that the simplified circuit of Figure 3.8 does not represent the full thermoelectric behavior of an actual installation. For example, our refrigerant-side circuits are actually wired as shown in Figure 3.12, and a more appropriate equivalent circuit for the arrangement is shown in Figure 3.13a. Figure 3.13a exemplifies the fact that the Type-T circuit components are each comprised of slightly different grades of copper and constantan and create inadvertent couples amongst each other. In addition, the connections formed by the dissimilar-metal junctions at the zone box terminal strip and the DAS terminal strip create several other inadvertent couples within the circuit. The circuit of Figure 3.13a can be simplified by invoking the Thermocouple Law of Intermediate Materials, which states that a material B inserted between materials A and C has no effect on the thermoelectric output voltage measured between A and C as long as the two junctions formed with B are at the same temperature (Benedict, 1977). The law is illustrated graphically in Figure 3.13b. If each blade of the Type-T connector, each lug of the DAS terminal strip, and each bar of the zone box terminal strip is assumed to be isothermal (all likely assumptions for our installations), the circuit can be reduced to that of Figure 3.13c.

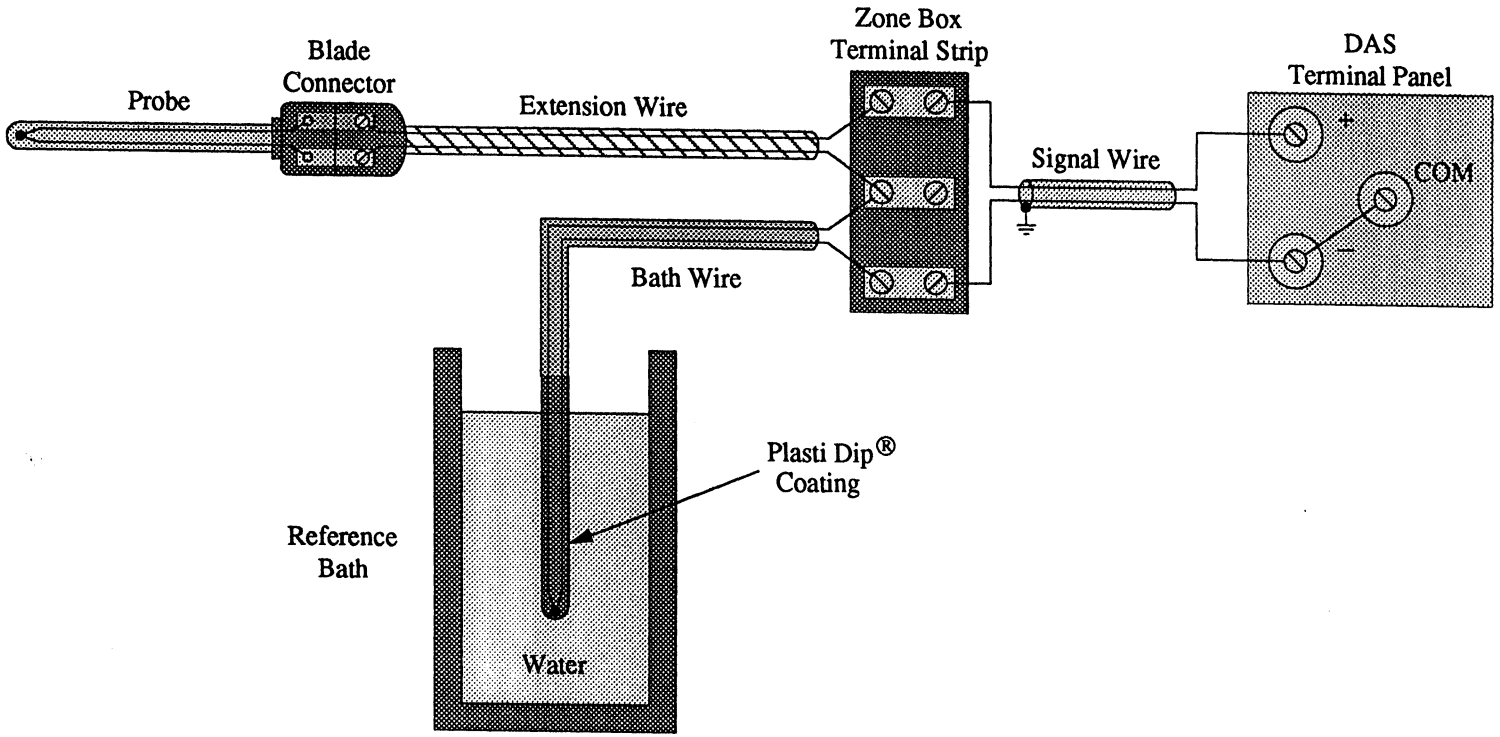


Figure 3.12 A detailed schematic of a refrigerant-side probe circuit.

(a)

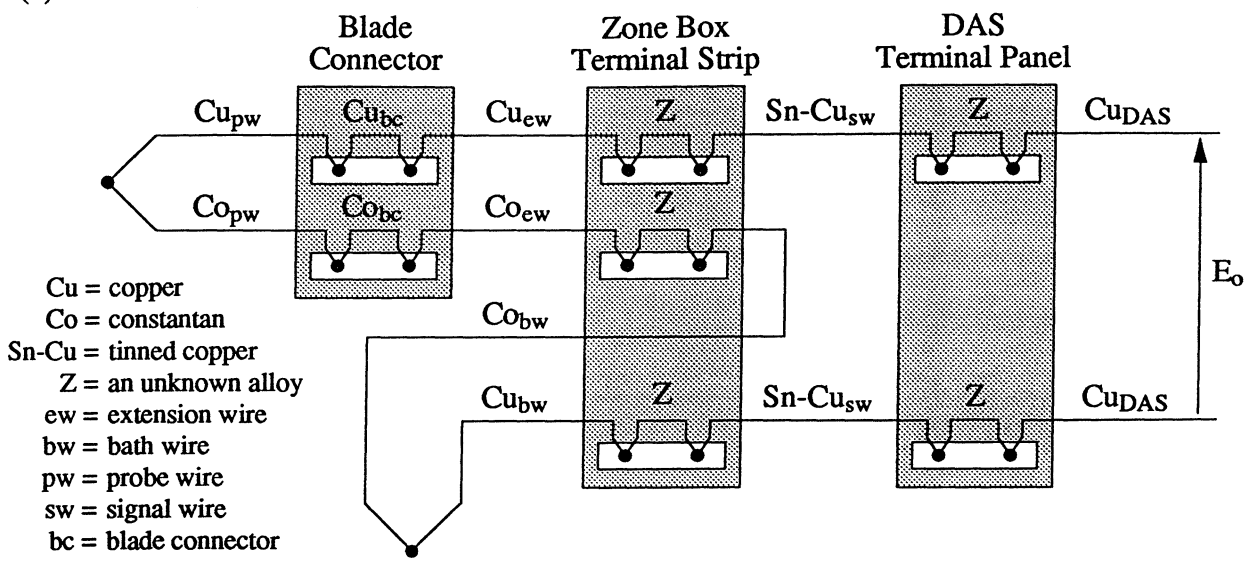


(b) The Thermocouple Law of Intermediate Materials

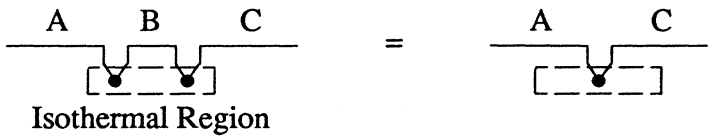


(c)

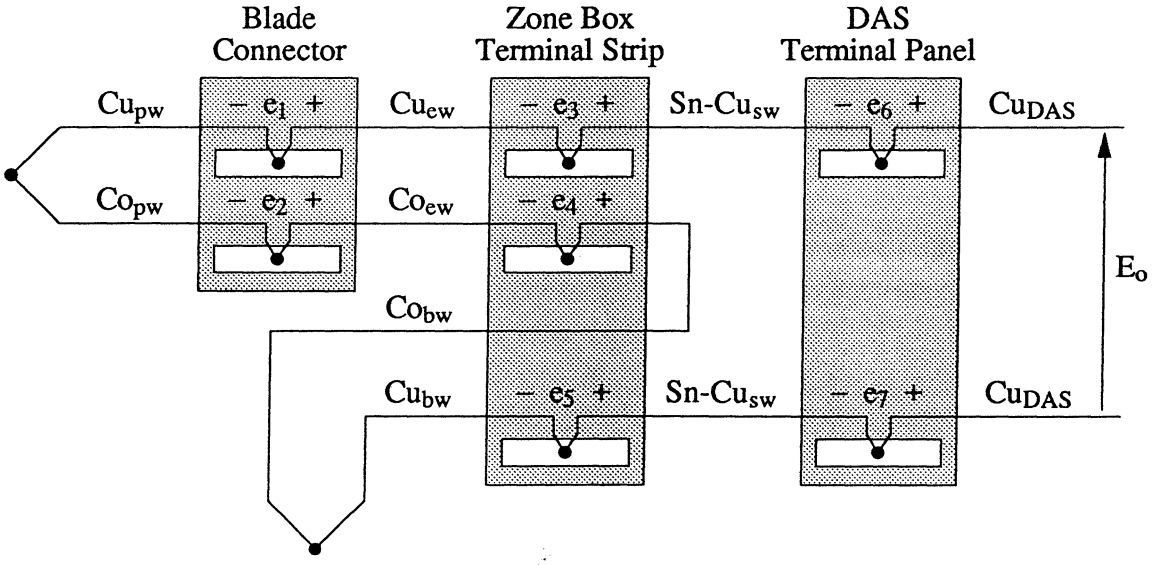


Figure 3.13 Circuit diagrams which illustrate (a) a refrigerant-side probe installation, (b) the Thermocouple Law of Intermediate Materials, and (c) a more simplified version of the circuit of part (a).

Referring to Figure 3.13c, the effects of the small thermoelectric voltages $e_1$, $e_2$, and $e_4$ introduced to the circuit by the inhomogeneous copper junction at the blade connector, the inhomogeneous constantan junction at the blade connector, and the inhomogeneous constantan junction at the zone box terminal strip can be minimized by calibrating the entire circuit with the connector and the strip at the temperatures they are most likely to be at during a test (room temperature for our installations). The thermoelectric voltages $e_3$ and $e_5$ introduced by the two signal-wire connections at the zone box terminal strip nearly cancel each other if the temperatures of the two junctions are equal. The voltages do not completely cancel because the extension wire and the reference-junction wire are comprised of slightly different grades of copper. However, in an air-side circuit, the wires comprising the measuring and reference junctions are cut from the same spool of 30-AWG Type-T material, so $e_3$ and $e_5$ do cancel if the two junction temperatures are equal. The insulated zone box construction helps ensure that the terminal strips are isothermal so as to eliminate and/or minimize the effects of $e_3$ and $e_5$ in each of the thermocouple circuits. Similarly, the thermoelectric voltages $e_6$ and $e_7$ introduced by the two signal-wire connections at the DAS cancel each other if the temperatures of those two junctions are equal. Each thermocouple circuit used in our facility is wired to one of the STI Model No. T21 input panels. The input terminals of the T21 panels are built into isothermal aluminum blocks, so $e_6$ and $e_7$ are likely to cancel in our installations.

### 3.2.2 Thermopiles

At present, only two DAS channels (one channel per heat exchanger) are available to measure the outlet air temperatures of the evaporator and condenser. In either case, the outlet air temperature profile is rarely (if ever) homogeneous because the heat transfer across any given part of the heat exchanger coil largely depends upon the state of the refrigerant in the given part of the coil (i.e., whether the refrigerant is subcooled, two-phase, or superheated). Thus, we instrumented each heat exchanger with a thermopile circuit. A thermopile circuit yields a spatially averaged temperature reading from a single voltage reading. A thermopile consists of N circuits of the form of Figure 3.8 collectively wired in series as is shown in Figure 3.14 (Benedict, 1977). The output voltage of the thermopile is

$$E_o = \sum_{k=1}^{N} V(T_k) - \sum_{k=1}^{N} V(T_{ref,\,k}) \tag{3.37}$$

where $T_k$ is the temperature of the $k^{th}$ junction in the measuring region, and $T_{ref,\,k}$ is the temperature of the $k^{th}$ junction in the reference region. Dividing both sides of Equation 3.37 by N gives

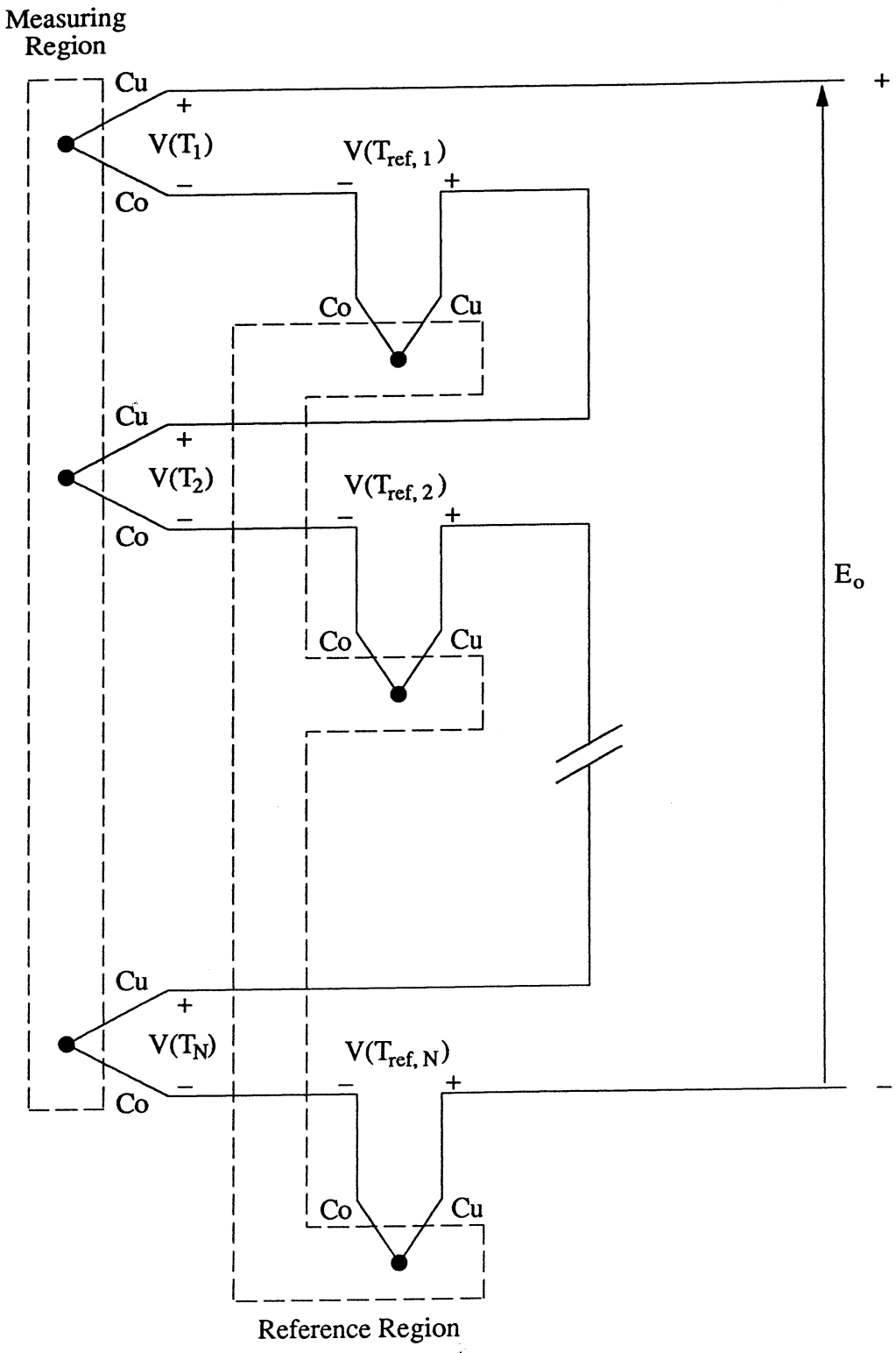


Figure 3.14 A typical thermopile circuit.

$$\frac{1}{N}E_o = \frac{1}{N}\sum_{k=1}^{N} V(T_k) - \frac{1}{N}\sum_{k=1}^{N} V(T_{ref,k}) \qquad (3.38)$$
$$= \overline{V}_T - \overline{V}_{ref}$$

where $\overline{V}_T$ is the average emf produced by the N measuring junctions, and $\overline{V}_{ref}$ is the average emf produced by the N reference junctions. Solving Equation 3.38 for $E_o$ shows that the output voltage is N-times as great as the average voltage difference produced by the couples. Thus, compared to the classical two-junction circuit of Figure 3.8, a thermopile generates a higher level signal which is easier to resolve by the DAS and is more immune to the effects of noise, particularly if a small temperature difference is being sensed.

We pause here to note that a thermopile is, in fact, generally used to measure a small average temperature difference $\overline{\Delta T} = \overline{T} - \overline{T}_{ref}$, where $\overline{T}$ and $\overline{T}_{ref}$ are, respectively, the average temperatures of the measuring and reference regions. When using a thermopile in this manner, the following assumptions are made:

1. All of the couples are assumed to conform to the same calibration function V(T), and this function is assumed to be linear between the minimum and the maximum of the N temperatures $T_k$ sensed in the measuring region, as well as between the minimum and the maximum of the N temperatures $T_{ref,k}$ sensed in the reference region. Under these assumptions, $\overline{V}_T = V(\overline{T})$, $\overline{V}_{ref} = V(\overline{T}_{ref})$, and Equation 3.38 reduces to

$$\frac{1}{N}E_o = V(\overline{T}) - V(\overline{T}_{ref}) \qquad (3.39)$$

2. The function V(T) is assumed to be linear between $\overline{T}$ and $\overline{T}_{ref}$. Under this assumption, Equation 3.39 reduces to

$$\frac{1}{N}E_o = (\alpha\,\overline{T} + b) - (\alpha\,\overline{T}_{ref} + b) \qquad (3.40)$$
$$= \alpha\,(\overline{T} - \overline{T}_{ref})$$
$$= \alpha\,\overline{\Delta T}$$

where $\alpha$ is the slope (i.e., the Seebeck coefficient) of the function V(T) between $\overline{T}$ and $\overline{T}_{ref}$.

A higher order polynomial may be used to fit calibration data relating $E_o$ to $\overline{\Delta T}$ in Equation 3.40, but the underlying assumption is that the relation is linear.

Because Equation 3.40 gives the average temperature difference as a direct function of the output voltage $E_o$, a thermopile is useful for any situation in which a direct measurement of $\overline{\Delta T}$

is desired. For example, the air-side heat transfer rate $\dot{Q}_a$ across a heat exchanger is commonly given by

$$\dot{Q}_a = \dot{m}_a c_p \overline{\Delta T} \tag{3.41}$$

where $\dot{m}_a$ is the air mass flow rate, and $c_p$ is the specific heat of the air stream. The average air temperature change $\overline{\Delta T}$ in Equation 3.41 can be measured with a thermopile by respectively mounting the reference and measuring junctions on grids at the inlet and outlet of the heat exchanger. A direct measurement of $\overline{\Delta T}$ (as opposed to subtracting an independent measurement of the average outlet air temperature from an independent measurement of the average inlet air temperature) gives the lowest overall uncertainty in the measurement of $\dot{Q}_a$ provided that $\overline{\Delta T}$ itself is measured with sufficient accuracy. The accuracy achieved in the measurement of $\overline{\Delta T}$ depends upon how well the linearity conditions of Assumptions 1 and 2 are met, as well as upon differences between the conditions under which the thermopile is calibrated and those under which it is used.

Concerning the linearity conditions, we first note from Equation 3.27 that the function V(T) has the same shape as the function $E_o^{ice}(T)$ because the latter function is just V(T) offset by the constant but unknown amount V(0 °C). Figure 3.9 shows that the shape of $E_o^{ice}(T)$ (and, hence, the shape of V(T)) is, in fact, quite linear between the endpoints of any relatively small temperature interval. The smaller the interval, the more linear the shape, and the more accurate the relations of Equations 3.39 and 3.40. Concerning calibration and usage conditions, the measurement of $\overline{\Delta T}$ is only accurate if, in practice, the average temperature of the reference region is sufficiently close to the temperature the reference junctions were at when the circuit was calibrated. This latter condition cannot be met in our installations. For example, if we were to calibrate our condenser-side thermopile over a differential temperature range of $\overline{\Delta T} = 0$ to +25 °C (a suitable range for our facility) with the reference junctions held at, say, 20 °C, the calibration data would theoretically yield the same best-fit slope that the curve of Figure 3.9 has over the interval from 20 °C to (20 + 25) = 45 °C, which is $\alpha_{cal} = 0.041322$ mV/°C. Now, suppose that for a particular test, the actual temperature difference to be sensed is $\overline{\Delta T}_{act} = 15$ °C, and the condenser inlet air temperature (i.e., $\overline{T}_{ref}$) is, say, 35 °C. From Equation 3.40, the output voltage produced by the thermopile would be approximately

$$E_o = N \alpha_{act} \overline{\Delta T}_{act} \tag{3.42}$$

where $\alpha_{act}$ is the best-fit slope of the curve of Figure 3.9 over the interval from 35 °C to (35 + 15) = 50 °C, which is $\alpha_{act} = 0.042178$ mV/°C. The predicted value of $\overline{\Delta T}$ calculated from the calibration equation is

$$\overline{\Delta T} = \frac{E_o}{N\,\alpha_{cal}} \tag{3.43}$$

Substituting Equation 3.42 into the latter equation and solving for the ratio of $\overline{\Delta T}$ to $\overline{\Delta T}_{act}$ gives

$$\frac{\overline{\Delta T}}{\overline{\Delta T}_{act}} = \frac{\alpha_{act}}{\alpha_{cal}} \tag{3.44}$$

For the practical example at hand, Equation 3.44 yields a ratio of 1.02, or an unacceptable 2 % error in the measurement of $\overline{\Delta T}_{act}$. Because we test evaporators and condensers over a wide range of inlet air temperatures, thermopiles cannot be used in our facility to make direct, accurate measurements of the $\overline{\Delta T}$ across a heat exchanger.

In light of the results of the above example, we attempt to more accurately determine the air-side heat transfer rate $\dot{Q}_a$ across the evaporator or condenser through independent measurements of the inlet and outlet air temperatures. Our thermopiles are accordingly used to measure the average outlet air temperatures of the heat exchangers. A thermopile can be accurately used to measure an average measuring region temperature $\overline{T}$ given any reference region temperature $T_{ref}$ provided that:

(i) The reference region is isothermal at the known temperature $T_{ref}$.
(ii) The calibration and linearity conditions of Assumption 1 (defined earlier) are met, and
(iii) $\overline{T}$ can be adequately represented by an N-point average.

Under these conditions, Equation 3.39 reduces to

$$\frac{1}{N} E_o = V(\overline{T}) - V(T_{ref}) \tag{3.45}$$

Equation 3.45 is directly analogous to Equation 3.25 in the analysis of the classical two-junction thermocouple circuit, and the same three-step data reduction process used to calculate T from the output of the classical circuit can be used to calculate $\overline{T}$ from output of the thermopile circuit. Pending direct calibration of our thermopile circuits, the NIST equations and the three-step process are used to calculate $\overline{T}$, where the equation

$$E_o^{ice}(\overline{T}) = \frac{1}{N} E_o + E_o^{ice}(T_{ref}) \tag{3.46}$$

is used in place of Equation 3.30 in Step 2 of the process.

#### 3.2.2.1 Construction and Performance of the Thermopiles

Our thermopiles are constructed from 30-AWG Type-T thermocouple wire rated ANSI Special Limits of Error. Wiring schematics for the thermopiles are given in the zone box diagrams of Figures 3.4 and 3.6. Each thermopile consists of nine pairs of measuring and reference junctions (i.e., N = 9). Each junction wire is equipped with a Type-T blade connector (OMEGA Model No. SMP-T-MF) which allows the junction to be unplugged from the thermopile arrangement and monitored with a hand-held thermocouple reader (OMEGA Model No. HH23). By doing so, malfunctioning couples can be identified, and the individual junction temperatures can be recorded and compared to each other to indicate the level of temperature stratification across the measuring and reference regions. The connectors also allow the thermopiles to be quickly disconnected from the zone boxes to more easily facilitate the removal and installation of the duct sections.

As was previously discussed in Chapter 2, in each heat exchanger installation, the measuring junctions of the thermopile are mounted on a sheet of wire cloth at the outlet of the heat exchanger. Care is taken to ensure that the junction beads do not touch the wire cloth because the cloth is an electrical ground, and ground loops would be formed between the beads and cause erroneous measurements. As was also previously discussed in Chapter 2, the reference junctions of the thermopile are mounted on a grid of fishing line at the inlet of the heat exchanger. Hence, the reference temperature $T_{ref}$ used to calculate $\overline{T}$ is <u>not</u> the temperature of the thermocouple reference bath, but is instead the inlet air temperature to the heat exchanger as is measured by the single thermocouple junction positioned just upstream of the reference grid in the measurement section duct. We located the thermopile reference junctions at the inlets of the heat exchangers because we had initially thought that the inlet air temperature profiles would be isothermal enough to allow us to use the thermopiles to accurately measure average outlet air temperatures $\overline{T}$ while still retaining the option of being able to directly sense average air-side temperature changes $\overline{\Delta T}$. However, subsequent tests revealed that the inlet air temperature profiles can be significantly stratified, so we are presently unable to generate accurate measurements of $\overline{T}$. An alternative setup is needed. We shall return to this issue in Chapter 4.

### 3.2.3 Resistance Temperature Detectors (RTD's)

Each of the relative humidity probes used in our facility contains a four-wire platinum RTD having a nominal resistance of 100 Ω at 0 °C. This grade of platinum is commonly referred to as Pt 100. The RTD's sense the dry-bulb temperatures at the probe locations. The temperature measurements are used in conjunction with the relative humidity measurements to calculate the

humidity ratios of the air streams. The temperature-resistance relationship of an RTD is described by the Callendar-Van Dusen equation (SDI, 1986), given by

$$R = R_o + \alpha R_o\left[T - \delta\left(\frac{T}{100}\right)\left(\frac{T}{100} - 1\right) - \beta\left(\frac{T}{100}\right)^3\left(\frac{T}{100} - 1\right)\right] \tag{3.47}$$

where

$R$ = RTD resistance [Ω]
$T$ = RTD temperature [°C]
$R_o$ = 100 Ω
$\alpha$ = 0.003850 Ω/Ω-°C
$\delta$ = 1.50700 °C
$\beta$ = 0 °C (T ≥ 0 °C)
= 0.111 °C (T < 0 °C)

The values of $R_o$, $\alpha$, $\delta$, and $\beta$ given in Equation 3.47 are standard values for Pt 100. Equation 3.47 is solved implicitly for T given the RTD resistance R, where R is measured by the four-wire method discussed earlier. The RTD's are manufactured to the 1/3 DIN 43760B tolerance standard, meaning their temperature-resistance characteristics conform to Equation 3.47 to within $\delta T = \pm [0.08\ °C + 0.005\ |T|]$ (SDI, 1986).

The STI WorkBench software presently used in our facility contains a built-in routine which calculates R via the previously discussed four-wire technique and converts R to T via a 100-point lookup table which is most likely based on Equation 3.47. STI claims the overall measurement accuracy is ± 0.9 °C over a temperature range of -200 to 115 °C, excluding the accuracy of the RTD itself. The WorkBench routine was used to reduce all of the RTD data we have recorded to date. The WorkBench routine assumes that the set resistor $R_s$ employed in the technique is a 20-kΩ resistor manufactured to a tolerance of ± 0.1 % or better with a temperature coefficient of ± 25 ppm/°C or better. Our present set resistors have a suitable temperature coefficient of ± 25 ppm/°C but are manufactured to a ± 0.5 % tolerance, so the accuracy achieved to date is slightly worse than the accuracy claimed by STI. For future tests, we will manually program the RTD resistance measurement algorithm into our data reduction program so as to be able to use Equation 3.47 and in-house measurements of $R_s$ in the calculations and thereby achieve better accuracy in the RTD temperature measurements.

## 3.3 Pressure Instrumentation

### 3.3.1 Pressure Transducers

Thirteen Setra-brand electronic pressure transducers are used to measure the air- and refrigerant-side pressures in our facility. Table 3.6 lists the model number, range, rated accuracy,

Table 3.6 Summary of the pressure signals measured in the facility and the specifications of the transducers used to perform the measurements.

| Variable Name and Description | | Transducer Specifications | | | | | Calibration Curve Fit[1] |
|---|---|---|---|---|---|---|---|
| | | Model No. | Serial No. | Input Range | Output Range | Accuracy | |
| $P_{eri}$ | Evaporator inlet refrigerant pressure | Setra 207 | 247866 | 0–100 psig | 0.1–5.1 VDC | ± 0.13 %FS | $P = 20.032\ E_o - 2.6431$ |
| $P_{kri}$ | Compressor inlet refrigerant pressure | Setra 207 | 270489 | 0–100 psig | 0.1–5.1 VDC | ± 0.13 %FS | $P = 20.373\ E_o - 2.0569$ |
| $P_{kro}$<br>$P_{dv}$ | Compressor outlet refrigerant pressure, same as Discharge-line VFT inlet refrigerant pressure | Setra 207 | 202281 | 0–500 psig | 0.1–5.1 VDC | ± 0.13 %FS | $P = 121.03\ E_o - 13.386$ |
| $P_{cri}$ | Condenser outlet refrigerant pressure | Setra 207 | 253458 | 0–500 psig | 0.1–5.1 VDC | ± 0.13 %FS | $P = 100.60\ E_o - 9.2936$ |
| $P_{lv}$ | Liquid-line VFT inlet refrigerant pressure | Setra 207 | 253459 | 0–500 psig | 0.1–5.1 VDC | ± 0.13 %FS | $P = 100.83\ E_o - 7.0664$ |
| $P_{eav}$ | Evaporator air loop VFT inlet air pressure | Setra 239 | 409977 | 0–15 in. $H_2O$ | 0–5 VDC | ± 0.14 %FS | $P = 0.10838\ E_o - 0.0024549$ |
| $P_{cav}$ | Condenser air loop VFT inlet air pressure | Setra 239 | 398563 | 0–15 in. $H_2O$ | 0–5 VDC | ± 0.14 %FS | $P = 0.10722\ E_o - 0.034696$ |
| $\Delta P_{cav}$ | Condenser air loop VFT pressure differential | Setra C239 | 307533 | 0–30 in. $H_2O$ | 4–20 mA | ± 0.14 %FS | $\Delta P = 0.068315\ I_t - 0.27727$ |
| $\Delta P_{er}$ | Evaporator refrigerant pressure drop | Setra 228-1 | 258209 | 0–25 psid | 0–5 VDC | ± 0.21 %FS | $\Delta P = 5.1432\ E_o - 0.25026$ |
| $\Delta P_{cr}$ | Condenser refrigerant pressure drop | Setra 228-1 | 258208 | 0–25 psid | 0–5 VDC | ± 0.21 %FS | $\Delta P = 4.9426\ E_o - 2.5470$ |
| $\Delta P_{dv}$ | Discharge-line VFT pressure differential | Setra 228-1 | 287546 | 0–1 psid | 0–5 VDC | ± 0.15 %FS | $\Delta P = 0.20231\ E_o - 0.0024777$ |
| $\Delta P_{lv}$ | Liquid-line VFT pressure differential | Setra 228-1 | 287547 | 0–1 psid | 0–5 VDC | ± 0.15 %FS | $\Delta P = 0.20048\ E_o + 0.0038068$ |
| $\Delta P_{eav}$ | Evaporator air loop VFT pressure differential | Setra C228-1 | 355739 | 0–1 psid | 4–20 mA | ± 0.15 %FS | $\Delta P = 0.065652\ I_t - 0.26203$ |

[1] Units are $E_o$ [VDC], $I_t$ [mA], P [psig], and $\Delta P$ [psid] for all cases.

and calibration equation for each transducer and gives the variable name associated with each measurement. The accuracy ratings listed in Table 3.6 are RSS combinations of linearity, hysteresis, and repeatability errors reported by Setra in terms of a percentage of the full-scale range of the transducer. The calibration equations listed in Table 3.6 were generated in-house as is further discussed below. In addition to using the instruments listed in Table 3.6, we also installed a dial-type refrigerant pressure gage at the inlet of the condenser, and another at the inlet of the evaporator. The dial gages are used to spot-check the readings of the refrigerant-side pressure transducers. More importantly, the gages allow the researcher to identify the high- and low-side system pressures when the DAS is not in operation.

#### 3.3.1.1 Refrigerant-Side Pressure Transducers

Setra Model 207 gage pressure transducers are used to sense the refrigerant pressures at the inlets of (1) the evaporator, (2) the condenser, (3) the compressor, (4) the discharge-line VFT, and (5) the liquid-line VFT. These five transducers were salvaged from previous research projects in an effort to conserve costs. Each transducer contains a stainless steel diaphragm which forms a variable capacitor with a dry, stationary electrode plate. Applying pressure to the fluid-wetted side of the diaphragm causes the diaphragm to deflect, thereby changing the capacitance between the electrode plate and the dry side of the diaphragm. A circuit internal to the transducer converts the capacitance signal to a 0.1–5.1 VDC output voltage which is linearly proportional to the applied pressure. The sensors have a rated response time of 5 ms and can be used with gases or liquids. Each of the gage pressure transducers can, without damaging the sensor or changing its nominal output characteristics, withstand the vacuum pressure (30 in. Hg) applied to it prior to charging the refrigerant loop, or the nitrogen gas pressure (up to 300 psig) applied to it when testing the refrigerant loop for leaks. Gage pressure transducers are used to make the measurements because, unlike absolute pressure transducers, gage pressure sensors can be easily rezeroed by exposing the sensing port to atmospheric pressure.

Setra Model 228-1 differential pressure transducers are used to sense the refrigerant-side pressure drops across (1) the evaporator and (2) the condenser, as well as the differential pressure signals generated by (3) the discharge-line VFT and (4) and liquid-line VFT. These four transducers were also salvaged from previous research projects. Each of the four transducers contains a linkage which transmits the motion of a fluid-wetted differential pressure sensing diaphragm (i.e., wetted on both sides) to a dry air enclosure where the linkage moves one of a pair of capacitor plates in proportion to the diaphragm movement. An amplifier circuit internal to the transducer converts the capacitance signal to a 0–5 VDC output voltage which is linearly proportional to the applied differential pressure. The sensors have a rated response time of 30–50 ms and can be used with gases or liquids. Differential pressure sensors are used to make the

measurements because, in each case, the direct measurement of a $\Delta P$ signal results in the lowest overall uncertainty in the desired end result. For example, the mass flow rate through a VFT is proportional to the pressure difference

$$\Delta P = P_1 - P_2 \tag{3.48}$$

where $P_1$ and $P_2$ are, respectively, the pressures at the inlet and throat of the VFT. If $P_1$ and $P_2$ were sensed independently and then combined to give $\Delta P$ as per Equation 3.48, the uncertainty in the result for $\Delta P$ would be

$$\delta\Delta P = \sqrt{(\delta P_1)^2 + (\delta P_2)^2} \tag{3.49}$$

where $\delta P_1$ and $\delta P_2$ are, respectively, the uncertainties in the measurements of $P_1$ and $P_2$. For each of our refrigerant-side VFT's, a Setra Model 207 gage pressure transducer with an input range of 0–500 psig and an accuracy of $\pm$ 0.13 %FS ($= \pm$ 0.65 psig) is used to sense the inlet pressure $P_1$. If an equivalent sensor were used to sense $P_2$ (as would be necessary), the uncertainty in calculated value of $\Delta P$ would be $\pm$ 0.92 psid, which is unacceptable because the actual $\Delta P$ signal generated by each VFT only spans a 0–1 psid range over the range of mass flow rates measured in our facility. In comparison, a 0–1 psid Setra Model 228-1 transducer has a rated accuracy of $\pm$ 0.15 %FS ($= \pm$ 0.0015 psid), yielding a $\Delta P$ measurement which is 613 times more accurate.

By the same logic, the refrigerant-side pressure drop $\Delta P_r$ across the evaporator or condenser is sensed directly with a differential pressure sensor because $\Delta P_r$ is an important modeling and design parameter. Although the heat exchanger outlet refrigerant pressure $P_{ro}$ is then calculated as

$$P_{ro} = P_{ri} - \Delta P_r \tag{3.50}$$

where $P_{ri}$ is the measured inlet refrigerant pressure, the uncertainty in the calculated value of $P_{ro}$ is acceptably small because the uncertainty in the measurement of $\Delta P_r$ is small. Likewise, the pressure $P_2$ at the throat of each VFT can be (and is) calculated from independent measurements of $P_1$ and $\Delta P$ with an acceptable level of accuracy.

#### 3.3.1.2 Air-Side Pressure Transducers

Setra Model 239 differential pressure transducers are used to sense the air pressures at the inlets of (1) the evaporator air-side VFT and (2) the condenser air-side VFT. Like a Setra Model 207 gage pressure transducer, a Setra Model 239 differential pressure transducer contains a

stainless steel diaphragm which forms a variable capacitor with a stationary electrode plate. An amplifier circuit internal to the transducer converts the capacitance signal to a 0–5 VDC output voltage which is linearly proportional to the differential pressure. The sensors have a rated response time of 10 ms. The high-side port of a Setra Model 239 transducer can be exposed to either wet or dry gases, but the low-side port (which contains the electrode) must be exposed to noncondensable, noncorrosive gases only. In our facility, the high-side ports are attached to the VFT inlet taps (which see dry or moist air), and the low-side ports are left open to the ambient atmosphere (dry, air-conditioned air). In this manner, the sensors act as accurate low-range gage pressure transducers. The gage pressure readings are then added to a highly accurate barometer reading to give accurate measures of the absolute pressures at the VFT inlets. The calculation results are more accurate than readings obtainable from most absolute pressure transducers.

A Setra Model C239 differential pressure transducer is used to sense the $\Delta P$ signal generated by the condenser air-side VFT. A Setra Model C239 transducer is constructed the same as a Setra Model 239 transducer, except a Model C239 outputs a 4–20 mA current. In the installation, both ports of the transducer are exposed to dry, warm air, so there is little to no risk of condensing moisture in the reference port of the transducer. However, the cool, moist conditions of the evaporator air loop do impose such a risk. Hence, a Setra Model C228-1 differential pressure transducer is used to sense the $\Delta P$ signal generated by the evaporator air-side VFT because a Model C228-1 transducer can be wetted on both sides of the diaphragm. Like before, a Setra Model C228-1 transducer is constructed the same as a Setra Model 228-1 transducer, except a Model C228-1 outputs a 4–20 mA current.

#### 3.3.1.3 Wiring Connections

The transducer wiring connections are shown in the zone box diagrams of Figures 3.4–3.6. Each transducer cable is equipped with a grounded shield to reduce electrical noise interference. The sensor end of the shield is internally attached to the case of the transducer by the manufacturer. The case (and, hence, the shield) of each refrigerant-side transducer is earth-grounded via the 1/8-in. O.D. runs of copper tubing which connect the sensor ports to the copper piping of the refrigerant loop (the loop piping clamps to supporting Unistrut framework which, in turn, is in electrical contact with motor housings; the housings, in turn, are earth-grounded through their power cords). To verify that the case is grounded, we check for continuity between the case and the earth ground terminal of a wall socket in the lab. Transducer cases which are not inherently grounded through normal installation (such as refrigerant-side sensors which connect to pipes electrically isolated between hoses, or the air-side sensors, which are all installed using plastic tubing) are grounded by connecting a piece of flat, tinned-copper braid between the case and a nearby ground.

Concerning the input and output wiring, each transducer receives its input excitation from the 24-VDC power supply. Setra specifies that either the negative excitation lead or the negative output lead of each transducer must be grounded to the sensor case avoid common-mode voltage problems at the inputs of the internal amplifier. The excitation-grounded configuration is preferred by Setra. Setra suggests that the ground connection be made by tying the DAS-side end of the shield to the negative excitation lead. However, because all of our transducers share the same power supply, this would be equivalent to tying together the DAS-side ends of all of the shields. Such a configuration is highly undesirable because it creates multiple ground loops between the sensors (i.e., the earth-grounded end of each shield becomes connected to the earth-grounded ends of all of the other shields). Hence, instead of grounding the negative excitation leads to the shields, we formed an equivalent arrangement by earth-grounding the negative lead of the 24-VDC power supply as is shown in Figure 3.7. This way, the negative excitation leads and the cases share the same ground potential (i.e., earth ground), and no ground loops are created.

#### 3.3.1.4 Pressure Transducer Calibrations

We calibrated each transducer with a Bell and Howell Model No. 6-201-0001 deadweight tester. The Bell and Howell deadweight tester is a primary pressure standard, meaning it conforms to NIST certification standards and can be used to accurately calibrate secondary pressure-sensing devices (such as pressure transducers and dial gages). The deadweight tester operates on the principle that if a piston of mass $m_p$ and cross sectional area $A_p$ is placed on top of a column of hydrostatic fluid confined in a frictionless cylinder, then a pressure of

$$P_o = \frac{m_p g}{A_p} \tag{3.51}$$

is generated in the fluid, where g is the standard acceleration of gravity. The deadweight tester is accompanied by a chart which gives the pressure $P_o$ generated by the tester for the various combinations of masses and piston sizes supplied with the tester. Because the tabulated values of $P_o$ are based upon the weight of a piston in standard gravity, a correction factor must be applied to data collected under local gravity conditions to obtain a proper calibration. The gravity correction factor is derived by noting that the pressure P generated by the tester under local gravity conditions for a given piston mass $m_p$ and area $A_p$ is

$$P = \frac{g_l}{g} P_o \tag{3.52}$$

where $g_l$ is the local acceleration of gravity. The gravity ratio appearing in Equation 3.52 is given by

$$\frac{g_l}{g} = \frac{980.616}{980.665} \left[1 - 0.0026373 \cos 2\phi + 0.0000059 \cos^2 2\phi\right] \tag{3.53}$$

where $\phi$ [°N or °S] is the geographic latitude of the test facility, which is 40.109 °N for our Urbana, Illinois location (PRINCO, 1992). The standard deadweight pressures $P_o$ were corrected for gravity as per Equation 3.52 to obtain the actual pressures P applied to the transducers during our calibration runs.

Continuing, we used an inclined water manometer to collect data below the low-pressure limit of the deadweight tester (0.3 psi, or 8.32 in. $H_2O$) when calibrating the transducers having a 0–1 psid, 0–15 in. $H_2O$, or 0–30 in. $H_2O$ range (the unit "in. $H_2O$" refers to a height of water column at a standard manometer temperature of 68 °F). The following standard relation was used to convert the manometer readings to equivalent pressures in units of psi:

$$P = \rho\, g\, h \left(\frac{1\ [ft^3]}{1728\ [in.^3]}\right)\left(\frac{1\ [lb_f]}{g_c\ [lb_m\text{-}ft/s^2]}\right) \tag{3.54}$$

where

P = pressure [psi]
$\rho$ = fluid density [$lb_m/ft^3$]
h = fluid column height in standard gravity [in.]
g = standard acceleration of gravity
= 32.1740 $ft/s^2$
$g_c$ = gravity proportionality constant
= 32.1740

Equation 3.54 assumes standard gravity conditions. Hence, manometer readings taken under local gravity conditions must be referenced to standard gravity to properly obtain the pressure P from Equation 3.54. The gravity correction is derived by noting that a pressure P supporting a manometer fluid column of height $h_l$ in local gravity will equivalently support a column of height

$$h = \frac{g_l}{g} h_l \tag{3.55}$$

in standard gravity. Equation 3.55 was used to convert the local manometer readings $h_l$ to standard heights h for use in Equation 3.54.

In addition, for each calibration run involving the manometer, the temperature of the manometer water was recorded and used to determine the density $\rho$ appearing in Equation 3.54. Density values for liquid water at the various manometer temperatures were calculated from

curve fits of NIST data for saturated liquid steam. The latter curve fits are supplied by the Engineering Equation Solver (EES) Version 4.10 software package we presently use to reduce our facility data. The water density $\rho_w$ is calculated in EES as the reciprocal of the specific volume via the function call

$$\rho_w\ [lb_m/ft^3] = 1/\text{Volume}(\text{Steam\_NBS}, T = T_w\ [°F], x = 0.0) \tag{3.56}$$

where $T_w$ is the water temperature, and x is the dimensionless steam quality, which is set equal to zero to obtain saturated liquid water properties. The function may also be used in the compressed-liquid regime if the absolute water pressure $P_w$ is known. We neglected to measure $P_w$ (i.e., ambient atmospheric pressure) during the calibration runs, but the compressibility effects are negligible. As a side note, the suffix "NBS" appears in the function call because NIST is formerly known as the National Bureau of Standards.

Continuing, the HP 34401A multimeter was used to measure the output signal X during each of the calibrations, where X is either an output voltage $E_o$ or a transmitted current $I_t$. Then, for each transducer, the corrected pressure data were plotted against the output signal data and fit with a linear least-squares curve fit of the form

$$P = k\,X + p_o \tag{3.57}$$

where k is the slope and $p_o$ is the intercept of the relation. The resulting best-fit equations are listed in Table 3.6.

Due to the large number of pressure transducers used in our facility, we did not attempt to perform multiple calibrations of each sensor so as to evaluate hysteresis and repeatability errors to obtain an overall sensor accuracy. Instead, all uncertainty calculations are based upon the rated sensor accuracies given in Table 3.6 because these ratings do include such errors. Also, when calibrating the Setra Model C239 and C228-1 transducers, we measured the transmitted currents $I_t$ directly with the HP 34401A. For future calibrations, we will install the proper shunt loads across the output leads of the transducers and correlate the input pressures to the voltage drops measured across the shunts. Calibrating the transducer/shunt combinations as matched pairs is expected to yield more accurate results because the effects of driving the loads become accounted for in the calibration equations.

#### 3.3.1.5 Pressure Transducer Drift Corrections

As was previously discussed, each of the Setra transducers contains an internal amplifier circuit which converts the applied pressure to a linear, high-level DC output signal. The gain (i.e., the slope k of Equation 3.57) and the zero-pressure output signal $X_{zo}$ (or, equivalently, the

intercept $p_o$ of Equation 3.57) of each transducer tend to drift slowly with age and/or the ambient temperature conditions surrounding the electronics. The researcher must account for these drifts to obtain the most accurate results.

Drift Correction Equations

Concerning drift in the slope k, many pressure transducers (including ours) can be optionally equipped with a special shunt calibration reference which creates a simulated pressure signal of a known value $P_{cal}$ when it is applied across appropriate leads in the transducer circuit. By measuring the shunt calibration output $X_{cal}$ and the zero-pressure output $X_{zo}$, the slope k can be calculated by fitting a line through the two coordinate pairs ($X_{cal}$, $P_{cal}$) and ($X_{zo}$, 0). At present, our transducers are not equipped with shunt calibration options, so we can only detect drifts in the amplifier gains by periodically recalibrating each of the thirteen transducers with the deadweight tester.

Concerning drift in the zero-pressure output signal $X_{zo}$, each Setra transducer is equipped with an internal potentiometer for rezeroing the output. However, to actually rezero each transducer via its potentiometer before collecting data is both impractical and undesirable because the potentiometers are located beneath secured covers, and adjusting the zeroing potentiometer is suspected to slightly effect the amplifier gain. Instead, we measure the zero-pressure output $X_{zo}$ of each transducer before collecting data, and the offset between the measured value and the nominal value $X_{zo}^{nom}$ is applied as an off-line correction to the data. The nominal value of the zero-pressure output signal is found by solving Equation 3.57 for X with P = 0, which gives

$$X_{zo}^{nom} = -\frac{p_o}{k} \tag{3.58}$$

The amount of drift (i.e., the difference $X_{zo} - X_{zo}^{nom}$) is subtracted from the output signals X recorded in the data file to effectively trim out the drift from the measurements of X. Hence, the corrected pressure reading is given by

$$\begin{aligned} P &= k\,[X - (X_{zo} - X_{zo}^{nom})] + p_o \\ &= k\,[X - (X_{zo} + \frac{p_o}{k})] + p_o \\ &= k\,(X - X_{zo}) \end{aligned} \tag{3.59}$$

The intercept $p_o$ is seen to drop from the equation.

Transducer Valving

We valved the refrigerant-side pressure transducers in the manner shown in Figure 3.15 so that the zero-pressure outputs $X_{zo}$ could be measured with relative ease. The zero-pressure output of the differential pressure transducer shown in the figure is obtained by opening the cross-connect valve which extends between the high- and low-side ports of the transducer. This exposes the sensor to zero differential pressure. The zero-pressure output of the gage pressure transducer shown in the figure is obtained by first closing the ball valve located between the sensor and the main refrigerant line. This isolates the transducer from the loop. Next, the core-depressing end of a refrigerant hose is threaded onto the Schrader valve located between the ball valve and the sensor to vent the small amount of refrigerant and oil trapped in the 1/8-in. O.D. (0.065-in. I.D.) pressure transmission line. The opposite end of the hose is left open to the atmosphere so as to expose the transducer to zero gage pressure. The line is evacuated with a vacuum pump before returning the sensor to normal operation. Unfortunately, the refrigerant loop must be periodically recharged with refrigerant and oil to replace the fluids lost when zeroing the gage transducers. The full procedure for zeroing and evacuating the gage pressure transducers is given in Weston (1996).

The air-side transducers, all of which are used on VFT's, are valved in the manner shown in Figure 3.16. Referring to this figure, the zero-pressure output of the differential pressure transducer installed across the inlet and throat taps of the VFT is obtained by opening the cross-connect valve extending between the high- and low-side ports of the sensor (just as before). The zero-pressure output of the differential pressure transducer installed at the inlet of the VFT (i.e., the one used to sense the gage pressure at the VFT inlet) is obtained by opening the atmospheric venting valve located on the high-side port. This ensures that both ports of the transducer are exposed to atmospheric pressure (i.e., zero gage pressure).

Zero-Point Drift Results

Table 3.7 shows a record of the zero-pressure output signals $X_{zo}$ measured via the above techniques on 19 different days of operation spanning a period of approximately nine weeks. Each $X_{zo}$ value listed in the table is an average of 8–10 min. of data sampled with the DAS at a rate of 1 Hz. For comparison purposes, the nominal zero-pressure output values $X_{zo}^{nom}$ (i.e., the values derived from the calibration curves) are also given in Table 3.7, along with the dates upon which the calibrations were performed. Table 3.8 summarizes the minimum and maximum values of the absolute percent drift between $X_{zo}$ and $X_{zo}^{nom}$ for each transducer. The zero point of each sensor is seen to deviate a significant percentage away from the nominal zero point of the calibration, clearly supporting the need to correct all data for drift as per Equation 3.59. Because

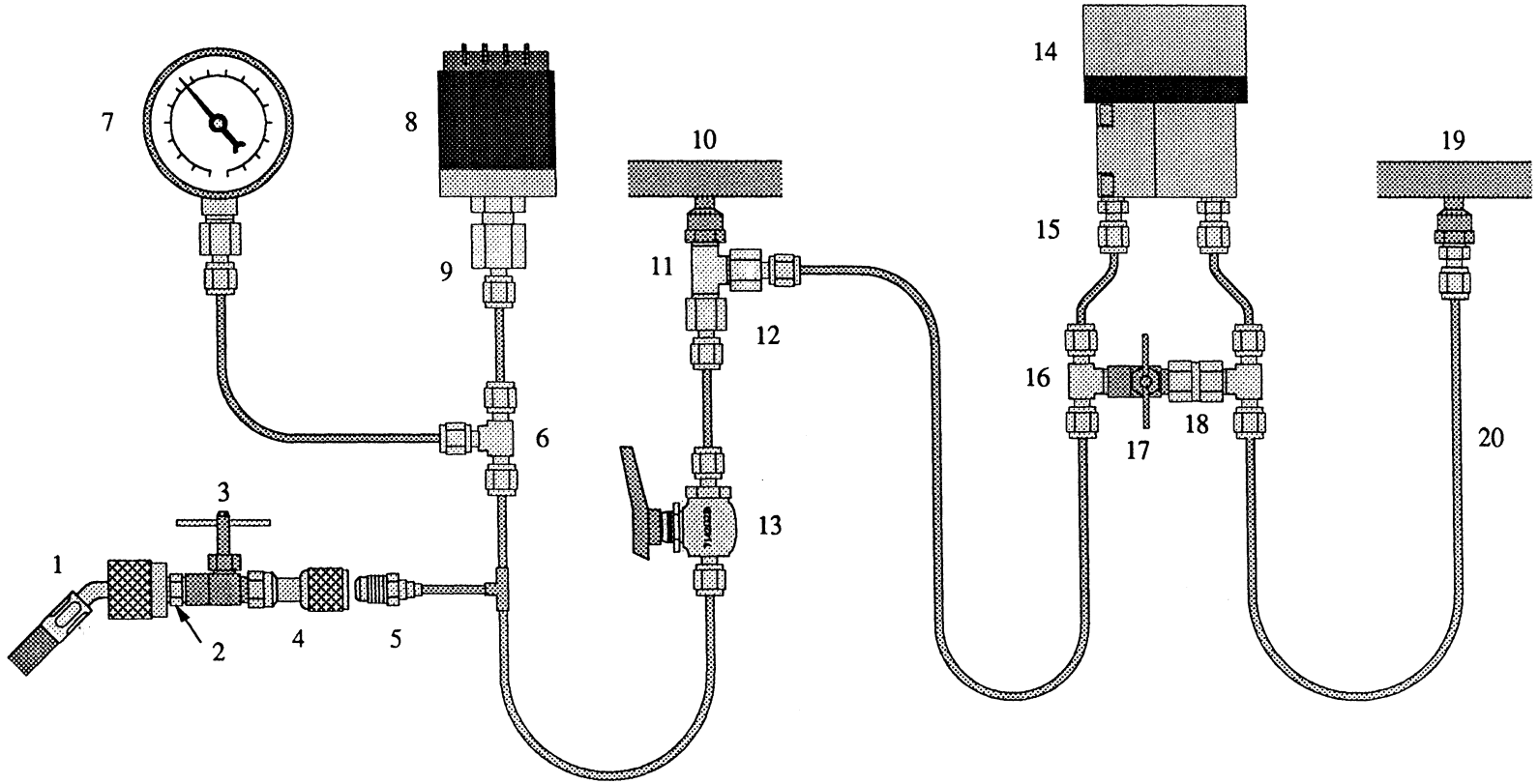


1. Refrigerant Manifold Hose
2. 1/4-in. SAE Flare x 1/8-NPTM Adapter
3. Auxiliary Valve
4. 1/8-NPTF x 1/4-in. SAE Flare Adapter with Valve Core Depressor
5. Schrader Valve
6. 1/8 x 1/8 x 1/8-in. Compression Tee
7. Dial-Type Pressure Gage
8. Gage Pressure Transducer
9. 1/8-in. x 1/4-NPTF Compression Fitting
10. Heat Exchanger Inlet Pressure Tap
11. 1/8 x 1/8 x 1/8-NPTM Brass Tee
12. 1/8-in. x 1/8-NPTF Compression Fitting
13. Ball Valve
14. Differential Pressure Transducer
15. 1/8-in. x 1/8-NPTM Compression Fitting
16. 1/8-in. x 1/8-in. x 1/8-NPTM Compression Tee
17. Cross-Connect Valve
18. 1/8-NPTF Union
19. Heat Exchanger Outlet Pressure Tap
20. 1/8-in. O.D. Copper Tubing

Figure 3.15 The refrigerant-side pressure transducer connections.

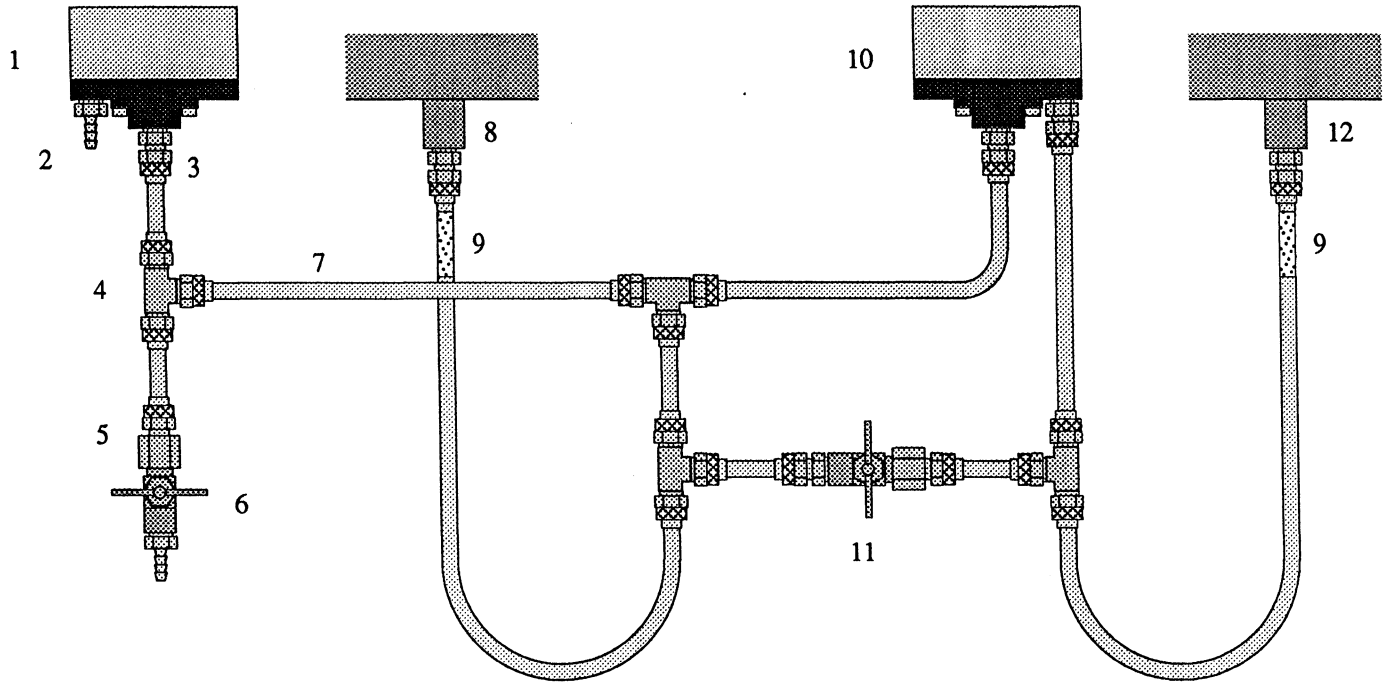


1. Differential Pressure Transducer (used as a gage pressure transducer)
2. 1/8-in. x 1/8-NPTM Hose Barb
3. 1/4-in. x 1/8-NPTM Compression Fitting
4. 1/4 x 1/4 x 1/4-in. Compression Tee
5. 1/4-in. x 1/8-NPTF Compression Fitting
6. Atmospheric Venting Valve
7. 1/4-in. O.D. Polyflo™ Tubing
8. VFT Inlet Pressure Tap
9. Turbulence Damper
10. Differential Pressure Transducer
11. Cross-Connect Valve
12. VFT Throat Pressure Tap

Figure 3.16 The air-side pressure transducer connections.

Table 3.7 Summary of the zero-pressure output signals of the Setra pressure transducers over 19 days of operation.

| Date | Setra 207 # 247866 [VDC] | Setra 207 # 270489 [VDC] | Setra 207 # 202281 [VDC] | Setra 207 # 253458 [VDC] | Setra 207 # 253459 [VDC] | Setra 239 # 409977 [VDC] | Setra 239 # 398563 [VDC] | Setra C239 # 307533 [mA] | Setra 228-1 # 258209 [VDC] | Setra 228-1 # 258208 [VDC] | Setra 228-1 # 287546 [VDC] | Setra 228-1 # 257547 [VDC] | Setra C228-1 # 355739 [mA] |
|---|---|---|---|---|---|---|---|---|---|---|---|---|---|
| 9/15/94 | 0.1435 | 0.1800 | 0.1094 | 0.0992 | 0.0977 | 0.0282 | 0.3312 | 3.984 | –0.070 | 0.612 | –0.0333 | 0.0158 | 3.651 |
| 9/19/94 | 0.1416 | 0.1926 | 0.1107 | 0.0982 | 0.0969 | 0.0257 | 0.3278 | 3.977 | –0.125 | 0.671 | –0.2565 | –0.1003 | 3.664 |
| 9/20/94 | 0.1399 | 0.1887 | 0.1099 | 0.0963 | 0.0983 | 0.0250 | 0.3264 | 3.974 | –0.091 | 0.699 | –0.2088 | –0.0509 | 3.665 |
| 9/28/94 | 0.1407 | 0.1780 | 0.1119 | 0.0990 | 0.0979 | 0.0258 | 0.3270 | 3.976 | –0.099 | 0.536 | –0.3137 | –0.4897 | 3.671 |
| 9/30/94 | 0.1397 | 0.1729 | 0.1101 | 0.0985 | 0.0962 | 0.0250 | 0.3253 | 3.997 | –0.118 | 0.675 | –0.2828 | –0.4736 | 3.689 |
| 10/24/94 | 0.1429 | 0.1920 | 0.1120 | 0.1003 | 0.1017 | 0.0273 | 0.3261 | 4.002 | –0.431 | 0.622 | –0.4158 | –0.4407 | 3.697 |
| 10/25/94 | 0.1425 | 0.1891 | 0.1118 | 0.1004 | 0.1012 | 0.0253 | 0.3249 | 3.999 | –0.454 | 0.595 | –0.4032 | –0.8575 | 3.700 |
| 10/26/94 | 0.1435 | 0.1911 | 0.1106 | 0.1010 | 0.1007 | 0.0260 | 0.3256 | 4.001 | –0.411 | 0.570 | –0.1811 | –0.3888 | 3.698 |
| 10/27/94 | 0.1431 | 0.1895 | 0.1116 | 0.1012 | 0.1014 | 0.0270 | 0.3254 | 3.999 | –0.437 | 0.599 | –0.6670 | –0.3482 | 3.700 |
| 11/02/94 | 0.1435 | 0.1919 | 0.1121 | 0.1026 | 0.1024 | 0.0274 | 0.3249 | 3.999 | –0.421 | 0.512 | –0.2862 | 0.4103 | 3.719 |
| 11/04/94 | 0.1442 | 0.1897 | 0.1115 | 0.1009 | 0.0992 | 0.0309 | 0.3278 | 4.003 | –0.244 | 0.537 | –0.0916 | –0.3824 | 3.717 |
| 11/05/94 | 0.1401 | 0.1882 | 0.1103 | 0.0958 | 0.0963 | 0.0281 | 0.3235 | 3.997 | –0.466 | 0.541 | –0.1971 | –0.2399 | 3.724 |
| 11/07/94 | 0.1441 | 0.1909 | 0.1121 | 0.0988 | 0.1012 | 0.0254 | 0.3244 | 3.999 | –0.445 | 0.107 | –0.2213 | –0.4291 | 3.726 |
| 11/08/94 | 0.1431 | 0.1889 | 0.1105 | 0.0980 | 0.1000 | 0.0282 | 0.3245 | 3.998 | –0.441 | 0.339 | –1.0185 | –0.4515 | 3.719 |
| 11/17/94 | 0.1455 | 0.1917 | 0.1117 | 0.0991 | 0.1020 | 0.0274 | 0.3243 | 4.000 | –0.434 | 0.621 | –0.1542 | –0.3432 | 3.728 |
| 11/18/94 | 0.1471 | 0.1866 | 0.1105 | 0.0993 | 0.1026 | 0.0274 | 0.3245 | 4.001 | –0.418 | 0.583 | –0.1963 | –0.3891 | 3.725 |
| 11/19/94 | 0.1447 | 0.1929 | 0.1117 | 0.0979 | 0.1010 | 0.0249 | 0.3220 | 3.997 | –0.394 | 0.600 | –0.1948 | –0.4263 | 3.733 |
| 11/20/94 | 0.1429 | 0.1916 | 0.1102 | 0.0978 | 0.0995 | 0.0252 | 0.3213 | 3.993 | –0.389 | 0.613 | –0.1314 | –0.4185 | 3.738 |
| 11/21/94 | 0.1450 | 0.1914 | 0.1102 | 0.0983 | 0.0969 | 0.0264 | 0.3227 | 3.995 | –0.377 | 0.615 | –0.1818 | –0.4162 | 3.739 |
| $X_{zo}^{nom}$ | 0.1319 (7/14/94) | 0.1010 (9/19/93) | 0.1106 (9/16/94) | 0.0924 (10/22/93) | 0.0701 (9/20/93) | 0.0227 (8/17/94) | 0.3236 (8/17/94) | 4.059 (10/4/93) | 0.049 (10/22/93) | 0.515 (7/14/94) | 0.0122 (9/13/94) | –0.0190 (9/13/94) | 3.991 (10/5/93) |

Table 3.8 Summary of the zero-point drift behavior of the air- and refrigerant-side pressure transducers.

| Transducer | | Sensed Variable | Drift from $X_{zo}^{nom}$ | | $\lvert\Delta X_{zo}\rvert_{max}$ | | Accuracy $\delta X_{zo}$ | |
|---|---|---|---|---|---|---|---|---|
| Model No. | Serial No. | | Min [%] | Max [%] | [VDC or mA] | [% Full Scale] | [VDC or mA] | [% Full Scale] |
| Setra 207 | 247866 | $P_{eri}$ | 5.91 | 11.52 | 0.0074 VDC | 0.15 | 0.0082 VDC | 0.16 |
| Setra 207 | 270489 | $P_{kri}$ | 71.19 | 90.99 | 0.0200 VDC | 0.40 | 0.0082 VDC | 0.16 |
| Setra 207 | 202281 | $P_{kro}$ | 0.00 | 1.36 | 0.0027 VDC | 0.05 | 0.0082 VDC | 0.16 |
| Setra 207 | 253458 | $P_{cri}$ | 3.68 | 11.04 | 0.0068 VDC | 0.14 | 0.0082 VDC | 0.16 |
| Setra 207 | 253459 | $P_{lv}$ | 37.23 | 46.36 | 0.0064 VDC | 0.13 | 0.0082 VDC | 0.16 |
| Setra 239 | 409977 | $P_{eav}$ | 9.69 | 36.12 | 0.0060 VDC | 0.12 | 0.0086 VDC | 0.17 |
| Setra 239 | 398563 | $P_{cav}$ | 0.03 | 2.35 | 0.0099 VDC | 0.20 | 0.0086 VDC | 0.17 |
| Setra C239 | 307533 | $\Delta P_{cav}$ | 1.38 | 2.09 | 0.029 mA | 0.18 | 0.029 mA | 0.18 |
| Setra 228-1 | 258209 | $\Delta P_{er}$ | 242.86 | 1051.02 | 0.396 VDC | 7.92 | 0.012 VDC | 0.24 |
| Setra 228-1 | 258208 | $\Delta P_{cr}$ | 0.58 | 79.22 | 0.592 VDC | 11.84 | 0.012 VDC | 0.24 |
| Setra 228-1 | 287546 | $\Delta P_{dv}$ | 372.95 | 8448.36 | 0.9852 VDC | 19.70 | 0.0090 VDC | 0.18 |
| Setra 228-1 | 257547 | $\Delta P_{lv}$ | 167.89 | 4413.16 | 1.2678 VDC | 25.36 | 0.0090 VDC | 0.18 |
| Setra C228-1 | 355739 | $\Delta P_{eav}$ | 6.31 | 8.52 | 0.088 mA | 0.55 | 0.031 mA | 0.19 |

we operate the transducers in a climate-controlled laboratory, only a small portion of each drift percentage can be attributed to daily changes in the ambient temperature surrounding the electronics. The following factors may account for other portions of the drifts:

(i) For some of the sensors, over a year had elapsed between the time the data of Table 3.7 were recorded and the time the sensor was last calibrated, so the zero points of some of the sensors may have shifted naturally with age.

(ii) The compression fittings installed on the ports of the sensors are sometimes disconnected to perform maintenance procedures and to remove the sensor from the loop for calibration. Stresses induced by removing and retightening the fittings can slightly effect the zero point.

(iii) In the refrigerant-side installations, the 1/8-in. O.D. pressure transmission lines tend to fill with viscous compressor oil. The presence of the oil may affect the zero-point readings, as well as the pressure measurements in general. This issue warrants future investigation.

(iv) Some of the transducers are undoubtedly damaged, namely the Model 228-1 differential pressure sensors used in the refrigerant loop.

Concerning natural drift with age, Table 3.8 also shows the maximum absolute difference between the 19 values of $X_{zo}$ observed for each transducer. The differences are expressed both in electrical signal units (VDC or mA) and, more conveniently, as a percentage of a full-scale change $\Delta X_{FS}$ in the output of the sensor ($\Delta X_{FS}$ = 5 VDC or 16 mA). For comparison purposes, the uncertainty $\delta X_{zo}$ in the measurement of $X_{zo}$ is also given in the table. The latter uncertainty is calculated from the relation

$$\delta X_{zo} = \sqrt{\left(\frac{\delta X_{\%FS}}{100}\Delta X_{FS}\right)^2 + (\delta X)^2} \tag{3.60}$$

where $\delta X$ is the accuracy of the DAS voltage or current measurement, and $\delta X_{\%FS}$ (given by Table 3.6) is the rated accuracy of the pressure transducer expressed as a percentage of a full-scale change in the input or output of the sensor (the same percentage applies to both because the two are linearly related). For all but one of the Setra Model 207 gage pressure transducers, the maximum absolute change in $X_{zo}$ observed over the nine-week period falls within the measurement uncertainty $\delta X_{zo}$. Thus, the zero-pressure output readings of these refrigerant-side transducers can likely be updated just once every three to four weeks as opposed to each and every day that system data are recorded. Less frequent updates are certainly advantageous from

a charge inventory perspective because the process of zeroing these transducers leads to a significant loss of refrigerant and oil over time.

The remaining transducers are all differential pressure sensors whose zero points can be easily measured on a daily basis without the loss of fluids. The maximum changes in $X_{zo}$ observed for the Setra Model 239/C239 transducers are within (or very close to) the respective measurement uncertainties. However, the maximum changes observed for the Setra Model 228-1 transducers greatly exceed the respective measurement uncertainties. Unbeknownst to us at the time of testing, these salvaged transducers have an internal Viton® O-ring which presumably seals around the linkage between the wet and dry diaphragm chambers. Viton is reportedly incompatible with the refrigerant we presently use (R-134a) and with the refrigerant these salvaged sensors were known to have been used with in the past (R-12) (DuPont, 1993), so these sensors may have gradually become damaged over time.

### 3.3..2 Barometer

In our data reduction process, the absolute pressures of the refrigerant and air streams must be known in order to calculate other thermophysical properties such as densities and enthalpies. Thus, a NIST-traceable mercury barometer (PRINCO Nova™ Model No. 469) with a sliding vernier scale is used to measure the ambient atmospheric pressure in our lab, and the barometer reading is added to all of the gage pressure measurements recorded in the data set to convert them to absolute pressures. Because we collect data over relatively short time periods (typically under 30 min. per data set), the changes in the atmospheric pressure over the course of any given test are generally negligible. Equation 3.54 is used to convert the reading of the barometer column height $h_b$ [in. Hg] to the atmospheric pressure $P_{atm}$ [psia]. As with manometer readings, the height $h_b$ is multiplied by the gravity ratio of Equation 3.53 to reference the reading to standard gravity. In addition, a dimensionless temperature correction factor $F_T$ is applied to the reading to account for thermal expansion of the barometer scale and to reference the reading to the standard density of mercury (PRINCO, 1992). The temperature correction factor, as given by the barometer instruction manual, is

$$F_T = \frac{1 + L\,(T_b - T_s)}{1 + M\,(T_b - T_m)} \tag{3.61}$$

where

$T_b$ = barometer scale and fluid temperature [°F]

$T_s$ = 62 °F (standard temperature for English scales)

$T_m$ = 32 °F (standard temperature of mercury)

$L$ = 0.0000102 in./in.-°F

$M$ = 0.0001010 $in.^3/in.^3$-°F

A mercury-in-glass thermometer supplied on the barometer housing is used to measure the temperature $T_b$ appearing in Equation 3.61. The thermometer is accurate to ± 0.5 °C. The final corrected reading of the column height h [in. Hg] used in Equation 3.54 is

$$h = \frac{g_l}{g} F_T h_b \tag{3.62}$$

The density ρ used in Equation 3.54 is $\rho_{Hg} = 848.739\ lb_m/ft^3$, which is the density of mercury at the standard reference temperature of 32 °F (CRC, 1994). After all corrections have been applied, the barometer reading is accurate to ± 0.01 in. Hg, or ± 0.005 psia (PRINCO, 1992).

## 3.4 Compressor Speed and Torque Instrumentation

A Lebow Model No. 1805-2K-04 sensor is used to sense the speed $N_{jack}$ [rpm] and the torque $\tau_{jack}$ [in.-$lb_f$] of the jackshaft of the compressor drive assembly shown in Figure 2.12. The speed and torque of the actual compressor shaft are calculated from the jackshaft sensor readings as

$$N_{comp} = \frac{d_{jack}}{d_{comp}} N_{jack} = R_p N_{jack} \tag{3.63}$$

and

$$\tau_{comp} = -\frac{d_{comp}}{d_{jack}} \tau_{jack} = -\frac{1}{R_p} \tau_{jack} \tag{3.64}$$

where $R_p$ ($= d_{jack}/d_{comp}$) is the jackshaft-to-compressor pulley diameter ratio. For any given compressor installation, we calculate an average value for $R_p$ via Equation 3.63 by running the drive motor at several different frequencies and measuring the resulting pulley speeds $N_{jack}$ and $N_{comp}$ with a strobe tachometer. The tests are performed with the compressor clutch engaged so as to absolve the typical effects of belt slip (if any) into the value of $R_p$.

The Lebow device uses a magnetic pickup sensor to sense $N_{jack}$. A Daytronic Model No. 3240A frequency conditioner converts the Lebow speed sensor output to a 0–5 VDC signal which is linearly proportional to $N_{jack}$ over a range of 0–10,000 rpm. The output calibration equation is

$$N_{jack} = 2000\ E_o \tag{3.65}$$

where $E_o$ [VDC] is the output voltage of the Daytronic 3240A. The frequency conditioner output is accurate to ± 2 rpm.

Next, the Lebow device uses a rotary-transformer strain gage bridge to sense $\tau_{jack}$. A Daytronic Model No. 3278 strain gage conditioner provides the input excitation to the bridge and converts the output to a 0–5 VDC signal which is linearly proportional to $\tau_{jack}$ over a range of 0–2000 in.-$lb_f$. A Lebow Model No. 7927 precision shunt calibration reference is wired between the torque sensor and the Daytronic 3728 device. The shunt creates a simulated torque sensor output of 1150 in.-$lb_f$ against which the strain gage conditioner is calibrated. The output calibration equation is

$$\tau_{jack} = 400\ E_o \tag{3.66}$$

where $E_o$ [VDC] is the output voltage of the Daytronic 3278. The strain gage conditioner output is accurate to $\pm$ 1 in.-$lb_f$.

As a final note, the capacitances of the long cables connecting the Daytronic signal conditioners to the DAS caused the 0–5 VDC analog outputs of the signal conditioners to oscillate. The oscillation problems were resolved by placing 1-k$\Omega$ resistors in series with the positive output leads of the Daytronic devices as is shown in Figure 3.6 (Horowitz, 1989).

## 3.5 Humidity Instrumentation

Vaisala Model No. HMP 35A humidity probes are used to sense the relative humidities of (1) the evaporator inlet air stream ($\phi_{eai}$), (2) the evaporator outlet air stream ($\phi_{eao}$), and (3) the condenser outlet air stream ($\phi_{cao}$). Only one relative humidity measurement is needed in the condenser air loop because the condenser does not remove moisture from the air stream (i.e., the humidity ratio $\omega$ is theoretically the same in any part of the loop). The evaporator-side inlet humidity probe is mounted in the measurement section duct as is discussed in Chapter 2. The evaporator- and condenser-side outlet humidity probes are mounted in the rectangular-to-round transition ducts at the inlets of the blowers. For future tests, we will relocate the latter two probes to locations downstream of the blowers where the temperature and humidity profiles of the air streams are better mixed.

Each probe contains a four-wire RTD (discussed earlier) and a HUMICAP® thin-film capacitive humidity sensor. The RTD and the humidity sensor are located at the tip of the probe and are protected by a membrane filter. The sensor excitation is provided by the 24-VDC power supply, although the probe can accept any supply voltage within the range of 7–35 VDC. The humidity sensor has a rated operating range of 0.2–100 % RH and a rated temperature range of -40 to 60 °C. The probe converts the output to a 0.002–1 VDC signal which is linearly proportional to the relative humidity. The output calibration equation is

$$\phi = 100\ E_o \tag{3.67}$$

where $\phi$ [% RH] is the relative humidity, and $E_o$ [VDC] is the sensor output voltage. The probes have a rated accuracy of ± 1 % RH, and the rated 90 % response time for a step change in humidity is 15 s at 20 °C. We have not yet calibrated the probes in-house to verify the calibration of the manufacturer. Vaisala recommends that the probes be recalibrated against saturated salt solution references at least once per year.

## 3.6 Mass Flow Instrumentation

### 3.6.1 Coriolis Mass Flow Meter

A Coriolis-type mass flow meter (Micro Motion® Model No. DS025S119SU) is installed in the refrigerant loop to give accurate mass flow measurements during steady-state calorimetry tests and to calibrate the VFT's used in the discharge and liquid lines. The sensor contains a U-shaped tube which is vibrated by an electromagnetic drive. As fluid flows through the tube, the momentum of the vibrating walls is imparted to the fluid. The fluid resists these changes in the momentum, causing the tube to twist via a Coriolis effect. The amount of twist is proportional to the mass flow rate. An accompanying transmitter unit (Model No. RFT97121PRU) processes the sensor readings and converts the output to a 4–20 mA signal which is linearly proportional to the mass flow rate. The transmitter also displays the fluid temperature, density, and mass flow rate in real time on a built-in digital display window. At present, the sensor/transmitter combination is factory calibrated to span a 0–400 $lb_m$/hr range (a suitable range for our facility applications), but can be reconfigured to span a higher range (up to 2700 $lb_m$/hr) if desired. The output calibration equation is

$$\dot{m} = 25\, I_t - 100 \tag{3.68}$$

where $\dot{m}$ [$lb_m$/hr] is the mass flow rate, and $I_t$ [mA] is the transmitted current. The rated accuracy of the calibration (excluding errors in the measurement of $I_t$) is ± 0.2 % of reading plus an additional ± 0.3 $lb_m$/hr which accounts for instability of the zero point.

We installed the Micro Motion flow meter in the liquid line of our refrigerant loop because the refrigerant and oil most often combine in a single-phase flow in this line. In contrast, the discharge line always contains a two-phase flow pattern comprised of liquid oil and superheated refrigerant vapor. Calculations based upon data provided in the Micro Motion product literature show that the maximum head loss through the flow meter is expected to be less than 1 psi for flooded liquid-line operation. Hence, unless the amount of subcooling is very low and the flow rate is very high, the refrigerant can be expected to remain in its subcooled state after passing through the meter. However, during transient modes of operation in which the liquid line may carry a two-phase or superheated refrigerant flow, the maximum head loss is predicted to be on

the order of 10–15 psi for high flow rates. Such a large pressure drop is uncharacteristic of an actual mobile a/c system. Thus, for transient tests, the Micro Motion is placed on a bypass, and the liquid-line VFT (which always has a low head loss) is used instead. The bypass line will be installed in the future and is not shown in Figure 1.2. Fortunately, we have not observed any unduly high pressure drops in any of the transient or steady-state data we have collected to date.

### 3.6.2 Venturi Flow Tubes (VFT's)

#### 3.6.2.1 The Operating Principle of a Venturi Tube

Figure 3.17 shows a schematic of several Venturi tube designs. In each case, the flow entering the tube is contracted from an inlet area $A_1$ to a throat area $A_2$. For steady flow, the number of fluid particles passing through $A_1$ in a given amount of time must also pass through the smaller throat area $A_2$ in the same amount of time. Hence, the fluid velocity increases at the throat, which gives rise to an increase in kinetic energy at the throat. The total energy of the fluid must be conserved, so the increase in kinetic energy is accompanied by (i) a decrease in potential energy, as is evidenced by a decrease in the static pressure of the fluid at the throat, and (ii) a decrease in internal energy, as is evidenced by a decrease in the temperature of the fluid at the throat. The changes in temperature and pressure correspondingly cause a change in density at the throat. As the cross-sectional area of the flow smoothly re-expands to the original area $A_1$ at the exit of the tube, the velocity, pressure, temperature, and density of the fluid tend to return to nearly the same values as at the inlet, resulting in a mass flow measurement which is relatively unobtrusive to the flow system.

#### 3.6.2.2 The Venturi Flow Equation

The expression which yields the theoretical rate of flow through a Venturi tube is derived via the equations of continuity and energy. The general energy equation for steady flow (i.e., for no storage of energy between $A_1$ and $A_2$) states that as the fluid passes between sections $A_1$ and $A_2$, the change in the total energy (kinetic plus internal) of the fluid is equal to the total work done on the fluid (the sum of gravitational work, flow work, and external work) plus the heat transferred to the fluid. That is,

$$(KE_2 + u_2) - (KE_1 + u_1) = (P_1\upsilon_1 - P_2\upsilon_2) + (\lambda_1 - \lambda_2) + w_{ext} + q \qquad (3.69)$$

where

$KE$ = kinetic energy per unit mass
$u$ = internal energy per unit mass
$P$ = absolute static fluid pressure
$\upsilon$ = specific volume ($= 1/\rho$)

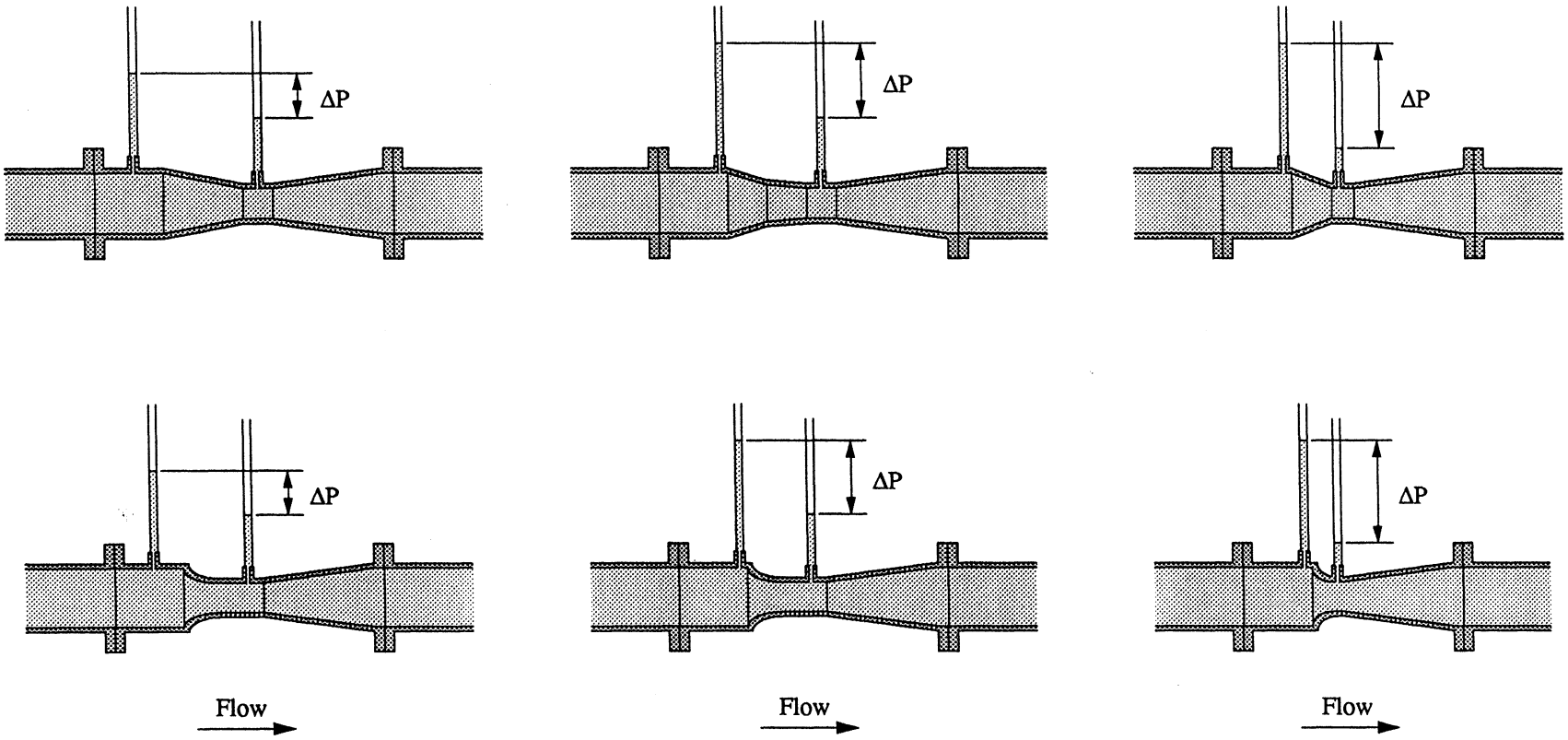


(a) Classical Venturi Tubes (b) Modified Venturi Tubes (c) Venturi Flow Tubes

Figure 3.17 A schematic of several types of Venturi flow meters.

$\lambda$ = total gravitational potential energy per unit mass

$w_{ext}$ = external work done on the fluid per unit mass

$q$ = heat transfer per unit mass

The following assumptions are then made:

(i) The Venturi tube is assumed to be horizontal. Consequently, there is no net change in the gravitational potential energy of the fluid (i.e., $\lambda_1 = \lambda_2$).

(ii) No external work is assumed to be done on or by the fluid (i.e., $w_{ext} = 0$).

(iii) The density and velocity profiles of the flow at sections $A_1$ and $A_2$ are assumed to be flat. Accordingly, the general equational form for the kinetic energy per unit mass at either section is given by

$$KE = \frac{1}{2}\frac{V^2}{g_c} \tag{3.70}$$

and the general form for the mass flow rate across either section is given by

$$\dot{m} = \rho A V \tag{3.71}$$

where $\rho$ and $V$ are, respectively, the density and velocity of the flow at the given section.

(iv) The process is assumed to be adiabatic (i.e., $q = 0$). This assumption implies a frictionless flow between the fluid and the pipe, which allows us to further assume that the change of state between $A_1$ and $A_2$ is a reversible, isentropic process (ASME, 1971).

Under these assumptions, Equation 3.69 reduces to

$$\frac{1}{2g_c}(V_2^2 - V_1^2) = (u_1 + P_1\upsilon_1) - (u_2 + P_2\upsilon_2) \tag{3.72a}$$

$$= h_1 - h_2 \tag{3.72b}$$

where $h \equiv u + P\upsilon$ is the enthalpy per unit mass. Next, the continuity equation for steady flow (i.e., for no storage of mass between $A_1$ and $A_2$) dictates that the mass flow across section $A_1$ is equal to the mass flow across section $A_2$ (i.e., $\dot{m}_1 = \dot{m}_2$). Hence, by applying Equation 3.71, the expression

$$\rho_1 A_1 V_1 = \rho_2 A_2 V_2 \tag{3.73}$$

can be written. Solving this latter expression for $V_2$ gives

$$\begin{aligned} V_2 &= \frac{A_1}{A_2}\frac{\rho_1}{\rho_2} V_1 \\ &= \left(\frac{d_1}{d_2}\right)^2 \frac{\rho_1}{\rho_2} V_1 \\ &= \frac{1}{\beta^2}\frac{\rho_1}{\rho_2} V_1 \end{aligned} \tag{3.74}$$

where $\beta = d_2/d_1$ is commonly known as the beta ratio, or the ratio of the throat diameter $d_2$ to the inlet diameter $d_1$. Substituting Equation 3.74 into Equation 3.72b and solving for $V_1$ gives

$$V_1 = \left[\frac{2\, g_c\, (h_1 - h_2)}{\frac{1}{\beta^4}\left(\frac{\rho_1}{\rho_2}\right)^2 - 1}\right]^{1/2} \tag{3.75}$$

Thus, the mass flow rate of a real fluid, compressible or incompressible, is given by

$$\begin{aligned} \dot{m}_{\text{real fluid}} &= \rho_1 A_1 V_1 \\ &= \rho_1 \left(\frac{\pi d_1^2}{4}\right)\left[\frac{2\, g_c\, (h_1 - h_2)}{\frac{1}{\beta^4}\left(\frac{\rho_1}{\rho_2}\right)^2 - 1}\right]^{1/2} \end{aligned} \tag{3.76}$$

where units are as follows: $\dot{m}$ [$lb_m/s$], $\rho$ [$lb_m/ft^3$], d [ft], and h [$ft\text{-}lb_f/lb_m$].

In order to evaluate Equation 3.76, the density and enthalpy of fluid must be known at both the inlet and the throat. In general, $\rho_1$ and $h_1$ are determined from thermophysical property data given the static pressure $P_1$ sensed at the inlet pressure tap and the temperature $T_1$ sensed by a probe positioned far enough upstream of the Venturi so as not to disturb the flow at the inlet. Each VFT used in our facility is accordingly instrumented with an inlet pressure transducer and an upstream temperature probe as is shown in Figure 1.2. We pause here to note that the refrigerant-side VFT mass flow readings are invalid for two-phase refrigerant flow because the state of a two-phase refrigerant mixture cannot be identified from measurements of just P and T. Also, the contributions of oil to the property values of $\rho$ and h are presently neglected and warrant future investigation. Continuing, $\rho_2$ and $h_2$ are determined from $P_2$ and $T_2$. $P_2$ is calculated from measurements of $P_1$ and $\Delta P$ as per Equation 3.48, whereas $T_2$ is determined implicitly from the isentropic relation

$$s_1(P_1,T_1) = s_2(P_2,T_2) \tag{3.77}$$

where s is the specific entropy of the fluid. Finally, because property tables most often give enthalpies in units of h [Btu/$lb_m$], the conversion factor

$$h\ [\text{ft-lb}_f/\text{lb}_m] = \left(\frac{777.649\ [\text{ft-lb}_f]}{1\ [\text{Btu}]}\right) h\ [\text{Btu}/\text{lb}_m] \tag{3.78}$$

is also needed to evaluate Equation 3.76.

In practice, the working fluid is typically assumed to behave as an incompressible liquid or an ideal gas to further simplify the flow equation and eliminate the need to implicitly solve a function s(P,T) for $T_2$. We make such assumptions in reducing our facility data. The software package we presently use to reduce our data (EES) models air as an ideal gas, so Equation 3.76 offers no significant advantage over a simplified ideal gas solution when reducing the air-side VFT data. Likewise, subcooled liquid refrigerant is treated as an incompressible fluid in EES, so Equation 3.76 offers no significant advantage over a simplified incompressible solution when reducing the liquid-line VFT data. Although EES does treat superheated refrigerant vapor as a real fluid, calculations show that the differences between mass flow rates calculated from Equation 3.76 and those calculated from an ideal gas solution are insignificant (less than 0.06 % for data collected to date), so the simplified ideal gas solution is also used to reduce our discharge-line VFT data.

The Venturi Equation for Incompressible Flow

For an incompressible fluid such as water or liquid refrigerant, changes in entropy are given by

$$s_2 - s_1 = c \ln\frac{T_2}{T_1} \tag{3.79}$$

and changes in internal energy are given by

$$u_2 - u_1 = c\,(T_2 - T_1) \tag{3.80}$$

where $c = c_p = c_v$ is the specific heat of the liquid. The specific heat is assumed to be constant between $T_1$ and $T_2$. By assumption (iv), the change of state between $A_1$ and $A_2$ is isentropic (i.e., $s_2 = s_1$), so Equation 3.79 yields $T_2 = T_1$, which gives $u_2 = u_1$ from Equation 3.80. Also, because small changes in the pressure of an incompressible fluid cause negligible changes in density, it can be assumed that $\upsilon_2 = \upsilon_1 = 1/\rho_1$. Thus, Equation 3.72a reduces to

$$\frac{1}{2\,g_c}(V_2^2 - V_1^2) = \frac{P_1 - P_2}{\rho_1} \tag{3.81}$$

Substituting Equation 3.74 into Equation 3.81 and solving for $V_1$ with $\rho_2 = \rho_1$ gives

$$V_1 = \left(\frac{\beta^2}{\sqrt{1-\beta^4}}\right)\sqrt{2\, g_c \frac{P_1 - P_2}{\rho_1}} \tag{3.82}$$

Hence, for an incompressible fluid, the mass flow rate is given by

$$\begin{aligned} \dot{m}_{incomp} &= \rho_1 A_1 V_1 \\ &= \rho_1 \left(\frac{\pi d_1^2}{4}\right)\left(\frac{\beta^2}{\sqrt{1-\beta^4}}\right)\sqrt{2\, g_c \frac{P_1 - P_2}{\rho_1}} \\ &= \left(\frac{\pi d_1^2}{4}\right)\left(\frac{\beta^2}{\sqrt{1-\beta^4}}\right)\sqrt{2\, g_c\, \rho_1\, \Delta P} \end{aligned} \tag{3.83}$$

where $\Delta P = P_1 - P_2$ is the differential pressure sensed across the inlet and throat taps of the Venturi. Units in Equation 3.83 are as follows: $\dot{m}$ [$lb_m/s$], $\rho$ [$lb_m/ft^3$], d [ft], and $\Delta P$ [psfd]. For liquid refrigerant R-134a, the density $\rho_1$ appearing in Equation 3.83 is given by the EES function call

$$\rho_1\ [lb_m/ft^3] = 1/\text{Volume}(\text{R134a, T} = T_1\ [°F], \text{P} = P_1\ [\text{psia}]) \tag{3.84}$$

The function automatically checks for a subcooled state and returns the saturated liquid density.

The Venturi Equation for Compressible Flow

For a compressible fluid such as air or refrigerant vapor, the change in density at the throat can be significant and must be accounted for in the flow equation. If the fluid is assumed to behave as an ideal gas with constant specific heats, then the following isentropic relation holds true:

$$P\upsilon^\gamma = \text{constant} = P_1\upsilon_1^\gamma = P_2\upsilon_2^\gamma \tag{3.85}$$

The latter equation can be equivalently expressed as

$$\left(\frac{\rho_2}{\rho_1}\right) = \left(\frac{P_2}{P_1}\right)^{1/\gamma} \tag{3.86}$$

where $\gamma = c_p/c_v$ is the ratio of the specific heat at constant pressure ($c_p$) to the specific heat at constant volume ($c_v$). Using the fact that $P\upsilon^\gamma$ = constant, the change in enthalpy of the ideal gas for the isentropic process is given by

$$h_1 - h_2 = \int_{P_1}^{P_2} \upsilon \, dP \qquad (3.87)$$
$$= P_1 \upsilon_1 \left(\frac{\gamma}{\gamma - 1}\right)\left(1 - r^{\frac{\gamma-1}{\gamma}}\right)$$

where $r = P_2/P_1$ is the throat-to-inlet static pressure ratio (ASME, 1971). By substituting Equations 3.74, 3.86, and 3.87 into Equation 3.72b and solving for $V_2$ (or $V_1$ as before), it can be shown (ASME, 1971) that the mass flow rate for an ideal gas is given by

$$\dot{m}_{\text{ideal gas}} = Y \, \dot{m}_{\text{incomp}} \qquad (3.88)$$

where Y is a dimensionless compressibility factor given by

$$Y = \left[ r^{2/\gamma} \left(\frac{\gamma}{\gamma - 1}\right)\left(\frac{1 - r^{\frac{\gamma-1}{\gamma}}}{1 - r}\right)\left(\frac{1 - \beta^4}{1 - \beta^4 r^{2/\gamma}}\right)\right]^{1/2} \qquad (3.89)$$

To evaluate Equation 3.89, the polytropic exponent $\gamma = c_p/c_v$ must be known. EES contains $c_p$ property functions for moist air and refrigerant R-134a, but EES does not contain $c_v$ property functions for these fluids. Hence, for R-134a, $c_v$ is determined from its definition using the real-fluid properties of EES:

$$c_v \equiv \left(\frac{\partial u}{\partial T}\right)_{\upsilon} \qquad (3.90)$$

We implement Equation 3.90 in EES as a difference equation evaluated at the known inlet conditions. That is, the relation

$$c_v = \frac{u(T_1 + \frac{\Delta T}{2}, \upsilon_1) - u(T_1 - \frac{\Delta T}{2}, \upsilon_1)}{\Delta T} \qquad (3.91)$$

is used, where $\Delta T$ is a small change in temperature (we use $\Delta T = 0.02$ °R). Units in Equation 3.91 are as follows: $c_v$ [Btu/lb$_m$-°R], T [°F], $\upsilon$ [ft$^3$/lb$_m$], u [Btu/lb$_m$], and $\Delta T$ [°R] or [°F] ($\Delta T$ has the same numerical value in either unit). EES contains the function u(T,$\upsilon$) needed to evaluate Equation 3.91, where the specific volume $\upsilon_1$ passed to the function is given by the reciprocal of the function call of Equation 3.84. EES does not contain an equivalent function u(T,$\upsilon$,$\omega$) for moist air, so the relation

$$c_v = T\left(\frac{\partial s}{\partial T}\right)_{\upsilon} \tag{3.92}$$

is used to reduce the air-side data, where T [°R] is the absolute temperature of the fluid. As before, we implement Equation 3.92 in EES as a difference equation evaluated at the known inlet conditions. That is, the relation

$$c_v = (T_1 + 459.16)\left[\frac{s(T_1 + \frac{\Delta T}{2}, \upsilon_1) - s(T_1 - \frac{\Delta T}{2}, \upsilon_1)}{\Delta T}\right] \tag{3.93}$$

is used, where units are: $c_v$ [Btu/$lb_m$-°R], T [°F], $\upsilon$ [$ft^3/lb_m$], s [Btu/$lb_m$-°R], and $\Delta T$ [°R] or [°F]. The total specific entropy s of the moist air mixture is given by

$$s(T,\upsilon) = s_{air}(T,\upsilon_{air}) + \omega\, s_{H_2O}(T,\upsilon_{H_2O}) \tag{3.94}$$

where $\omega$ [$lb_m$ $H_2O$/$lb_m$ dry air] is the humidity ratio of the mixture, and the subscripts "air" and "$H_2O$" designate the individual mixture components. The specific volumes $\upsilon_{air}(T_1,P_{1,\,air})$ and $\upsilon_{H_2O}(T_1,P_{1,\,H_2O})$ of the mixture components are each calculated from EES function calls which evaluate the $\upsilon$ of the given substance via the ideal gas law given the mixture temperature $T_1$ and the partial pressure $P_{1,\,air}$ or $P_{1,\,H_2O}$. The latter pressures are given by

$$P_{1,\,H_2O} = \frac{\omega_1 P_1}{\omega_1 + 0.62198} \tag{3.95}$$

and

$$P_{1,\,air} = P_1 - P_{1,\,H_2O} \tag{3.96}$$

where $P_1$ is the total static pressure of the mixture. Finally, the inlet density $\rho_1$ [$lb_m$ wet air/$ft^3$] is given by

$$\rho_1 = \frac{1}{\upsilon}(1 + \omega_1) \tag{3.97}$$

where $\upsilon$ [$ft^3/lb_m$ dry air] is the specific volume of the moist air mixture. The EES function calls needed to evaluate all of the above relations are given in the data reduction program of Weston (1996).

Area Expansion Factor

If a Venturi is used at an operating temperature which deviates significantly from the temperature at which the inlet and throat dimensions were initially measured (as in our facility), then a correction factor must be applied to account for thermal expansion and contraction of the

diameters $d_1$ and $d_2$ (or, equivalently, to account for thermal changes in the area $A_1$ and the diameter ratio $\beta$ appearing in Equations 3.76 and 3.83). To perform the correction, the Venturi material is first assumed to follow the law of linear thermal expansion. According to this law, a diameter $d_i$ measured at an initial temperature $T_i$ will expand or contract to a final diameter of

$$d_f = [1 + \alpha (T_f - T_i)]\, d_i \tag{3.98}$$

at a temperature $T_f$, where $\alpha$ is the coefficient of linear expansion of the material (Sears, 1987). Because the change in the fluid temperature between sections $A_1$ and $A_2$ is typically small (calculations show that $T_1$ and $T_2$ differ by less than a few degrees Fahrenheit in our facility applications), the difference between the temperatures of the inlet and throat materials is also likely to be small. Thus, for a general case in which the inlet and throat materials have the same $\alpha$ (i.e., a case in which the inlet and throat are made of the same material), the difference between the percent change in $d_1$ and the percent change in $d_2$ can be neglected, and the diameter ratio $\beta$ can be assumed to remain unchanged for any given operating temperature. Hence, Equations 3.76 and 3.83 need only be corrected for thermal changes to $A_1$. The area $A_1$ changes in proportion to the square of the ratio of the operating inlet diameter to the initial inlet diameter. That is,

$$\begin{aligned} A_{1,f} &= \left(\frac{d_{1,f}}{d_{1,i}}\right)^2 A_{1,i} \\ &= [1 + \alpha (T_f - T_i)]^2 A_{1,i} \end{aligned} \tag{3.99}$$

where $A_{1,f}$ is the final operating area, and $A_{1,i}$ is the initial area. In our facility, the dimensions of each VFT were initially measured with the VFT's being at room temperature, which is assumed to be $T_i = 68$ °F. During any given test, the VFT material at section $A_1$ is assumed to be at the inlet fluid temperature $T_1$ [°F]. Hence, in accord with Equation 3.99, the theoretical rate equations are multiplied by the dimensionless area expansion factor

$$F_a = [1 + \alpha (T_1 - 68)]^2 \tag{3.100}$$

to convert the measured inlet area to the operating inlet area. Concerning values of $\alpha$, our refrigerant-side VFT's are made of brass ($\alpha_{brass} = 1.0 \times 10^{-5}$ in./in.-°F) and our air-side VFT's are made of zinc-plated steel ($\alpha_{steel} = 6.7 \times 10^{-6}$ in./in.-°F) (CRC, 1994). Expansion and contraction of the zinc plating on the air-side VFT's is assumed to be constrained by the smaller expansion coefficient of the larger steel body.

Discharge Coefficient

To summarize thus far, the theoretical rate of ideal fluid flow through a Venturi device is given by

$$\dot{m}_{theo} = F_a\, Y\, \dot{m}_{incomp} \tag{3.101}$$

where Y is set equal to unity for incompressible flow. However, this theoretical flow equation does not fully describe the real behavior of a Venturi flow device because actual operating conditions are seldom ideal. Actual rates of flow are given by

$$\begin{aligned} \dot{m} &= C\, \dot{m}_{theo} \\ &= \left(\frac{\pi\, d_1^2}{4}\right)\left(\frac{F_a\, Y\, C\, \beta^2}{\sqrt{1-\beta^4}}\right)\sqrt{2\, g_c\, \rho_1\, \Delta P} \end{aligned} \tag{3.102}$$

where the dimensionless factor C, called the discharge coefficient, accounts for the following real flow effects (Halmi, 1972):

(i) A frictional energy loss occurs between the inlet and the throat.
(ii) The actual velocity profiles at the inlet and throat are not flat.
(iii) The inlet and/or throat tap may not sense static pressure.
(iv) The cross-sectional area of the flow at the location of the throat tap may not be equal to the measured geometrical area.

Points (i) and (ii) are common characteristics of all Venturi devices. Because a small head loss occurs between sections $A_1$ and $A_2$, the pressure measured at section $A_2$ is actually less than it would be for a frictionless flow. Thus, the $\Delta P$ measured in a real case is larger than the $\Delta P$ one would expect in a frictionless case, so evaluating the theoretical rate equation with the actual value of $\Delta P$ results in a slight overprediction of the mass flow rate. Consequently, the result must be multiplied by a discharge coefficient which is slightly less than unity to obtain the true flow rate. Furthermore, in a real flow situation, the velocity profiles at the inlet and throat sections are rounded to a certain degree as is shown in Figure 3.18. As a result, Equations 3.70 and 3.71 only approximate the true values of KE and $\dot{m}$ at sections $A_1$ and $A_2$. Because the shape of the velocity profile depends upon the Reynolds number of the flow ($Re_D$), C is also a function of $Re_D$. The Reynolds number is given by

$$Re_D = \frac{4\, \dot{m}}{\pi\, d_1\, \mu} \tag{3.103}$$

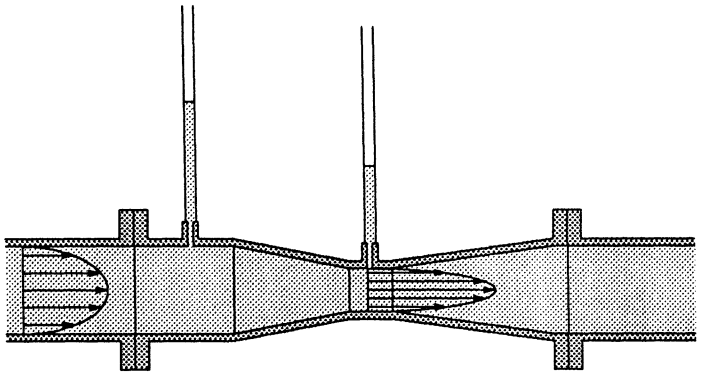

(a) Typical velocity profiles for a low (laminar) $Re_D$

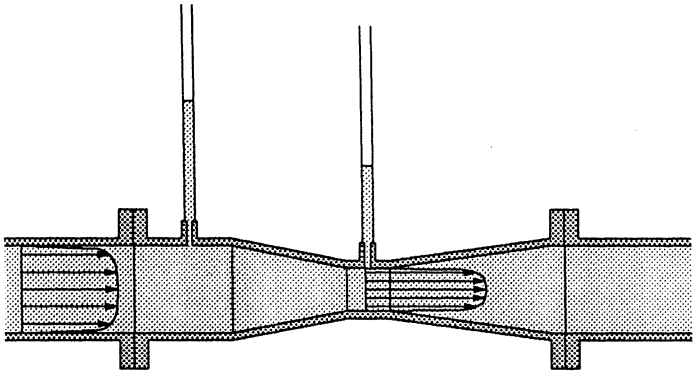

(b) Typical velocity profiles for a high (turbulent) $Re_D$

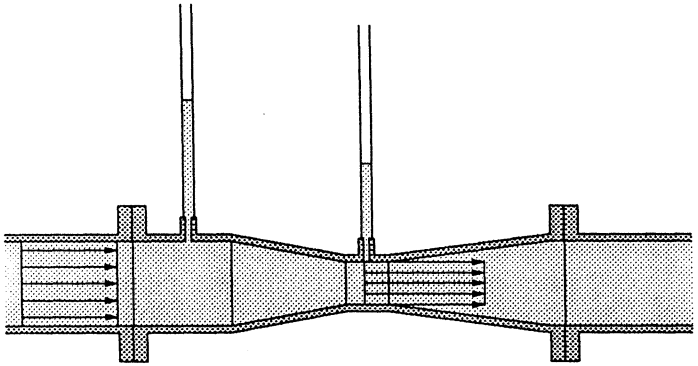

(c) The ideal (flat) velocity profiles

Figure 3.18 A comparison of actual and ideal velocity profiles in a Venturi flow device.

where $\mu$ is the fluid viscosity. In general, the higher the Reynolds number, the flatter the velocity profile, and the better Equations 3.70 and 3.71 approximate the true values of KE and $\dot{m}$ at $A_1$ and $A_2$. Hence, the discharge coefficient generally tends to approach a constant value at high Reynolds numbers. For example, for Classical Venturi Tube (CVT) designs such as those of Figure 3.17a, C remains constant at a value on the order of 0.970–0.995 for Reynolds numbers greater than approximately $2 \times 10^5$ (ASME, 1971). The value of the constant is slightly dependent upon other factors such as line size, beta ratio, and the machining or casting process used to form the convergent (i.e., the roughness or friction factor of the convergent). In general, one wishes to size a Venturi for a given application such that $Re_D$ always falls within the range where C is constant—otherwise, an accurate curve fit relating C to $Re_D$ must be found, and Equation 3.102 must be solved implicitly for $\dot{m}$ because C will then be a function of $\dot{m}$ through its dependence on $Re_D$. In addition, because pipe fittings upstream and downstream of the Venturi can influence the velocity profile of the flow, C is also dependent upon the particular geometry of the piping installation. Installation effects can be minimized by supplying sufficient lengths of straight pipe upstream and downstream of the Venturi to ensure well-developed velocity profiles at the inlet and outlet. Alternatively, the installation effects can be absolved into the value of C by calibrating the Venturi in the exact piping configuration in which it is to be used.

Points (iii) and (iv) are characteristic of orifice plates and alternative Venturi designs and do not generally apply to the designs of classical flow metering devices. For example, Figure 3.17 compares two different CVT designs to analogous designs of Modified Venturi Tubes (MVT's) and VFT's. In the CVT designs, the convergent and throat sections are hydraulically long, and the inlet and throat taps are each located at a significant distance away from the area transitions. As a result, the inlet and throat taps properly sense the static pressures $P_1$ and $P_2$. In comparison, an MVT has the same or similar shape as a CVT, except the inlet pressure tap is located just upstream of the corner formed by the inlet pipe bore and the upstream edge of the convergent. For this configuration, the inlet tap does not sense true static pressure, but instead senses the static pressure plus a portion of the velocity pressure (Halmi, 1972). Thus, $P_1$ (and, hence, $\Delta P$) reads higher on an MVT than on a CVT for the exact same flow rate, so the discharge coefficient of an MVT is correspondingly lower than that of a CVT. The major advantage of the MVT design is that random pressure noise fluctuations naturally present in the tap readings become less significant compared to the amplified magnitude of $\Delta P$, so the overall uncertainty in the mass flow measurement decreases. The VFT designs of Figure 3.17 take the MVT concept one step further by employing a short throat section whose pressure tap is located near the exit of a short and sharp convergent. The end result is a negative Pitot effect (i.e., a small degree of suction) at the throat tap, which causes $P_2$ to read lower on the VFT than on the

MVT or CVT, thereby making $\Delta P$ read even larger for the same flow rate (Halmi, 1972). Because $\Delta P$ is larger for a VFT, the C is correspondingly even lower. In addition, due to the abrupt transition from $A_1$ to $A_2$, the flow area continues to contract a short distance downstream of the exit of the convergent (known as the "vena contracta" effect), so the area of the flow at the location of the throat tap is not truly the measured geometrical area $A_2$, but is somewhat less than $A_2$ (Halmi, 1972). The discharge coefficient of a VFT accounts for this additional real flow effect.

We pause here to note that although alternative Venturi designs are advantageous from the perspective of an amplified $\Delta P$ for a given flow rate, they are disadvantageous in the respect that the value of the discharge coefficient is more sensitive to the presence of inlet and outlet pipe fittings which influence the velocity profile of the flow because the pressure taps are influenced by velocity boundary layer effects. Similarly, the functional relationship between C and $Re_D$ does not follow the same form as that of a CVT due to these inherent boundary layer effects (Halmi, 1972). Hence, the discharge coefficient of an alternative Venturi design is best determined by calibrating the tube in the exact piping configuration in which it is to be used over the appropriate range of $Re_D$ for which it is to be used. Also, when using an alternative Venturi design to meter a compressible fluid, the general relation for the gas expansion factor Y given by Equation 3.89 does not truly apply because MVT's and VFT's do not sense the static pressures $P_1$ and/or $P_2$ needed to evaluate the relation (Halmi, 1972). The true expression for Y for a given alternative Venturi design can only be accurately determined by calibrating the device with a compressible fluid.

#### 3.6.2.3 The Selected Venturi Flow Devices

Because VFT's typically have a lower head loss and a shorter laying length than a CVT or MVT for the same output $\Delta P$, VFT designs have practically eliminated the CVT from common usage (Halmi, 1973) and are widely available at relatively low costs. All of the Venturi devices used in our facility are advertised by the manufacturer (Gerand Engineering Co.) simply as Venturi meters, and it is rather difficult to tell by visual inspection whether or not the sections upstream and downstream of the inlet and throat taps on some of the tubes are hydraulically long (i.e., whether or not the inlet and throat taps sense static pressure). However, quantitative analyses reveal that the discharge coefficients of the Gerand devices are much less that of a CVT over the same range of $Re_D$, thereby identifying each device as an alternative Venturi design, presumably of the VFT variety. Our air-side VFT's were chosen specifically for their low head loss property, ease of availability, and, most decisively, their markedly low cost. The refrigerant-side VFT's were salvaged from a previous research project to further meet budgetary restrictions. The next few sections further describe the tubes and their usage.

Geometrical Parameters

Table 3.9 shows the inlet diameter, throat diameter, and beta ratio of each of the selected VFT's. The table also lists the model number of each VFT and identifies its location in the facility. The salvaged refrigerant-side VFT's have threaded inlets and outlets, and air-side VFT's have flanged inlets and outlets. For the refrigerant-side VFT's, the first part of the model number (i.e., the part preceding the dash) signifies the NPT thread size at the inlet and outlet. For the air-side VFT's, the first part of the model number signifies the nominal inlet diameter $d_1$ in inches. For all of the VFT's, the last three digits of the model number indicate the nominal value of $\beta$ in thousandths. The measured values of $d_1$, $d_2$, and $\beta$ are also given in the table. Each diameter measurement listed in the table is the average of several vernier caliper readings taken in the plane of the inlet or throat pressure tap. However, for each of the refrigerant-side VFT's, the inlet diameter measurements were taken at the inlet of the convergent (i.e., just downstream of the inlet tap) because the inlet tap on each of these tubes is a large, threaded through-hole poorly located in the midst of the threads which mate with the inlet pipe (the through-hole seats a 1/8-NPTM valve fitting whose inner bore serves as the pressure tap hole). Concerning beta ratios, the deviations between the measured and nominal values of $\beta$ are shown in the table. The salvaged 1/2"-230 VFT appears to have been manufactured grossly out of tolerance. However, the discrepancy is unimportant because the tube is to be calibrated in-house. The measured values of $d_1$, $d_2$, and $\beta$ are the values used to reduce our facility data.

Inlet and Outlet Piping

Figures 2.1 and 2.2 show the structures of the air-side VFT piping installations. Each air-side VFT is mounted in a straight run of polyvinyl chloride (PVC) pipe with ANSI flanges rated for 150-$lb_f$ loads. A stiff-rubber gasket was made for each flange to provide a smooth, airtight seal. Care was taken during the installations to ensure that the VFT axes were correctly aligned with the PVC pipe axes, and that the gaskets were aligned flush with the inner edges of the pipes, particularly when compressed. Figure 3.19 shows the structure of the refrigerant-side VFT piping installations. Each refrigerant-side VFT is mounted in a straight run of brass pipe nipples which thread into the inlet and outlet of the VFT. The outer ends of the brass pipes are threaded into compression fittings which allow the VFT assembly to be removed from the loop and calibrated as a unit. The lengths of the inlet and outlet pipes used in the air- and refrigerant-side installations are listed in Table 3.10. The VFT manufacturer specifies that all installations should be made with inlet and outlet pipe lengths of at least 5 $d_1$ and 2 $d_1$, respectively. As is shown in Table 3.10, this requirement is met in each of our installations.

Table 3.9 Comparison of the nominal and measured values of the VFT dimensions and discharge coefficients.

| VFT Model No. | Application | $d_1$ [in.] | $d_2$ [in.] | β | C |
|---|---|---|---|---|---|
| 1/2"-230 | Liquid Line | Nominal: Unknown<br>Measured: 0.7200 | Nominal: Unknown<br>Measured: 0.1890 | Nominal: 0.230<br>Measured: 0.263<br>% Difference: 14.3 | Nominal: 0.888<br>Measured: —<br>% Difference: — |
| 3/4"-414 | Discharge Line | Nominal: Unknown<br>Measured: 0.9167 | Nominal: Unknown<br>Measured: 0.3750 | Nominal: 0.414<br>Measured: 0.409<br>% Difference: –1.2 | Nominal: 0.925<br>Measured: —<br>% Difference: — |
| 3"-623 | Evaporator Air Loop | Nominal: 3.0000<br>Measured: 3.0848 | Nominal: 1.8690<br>Measured: 1.8767 | Nominal: 0.623<br>Measured: 0.608<br>% Difference: –2.4 | Nominal: 0.883<br>Measured: 0.867<br>% Difference: –1.8 |
| 6"-743 | Condenser Air Loop | Nominal: 6.0000<br>Measured: 6.1225 | Nominal: 4.4580<br>Measured: 4.4913 | Nominal: 0.743<br>Measured: 0.734<br>% Difference: –1.2 | Nominal: 0.710<br>Measured: 0.726<br>% Difference: 2.3 |



Table 3.10 The inlet and outlet pipe lengths used in our VFT installations.

| VFT Model No. | Application | Inlet Pipe Length [in.] | Outlet Pipe Length [in.] |
|---|---|---|---|
| 1/2"-230 | Liquid Line | $3\frac{1}{2}$ (4.9 $d_1$) | 2 (2.8 $d_1$) |
| 3/4"-414 | Discharge Line | 5 (5.5 $d_1$) | $2\frac{1}{2}$ (2.7 $d_1$) |
| 3"-623 | Evaporator Air Loop | $43\frac{1}{2}$ (14.1 $d_1$) | 37 (12.0 $d_1$) |
| 6"-743 | Condenser Air Loop | $44\frac{1}{4}$ (7.2 $d_1$) | $22\frac{3}{4}$ (3.7 $d_1$) |

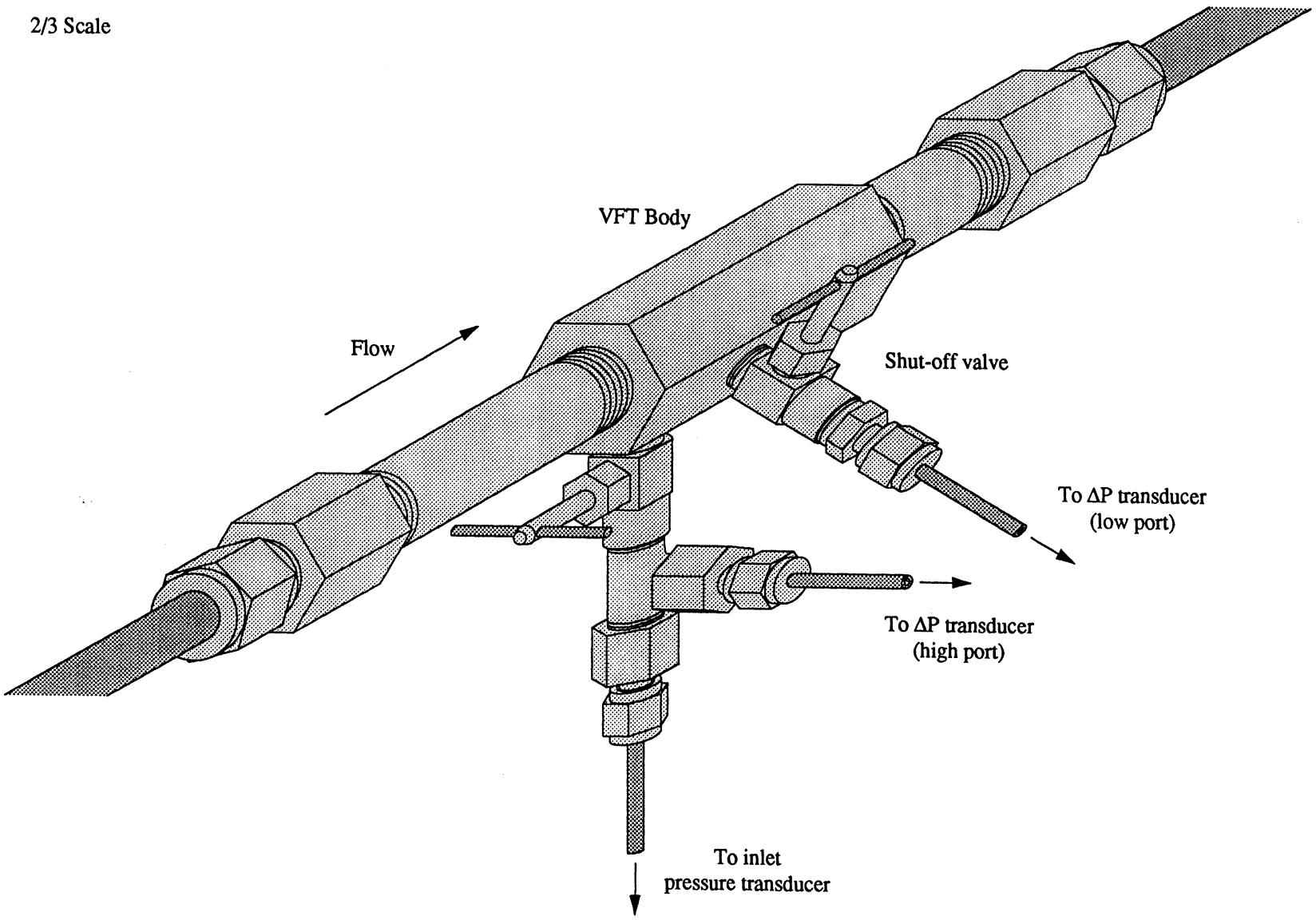


Figure 3.19 The structure of the refrigerant-side VFT assemblies.

Flow Conditions and Discharge Coefficients

Figure 3.20 shows a reproduction of the flow capacity curves provided in the VFT product literature. The curves are for water flow at 70 °F ($\rho_1 = 62.3020\ lb_m/ft^3$) and represent the nominal behavior of each given model number as tested by the manufacturer. The manufacturer claims that stock tubes conform to the given curves to within ± 1 %. The constant slope of each curve implies that each discharge coefficient is constant over the plotted range of flows. The nominal value of each discharge coefficient was calculated by selecting a few coordinate pairs ($\dot{\forall}$, $\Delta P$) from each curve, converting the volumetric flow rates $\dot{\forall}$ to mass flow rates via the relation

$$\dot{m} = \rho_1 \dot{\forall} \tag{3.104}$$

and then evaluating Equation 3.102 for C using the nominal values for $d_1$ and $\beta$ presented in Table 3.9. For the threaded VFT's, the nominal values of $d_1$ were necessarily calculated from the nominal values of $\beta$ and the measured values of $d_2$. The results are shown in Table 3.9. Each C value falls well below the range of C values common to CVT designs, thereby identifying each tube as an alternative Venturi design.

Next, Table 3.11 shows the estimated range of flow conditions ($\dot{m}$, $\rho_1$, and $Re_D$) over which each VFT is expected to be used in our facility. The values of $\Delta P$ corresponding to these flow conditions are also listed in the table. The values were calculated from Equation 3.102 using the nominal values $d_1$, $\beta$, and C. Each VFT is sized such that the $\Delta P$ signal spans the majority of the range of a 0–1 psid pressure transducer (a stock transducer range) while still yielding an acceptable permanent head loss across the VFT over the given range of flows. As is indicated by the right-hand axis of Figure 3.20, the head loss of a Gerand VFT is nominally one-tenth of $\Delta P$. Table 3.12 shows the equivalent flow rates of 70-°F water which reproduce the operating ranges of $Re_D$ given in Table 3.11. For each refrigerant-side VFT, the water flow rate corresponding to the maximum expected value of $Re_D$ greatly exceeds the maximum flow rate plotted in the respective capacity curve of Figure 3.20. Hence, the behavior of C at high $Re_D$ these VFT's cannot be inferred from Figure 3.20 and must be determined through calibration. In addition, the value of C derived from the manufacturer's curve for the 1/2"-230 VFT cannot be used to accurately describe the behavior of our salvaged tube because the $\beta$ of our tube is out of specification. Also, as was previously mentioned, a VFT should be calibrated in the specific piping section in which it is to be used because VFT's are much more sensitive to installation effects than classical flow devices. For the above reasons, and as a check on the accuracy claimed by the manufacturer, it was desired to calibrate each of the VFT's in-house.

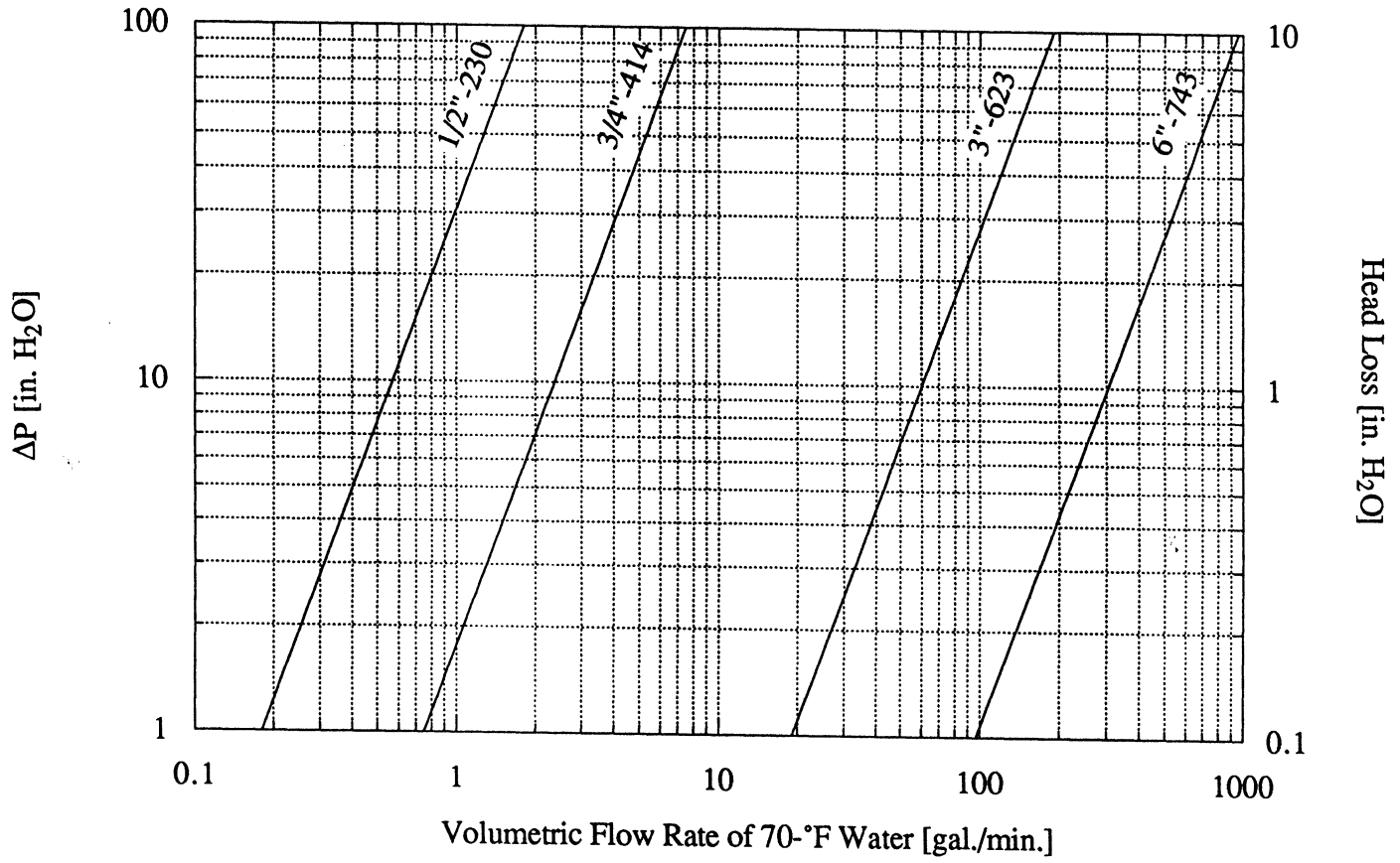


Figure 3.20 A reproduction of the flow capacity curves provided in the Gerand VFT product literature.

Table 3.11 Summary of the flow conditions used to size each VFT.

| VFT Model No. | Application | Expected Operating Conditions | | | |
|---|---|---|---|---|---|
| | | $\dot{m}$ [$lb_m/hr$] | $\rho_1$ [$lb_m/ft^3$] for the Given $\dot{m}$ | $Re_D$ | $\Delta P$ [psid] |
| 1/2"-230 | Liquid Line | Min: 80 | 75.5711 (120 psia, 15 °F subcool) | $2.46 \times 10^3$ | 0.0235 |
| | | Max: 500 | 66.8989 (240 psia, 5 °F subcool) | $2.23 \times 10^4$ | 1.0364 |
| 3/4"-414 | Discharge Line | Min: 80 | 1.9232 (120 psia, 100 °F superheat) | $3.82 \times 10^4$ | 0.0532 |
| | | Max: 500 | 4.5038 (240 psia, 40 °F superheat) | $2.35 \times 10^5$ | 0.8915 |
| 3"-623 | Evaporator Air Loop | Min: 180 | 0.0750 ($\dot{V}$ = 40 scfm) | $2.08 \times 10^4$ | 0.0108 |
| | | Max: 1440 | 0.0750 ($\dot{V}$ = 320 scfm) | $1.66 \times 10^5$ | 0.7395 |
| 6"-743 | Condenser Air Loop | Min: 1800 | 0.0750 ($\dot{V}$ = 400 scfm) | $1.04 \times 10^5$ | 0.0424 |
| | | Max: 8100 | 0.0750 ($\dot{V}$ = 1800 scfm) | $4.67 \times 10^5$ | 0.9560 |



Table 3.12 Equivalent flow rates of 70-°F water which reproduce the range of $Re_D$ each VFT sees in our facility.

| VFT Model No. | Application | 70-°F Water Flow Condtions which Match $Re_D$ | | | |
|---|---|---|---|---|---|
| | | $Re_D$ | $\dot{m}$ [$lb_m/s$] | $\dot{V}$ [gal./min.] | $\Delta P$ [psid] |
| 1/2"-230 | Liquid Line | Min: $2.46 \times 10^3$ | 0.087 | 0.63 | 0.4358 |
| | | Max: $2.23 \times 10^4$ | 0.786 | 5.67 | 35.7703 |
| 3/4"-414 | Discharge Line | Min: $3.82 \times 10^4$ | 1.485 | 10.70 | 7.3636 |
| | | Max: $2.35 \times 10^5$ | 9.123 | 65.72 | 277.9658 |
| 3"-623 | Evaporator Air Loop | Min: $2.08 \times 10^4$ | 2.669 | 19.23 | 0.0370 |
| | | Max: $1.66 \times 10^5$ | 21.353 | 153.83 | 2.3702 |
| 6"-743 | Condenser Air Loop | Min: $1.04 \times 10^5$ | 26.691 | 192.29 | 0.1449 |
| | | Max: $4.67 \times 10^5$ | 120.111 | 865.30 | 2.9333 |

### 3.6.2.4 VFT Calibrations

A VFT calibration is performed by passing fluid through the device over the operating range of $Re_D$ and collecting and weighing the discharge flow over a known time interval so as to determine the actual mass flow rate $\dot{m}$. All other parameters necessary to evaluate $\dot{m}_{theo}$ (namely, $\rho_1$ and $\Delta P$) are simultaneously recorded during the calibration process so that C or Y can be calculated from Equation 3.102 for each trial $Re_D$. Because the nature of C is theoretically independent of the fluid type (i.e., whether the fluid is compressible or incompressible), standard practice dictates that a VFT should first be calibrated with an incompressible fluid having well-known properties (such as water) so as to eliminate the effects of the gas expansion factor Y and allow the researcher to directly compute the value of C (Halmi, 1974). Once the value of C is known, a second calibration is performed with a compressible fluid to determine the true relation for Y (recall that Equation 3.89 does not truly apply to alternative Venturi designs). A compressible calibration involves more difficult experimental methods, such as passing superheated steam through the VFT and then condensing and weighing the discharge flow, or passing air (or a similar gas having well-known properties) through the tube and measuring the flow with another device known to be accurate.

The major obstacle of any VFT calibration is the availability of accurate equipment and an adequate source of steady fluid flow. For example, Table 3.12 shows the nominal values of $\Delta P$ which correspond to the flow rates of 70-°F water which reproduce our operating ranges of $Re_D$. For the 1/2"-230 VFT, the maximum flow rate of water shown in the table is obtainable from our laboratory wall faucet at a similar temperature, but the maximum $\Delta P$ exceeds the limits of available manometers and differential pressure transducers. For the 3/4"-414 VFT, both the maximum $\Delta P$ and the maximum flow rate are unrealizable in the lab. If a 200-°F water flow were used instead, more reasonable values result ($\Delta P$ = 27.7 psid with $\dot{V}$ = 21.2 gal./min.), but the design and construction of a suitable heated-flow calibration system would be a significant project in itself. Thus, as an alternative to water calibrations, we installed the highly accurate Micro Motion flow meter in the refrigerant loop to allow us to directly calibrate the liquid- and discharge-line VFT's in their exact piping configurations with the working fluid. The Micro Motion transmitter unit displays a direct and accurate ($\pm$ 0.2 $lb_m/ft^3$) reading of the density of the refrigerant/oil mixture in addition to the mass flow rate, thereby providing an alternative to the possibly more erroneous process of using pressure measurements, temperature measurements, and pure-refrigerant property routines to obtain the density data. Unfortunately, the differential pressure transducers presently installed on the refrigerant-side VFT's are unreliable and have likely suffered damage, so the calibrations have been postponed pending repair or replacement of the sensors.

Incompressible Calibration of the Gerand 3"-623 VFT

To incompressibly calibrate the Gerand Model No. 3"-623 VFT used in our evaporator air loop, we constructed a suitable PVC piping run at Newmark Hydraulic Laboratory here at the University of Illinois. The setup is shown in Figure 3.21. A large storage tank atop a tower outside of Newmark Lab supplied water at a constant, steady pressure upstream of the control valve shown in the figure. A serpentine piping arrangement (not shown) maneuvered the flow around obstructions and reduced the supply piping to our 3-in. I.D. line size. A long inlet section (as opposed to the exact inlet pipe length used in our facility) was provided upstream of the VFT to ensure a well-developed flow after the serpentine arrangement. A vertical head pipe was provided downstream of the VFT to elevate the discharge flow above the level of the control valve so as to ensure that the entire system was back-pressured and completely filled with water. Without the head pipe in place, the water level in the serpentine piping tended to fluctuate and destroy the smooth, steady flow established by the gravity feed tower. An additional open-ended pipe was installed on a tee at the exit of the head pipe to prevent siphoning effects from causing instabilities at low flow rates. We capped the anti-siphon pipe at higher flow rates.

Concerning instrumentation, a 100-in. manometer filled with a gage fluid having a specific gravity of 1.75 at 68 °F was used to measure $\Delta P$. The manometer lines were bled to expel all air bubbles, and care was taken in the VFT installation to ensure that the inlet and throat taps were in the same horizontal plane so that the manometer correctly indicated the $\Delta P$ due solely to energy changes in the VFT. The equation for converting the manometer reading to $\Delta P$ is derived and explained in Weston (1996). A mercury-in-glass thermometer was used to measure the water temperature during each test, and the corresponding density $\rho_1$ was calculated from the EES function call of Equation 3.56. A 32-gal. trash container and a tared balance-arm scale were used to collect and weigh the discharge flow. A 55-gal. drum was used at higher flow rates to allow a longer collection time. Like the manometer readings, the weight measurements were referenced to standard gravity by multiplying the raw scale readings by the inverse of the gravity ratio of Equation 3.53. A digital stopwatch was used to time each collection process. Several collections were taken for each flow rate, and the corresponding value of C for each trial was calculated from Equation 3.102 using the measured values of $d_1$ and $\beta$ given in Table 3.9. The calibration data are given in Weston (1996).

Figure 3.22 shows the resulting plot of C versus $Re_D$. The discharge coefficient is seen to be reasonably constant at an average value of $C = 0.867 \pm 0.014$ with 95 % confidence. The latter uncertainty interval was calculated as $\pm 2\sigma$, where $\sigma$ is the standard deviation of the mean. The measured value of C deviates from the nominal value by 1.8 % as is shown in Table 3.9. However, if the nominal value of C is taken to have an accuracy of $\pm$ 1 % (the rated accuracy of

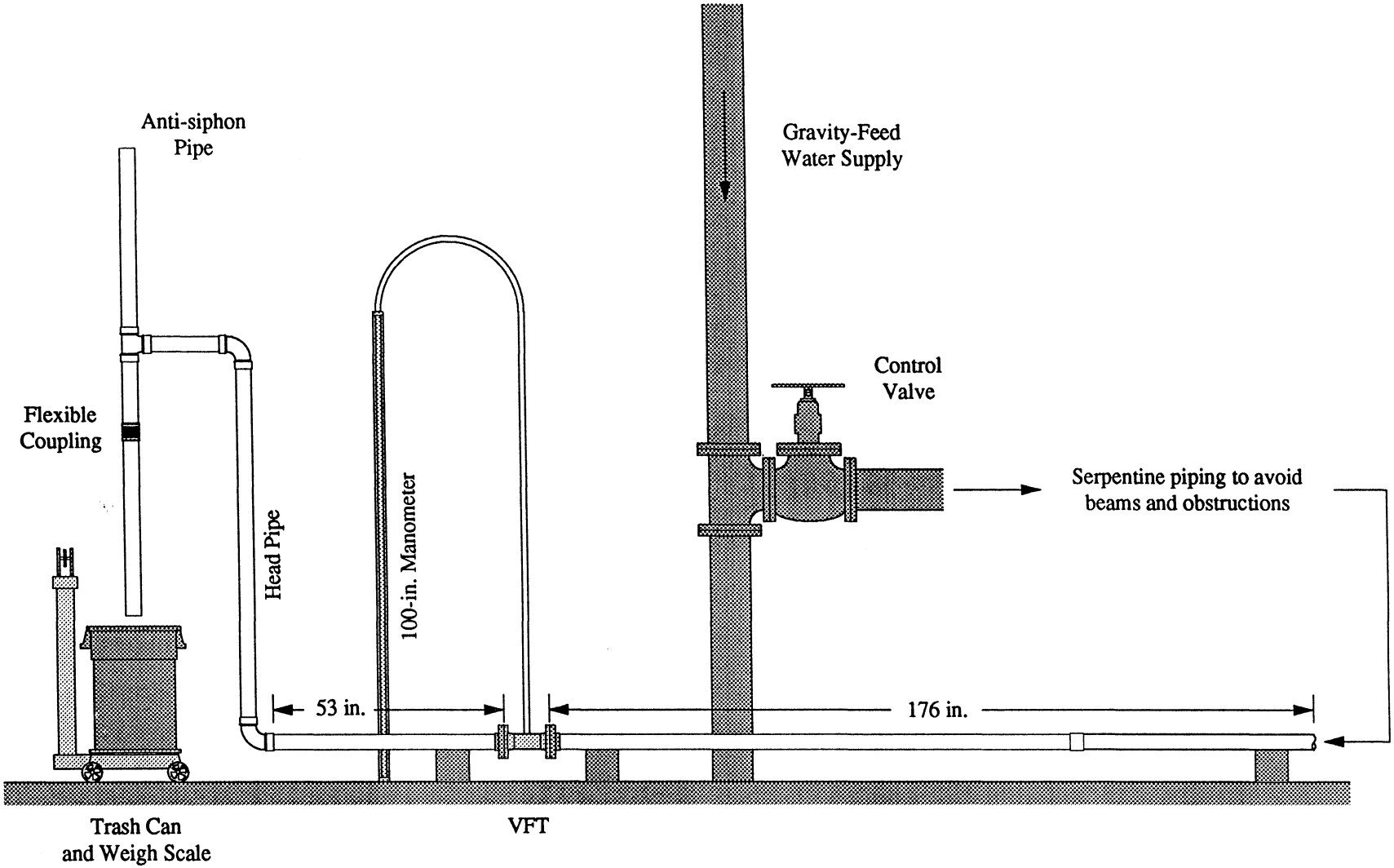


Figure 3.21 The setup used to calibrate the 3"-623 VFT.

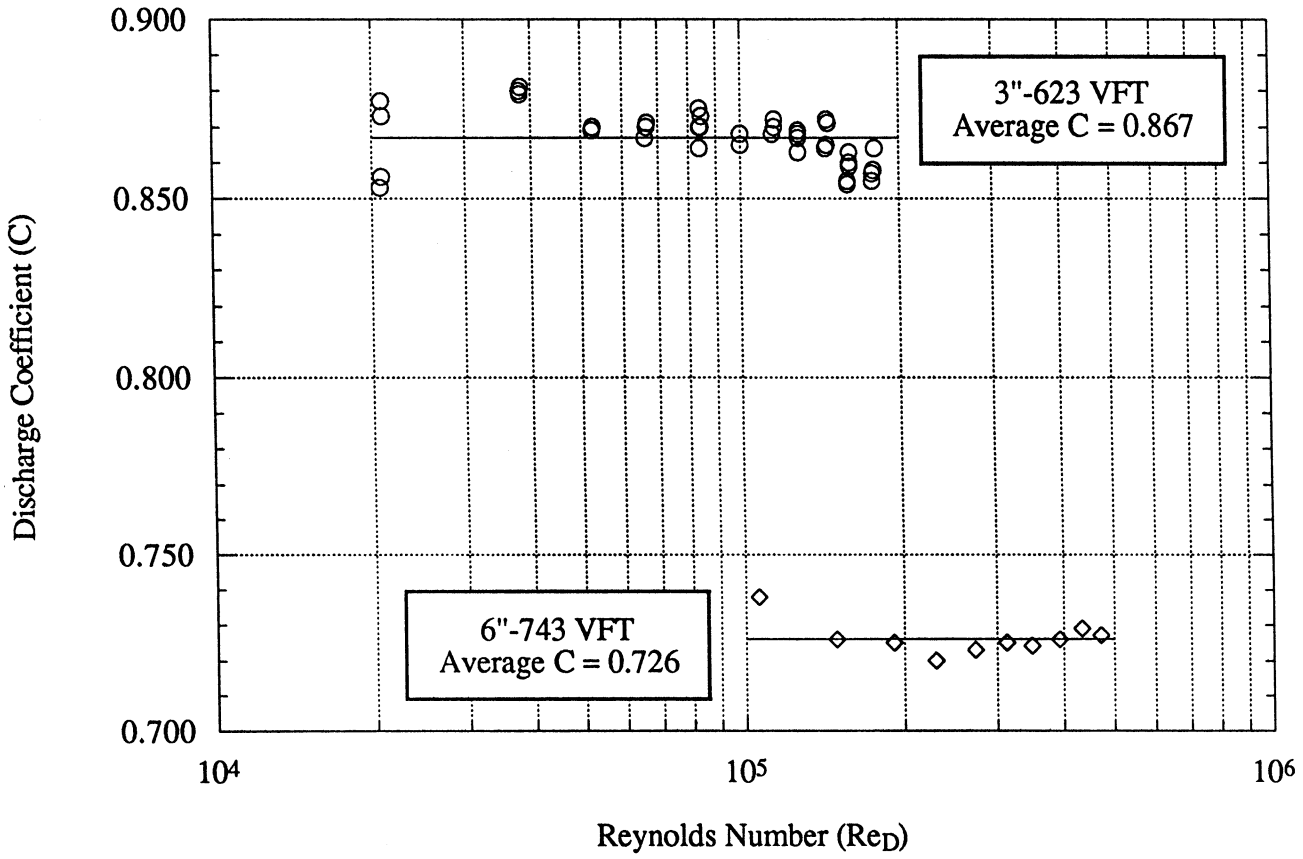


Figure 3.22 The resulting plots of C versus $Re_D$ for the air-side VFT calibration data.

the curves of Figure 3.20), then the two values can be said to agree within the stated uncertainties. The measured value of C is the value used to reduce our facility data.

Incompressible Calibration of the Gerand 6"-743 VFT

To incompressibly calibrate the Gerand Model No. 6"-743 VFT used in our condenser air loop, the 3"-623 calibration arrangement was dismantled and replaced with the similar piping arrangement shown in Figure 3.23. Because the larger diameter inlet pipe of the 6"-743 VFT setup was spatially constrained to be approximately the same length as in the 3"-623 calibration but was to carry much higher flow rates, a tube-bundle flow straightener was soldered from approximately fifty 8-in. lengths of 3/4-in. O.D. (21/32-in. I.D.) copper pipe and affixed in the inlet pipe to assist in conditioning the flow after the serpentine arrangement (Laws, 1993). Also, the 3-in. I.D. exit pipes used in the 3"-623 calibration were replaced with 4-in. I.D. pipes to reduce momentum forces and head losses in the piping system so that higher flow rates could be obtained. The 100-in. manometer was again used to measure $\Delta P$, and the VFT was again installed with the inlet and throat taps in a horizontal plane. The discharge flow was collected in a large storage tank (15 ft x 15 ft x 30 ft) equipped with a mercury manometer which indicates the pressure near the bottom of the tank. The latter manometer reading is converted to the weight of water in the tank by a calibration equation established by the University of Illinois Civil Engineering department. The calibration data and the associated data reduction equations are given in Weston (1996). Figure 3.22 shows the resulting plot of C versus $Re_D$. The discharge coefficient is seen to be reasonably constant at an average value of $C = 0.726 \pm 0.010$ with 95 % confidence. The latter value deviates from the nominal value by 2.3 % as is shown in Table 3.9, but the two values again agree within the respective uncertainties. The measured value of C is the value used to reduce our facility data.

Compressible Calibrations

Equipment was not available to perform compressible calibrations of the air-side VFT's and the discharge-line VFT, so the determination of proper functions for Y for these tubes is left for future work. The classical relation of Equation 3.89 is used to approximate Y pending such calibrations. Recall that Equation 3.89 does not truly apply to a VFT because the pressure taps of a VFT do not sense static pressure. No compressible calibration data are given by the VFT manufacturer, so no basis of comparison exists to determine how well Equation 3.89 represents the expansion factor of each VFT. Strictly speaking, calculations of the inlet density of a compressible fluid will also be slightly in error if $\rho_1$ is computed from the nonstatic measurement of $P_1$. For example, consider the case of the maximum air flow rate of shown in Table 3.11 for the 6"-743 VFT ($\dot{m} = 8100$ $lb_m/hr$) for which the expected value of $\Delta P$ is 0.9560 psid (i.e.,

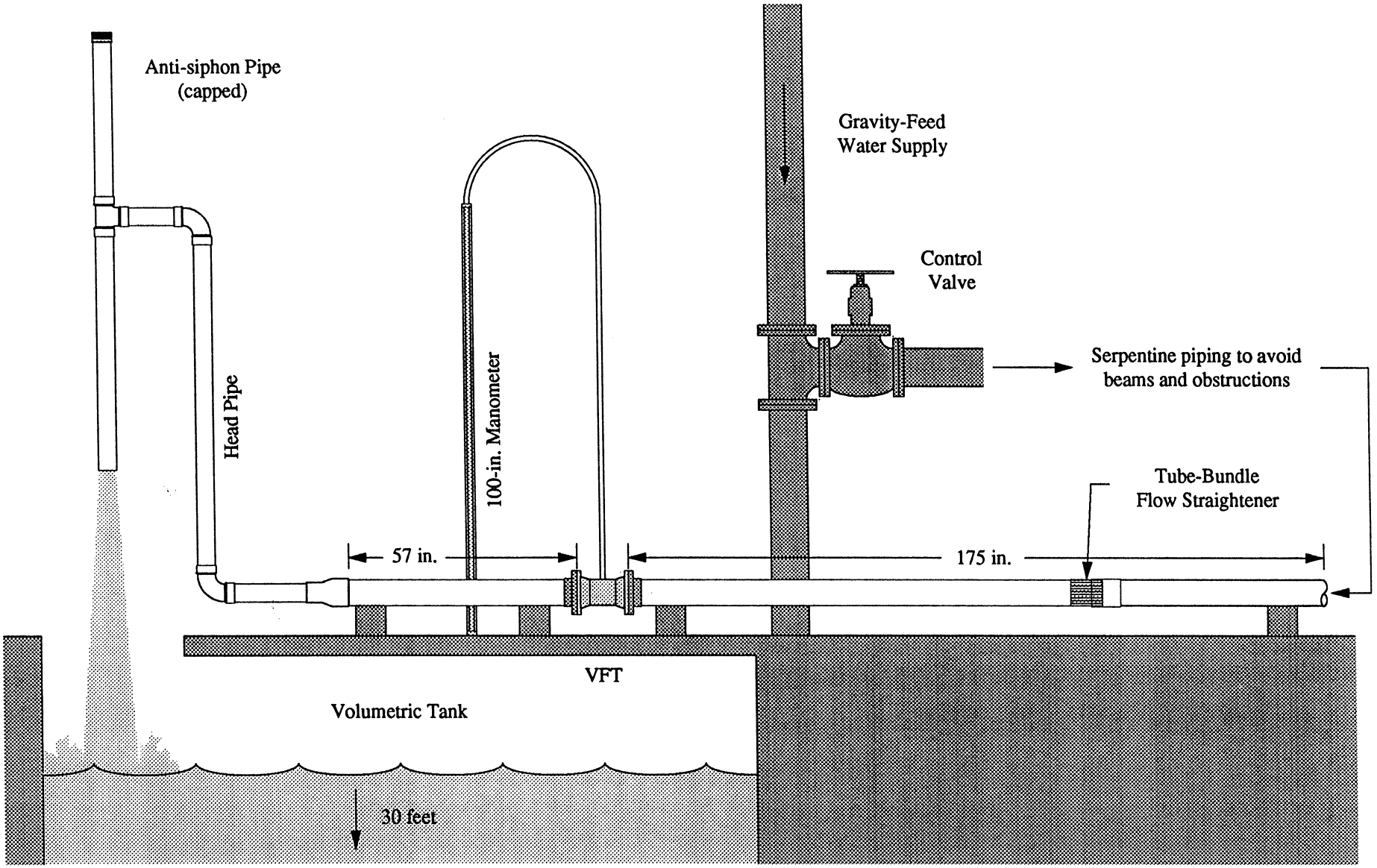


Figure 3.23 The setup used to calibrate the 6"-743 VFT.

assuming the classical value of Y applies). Under the exact same flow conditions, a CVT having the same nominal $d_1$ and $\beta$ will produce a $\Delta P$ of 0.4691 psid given a discharge coefficient of 0.985 (a typical value for a CVT). Hence, the nonstatic taps of the VFT sense approximately (0.9560 – 0.4691) = 0.4869 psid of velocity pressure. If, say, one-third of this velocity pressure is sensed at the inlet tap where the true static pressure of the air stream is, say, 14.7 psia, then the pressure $P_1$ will read 14.86 psia on the VFT, resulting in a calculated value of $\rho_1$ which is 1.10 % in error, and a calculated value of $\dot{m}$ which is 0.55 % in error. Hence, it may be advantageous to provide separate, static pressure taps upstream of each of our gas-metering VFT's in the future to obtain better inlet density measurements.

#### 3.6.2.5 $\Delta P$ Signal Conditioning

As was discussed earlier, each VFT used in our facility is sized to produce a 0–1 psid differential pressure signal over the operating range of flows. Because the $\Delta P$ signals span such a small range, the measurements are sensitive to the effects of pressure noise. For example, the $\Delta P$ signals of the air-side VFT's normally appear excessively noisy at high air flow rates due to turbulent pressure fluctuations in the lines. As is shown in Figure 3.16, we installed turbulence dampers in the tubes connecting the VFT pressure taps to the $\Delta P$ transducers to dampen this unwanted measurement noise. Each damper is a 1-in. long plug of tightly rolled Kleenex® facial tissue which is packed snugly into the pressure transmission line. The dampers dramatically reduce the turbulent noise fluctuations in the $\Delta P$ signals and cause no significant shift in the average value of the signal for any given blower speed. Also, when ramping from one blower speed to another, the dampers cause no noticeable delay in the response time of the measurements.

Concerning the refrigerant-side VFT's, we monitored the output signal of the $\Delta P$ transducer of the discharge-line VFT in real time with a dynamic signal analyzer (Hewlett Packard Model No. 3562A), and the analysis showed a significant spike in the power spectrum of the signal at a frequency which varied with the compressor speed. For example, the spike was present at a signal frequency of 87.9 Hz for a compressor drive motor speed of 1760 rpm, and at a frequency of 805 Hz for a compressor drive motor speed of 3552 rpm. The high-frequency components of the $\Delta P$ signal are thought to be the result of acoustic pulsations which develop in the discharge line due to the piston-pumping action of the compressor. Because the DAS sampling rate is relatively low (1 Hz or slower for tests conducted to date), the pulsations become aliased into the measured data and cause the $\Delta P$ signal to appear excessively noisy. For future tests, mufflers should be installed at the inlet and outlet of the compressor to reduce or eliminate the pulsations at the source. Alternatively, low-pass filters with stable DC gains of 0 dB can be installed across the outputs of the $\Delta P$ transducers of the refrigerant-side VFT's to prevent the high-frequency

pressure pulsations from being aliased into the data. A more rigorous investigation is needed to determine the required filter cutoff frequency. Unfortunately, a low-pass filter will also remove any high-frequency dynamics which naturally occur in a transient response. Hence, each filter should be equipped with a bypass switch so that the researcher can easily exclude the filter from the circuit and measure the natural dynamic response.

## 3.7 Control Devices and Circuits

### 3.7.1 AC Motor Speed Controllers

AC motor speed controllers are used to regulate the speeds of the compressor drive motor, the evaporator-side blower, and the condenser-side blower. Table 3.13 shows the make, model, and output rating of each controller. The power ratings are sized to match the horsepower ratings listed on the motor nameplates. The blower motors are regulated by Toshiba drives which were purchased new, whereas the compressor drive motor is regulated by a PoWrMaster drive which was salvaged from a previous research project. Weston (1996) contains brief instructions on how to manually operate each drive. The reader is referred to the individual controller manuals for detailed operating instructions and descriptions of the controller parameters and features. The basic attributes of our controller applications are further discussed below.

Table 3.13 Summary of the AC motor speed controller specifications.

| Motor Application | Speed Controller Specifications | | |
|---|---|---|---|
| | Make and Model | Power Rating [hp] | Max. Output Current [A] |
| Evaporator Air Loop Blower | Toshiba VFSX-2007P | 1.0 | 5.0 |
| Condenser Air Loop Blower | Toshiba VFSX-2037P | 5.0 | 16.5 |
| Compressor Drive Motor | PoWrMaster CIMR-7.5G2-E-10 | 7.5 | 36.0 |

#### 3.7.1.1 Basic Principle of Operation

In general, depending upon the number of poles of the motor, the magnetic field generated by the stator windings of a synchronous AC motor makes one revolution or a whole fraction (1/2, 1/3, 1/4, etc.) of a revolution for each cycle of line frequency. The rotor of the motor attempts to turn at the same speed as the magnetic field (the synchronous speed) but actually turns at a slightly slower rate (the rated speed) due to slip imposed by the mechanical load on the motor. Each of our motors has a synchronous speed of 3600 rpm and a rated speed of 3450 rpm for a base AC line frequency of 60 Hz. A speed controller varies the speed of the motor by changing

the AC line frequency supplied to the motor (e.g., at a line frequency of 30 Hz, the motor runs at half speed). Hence, a speed controller is not a controller in the true sense of the word because it does not regulate the motor speed in a closed-loop fashion based upon a feedback variable. Rather, a speed controller is more of an actuator which converts the basic 60-Hz power line frequency into some other motor input frequency, although many speed controllers can be equipped with a tachometer feedback option if desired (ours are not). All of our speed controllers operate on the principle of pulse width modulation (PWM). In the PWM scheme, the sinusoidal 60-Hz building supply voltage applied across the controller inputs is first converted to a rectified DC signal. The DC signal is then inverted back into an AC signal comprised of a repeating series of positive and negative voltage pulses of varying widths. The repeating pulse pattern emulates the desired sinusoidal motor input frequency. Speed controllers which operate on this PWM principle are also commonly referred to as "inverters."

To ensure optimal motor performance, a speed controller must also vary the magnitude of the motor input voltage in proportion to the frequency. Standard motors are rated for use at a specific line voltage (230 VAC at 60 Hz for our motors) which ensures that the motor delivers the proper torque at the rated speed. If the voltage is not reduced when the frequency is reduced, then the motor will heat excessively and waste energy. If the voltage is reduced too much, then the motor will not deliver the required torque. The required relationship between the voltage and frequency signals is determined by the load type. For a centrifugal blower, the torque load on the drive motor is proportional to the square of the speed. Hence, each of our blower speed controllers is configured to operate in a "$V/Hz^2$" mode in which voltage is supplied to the motor in proportion to the square of the operating frequency. The compressor drive is also configured to operate in the "$V/Hz^2$" mode.

#### 3.7.1.2 Wiring Configurations

Figure 3.24 shows the wiring connections of the Toshiba speed controllers, and Figure 3.25 shows the wiring connections of the PoWrMaster speed controller. As is shown in the figures, each controller is able to accept a 4–20 mA, 0–5 VDC, or 0–10 VDC remote setpoint signal from a command device such as a potentiometer, a common benchtop function generator, or an analog output of our facility's environment controller. These remote setpoint options allow us to vary the motor speeds in repeatable, transient patterns which simulate changes in vehicle operating conditions, such as the changes in condenser air flow rate and compressor speed which occur as a vehicle is being driven. Figure 3.24 also shows that we installed noise filters in series with the input and output power lines of the Toshiba controllers to attenuate the high-frequency (MHz) noise these controllers introduce to the lab environment via the generation of the PWM waveforms and associated carrier frequencies. Noise filters have not yet been installed on the

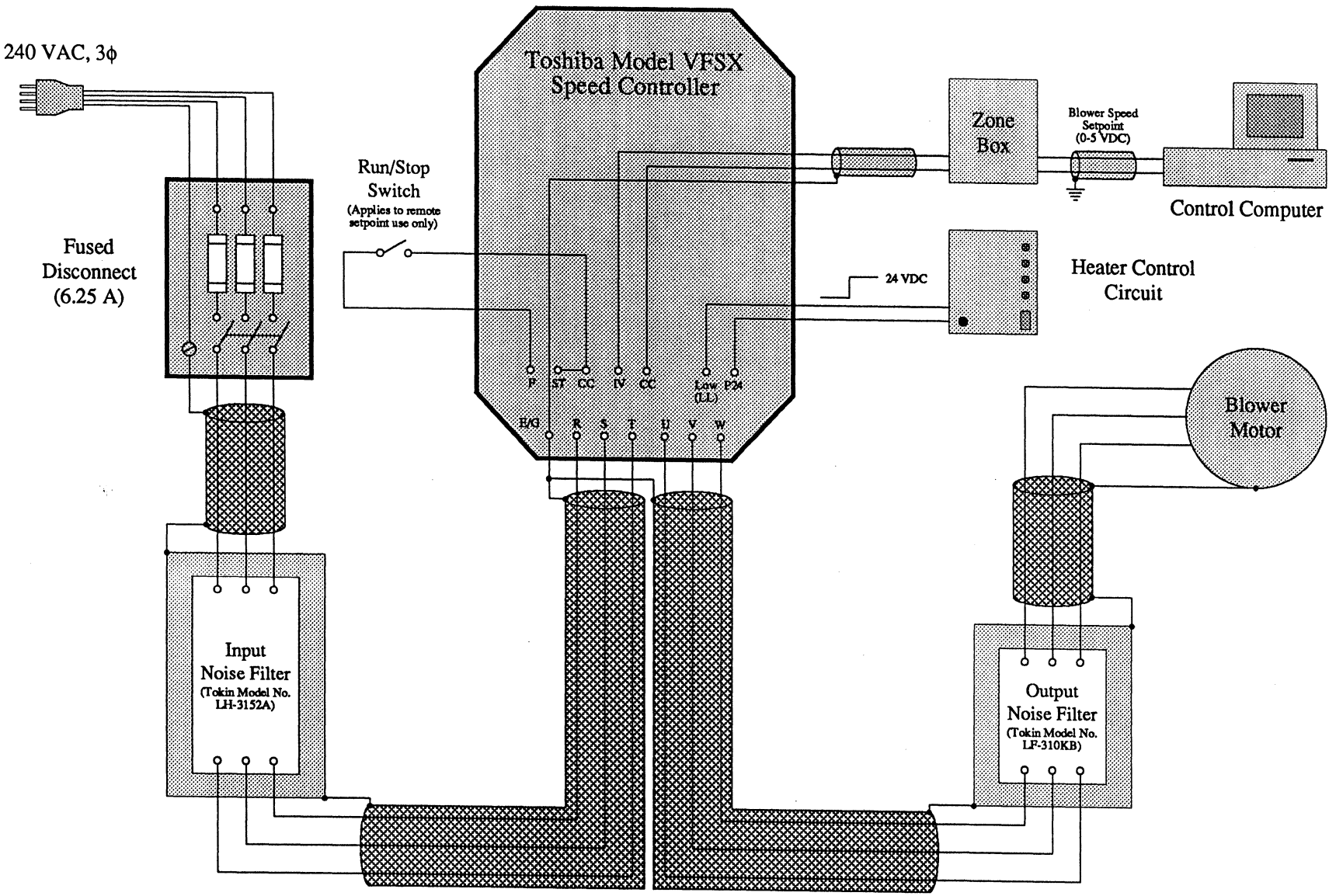


Figure 3.24 The wiring connections of the Toshiba speed controllers (evaporator side shown).

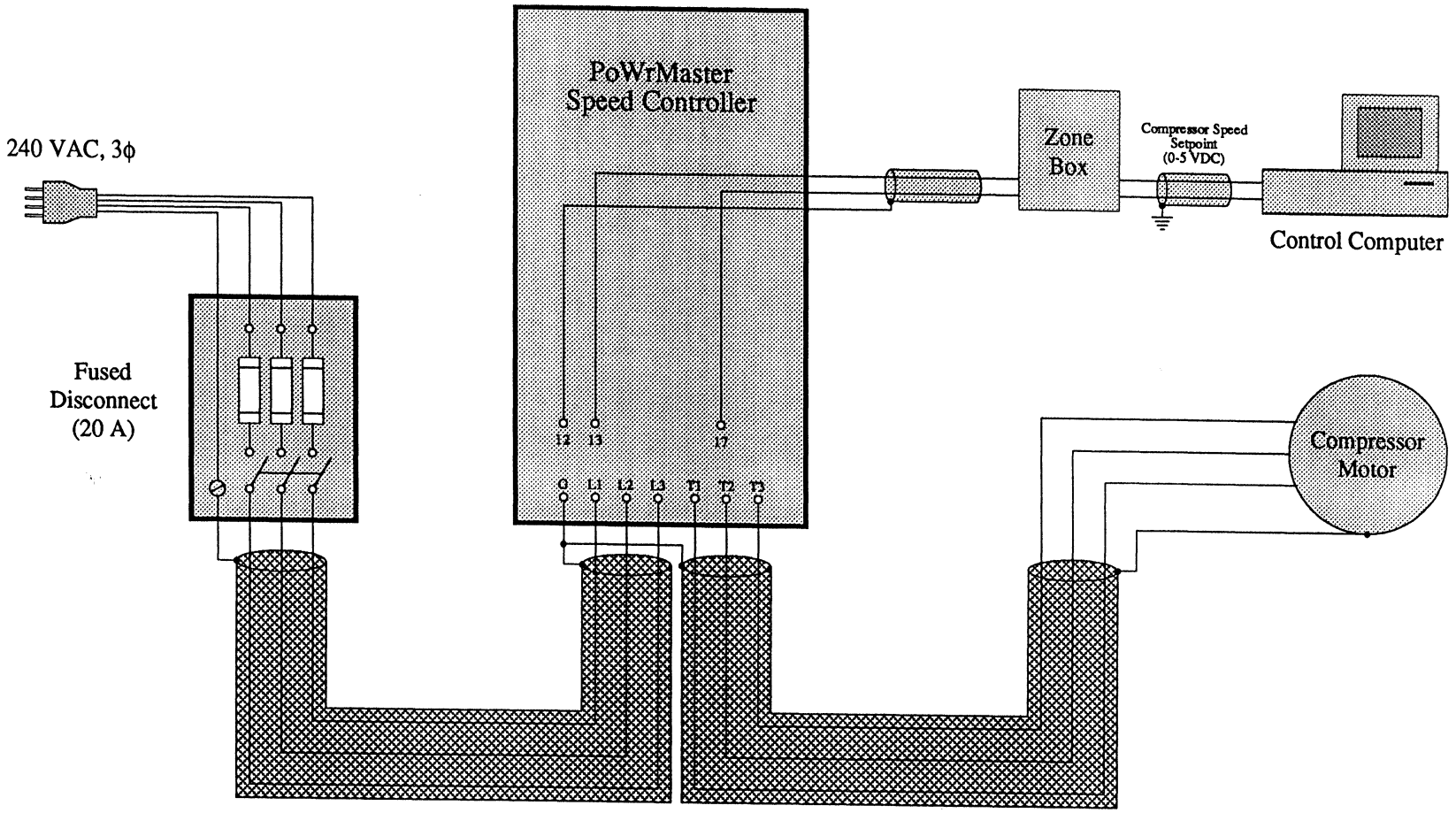


Figure 3.25 The wiring connections of the PoWrMaster compressor speed controller.

PoWrMaster unit. To further shield the lab environment from drive noise, we encased each power cord in a braided tinned-copper sheath as is shown Figures 3.24 and 3.25. The braiding is actually used in place of the earth ground wire located within each power cord because the 3-phase power leads within each cord strongly couple the drive noise into the ground wire due to the fact that the ground wire is twisted in with these other leads. The ground noise caused severe interference with an initial design of our oil concentration sensor because the ultrasonic transducers of the sensor are earth-grounded via contact with the refrigerant pipes, and the transducer regulator circuit amplifies electrical signals in the MHz range. Subsequent improvements to the regulator circuit and the use of braided sheaths in place of the power cord ground wires corrected the problem.

### 3.7.2 Heater Control Circuit

#### 3.7.2.1 Basic Principle of Operation

The evaporator inlet air temperature is controlled by proportioning the amount of time the evaporator-side heater remains ON or OFF throughout a fixed cycle period. By choosing the cycle period to be sufficiently short, temperature oscillations induced by the intermittent heating action are made negligibly small, and a smooth response is achieved. We use a PID process controller (CAPP/USA Model No. 535-44120B0S01) to perform the ON/OFF proportioning action. The cycle period is adequately set at 1 s in the controller menus. The controller calculates an appropriate ON/OFF time ratio based upon the difference between the measured and desired values of the evaporator inlet air temperature. The desired value (i.e., the setpoint) can be entered either manually via the controller's keypad or remotely via a 4–20 mA or 0–5 VDC input signal. The measured value (i.e., the feedback value or process input value) is sensed by a Type-T thermocouple junction wired directly to the controller. The controller is factory-equipped with the circuitry and software needed to process the junction temperature. The junction protrudes from the end of the brass support tube which inserts into the ports of the measurement section duct at the inlet of the evaporator. The junction wired to the PID controller is separate from the one wired to the DAS, although the two share the same probe tube and sense the evaporator inlet air temperature at the same location. Basic instructions for operating the controller and the heater are given in Weston (1996). The reader is referred to the controller manual for detailed discussions of the controller's functions and features.

#### 3.7.2.2 Power and Control Wiring

Figure 3.26 shows a schematic of the heater power/control circuit. The heater consists of three stages of resistive wire heating elements which are powered by a 240-VAC, 3-phase

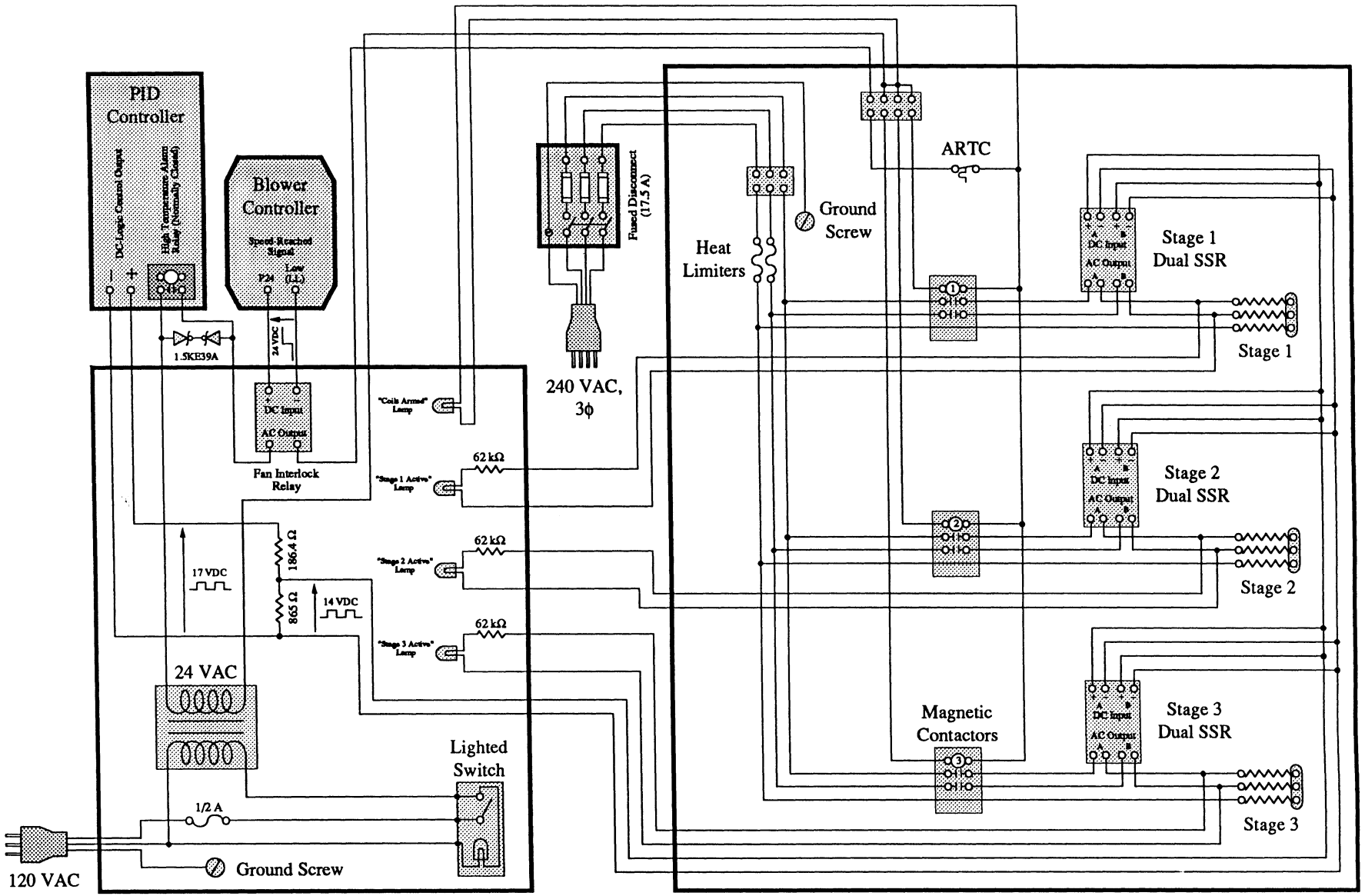


Figure 3.26 The heater power/control circuit.

supply. The elements dissipate a total of 7 kW of power. Each stage is factory-wired in a 3-phase wye configuration. The stages are turned ON or OFF by making or breaking the power line connections at two of the three legs of each wye. Accordingly, the heater is factory-equipped with three magnetic contactors (one contactor per stage), each of which switches two of the three legs of its assigned wye. However, because magnetic contactors are not meant to be extensively cycled over short time periods, we spliced a dual solid-state relay (SSR) package (Crydom Model No. D2425D) between each contactor and wye to perform the switching action. Each relay package contains two independent SSR's which are zero-switching for RFI suppression. That is, each SSR switches its power line ON or OFF only when the AC waveform crosses zero; otherwise, the nonzero voltage and current signals would suddenly collapse and generate electromagnetic noise fields. Each SSR is normally open in style and closes whenever a 4–15 VDC signal is applied across its input terminals. The SSR's are driven by a 17-VDC logic output of the PID controller. As is shown in Figure 3.26, we installed a simple voltage divider across the output of the controller to reduce the magnitude of the logic signal from 17 VDC to 14 VDC in order to stay within the 15-VDC control voltage limit of the SSR's. For diagnostic purposes, we also wired three 125-V, 1/3-W neon lamps across the switched legs of the stages (one lamp per stage) to provide a visual indication of the SSR switching action. The lamps illuminate whenever the 240-VAC supply voltage is applied across the two switched legs of each wye. Three 62-kΩ, 1/2-W resistors are wired in series with the lamps to limit the currents and voltages through the lamps.

#### 3.7.2.3 Safety Devices

Although not used to perform the ON/OFF control action, the three factory-supplied magnetic contactors were left in place to act as safety devices which disconnect the 240-VAC power lines from the three stages of control relays and heater coils whenever a fault condition occurs. The contactors are normally open in style and close whenever their input coils are energized with a 24-VAC signal. We generate the 24-VAC arming voltage with a 40-VA transformer (McMaster-Carr Stock No. 7708K74) whose "hot" 120-VAC input lead is routed through a 1/2-A fuse and a single-pole single-throw lighted rocker switch which cuts off the input power to the transformer. We also wired a 24-V indicator lamp in the arming circuit to indicate the state of the contactors. The lamp illuminates whenever the 24-VAC arming voltage is applied across the contactor inputs, thereby implying that the contactors are closed and that the heater is ready for operation. If any one of three safety devices wired in series in the arming circuit is tripped, the indicator lamp extinguishes, and the contactors open to disconnect the 240-VAC power lines from the control relays and heater coils. The next few sections discuss the safety devices.

Automatic Reset Thermal Cutout (ARTC)

The first safety device is a factory-wired Automatic Reset Thermal Cutout (ARTC) switch which helps prevent heater-coil burnout. The thermal sensing element of the ARTC protrudes approximately 3/4 in. into the duct, as this is where the coils typically run the hottest. The ARTC is normally closed in style and opens whenever the temperature of the sensing element exceeds 125 °F. The switch resets to the closed position when the temperature falls back below 85 °F. Unfortunately, in our installation, the ARTC undesirably trips when attempting to obtain evaporator inlet air temperatures of approximately 90 °F or greater for air flow rates of approximately 125 cfm or less. Temperature settings of up to approximately 110 °F can be sustained for air flow rates of approximately 220 cfm or greater, but this still falls below the desired maximum evaporator inlet air temperature of 120 °F. The fault conditions are the result of an underdeveloped velocity profile at the heater inlet. As is shown in Figure 2.1, our heater is installed at a location where the air stream abruptly expands from the face area of the evaporator to the full size of the tunnel duct. Due to the spatial constraints of our lab, we could not locate heater far enough downstream of the evaporator to allow a fully developed flow at the heater inlet. In addition, the fine-mesh screen mounted across the exit of the evaporator section further prevents the flow from abruptly expanding to the size of the heater. Hence, the velocity of the air stream is particularly low near the walls of the heater in our application, thereby causing the heating elements near the walls run much hotter than those in the center of the duct. For future tests, it is recommended that the evaporator outlet screen be made larger and moved further downstream of the evaporator, thereby allowing the flow to fill the entire duct area before entering the heater. Ultimately, the heater may have to be replaced with one which has a greater number of stages and longer heating elements which have less resistance per unit length (i.e., elements which dissipate less wattage per unit area at any given part of the coil surface) so that the coils do not overheat under low-flow conditions.

High Temperature Alarm Relay

The second safety device is a normally closed mechanical relay located within the PID controller. The relay opens and disarms the heater whenever the evaporator inlet air temperature exceeds a preset alarm value programmed into the controller menus. The alarm value is presently set at 125 °F. To reset the relay to the closed position, the user must acknowledge the alarm condition by pressing the "ACK" button on the controller keypad. As is shown in Figure 3.26, we installed a series combination of two transient voltage suppressors (General Instrument Model No. 1.5KE39A) across the controller's relay output terminals to prevent the controller from being damaged by any inductive kick which may occur when the coils of the

magnetic contactors are de-energized (Horowitz, 1989). We later discovered that the PID controller is factory-equipped with an RC snubber circuit which serves the same purpose, but we left our suppressors in place as an added precaution.

Fan Interlock Relay

The last safety device is a normally open SSR which closes only after the evaporator blower reaches a preset speed so as to prevent the heater from operating when there is little or no air flow in the loop. The SSR operates off a control voltage of 3–32 VDC and is activated by a 24-VDC digital output of the evaporator-side blower speed controller. The speed controller parameters are set such that the digital output does not activate the SSR until the blower motor is running at a frequency of at least 10 Hz, which corresponds to an air flow rate of approximately 40 cfm. The fan-interlocked SSR is used in place of a mechanical air flow switch supplied with the heater because the Pitot-type sensing element of the factory-supplied switch only protrudes a short distance into the duct and does not activate due to the abnormally low air flow conditions near the duct walls in our application.

### 3.7.3 Compressor Clutch Control Circuit

Figure 3.27 shows a diagram of our compressor clutch control circuit. We use a 12-VDC, 5.1-A regulated power supply (International Power Model No. IHN12-5.1) to power automotive compressor clutches, and a 24-VDC, 2.4-A regulated power supply (International Power Model No. IHC24-2.4) to power heavy-equipment compressor clutches. One can distinguish between 12- and 24-VDC clutches by the measuring the electrical resistance of the coil; a 12-VDC coil resistance will typically measure 3–4 Ω, whereas a 24-VDC coil resistance will typically measure 14–15 Ω. As is shown in Figure 3.27, we equipped the circuit with a four-pole double-throw toggle switch which allows the user to easily select the appropriate supply voltage. The bottom two poles of the switch connect 120-VAC input power leads to the transformer of the desired supply. The "hot" 120-VAC input lead is routed through a 1.5-A fuse and a single-pole single-throw lighted rocker switch which cuts off the main power to the circuit. The fuse was sized to match the smaller AC current limit of the two supplies but does not blow when used with the other supply. The third pole of the voltage selector switch attaches the negative output lead of the desired supply to one end of the clutch coil. The fourth pole of the switch attaches the positive output lead of the supply to the arm of a single-pole double-throw toggle switch which has a center OFF position. When toggled to the upward or ON position, the latter switch connects the positive supply lead directly to the remaining lead of the clutch, thereby energizing the coil. When toggled to the downward or COMPUTER position, the switch routes positive supply lead through a computer-controlled SSR (Crydom Model No. D1D20) which makes or

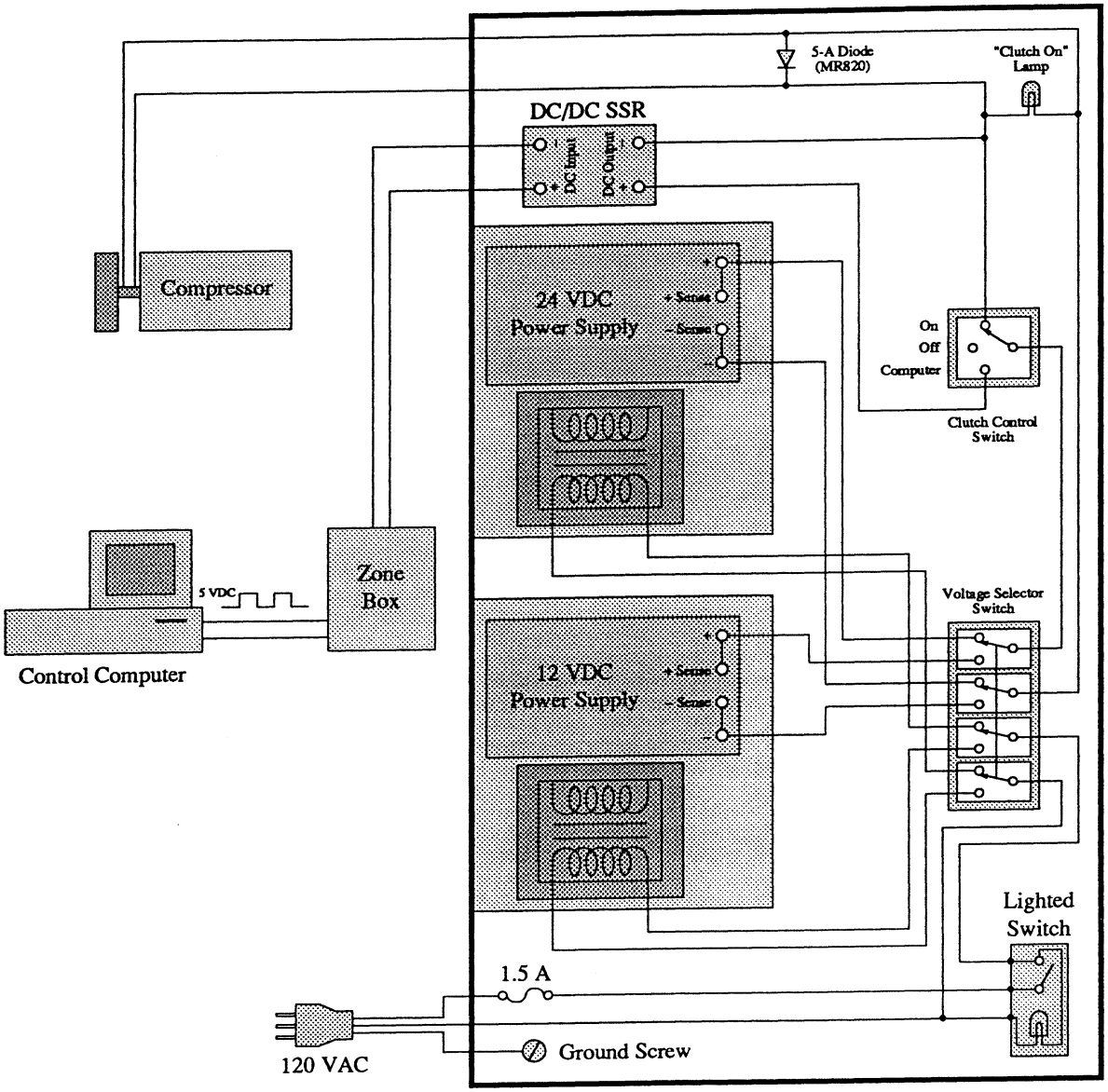


Figure 3.27 The compressor clutch control circuit.

breaks the connection to the remaining lead of the clutch. The SSR is normally open in style and closes whenever a 3.5–32 VDC signal is applied across its input terminals. We presently use a 5-VDC digital output of the DAS to drive the SSR. We wired a 24-V indicator lamp in parallel with the clutch coil to provide a visual indication of the clutch action. The lamp illuminates whenever the supply voltage is applied across the coil leads, thereby implying that the clutch is activated and the compressor is in operation. A 5-A rectifier diode (Motorola Model No. MR820) is also wired in parallel with the coil to prevent the components of the control circuit from being damaged by any inductive kick which may occur when the coil is de-energized.

# 4. VALIDATION AND PERFORMANCE OF THE TEST FACILITY

## 4.1 Steady-State Validation Testing

### 4.1.1 Motivation

The First Law of Thermodynamics dictates that the rate at which heat is transferred to or from the refrigerant stream of an air-cooled heat exchanger is equal to the rate at which heat is gained or lost by the air stream plus the rate at which heat is stored in the volume or the mass of the heat exchanger (i.e., assuming no heat is lost to the surrounding environment). During transient operating conditions, the refrigerant stream exiting the evaporator or condenser is often in a two-phase state. In such a case, refrigerant-side pressure and temperature measurements do not uniquely identify the properties needed to calculate a refrigerant-side heat transfer rate. Instead, the refrigerant-side rate must be calculated from measurements of the air-side rate and the energy storage term, so it is imperative that all of our measurements be accurate, particularly the air-side measurements. During steady-state operating conditions, the storage term is zero, and the air- and refrigerant-side heat transfer rates are theoretically equal. Hence, the level of agreement between air- and refrigerant-side heat transfer rates calculated from steady-state data reflects the accuracy of the system measurements and the data reduction techniques. Each system installed in our facility is run through a series of steady-state calorimetry tests to quantify this level of agreement and thereby validate the installation.

### 4.1.2 Steady-State Data Reduction Calculations

#### 4.1.2.1 Air-Side Heat Transfer Rates

The evaporator air-side heat transfer rate $\dot{Q}_{ea}$ [Btu/hr] and the condenser air-side heat transfer rate $\dot{Q}_{ca}$ [Btu/hr] are given by the equations

$$\dot{Q}_{ea} = \dot{m}_{ea,\,dry}\,[(h_{eai} - h_{eao}) - h_w\,(\omega_{eai} - \omega_{eao})] \tag{4.1}$$

and

$$\dot{Q}_{ca} = \dot{m}_{ca,\,dry}\,(h_{cao} - h_{cai}) \tag{4.2}$$

where

$\dot{m}_{a,\,dry}$ = mass flow rate of dry air [$lb_m$ dry air/hr]

$h_a$ = enthalpy of moist air [Btu/$lb_m$ dry air]

$h_w$ = enthalpy of liquid water [Btu/$lb_m$ $H_2O$]

$\omega$ = humidity ratio [$lb_m$ $H_2O$/$lb_m$ dry air]

In these equations and others which follow, the subscripts "i" and "o" signify inlet and outlet, and the subscripts "e" and "c" signify evaporator and condenser. For convenience, Equations 4.1 and

4.2 are written such that the results for $\dot{Q}$ are positive in sign. Both expressions are based upon the assumption that the air flow is homogenous across the face of the heat exchanger (i.e., that the velocity and temperature profiles at the inlet of the heat exchanger are flat). To obtain the dry air mass flow rate $\dot{m}_{a,\,dry}$ in each case, the psychrometric relation

$$\dot{m}_{a,\,dry} = \frac{\dot{m}_a}{1 + \omega} \tag{4.3}$$

is used, where $\dot{m}_a$ [$lb_m$/hr] is the moist air mass flow rate measured by the air-side VFT, and $\omega$ is the humidity ratio of the air stream flowing through the VFT. Humidity ratios are given by the EES function call

$$\omega = \text{HumRat}(\text{AirH}_2\text{O}, T = T_{RH}, P = P_{atm}, R = \phi/100) \tag{4.4}$$

where $T_{RH}$ [°F] and $\phi$ [% RH] are, respectively, the temperature and relative humidity of the air stream, and P is the static pressure of the air stream. As is indicated in the call statement, P is set equal to the ambient atmospheric pressure $P_{atm}$ measured by our barometer. The actual air pressures at the inlets and outlets of the heat exchangers are slightly different than $P_{atm}$ due to the static pressure rises generated by the blowers and the static pressure losses induced by the heat exchanger coils. However, these differences are small (on the order of a few inches of water column) and do not significantly effect the results obtained for $\omega$ or any other properties calculated using $\omega$.

Continuing, the moist air enthalpies $h_a$ are calculated from the psychrometric relation

$$h_a = h_{a,\,dry} + \omega\, h_v \tag{4.5}$$

where $h_{a,\,dry}$ [Btu/$lb_m$] is the enthalpy of dry air, and $h_v$ [Btu/$lb_m$] is the enthalpy of water vapor. The dry air enthalpy is given by the EES function call

$$h_{a,\,dry} = \text{Enthalpy}(\text{Air},\ T = T_a) \tag{4.6}$$

where $T_a$ [°F] is the dry-bulb temperature of the moist air mixture. EES models dry air as an ideal gas. The enthalpy $h_v$ is taken to be the enthalpy of saturated-vapor steam, as is given by the EES function call

$$h_v = \text{Enthalpy}(\text{Steam\_NBS}, T = T_a, x = 1.0) \tag{4.7}$$

where x is the steam quality. EES models steam as a real fluid. Although EES does contain moist air property routines which model both the air and water components as ideal gases, more

accurate results are obtained by using Equation 4.5 and the real-fluid water properties of EES because the real-fluid properties are based upon highly accurate NIST (formerly NBS) steam data. Finally, the enthalpy of the moisture condensed out of the evaporator air stream is taken to be the enthalpy of saturated-liquid steam, as is given by the EES function call

$$h_w = \text{Enthalpy}(\text{Steam\_NBS}, T = T_{eao}, x = 0.0) \tag{4.8}$$

where T [°F] is the temperature of the condensate. The latter temperature is assumed to be equal to the evaporator outlet air temperature $T_{eao}$.

#### 4.1.2.2 Refrigerant-Side Heat Transfer Rates

The evaporator refrigerant-side heat transfer rate $\dot{Q}_{er}$ [Btu/hr] and the condenser refrigerant-side heat transfer rate $\dot{Q}_{cr}$ [Btu/hr] are given by the equations

$$\dot{Q}_{er} = \dot{m}_r (h_{ero} - h_{eri}) \tag{4.9}$$

and

$$\dot{Q}_{cr} = \dot{m}_r (h_{cri} - h_{cro}) \tag{4.10}$$

where $\dot{m}_r$ [$lb_m$ R-134a/hr] is the mass flow rate of pure refrigerant, and $h_r$ [Btu/$lb_m$ R-134a] is the enthalpy of the refrigerant/oil mixture per unit mass of pure refrigerant. Again, for convenience, each expression is written such that the result is positive in sign. Because the refrigerant mass flow rate is the same through each component during a steady-state operating mode, any one of the following values may be used for $\dot{m}_r$ in Equations 4.9 and 4.10: (i) the Micro Motion flow meter reading ($\dot{m}_{Micro}$), (ii) the liquid-line VFT reading ($\dot{m}_{lv}$), or (iii) the discharge-line VFT reading ($\dot{m}_{dv}$). We presently use the Micro Motion flow meter reading for $\dot{m}_r$ in all calculations because it is the most accurate reading of the three, and because we suspect that the differential pressure transducers installed on our refrigerant-side VFT's are damaged. We pause here to note that all of our refrigerant-side flow meters actually sense the combined mass flow rate of refrigerant and oil. The oil component is expected to comprise 1–5 % of the flow by mass. Because our oil concentration sensor is still under development, we cannot yet separate our mass flow readings into refrigerant and oil components. Hence, the raw readings of the mixture flow rate are presently used for $\dot{m}_r$ in Equations 4.9 and 4.10.

Continuing, the refrigerant-side enthalpies are obtained from the EES function call

$$h_r = \text{Enthalpy}(\text{R134a}, T = T_r, P = P_r) \tag{4.11}$$

where $P_r$ [psia] and $T_r$ [°F] are the pressure and temperature of the refrigerant/oil mixture. EES models refrigerant R-134a as a real fluid via the Martin-Hou equation of state. Oil-enthalpy

contributions to $h_r$ are presently neglected and warrant future investigation. Like all refrigerant property routines which use P and T as the input arguments, the EES function call of Equation 4.11 is only valid for single-phase (i.e., subcooled or superheated) refrigerant states. Hence, the evaporator inlet refrigerant enthalpy $h_{eri}$ cannot be calculated from measurements of the evaporator inlet pressure and temperature because the evaporator receives a two-phase flow from the expansion device. Instead, the throttling process of the expansion device is assumed to be adiabatic and isenthalpic (a standard assumption for a/c system analysis), and $h_{eri}$ is accordingly set equal to the enthalpy of the refrigerant at the inlet of the device. The latter enthalpy can be usually be calculated from Equation 4.11 because the flow at the inlet of the expansion device is usually subcooled. In our facility, the pressure and temperature measurements taken at the inlet of the liquid-line VFT are used to determine $h_{eri}$ because these measurements are taken closest to the inlet of the expansion device. The VFT is assumed to cause no significant change in the refrigerant enthalpy between its inlet and outlet (recall that the enthalpy actually decreases at the throat of the VFT, but then returns to its former value at the outlet). The fact that the inlet pressure tap of the VFT does not sense static pressure is not of significant concern when calculating $h_{eri}$ because the dynamic pressure effects at the inlet are small relative to the total pressure in the line.

#### 4.1.2.3 Heat Exchanger Energy Balances

The evaporator- and condenser-side energy balances are quantified by calculating the error percentages between the measured air- and refrigerant-side heat transfer rates. That is, the expression

$$\delta\dot{Q} = \left( \frac{\dot{Q}_a - \dot{Q}_r}{\dot{Q}_r} \right) \text{x } 100\ \% \tag{4.12}$$

is used in each case, where a positive-valued error $\delta\dot{Q}$ [%] indicates that the air-side heat transfer rate $\dot{Q}_a$ measures greater than the refrigerant-side heat transfer rate $\dot{Q}_r$. Obviously, one wishes to have energy balance errors of $\delta\dot{Q} = 0$ %. However, one cannot realistically achieve a perfect steady-state energy balance because the measurements themselves are not perfect, and not all of the heat transferred to or from the refrigerant stream is gained or lost by the air stream (i.e., a small amount of heat is lost to the ambient environment via the ductwork and refrigerant pipes, although we attempt to minimize these losses through the use of insulation). We strive to achieve energy balances of $\pm$ 5 % or less.

#### 4.1.2.4 Other Calculations

Weston (1996) contains a listing of the EES code used to perform the calculations outlined in the previous sections. We also configured the program to output several other quantities which are not of direct interest in later discussions but are presented here for completeness. These quantities include the coefficient of performance (COP) of the system, the compressor input power, and the compressor-shell heat transfer rate. The COP of the system is given by

$$COP = \frac{\dot{Q}_{er}}{\dot{W}_{comp}} \tag{4.13}$$

where $\dot{W}_{comp}$ [Btu/hr] is the compressor input power. This latter quantity is given by

$$\dot{W}_{comp} = N_{comp}\,\tau_{comp}\left(\frac{1\ [ft]}{12\ [in.]}\right)\left(\frac{1\ [Btu]}{777.649\ [ft\text{-}lb_f]}\right)\left(\frac{2\,\pi\ [rad]}{1\ [rev]}\right)\left(\frac{60\ [min.]}{1\ [hr]}\right) \tag{4.14}$$

where $N_{comp}$ [rpm] is the compressor speed, and $\tau_{comp}$ [in.-$lb_f$] is the compressor torque. Belt losses in the compressor drive are considered to be negligible. Finally, the compressor-shell heat transfer rate $\dot{Q}_{comp}$ [Btu/hr] is given by the difference between the measured compressor input power and the measured rate at which work is performed on the refrigerant. That is,

$$\dot{Q}_{comp} = \dot{W}_{comp} - \dot{m}_r\,(h_{kro} - h_{kri}) \tag{4.15}$$

where $h_{kri}$ [Btu/hr] and $h_{kro}$ [Btu/hr] are, respectively, the inlet and outlet refrigerant enthalpies of the compressor.

### 4.1.3 Steady-State Data Collection Procedure

To generate steady-state data, the following system input parameters are held constant throughout the course of a test:

1. Compressor speed ($N_{comp}$)
2. Compressor displacement (if applicable)
3. Evaporator air flow rate ($\dot{\forall}_{ea}$)
4. Evaporator inlet air temperature ($T_{eai}$)
5. Evaporator inlet humidity ratio ($\omega_{eai}$)
6. Condenser air flow rate ($\dot{\forall}_{ca}$)
7. Condenser inlet air temperature ($T_{cai}$)
8. Expansion valve position (if applicable)

To determine the effect of each system input parameter on the energy balance results, we run any given system installed in our facility through a series of tests in which the compressor speed, the air-side flow rates, and the air-side inlet temperatures are varied independently over a broad range of operating conditions. At present, we do not control the moisture levels in the evaporator and condenser air loops, so the tests must be performed using ambient humidity levels.

Consequently, all tests conducted to date have been essentially dry-coil runs because (i) the ambient humidity level in our lab is generally very low due to the fact that the room is air-conditioned, and (ii) any moisture initially present in our closed evaporator air loop is usually condensed out of the air stream by the evaporator during the first few minutes of operation. A humidity addition and control scheme will be added to the evaporator air loop in the future. The condenser-side humidity level is not expected to have a significant impact on the system performance, so no condenser-side humidity addition or control scheme is planned.

Concerning the actual collection of data, instructions for operating the test stand and logging data are given in Weston (1996). We configured the STI WorkBench software such that the evaporator outlet refrigerant temperature is plotted in real time on the DAS display screen throughout the course of a test. The response generally becomes flat within 20–25 min. and serves as a good indicator that a steady state has been achieved. The values of the remaining system pressures and temperatures are also displayed in real time on the DAS display screen so that they can be monitored for steadiness and general correctness. When performing any given steady-state validation test, the opening of the expansion device is adjusted (if possible) until the condenser outlet flow is subcooled and the evaporator outlet flow is superheated. If these states cannot be obtained, then the energy balances cannot be calculated because two-phase pressure and temperature measurements cannot be used to calculate the outlet refrigerant properties. The subcooled and superheated states are verified both visually with the sight tubes and quantitatively through spot checks of a saturation chart given the appropriate pressure and temperature values displayed on the DAS screen. When the system appears to be steady, data are recorded at a sampling a rate of 1 Hz for a period of approximately 2 min. The recorded data are checked off-line to ensure that all of the measured variables were, in fact, steady throughout the course of the test. The average value of each parameter is then calculated in a spreadsheet, and the results are passed to the data reduction program in Weston (1996) for analysis.

### 4.1.4 Experimental Setups and Results

#### 4.1.4.1 Heavy-Equipment System Installation

The first mobile a/c system we installed in our facility was comprised of heavy-equipment components donated by Caterpillar, Inc. (CAT). Part numbers and basic descriptions of the components are given in Table 4.1. The components form a matched system in field usage. To join the evaporator, condenser, and compressor to our general-purpose lines, we constructed hose assemblies from nylon refrigerant hoses and reusable steel fittings which attach to the hoses via a threaded nipple-and-sleeve arrangement. The part numbers for these hoses and fittings are also given in Table 4.1. We could not find any fittings which matched the inlet and outlet thread

Table 4.1 The components of the heavy-equipment (CAT) system installation.

| Component | Description | Inlet and Outlet Installation Fittings Used in the Facility | |
|---|---|---|---|
| Evaporator | Type: Tube/fin<br>Material: Copper tubes with aluminum fins<br>Flow Area: 10-5/8 in. (W) x 14 in. (H)<br>Inlet: 3/4"-16 UNF male insert O-ring<br>Outlet: 7/8"-14 UNF male insert O-ring<br>Part No.: 3E-7713 (CAT) | Inlet: • 3/4"-16 UNF female O-ring pilot<br>• #8 hose<br>• #8 hose x 1/2-in. O.D. pipe compression adapter<br>Outlet: • 7/8"-14 UNF female O-ring pilot<br>• #10 hose<br>• #10 hose x 5/8-in. O.D. pipe compression adapter | 25920-8-8 (Parker)<br>235-8 (Parker)<br>21120-8-8 (Parker)<br>25920-10-10 (Parker)<br>235-10 (Parker)<br>21120-10-10 (Parker) |
| Condenser | Type: Plate/fin<br>Material: Steel<br>Flow Area: 34-3/16 in. (W) x 16-3/4 in. (H)<br>Inlet: 3/4"-16 UNF male insert O-ring<br>Outlet: 5/8"-18 UNF male insert O-ring<br>Part No.: 9D-6899 (CAT) | Inlet: • 3/4"-16 UNF female O-ring pilot<br>• #8 hose<br>• #8 hose x 1/2-in. O.D. pipe compression adapter<br>Outlet: • 5/8"-18 UNF female O-ring pilot<br>• #6 hose<br>• #6 hose x 3/8-in. O.D. pipe compression adapter | 25920-8-8 (Parker)<br>235-8 (Parker)<br>21120-8-8 (Parker)<br>25920-6-6 (Parker)<br>235-6 (Parker)<br>21120-6-6 (Parker) |
| Accumulator | Desiccant: None (desiccant is in an in-line dryer unit in the liquid line)<br>Inlet: 1-1/16"-16 UNF female insert O-ring<br>Outlet: 1-1/16"-16 UNF female insert O-ring<br>Part No.: 3E-7320 (CAT) | Inlet: • 1-1/16"-16 UNF 90° male O-ring pilot (steel) severed from a stock CAT hose assembly<br>• 3/4-in. x 5/8-in. reducer coupling (copper)<br>• High-silver braze alloy<br>• Flux for brazing steel-to-copper joints<br>Outlet: • Duplicate of inlet | 8X-9517 (CAT)<br>—<br>Safety-Silv No. 45 (Harris)<br>Stay-Silv Flux (Harris) |
| Expansion Device and Dryer Unit | Type: Orifice tube housed in an in-line dryer containing R-134a desiccant<br>Inlet: Male quick-disconnect stem<br>Outlet: Male quick-disconnect stem<br>Part No.: 3E-3535 (CAT) | Inlet: • 1/4-NPTF female quick-disconnect fitting<br>• 3/8-in. x 1/4-NPTM braze adapter (copper)<br>Outlet: • 1/4-NPTF female quick-disconnect fitting<br>• 1/2-in. x 1/4-NPTM compression fitting | 9W-0616 (CAT)<br>—<br>9W-0616 (CAT)<br>8CM4 (Gyrolok) |
| Compressor | Type: Piston/swashplate, 5 cylinders, fixed displacement (150 cc), R-134a demo version<br>Inlet: 7/8"-14 UNF male insert O-ring<br>Outlet: 3/4"-16 UNF male insert O-ring<br>Oil: PAG, 300 cc, Sanden SP-20<br>Part No.: SD-5H15 (Sanden) (compressor) 7803-1996 (Sanden) (oil), same as 4C-2959 (CAT) (oil) | Inlet: • 7/8"-14 UNF female O-ring pilot<br>• #10 hose<br>• #10 hose x 5/8-in. O.D. pipe compression adapter<br>Outlet: • 3/4"-16 UNF female O-ring pilot<br>• #8 hose<br>• #8 hose x 1/2-in. O.D. pipe compression adapter | 25920-10-10 (Parker)<br>235-10 (Parker)<br>21120-10-10 (Parker)<br>25920-8-8 (Parker)<br>235-8 (Parker)<br>21120-8-8 (Parker) |

sizes of the accumulator, so stock fittings made of steel were cut from the original-equipment hose assemblies and brazed to copper extension pipes with a 45 % silver brazing alloy and a flux suitable for forming steel-to-copper joints. The extension pipes were then joined to our general-purpose lines with compression unions. We ultimately purchased a hose crimping tool (Murray Model No. 400300) to avoid having to make such joints in the future, and to avoid long lead times associated with obtaining the reusable hose fittings. Although the cost of the crimping tool was quite high, the convenience of the tool far outweighs the expenditure. Crimp-type mobile a/c hose fittings are widely available at low costs through local suppliers of automotive parts. As a final note, we constructed a 3/8-in. O.D. general-purpose liquid line for use with the heavy-equipment system (as opposed to the present 1/2-in. O.D. line) because that is the line size used in the stock system.

Preliminary Test Results

Our attempts to achieve steady-state operation with the heavy-equipment system were unsuccessful. Instead, the refrigerant temperatures and pressures were found to oscillate in a recurring pattern under a wide range of system input conditions (compressor speeds, air flow rates, inlet air temperatures, refrigerant charge levels, and orifice tube sizes). Specifically, the refrigerant flow exiting the condenser was found to repeatedly cycle from a subcooled flow to a two-phase plug flow (a flow pattern in which large vapor bubbles or "plugs" travel in an otherwise flooded liquid line) or a two-phase stratified flow, while the refrigerant flow exiting the evaporator was found to simultaneously cycle from a two-phase misted flow to a superheated flow. Figure 4.1 shows an example of the typical responses obtained for the evaporator outlet refrigerant temperature, the condenser outlet refrigerant temperature, the liquid-line VFT mass flow rate, and the discharge-line VFT mass flow rate. We believe that the differential pressure sensors installed on the refrigerant-side VFT's were working properly at the time these data were collected, but the magnitudes of the readings may be slightly in error due to the fact that these VFT's have not yet been calibrated. The Micro Motion flow meter was not installed at the time the data were collected. The two-phase portions of the responses are indicated on the plot. Although the liquid-line VFT readings are technically invalid for two-phase flow, the pressure taps of the liquid-line VFT are located near the bottom of pipe (i.e., in the liquid portion of the plug or stratified flow), and the sight tube preceding the VFT was observed to be mostly flooded throughout the two-phase portion of the response. Hence, the two-phase portions of the liquid-line VFT response plotted in Figure 4.1 are probably good estimates of the true two-phase mass flow rates.

Referring to Figure 4.1, as a two-phase flow develops in the liquid line (i.e., at the outlet of the condenser and at the inlet of the expansion device (an orifice tube)), the flow rate in the

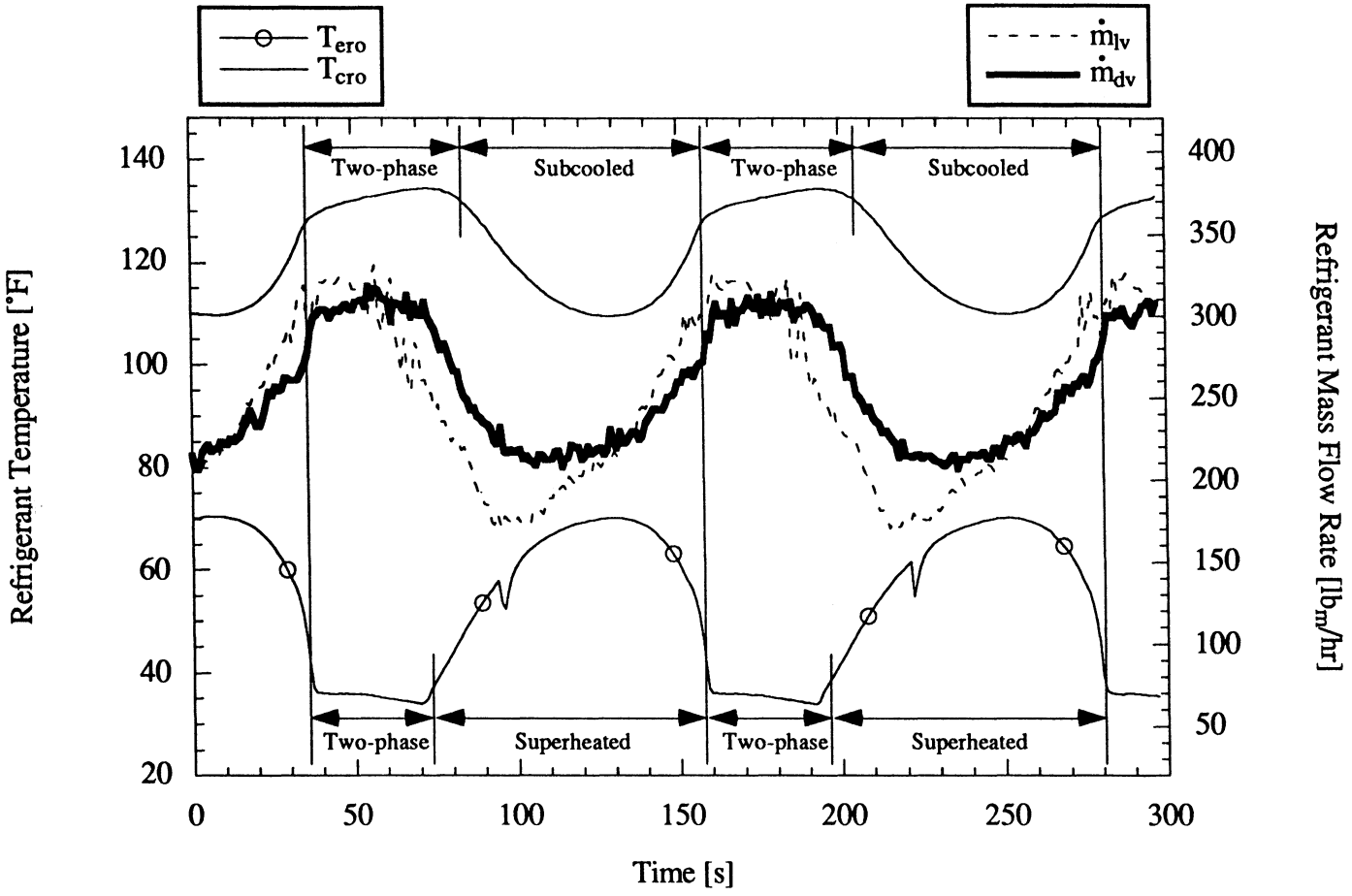


Figure 4.1 The typical refrigerant-side temperature and mass flow responses obtained from the heavy-equipment system.

liquid line inverts from an increasing flow to a decreasing flow. The initial part of the inversion corresponds to a period in which small bubbles begin to appear in the liquid-line sight tube. The remainder of the two-phase portion of the response corresponds to a period of plug or stratified flow. Concurrent studies in our research center show that the mass flow rate passed by an orifice tube decreases sharply with increasing inlet quality, and this fact likely explains the flow decrease observed in Figure 4.1. The decrease in the liquid-line flow rate is followed by a decrease in the discharge-line flow rate after a delay of approximately 10 s. Throughout the time that the two flow rates are decreasing, the discharge-line flow rate exceeds the liquid-line flow rate by approximately 50 $lb_m/hr$ (i.e., assuming the uncalibrated VFT readings are correct), indicating that the refrigerant charge is migrating from the evaporator to the condenser.

As the orifice tube allows less mass to flow into the evaporator while operating in the two-phase flow mode, the compressor begins to empty the evaporator volume, thereby causing the evaporator outlet (and inlet) pressure to fall as is shown in Figure 4.2. This decrease in pressure causes a corresponding decrease in the saturation temperature of the refrigerant within the evaporator as is indicated by the negative slope of the two-phase (i.e., saturated) portion of the evaporator outlet temperature response. Consequently, the difference between the inlet air temperature (held constant at 110 °F for the example at hand) and the refrigerant saturation temperature increases, and this increase in temperature potential generates an increased heat transfer from the hot air stream to the cold refrigerant stream. As a result, the evaporator outlet flow is driven to a superheated state. At the same time, the orifice tube allows less refrigerant to exit the condenser, thereby causing the condenser pressure to increase as the compressor forces more and more refrigerant into the condenser volume. In turn, the condenser refrigerant saturation temperature increases as is indicated by the positive slope of the two-phase portion of the condenser outlet temperature response shown in Figure 4.2. As with the evaporator, this results in an increased heat transfer from the hot condenser refrigerant stream to the cooler inlet air stream (77 °F for this example), and the condenser outlet flow is driven to a subcooled state.

Once the liquid-line flow becomes subcooled, the flow characteristics of the orifice tube change, and the liquid-line flow rate begins to increase. This change in flow characteristic appears to be accompanied by a single liquid slug which passes through the evaporator outlet sight tube at the same point in each cycle. As is indicated in Figure 4.1, the slug causes the superheated evaporator outlet temperature to spike downward toward the temperature of the saturated refrigerant entering the evaporator, but the 1-Hz sampling rate is too slow to capture the full dynamic pattern of the spike (even if the sampling rate were increased, the thermocouple response time may also be too slow to sense the full pattern). The liquid-line flow rate eventually grows to exceed the discharge-line flow rate, thereby indicating that the refrigerant charge is migrating from the condenser back to the evaporator. As an increasing amount of

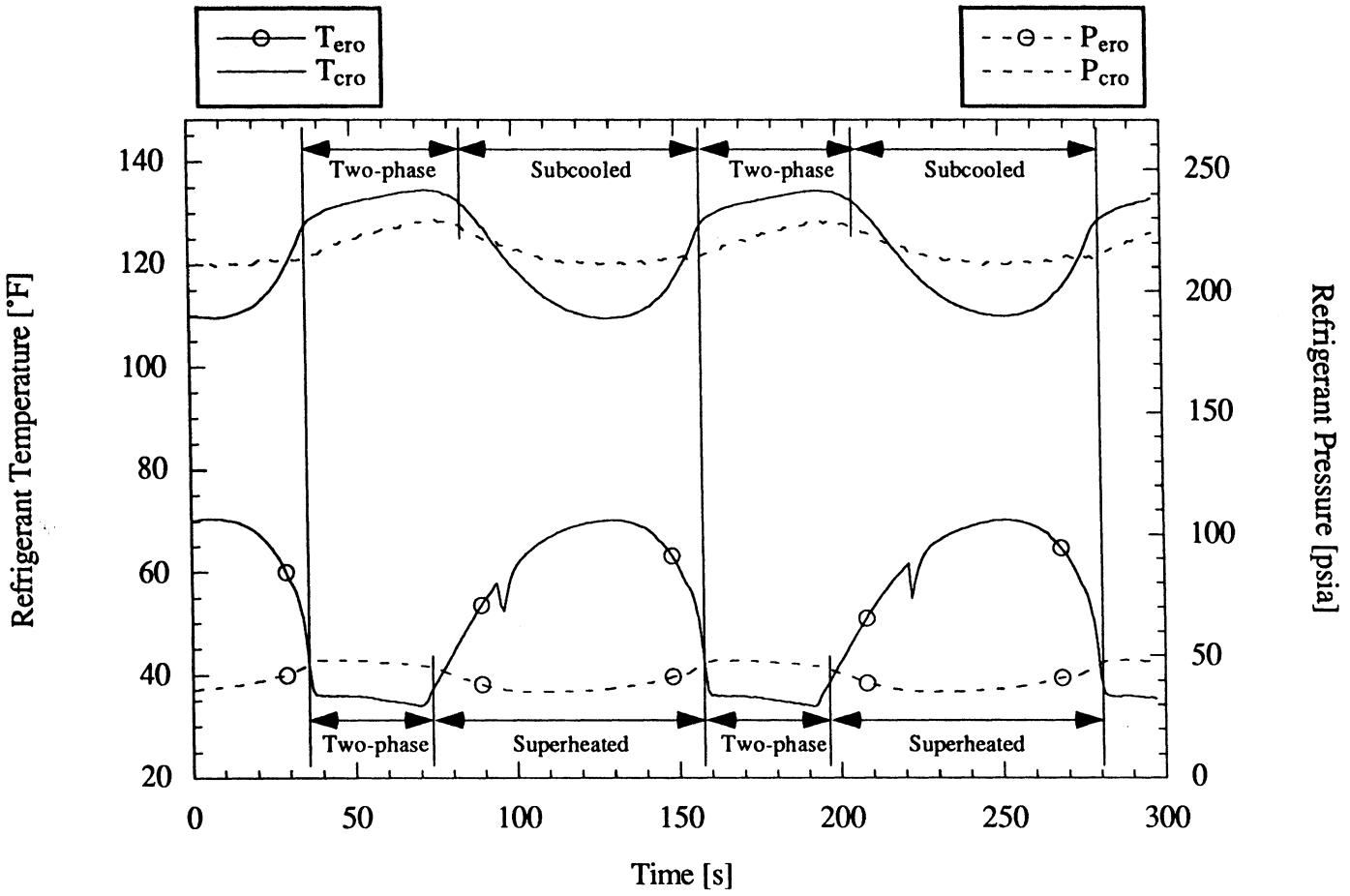


Figure 4.2 The typical refrigerant-side temperature and pressure responses obtained from the heavy-equipment system.

charge fills the volume of the evaporator, the evaporator pressure rises, and the outlet superheat is lost. Similarly, as an increasing amount of charge leaves the condenser, the condenser pressure falls, and the outlet subcooling is lost. The cycle then repeats.

The root cause of the cyclical behavior is thought to be an inadequate condenser air flow rate. Heavy-equipment systems typically operate with a condenser air velocity on the order of 1000 ft/min., which translates to an air flow rate of approximately 4000 cfm for the condenser we tested in our facility. Such a high air flow rate is obtainable in the field through the use of one or more open-blade fans because the fans only have to work against the relatively small air-side pressure drops of the condenser coil, the radiator coil, and the cosmetic grilles (if any) which precede the two coils. However, in a ducted laboratory system containing flow measurement and conditioning devices, a large and powerful blower is needed to obtain the same flow rate. As was discussed in Chapter 2, our condenser-side blower can produce a maximum air flow rate on the order of 1600 scfm, which is far less than the typical operating flow of the CAT system. As a result, the air-side heat transfer is insufficient to maintain subcooling at the condenser outlet. Our condenser air loop must be upgraded in order to facilitate proper testing of heavy-equipment systems in the future. Because the complex behavior obtained from our heavy-equipment system installation was uncharacteristic of normal field operation and undesirable for facility shakedown testing and initial experimental investigations, the system was sadly dismantled and replaced by the hybrid automotive system discussed next. However, we wish to note that the tests performed with the CAT equipment were instrumental in learning how to install and instrument a mobile a/c system in our laboratory, and the results remain valuable from a diagnostics perspective because they imply that a given fault condition (such as low condenser air flow) may produce transient signature patterns which can be used to identify the fault.

#### 4.1.4.2 Hybrid System Installation

The system currently installed in our facility is comprised of the automotive components listed in Table 4.2. The components form the a/c system of a General Motors (GM) 1994 Chevrolet Lumina sedan, with two exceptions. First, a stock Lumina system uses a GM Model V-5 variable-displacement compressor (GM Part No. 1135099). We did not wish to observe the dynamic effects of the variable-displacement action in our initial transient and steady-state experiments, so the fixed-displacement Sanden compressor used in the previous system installation was retained for use with the GM equipment. The displacement of the Sanden compressor is equal to the maximum displacement of the V-5 compressor (150 cc). Second, a stock Lumina system uses an orifice tube (GM Part No. 3033879) as the expansion device. We attempted to conduct our initial validation tests using the stock orifice tube, but soon discovered that we could generate superheat at the evaporator outlet only under a vary narrow range of

Table 4.2 The stock components of the hybrid (GM) system installation.

| Component | Description | Inlet and Outlet Installation Fittings Used in the Facility | |
|---|---|---|---|
| Evaporator | Type: Plate/fin<br>Material: Aluminum<br>Flow Area: 10-1/4 in. (W) x 7-1/2 in. (H)<br>Inlet: 1/2-in. O.D. pipe to manifold block<br>Outlet: 5/8-in. O.D. pipe to manifold block<br>Part No.: 3093285 (GM) | Inlet: • 1/2-in. compression union (attaches to evaporator inlet pipe after severing the manifold block from the component)<br>Outlet: • 5/8-in. compression union (attaches to evaporator outlet pipe after severing the manifold block from the component) | 8U (Gyrolok)<br>10U (Gyrolok) |
| Condenser | Type: Tube/fin<br>Material: Aluminum<br>Flow Area: 28 in. (W) x 16-1/2 in. (H)<br>Inlet: 1/2-in. O.D. pipe to manifold block<br>Outlet: 1/2-in. O.D. pipe to manifold block<br>Part No.: 52452050 (GM) | Inlet: • 1/2-in. 90° compression union (attaches to condenser inlet pipe after severing the manifold block from the component)<br>Outlet: • 1/2-in. compression union (attaches to condenser outlet pipe after severing the manifold block from the component) | 8LU (Gyrolok)<br>8U (Gyrolok) |
| Accumulator | Desiccant: R-134a compatible<br>Inlet: 1-1/16"-14 UNC female insert O-ring<br>Outlet: 1-1/16"-14 UNC male insert O-ring<br>Part No.: 2724831 (GM) | Inlet: • 1-1/16"-14 UNC male O-ring pilot severed from the stock GM tube assembly (3/4-in. O.D.)<br>• 3/4-in. x 5/8-in. compression union<br>Outlet: • 1-1/16"-14 UNC female O-ring pilot severed from the stock GM hose assembly<br>• #12 x #12 Parflex-to-rubber hose splicer<br>• #12 hose<br>• #12 hose x 5/8-in. O.D. pipe compression adapter | 10190635 (GM)<br>12RU10 (Gyrolok)<br>10190632 (GM)<br>201124 (Murray)<br>200052 (Murray)<br>401055 (Murray) |
| Stock Expansion Device (not used) | Type: Orifice tube housed in a 1/2-in. O.D. liquid-line assembly (line reduces to 3/8-in. O.D. at orifice outlet)<br>Part No.: 3033879 (GM) (orifice tube)<br>10220973 (GM) (line assembly) | Inlet: • 1/2-in. 90° compression union (attaches to inlet end of orifice tube section spliced out of the stock liquid line)<br>Outlet: • 1/2-in. x 3/8-in. compression union (attaches to outlet end of orifice tube section spliced out of the stock liquid line) | 8LU (Gyrolok)<br>8RU6 (Gyrolok) |
| Stock Compressor (not used) | Type: Piston/swashplate, 5 cylinders, variable displacement (150 cc max.)<br>Inlet: Female O-ring port (accepts pilot from manifold block of stock hose assembly)<br>Outlet: Female O-ring port (accepts pilot from the same manifold block used for inlet)<br>Oil: PAG, 265 cc<br>Part No.: 1135099 (GM) (compressor)<br>10190632 (GM) (hose assembly)<br>12345923 (GM) (oil) | Inlet: • 5/8-in. 90° compression union (attaches to the severed inlet pipe of a manifold block used with V-5 compressors on other GM vehicles)<br>Outlet: • 1/2-in. 90° compression union (attaches to the severed outlet pipe of the same manifold block used for inlet)<br>Both: • GM V-5 manifold block with a 5/8-in. O.D. inlet pipe and a 1/2-in. O.D. outlet pipe | 10LU (Gyrolok)<br>8LU (Gyrolok)<br>202170 (Murray) |

steady-state operating conditions (condenser subcooling was usually obtainable). Hence, we replaced the orifice tube with the metering valve discussed in Chapter 2 so that the refrigerant flow could be manually adjusted until the evaporator exit flow was superheated for any given set of system input conditions.

Concerning the remaining components, the Lumina condenser is a tube/fin heat exchanger equipped with a manifold block connector. We installed the condenser in our facility by cutting the manifold block from the inlet and outlet pipes and joining the severed pipe ends to our general-purpose lines with compression fittings. We mounted the condenser in our ductwork with the tubes horizontal and the inlet at the top, as in actual field usage. The Lumina evaporator is a two-pass plate/fin heat exchanger which is also equipped with a manifold block connector. As with the condenser, we cut the block from the component and joined the severed pipe ends to our general-purpose lines with compression fittings. In an actual Lumina sedan, the evaporator mounts with the plates vertical and the inlet at the top. In accordance with the recommendations of our contacts at GM, we mounted the evaporator in our ductwork with the plates horizontal and the inlet at the bottom. Finally, the Lumina accumulator is an aluminum canister equipped with male and female insert O-ring connections and a desiccant bag compatible with R-134a. To make the inlet connection, we cut the stock inlet line (a run of aluminum pipe) and joined the severed end to our line with a compression union. To make the outlet connection, we cut the stock outlet line (a hose assembly) and crimped a hose-to-pipe compression adapter to the severed end with our newly acquired crimping tool.

Hybrid-System Test Results

Table 4.3 shows the matrix of steady-state test conditions used to validate the hybrid system installation. The matrix consists of various combinations of three different compressor speeds, air-side flow rates, and air-side inlet temperatures. Only 37 of the possible 243 combinations were tested. The last column of the table indicates the semi-random order in which the tests were performed. Concerning the compressor speed and the air-side flow rates, the motor drive frequencies were the parameters actually held constant from test to test. The resulting values of $N_{comp}$, $\dot{V}_{ea}$, and $\dot{V}_{ca}$ differ by a few percent for each drive frequency setting. This is a direct result of the fact that our motor speed controllers are not closed-loop control devices. For example, in an actual test, the amount of slip generated between the rotor and the stator of the compressor drive motor varies with the load torque (i.e., with the state of the refrigerant entering the compressor), so the compressor does not always spin at the exact same speed each time the drive motor is run at a given frequency. Likewise, each air-side blower does not always generate the exact same flow rate each time its drive motor is run at a given frequency because the pressure rise generated by the blower is dependent upon the temperature (i.e., the

Table 4.3 The matrix of steady-state test conditions used to validate the hybrid system installation.

| Case No. | $N_{comp}$ | | $\dot{V}_{ea}$ | | $T_{eai}$ | $\dot{V}_{ca}$ | | $T_{cai}$ | Order Performed |
|---|---|---|---|---|---|---|---|---|---|
| | Drive Input [Hz] | Approx. Speed [rpm] | Drive Input [Hz] | Approx. Flow [cfm] | [°F] | Drive Input [Hz] | Approx. Flow [cfm] | [°F] | |
| 1 | 20.0 | 1140 | 25.0 | 125 | 70 | 25.0 | 760 | Ambient | 1 |
| 2 | 20.0 | 1140 | 25.0 | 125 | 70 | 40.8 | 1200 | Ambient | 12 |
| 3 | 20.0 | 1140 | 25.0 | 125 | 70 | 56.5 | 1610 | Ambient | 14 |
| 4 | 20.0 | 1140 | 42.5 | 220 | 70 | 25.0 | 760 | Ambient | 28 |
| 5 | 20.0 | 1140 | 42.5 | 220 | 90 | 25.0 | 760 | Ambient | 11 |
| 6 | 20.0 | 1140 | 42.5 | 220 | 90 | 25.0 | 760 | 85 | 32 |
| 7 | 20.0 | 1140 | 42.5 | 220 | 90 | 25.0 | 760 | 100 | 33 |
| 8 | 20.0 | 1140 | 42.5 | 220 | 90 | 40.8 | 1200 | Ambient | 3 |
| 9 | 20.0 | 1140 | 42.5 | 220 | 90 | 56.5 | 1610 | Ambient | 15 |
| 10 | 20.0 | 1140 | 42.5 | 220 | 110 | 25.0 | 760 | Ambient | 29 |
| 11 | 20.0 | 1140 | 60.0 | 315 | 110 | 25.0 | 760 | Ambient | 10 |
| 12 | 20.0 | 1140 | 60.0 | 315 | 110 | 40.8 | 1200 | Ambient | 13 |
| 13 | 20.0 | 1140 | 60.0 | 315 | 110 | 56.5 | 1610 | Ambient | 2 |
| 14 | 40.0 | 2340 | 25.0 | 125 | 70 | 25.0 | 760 | Ambient | 4 |
| 15 | 40.0 | 2340 | 25.0 | 125 | 70 | 40.8 | 1200 | Ambient | 18 |
| 16 | 40.0 | 2340 | 25.0 | 125 | 70 | 56.5 | 1610 | Ambient | 20 |
| 17 | 40.0 | 2340 | 42.5 | 220 | 90 | 25.0 | 760 | Ambient | 17 |
| 18 | 40.0 | 2340 | 42.5 | 220 | 90 | 40.8 | 1200 | Ambient | 6 |
| 19 | 40.0 | 2340 | 42.5 | 220 | 90 | 40.8 | 1200 | 85 | 34 |
| 20 | 40.0 | 2340 | 42.5 | 220 | 90 | 40.8 | 1200 | 100 | 35 |
| 21 | 40.0 | 2340 | 42.5 | 220 | 90 | 56.5 | 1610 | Ambient | 21 |
| 22 | 40.0 | 2340 | 60.0 | 315 | 70 | 40.8 | 1200 | Ambient | 30 |
| 23 | 40.0 | 2340 | 60.0 | 315 | 90 | 40.8 | 1200 | Ambient | 31 |
| 24 | 40.0 | 2340 | 60.0 | 315 | 110 | 25.0 | 760 | Ambient | 16 |
| 25 | 40.0 | 2340 | 60.0 | 315 | 110 | 40.8 | 1200 | Ambient | 19 |
| 26 | 40.0 | 2340 | 60.0 | 315 | 110 | 56.5 | 1610 | Ambient | 5 |
| 27 | 60.0 | 3540 | 25.0 | 125 | 70 | 25.0 | 760 | Ambient | 7 |
| 28 | 60.0 | 3540 | 25.0 | 125 | 70 | 40.8 | 1200 | Ambient | 24 |
| 29 | 60.0 | 3540 | 25.0 | 125 | 70 | 56.5 | 1610 | Ambient | 26 |
| 30 | 60.0 | 3540 | 42.5 | 220 | 90 | 25.0 | 760 | Ambient | 23 |
| 31 | 60.0 | 3540 | 42.5 | 220 | 90 | 40.8 | 1200 | Ambient | 9 |
| 32 | 60.0 | 3540 | 42.5 | 220 | 90 | 56.5 | 1610 | Ambient | 27 |
| 33 | 60.0 | 3540 | 42.5 | 220 | 90 | 56.5 | 1610 | 85 | 36 |
| 34 | 60.0 | 3540 | 42.5 | 220 | 90 | 56.5 | 1610 | 100 | 37 |
| 35 | 60.0 | 3540 | 60.0 | 315 | 110 | 25.0 | 760 | Ambient | 22 |
| 36 | 60.0 | 3540 | 60.0 | 315 | 110 | 40.8 | 1200 | Ambient | 25 |
| 37 | 60.0 | 3540 | 60.0 | 315 | 110 | 56.5 | 1610 | Ambient | 8 |

density) of the air stream entering the blower, and the pressure drops generated in the flow system are dependent upon the density of the air stream in each part of the system. These shortcomings can be resolved in the future by using the environment controller to regulate the values of $N_{comp}$, $\dot{\forall}_{ea}$, and $\dot{\forall}_{ca}$ (or $N_{comp}$, $\dot{m}_{ea}$, and $\dot{m}_{ca}$) based upon feedback of the values sensed by the compressor speed sensor and the air-side VFT's. For the test cases at hand, the approximate values of $N_{comp}$, $\dot{\forall}_{ea}$, and $\dot{\forall}_{ca}$ which correspond to the drive frequency settings are given in Table 4.3. The actual values recorded during the tests are given in Weston (1996) along with the values of all other measured and calculated system parameters.

The calculated values of the evaporator air-side heat transfer rates are plotted against the calculated values of the evaporator refrigerant-side heat transfer rates in Figure 4.3. The air-side heat transfer measurements systematically exceed the refrigerant-side measurements by an average error of $\delta\dot{Q}_e = 11.5$ %. The data fall within ± 11.4 percentage points of the 11.5 % error line with 95 % confidence. The confidence interval was calculated as $\pm 2\sigma$, where $\sigma$ is the standard deviation of the mean $\delta\dot{Q}_e$. Figure 4.4 shows the analogous plot for the condenser. The condenser data show a larger average error of $\delta\dot{Q}_c = 16.6$ % but a slightly better confidence interval of ± 10.6 %. The undesirably large energy balance errors can most likely be attributed to one or more of the following three factors:

1. The calibrated values of the air-side VFT discharge coefficients may be higher than the actual operating values, causing the calculated values of the air-side flow rates (and, hence, the heat transfer rates) to be too large.
2. As was previously discussed in Chapter 3, the gas expansion factor Y of each air-side VFT may not be adequately approximated by Equation 3.89.
3. The air-side temperature measurements recorded at the inlets and outlets of the heat exchangers suffer from the effects of stratification.

In addition to correcting these possible sources of error, many other improvements can be made to the air- and refrigerant-side measurement techniques to reduce the overall energy balance errors. The list of recommended improvements is given in Chapter 5, whereas the three main issues are discussed here.

Concerning the air-side VFT discharge coefficients, recall that these VFT's were calibrated using extra-long inlet pipes which promoted well-developed inlet flows during the calibration runs. In our laboratory installations, the air-side VFT inlet pipes are spatially constrained to be much shorter (although they still meet the minimum length requirements recommended by the VFT manufacturer), and the VFT's are located downstream of elbows and blowers which introduce nonuniformities to the velocity profiles of the air streams. Recall that the VFT flow

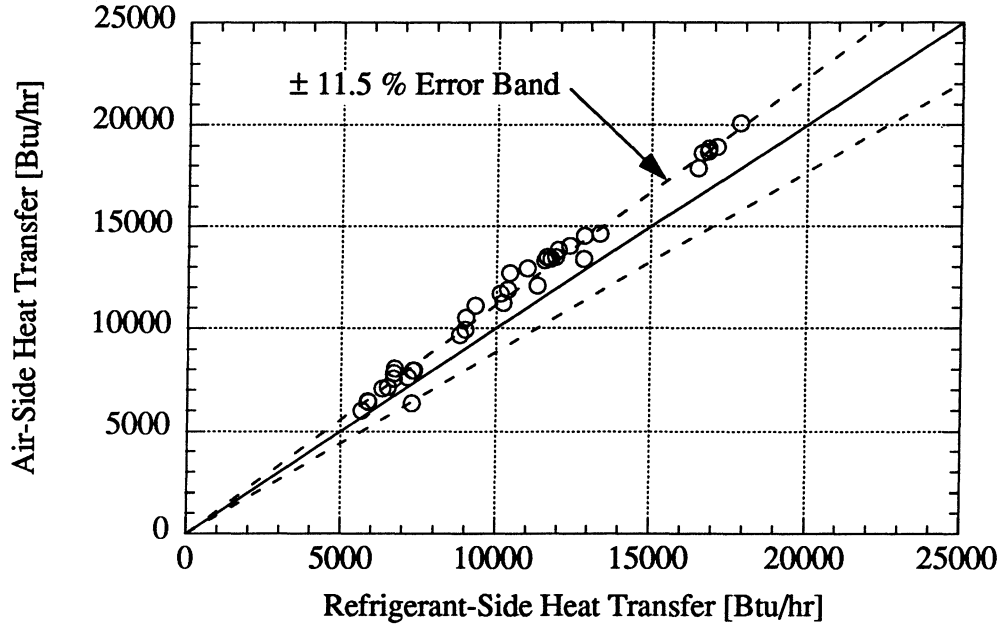


Figure 4.3 The evaporator-side calorimetry data.

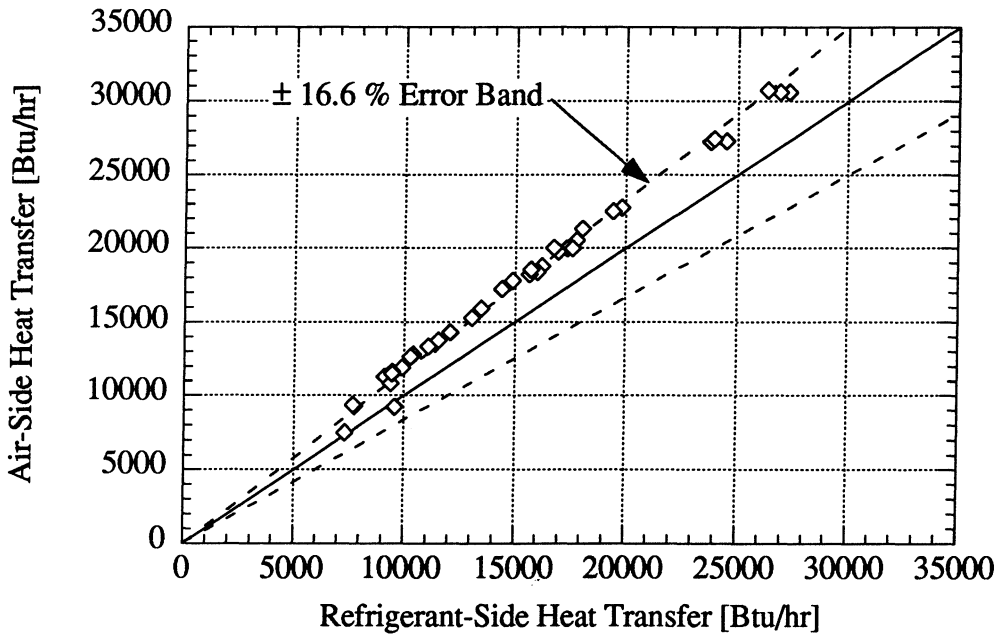


Figure 4.4 The condenser-side calorimetry data.

equation is based on the assumption that the velocity profiles at the inlet and throat are flat. Further recall that the discharge coefficient, in part, accounts for the presence of nonuniformities in the velocity profiles. If the operating velocity profiles contain nonuniformities which were not present during the calibration runs, then the operating values of C will differ from the calibrated values of C. Our flow meters are particularly sensitive to the effects of flow nonuniformities because the inlet and throat taps of the VFT's do not sense static pressure. The additional dynamic influences introduced at the taps by the nonuniformities (if any) not only serve to further change the value of C, but may also exaggerate any discrepancies which already exist between Equation 3.89 and the true function(s) for Y for the VFT's. Our air-side flow measurement problems can be reduced or resolved by installing flow conditioning devices upstream of the air-side VFT's and by increasing the inlet pipe lengths as much as possible. Ultimately, the VFT's may have to be replaced with CVT's to altogether avoid the sensitivities associated with the nonstatic pressure taps of the VFT's.

Concerning the air-side temperature measurements, recall that nine-point thermopiles are used to sense the average outlet air temperatures of the heat exchangers, and that single-point thermocouple measurements are used to sense the inlet air temperatures. Further recall that each inlet temperature profile is assumed to be isothermal at the temperature indicated by the single-point measurement, and that the true average outlet temperatures are assumed to be adequately represented by nine-point averages. To verify these assumptions, the inlet and outlet grid couples were unplugged from their respective thermopile circuits at the conclusion of each steady-state test, and the individual grid point temperatures were read using an OMEGA Model No. HH23 hand-held thermocouple meter. The degree of stratification across each grid was then quantified by a temperature value $T_{strat}$, calculated as

$$T_{strat} = T_{k,\,max} - T_{k,\,min} \tag{4.16}$$

where $T_{k,\,min}$ and $T_{k,\,max}$ are, respectively, the minimum and maximum temperatures measured across the grid. The individual grid point readings and the resulting values of $T_{strat}$ are tabulated in Weston (1996). The minimum, maximum, and average values of $T_{strat}$ observed at each grid over the 37 different cases of operation are summarized in Table 4.4. The uncertainty bands given with the average values listed in the latter table are intervals of 95 % confidence. The evaporator inlet air temperature profile shows the least amount of stratification, which is a direct result of the fact that the blower mixes the chilled (and then heated) evaporator outlet air stream before recirculating the flow to the inlet. The condenser inlet air temperature profile shows a much larger degree of stratification, which is a direct result of the fact that the recirculated air stream does not adequately mix with the ambient intake air stream in the turbulent region above the first

screen in the condenser-side plenum. Even with the recirculation damper closed, the condenser inlet temperature profile can still be slightly stratified because a small amount of hot condenser outlet air leaks by the damper. In addition, any condenser air flow which is exhausted out of the hood must be resupplied to the room by our building's ventilation system. The temperature of the air stream resupplied to the room can vary slightly from the temperature of the air already in the room, thereby causing an inhomogeneous mixture to enter the ambient intake port.

Table 4.4 Summary of the temperature stratification conditions recorded at the inlet and outlet thermopile grids.

| Heat Exchanger | Inlet Grid Stratification | | | Outlet Grid Stratification | | |
|---|---|---|---|---|---|---|
| | Min. | Max. | Average | Min. | Max. | Average |
| Evaporator | 0.4 °F (0.2 °C) | 5.1 °F (2.8 °C) | 1.9 ± 2.6 °F (1.1 ± 1.4 °C) | 26.8 °F (14.9 °C) | 79.2 °F (44.0 °C) | 50.4 ± 27.8 °F (28.0 ± 15.4 °C) |
| Condenser | 0.5 °F (0.3 °C) | 17.8 °F (9.9 °C) | 5.9 ± 9.6 °F (3.3 ± 5.3 °C) | 3.5 °F (1.9 °C) | 20.9 °F (11.6 °C) | 8.5 ± 8.0 °F (4.7 ± 4.4 °C) |

Because the inlet grid temperatures can be stratified to a fair degree in both air loops, the average outlet air temperatures indicated by the inlet-referenced thermopiles can be significantly in error. To resolve this problem, the thermopile reference junctions should be moved to the thermocouple reference bath so as to decouple the inlet stratification effects the from the outlet temperature measurements. Also, separate bath-referenced thermopiles should be used to make average inlet air temperature measurements as opposed to the present practice of making single-point inlet temperature measurements. Ultimately, a mixing scheme should be added upstream of each heat exchanger to altogether eliminate the effects of stratification and ensure a flat temperature profile enters the face of each coil. Because most mixing schemes introduce swirl to the air stream, each mixing section must be followed by a section of screens and flow straightening devices (e.g., a bank of straws or a sheet of honeycomb material) to remove the swirl and maintain a uniform velocity profile at the heat exchanger inlet (Farell, 1993).

Returning to Table 4.4, the outlet grid temperatures are seen to be stratified by up to 79.2 °F in the evaporator air loop, and up to 20.9 °F in the condenser air loop. Although the condenser-side maximum of 20.9 °F occurred when the inlet temperature profile was stratified by its maximum of 17.8 °F, another case (Case No. 35) showed the outlet profile to be stratified by 19.8 °F when the inlet profile was stratified by only 1.2 °F. Hence, like the evaporator outlet temperature profile, the condenser outlet profile can be significantly stratified simply due to the fact that unequal heat transfer rates occur across the subcooled, superheated, and two-phase zones of the coil. In light of the large stratification values observed across the outlet grids, the outlet temperature readings are undoubtedly very sensitive to where the nine outlet

thermocouples are placed in the profiles. Hence, nine-point thermopile grids are not likely to generate good representations of the true average outlet air temperatures. As with the inlet temperature measurements, the ultimate solution to the problem is to install mixing equipment at the outlet of each heat exchanger to reduce or eliminate the effects of stratification. However, each outlet mixing process would have to be adiabatic and free from external work to ensure that the enthalpy of the air stream does not change between the outlet of the heat exchanger and the point where the temperature (i.e., the enthalpy) of the air stream is measured. Also, like before, each mixing section would have to be followed by a section of flow straightening devices because the performance of the downstream blower is adversely affected by the presence of inlet swirl (AMCA, 1988). Due to the spatial constraints of our lab, it would be difficult to extend the test section tunnels to accommodate the addition of outlet mixing equipment. Hence, as an alternative solution, denser grids of, say, 50 outlet thermocouples per air loop are recommended for future installations. Unfortunately, thermopiles this large also require 50 reference junctions per air loop, or 200 thermocouple junctions in all. Such a setup can be expensive and time consuming to construct, so future users of the test facility may wish to consider using parallel-wired thermopiles instead of series-wired thermopiles. Like a series thermopile, a parallel thermopile yields an N-point average temperature reading from a single voltage reading, but the parallel-wired arrangement requires only one reference junction (as opposed to N reference junctions) to make the measurement (Benedict, 1977). However, one should note that a series thermopile is widely regarded as the most reliable setup for sensing an average temperature (Baker, 1975). The parallel technique is further discussed in Weston (1996).

## 4.2 Transient Capability Tests

The remaining sections of this chapter discuss several of the transient testing capabilities of our facility. Specifically, the sections provide examples of cabin pulldown simulations, clutch cycling scenarios, and vehicle driving simulations. All of the results were generated using the hybrid system. The discussions focus on the evaporator-side data because the evaporator cooling action is considered to be the main performance aspect of the system.

### 4.2.1 Cabin Pulldown Simulations

The term "cabin pulldown" refers to the process by which a vehicle cabin is cooled and dehumidified after having been soaked at a high temperature for an extended period of time (e.g., an automobile which has been parked outdoors on a hot summer day). During a cabin pulldown process, chilled air from the evaporator enters the passenger compartment of the vehicle and receives heat from the thermal loads of the cabin. The heated air stream then recirculates to the inlet of the evaporator and transfers the heat to the refrigerant. As the cabin air continuously

recirculates across the evaporator, the evaporator inlet and outlet air temperatures pull down over time. In our facility, the PID-controlled evaporator air loop heater acts as the thermal load of the cabin. The researcher must supply the controller with an evaporator inlet air temperature setpoint pattern which simulates the desired cabin cooling response. Figure 4.5 shows a plot of the evaporator inlet air temperature response generated in our facility for three simulated pulldown modes. In each case, the evaporator air stream was initially heated to 110 °F and allowed to flow at this temperature for 10–15 min. so as to thoroughly heat the evaporator coil and thermal masses of the surrounding ductwork to the initial temperature. This initial state of the system was recorded for 2 min. to provide a good base of initial conditions for modeling purposes. Then, at time t = 0, the compressor clutch was engaged, and the setpoint pattern for the desired evaporator inlet air temperature response was passed to the heater controller. The other system input conditions were held constant at the values given in Table 4.5. The compressor speed and condenser air flow rate shown in the table are representative of vehicle idle conditions, and the evaporator air flow rate is representative of a typical HIGH blower setting in a vehicle. In each case, the data were sampled at a rate of 0.5 Hz. The cases are further discussed below.

Table 4.5 The system input conditions for the pulldown tests.

| System Input Parameter | Value |
|---|---|
| Compressor Speed | 900 rpm |
| Condenser Air Flow Rate | 800 cfm |
| Evaporator Air Flow Rate | 280 cfm |
| Condenser Inlet Air Temperature | 70 °F (ambient) |
| Metering Valve Position | 3.40 turns open |
| Refrigerant Charge | 2.9965 $lb_m$ |

#### 4.2.1.1 Linear Pulldown Mode

For the first example, the heater controller was programmed to vary the evaporator inlet air temperature linearly from 110 °F to 60 °F over a time period of 14 min. These latter values were selected somewhat arbitrarily due to the lack of actual cabin pulldown data. Although a linear response pattern is probably uncharacteristic of an actual cabin pulldown process, the test reveals an important aspect of our facility—namely, an inherent time delay in the response of the heater controller. To generate the linear pattern, the temperature setpoint was instantly changed from 110 °F to 60 °F upon engagement of the clutch (the controller keypad allows the user to switch between up to eight setpoint values stored in memory), and the SP RAMP parameter of the

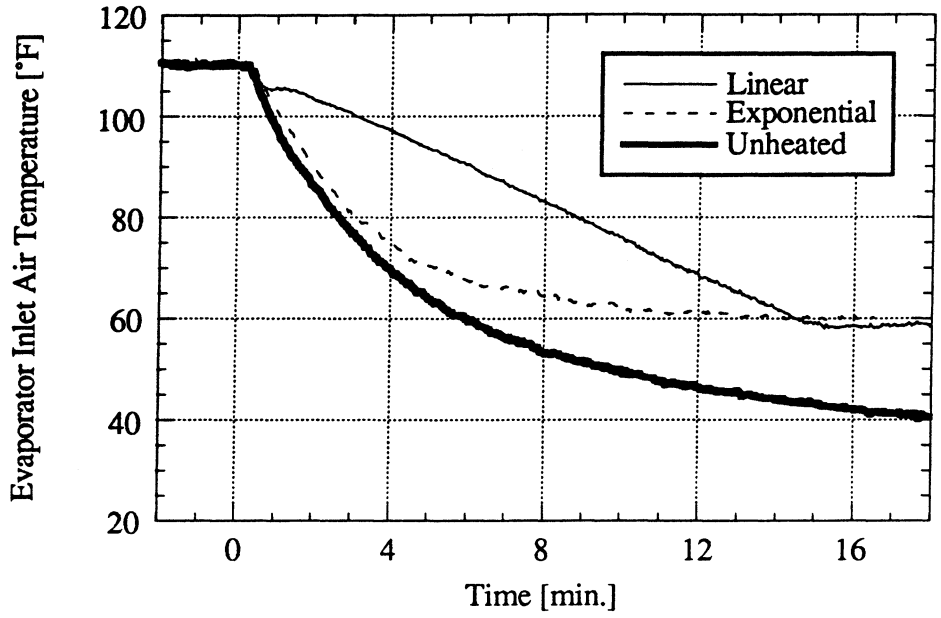


Figure 4.5 The evaporator inlet air temperature response for three cabin pulldown simulations.

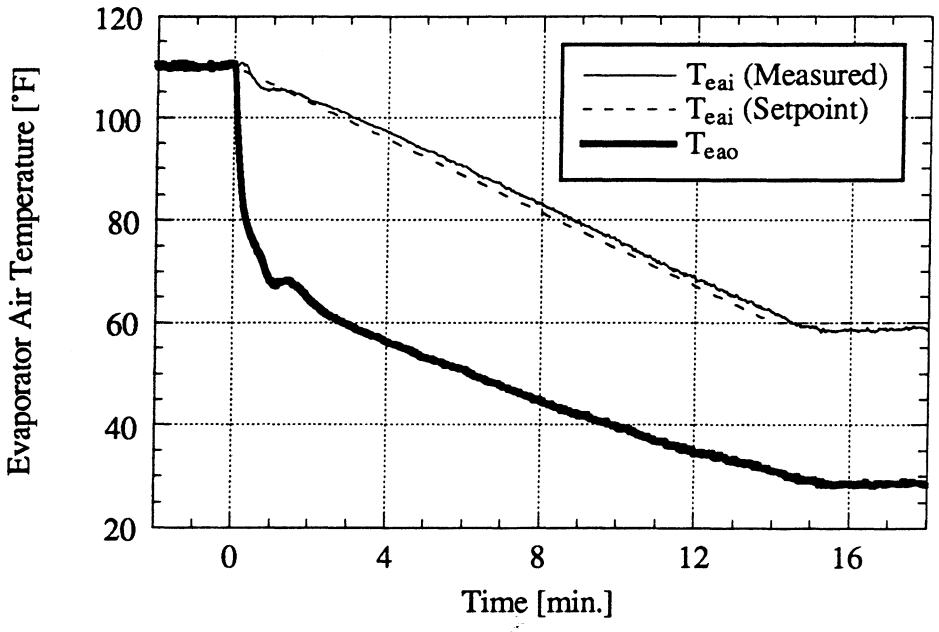


Figure 4.6 The evaporator air-side temperature responses for the linear pulldown mode.

controller was preset to 214 °F/hr (3.57 °F/min.) so that the setpoint ramped down to the new value of 60 °F in 14 min. Mathematically, the setpoint pattern is given by

$$T_{eai} = \begin{cases} 110 & (t < 0) \\ 110 - 3.57\,t & (0 \le t \le 14) \\ 60 & (t > 14) \end{cases} \tag{4.17}$$

where $T_{eai}$ [°F] is the evaporator inlet air temperature, and t [min.] is the elapsed time. The measured response of $T_{eai}$ is plotted against the controller setpoint pattern in Figure 4.6, as is the measured response of the evaporator outlet air temperature $T_{eao}$. The outlet air temperature is seen to drop very sharply upon engagement of the clutch. As a result, the heater output level suddenly becomes insufficient to heat the air stream back to the desired inlet temperature, causing the inlet air temperature to fall faster than the desired rate. The controller does not sense that the heater output needs adjustment until the underheated air stream transports from the heater outlet to the evaporator inlet. Hence, the measured inlet air temperature deviates from the desired setpoint pattern during the first 2 min. of the response and then lags the setpoint pattern by a 24-s transport delay throughout the remainder of the response. In the future, a feedforward control action based upon changes in the outlet air temperature will be added to the heater control loop to help compensate for the transport delay.

#### 4.2.1.2 Exponential Pulldown Mode

In an actual pulldown process, the cabin temperature is more likely to decay exponentially than linearly because the thermal masses of the vehicle cabin can likely be modeled as lumped capacitances. Hence, as a second example, the evaporator inlet air temperature was varied exponentially from 110 °F to 60 °F in accordance with the following setpoint pattern:

$$T_{eai} = \begin{cases} 110 & (t < 0) \\ 110 - 50\,(1 - e^{-t/\tau}) & (t \ge 0) \end{cases} \tag{4.18}$$

The time constant $\tau$ [min.] in Equation 4.18 was chosen to be 3 min. so that the response would be sufficiently close to (i.e., within 94 % of) the asymptotic value of 60 °F after a 14-min. period had elapsed. As in the linear case, the exponential setpoint pattern had to be implemented through manual manipulation of the controller constants because a benchtop device capable of generating an exponential remote setpoint signal was not available. To implement the pattern in the lab, the first 14 min. of the theoretical curve generated by Equation 4.18 were divided into seven linear 2-min. segments. The endpoints of the segments were entered as the eight setpoints which can be stored in the controller's memory, and the slopes of the segments were recorded on paper for use as the setpoint ramping rates. Every two minutes during the test, the setpoint was

changed to the next successive endpoint value, and the SP RAMP parameter was quickly changed to the slope of the approximating segment. The measured response is plotted against the theoretical setpoint pattern in Figure 4.7. The measured response is seen to follow the desired exponential form quite well, even though the setpoint pattern was actually implemented as a series of linear segments. As in the linear pulldown case, the measured response lags the desired pattern by a transport delay of 24 s. The effect of the delay diminishes as the response progresses because the changes in the air-side temperatures become increasingly smaller over time.

#### 4.2.1.3 Unheated Pulldown Mode

Although we are able to simulate several different types of cabin pulldown processes, we cannot simulate a process in which the cabin load cools faster than the thermal masses of our evaporator-side ductwork. To demonstrate this latter fact, a third test was performed in which the heater was turned off (and remained off) after the compressor clutch was engaged. Figure 4.8 shows the resulting evaporator air-side temperature responses. The inlet air temperature falls more slowly than the outlet air temperature because the outlet air stream receives heat from the thermal masses of the ductwork (and, for a brief period, the deactivated heater coils) before recirculating to the inlet. At present, we do not know if the inlet air temperature response plotted in Figure 4.8 is faster than the response which would actually occur in a vehicle given the same operating conditions. If not, then only "slow" cabin pulldown responses can be simulated in our facility. However, one should note that the response plotted in Figure 4.8 is not truly the fastest response which can be generated in our facility for the given set of operating conditions; faster responses can be generated by not allowing the ductwork to soak at the initial temperature before engaging the compressor clutch.

### 4.2.2 Clutch Cycling Scenarios

#### 4.2.2.1 Pressure-Based Clutch Cycle

Mobile a/c systems which utilize an orifice tube and a fixed-displacement compressor will generally have a pressure-sensing clutch cycling switch installed somewhere in the suction line. The switch opens and disengages the compressor clutch whenever the suction pressure falls below a preset level. When the compressor clutch disengages, the high-pressure refrigerant in the condenser blows down into the evaporator, causing the evaporator-side refrigerant pressures and temperatures to rise. The blowdown process continues until the evaporator-side pressures rise above a second (higher) preset level, whereupon the switch closes and re-engages the clutch. The switch remains closed until the compressor suction pulls the refrigerant pressure back below

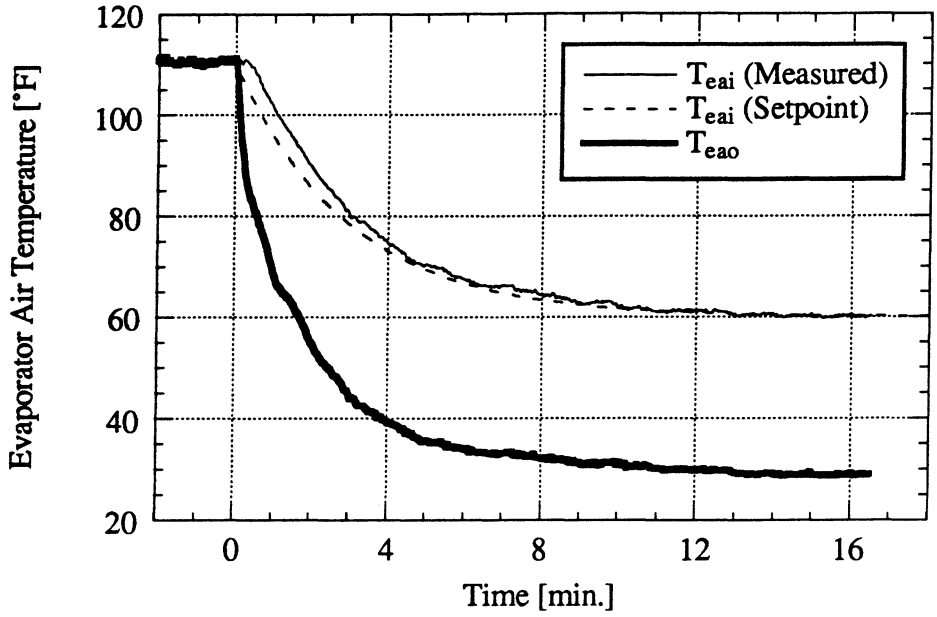


Figure 4.7 The evaporator air-side temperature responses for the exponential pulldown mode.

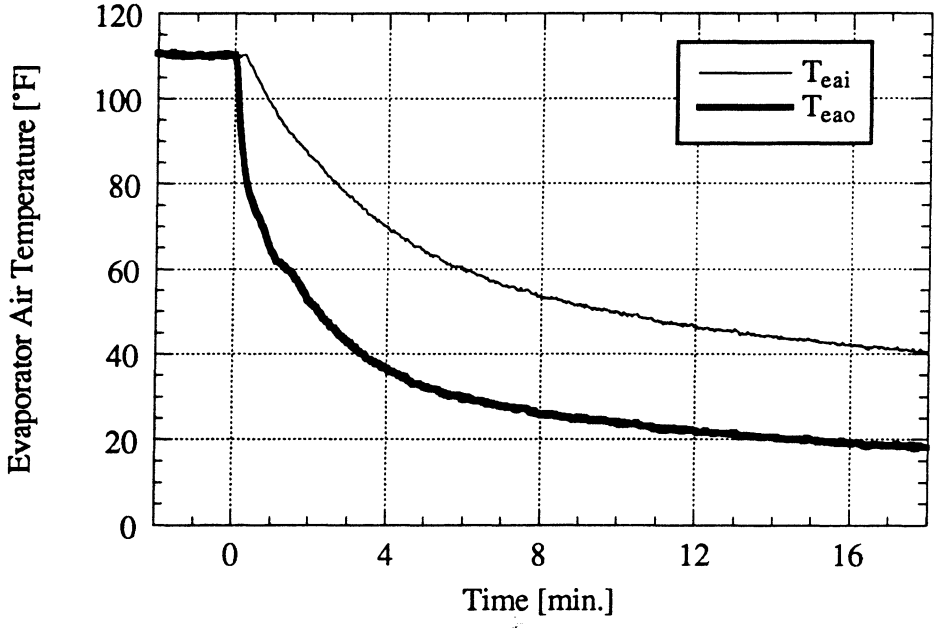


Figure 4.8 The evaporator air-side temperature responses for the unheated pulldown mode.

the lower limit of the switch. The switch action is referred to as "deadband control" because the state of the switch changes only when the suction pressure passes above or below the band of no action (i.e., the deadband) established between the preset limits. By keeping the suction pressure within a specified range, the switch prevents the temperature of the refrigerant within the evaporator from continuously running in a state which is so cold that frost forms on the evaporator surface. Frost blocks air flow through the coil, resulting in a poor cabin cooling response.

To implement a pressure-based clutch cycling scheme in our lab, we wired the SSR of our clutch control circuit to a digital output of the DAS. A deadband control routine built into the STI WorkBench software was used to switch the digital output (and, hence, the clutch) on or off. The evaporator outlet pressure was passed to the routine as the variable to be controlled. The upper and lower limits of the deadband were set to 50 psig and 20 psig, respectively. Actual deadband limits vary by manufacturer and are proprietary. The selected limits correspond to a mean deadband pressure of 35 psig—which, in turn, corresponds to a refrigerant saturation temperature of approximately 40 °F (an arbitrary 8 °F above freezing) for ambient pressures in the range of 14.1 to 14.5 psia (the typical range for our lab). Prior to beginning the test, the evaporator air stream was heated to the desired inlet air temperature with the compressor clutch disengaged, and the initial state of the system was recorded for 2 min. Then, at time t = 0, the compressor clutch control scheme was activated, and the system response was recorded for approximately 20 min. Throughout the course of the test, the system inputs were held constant at the values given in Table 4.6. The data were sampled at a rate of 1 Hz.

Table 4.6 The system input conditions for the clutch cycling tests.

| System Input Parameter | Value |
|---|---|
| Compressor Speed | 1060 rpm |
| Condenser Air Flow Rate | 800 cfm |
| Evaporator Air Flow Rate | 215 cfm |
| Condenser Inlet Air Temperature | 68 °F (ambient) |
| Evaporator Inlet Air Temperature | 90 °F |
| Metering Valve Position | 3.25 turns open |
| Refrigerant Charge | 2.9965 $lb_m$ |

Figure 4.9 shows the measured response of the evaporator outlet air temperature. The response reaches a quasi-steady state (i.e., a repeating, cyclical pattern) after approximately 500 s. In the quasi-steady state, the response exhibits peak-to-peak fluctuations of 15 °F about a mean operating temperature of 53 °F. Such temperature swings are an undesirable attribute of

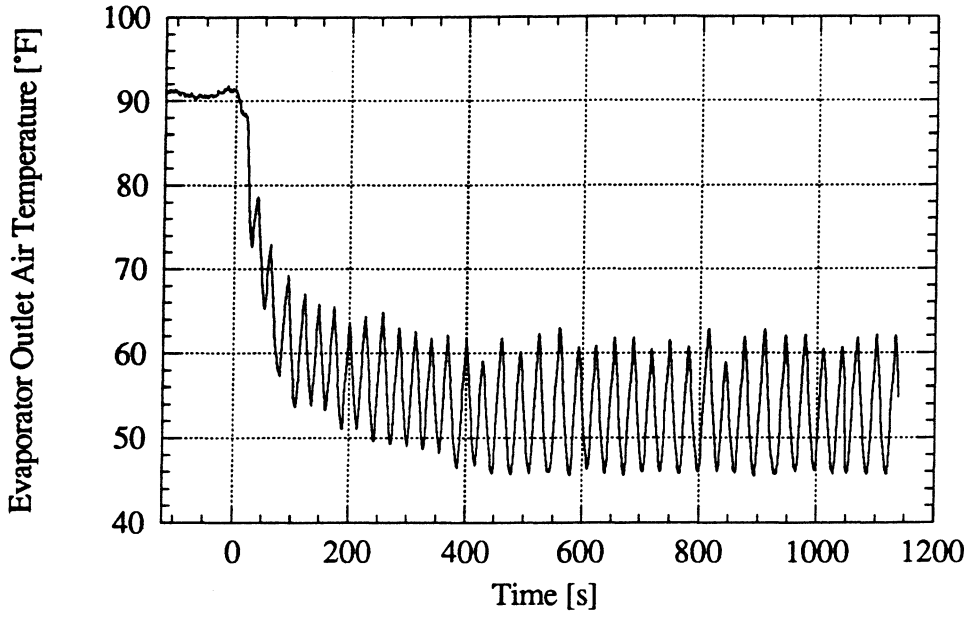


Figure 4.9 The evaporator outlet air temperature response for the pressure-based clutch cycle.

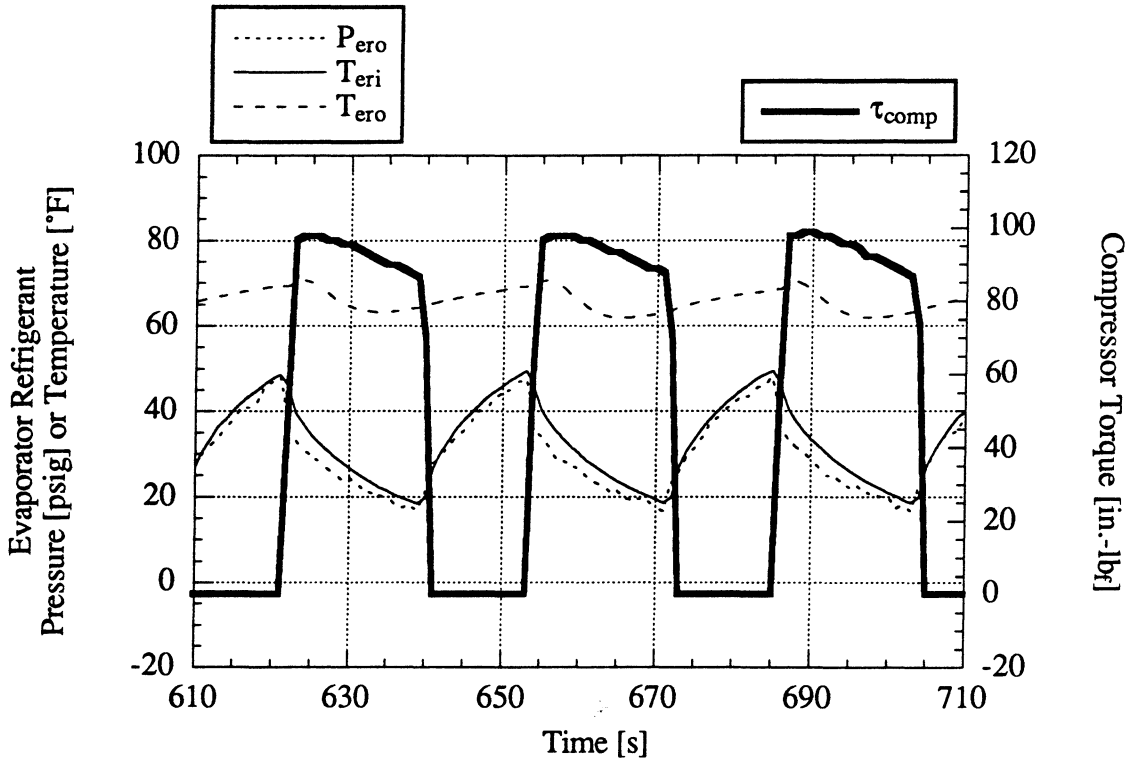


Figure 4.10 The evaporator refrigerant-side pressure and temperature responses for the pressure-based clutch cycle.

cycled-clutch systems because they are noticeable by the occupants of the vehicle. Figure 4.10 shows a plot of a few cycles of the responses of the evaporator outlet refrigerant pressure and the evaporator inlet and outlet refrigerant temperatures. The compressor torque response is overlaid on the plot to indicate the clutch action; a sharp rise in torque indicates engagement of the clutch, whereas a sharp drop in torque indicates disengagement of the clutch. The clutch is seen to properly engage or disengage whenever the evaporator outlet pressure crosses the deadband limits. Close analysis of the figure shows that the measured deadband limits are 1–2 psig less than the preset values of 50 psig and 20 psig. This is because the WorkBench control function utilizes pressure transducer readings which are not corrected for zero-point drift. The compressor requires 19 s to pull the suction pressure (i.e., the evaporator outlet refrigerant pressure) below the lower deadband limit, whereas the blowdown process requires only 13 s to raise the pressure above the upper deadband limit. As a result, the mean evaporator outlet pressure over the course of the cycle is 30.2 psig as opposed to the estimated value of 35 psig. Consequently, the mean evaporator inlet refrigerant temperature over the course of the cycle is 33 °F (i.e., only 1 °F above freezing) as opposed to the estimated value of 40 °F. The inlet refrigerant temperature remains above the freezing mark for 16 s during the 32-s cycle period. Because we do not add moisture to our evaporator air loop, the effects of evaporator frosting have not been observed.

#### 4.2.2.2 Time-Based Clutch Cycles

To further demonstrate the transient capabilities of our test stand, the compressor clutch was cycled according to fixed intervals of ON and OFF times. To do so, the clutch was wired in the same manner as in the pressure-based clutch cycling case, except a square wave generator routine built into the WorkBench software was used to drive the digital output of the DAS. The routine allows the user to set separate durations for the low and high pulses of the square wave and thereby establish separate ON and OFF times for the clutch. The next several sections describe four such time-based clutch cycling cases. In each case, the test conditions were kept the same as in Table 4.6, and the data were again sampled at a rate of 1 Hz. As in the pressure-based clutch cycling example, each response reached a quasi-steady state within a few minutes. The discussions presented below refer to the quasi-steady portions of the responses.

##### 80/20 Time Cycle

For the first example, the was cycled for 80 s ON and 20 s OFF, hereafter referred to as the 80/20 case. During the first 12 s of each 20-s OFF cycle, the liquid-line sight tube exhibited a subcooled liquid flow. The flow then transformed into a plug flow or a stratified flow over the remaining 8 s of OFF time. Refrigerant charge was observed to continuously blow down from

the condenser into the evaporator throughout each OFF cycle (i.e., the blowdown process did not have time to complete before the clutch re-engaged). During each 80-s ON cycle, the liquid-line sight tube became completely flooded within 3–4 s and remained flooded into the next OFF cycle. The evaporator outlet sight tube displayed a very lightly misted refrigerant flow for 20–25 s, and the accumulator outlet sight tube showed an even less misted flow for about 5 s. Thereafter, both of the latter two tubes contained a superheated vapor flow which was invisible to the eye. However, the vapor phase immediately became entrained with large, visible droplets of oil, and oil also began to flow along the walls of the tubes in a thin film. No oil flow was visible in the tubes during the periods of misted flow.

Figure 4.11 shows a plot of a few cycles of the evaporator refrigerant-side temperature responses. As before, the compressor torque response is overlaid on the plot to indicate the ON/OFF action of the clutch. In examining Figure 4.11 and later plots, one may find it convenient to note that the difference between the values of the inlet and outlet refrigerant temperatures is essentially equal to the amount of superheat at the outlet because the inlet refrigerant is saturated, and the pressure drop through the evaporator is relatively small (typically under 2 psid). Returning to Figure 4.11, the evaporator inlet refrigerant temperature rises during each OFF cycle as the warm, high-pressure refrigerant in the condenser blows down into the evaporator. The rising response momentarily dips at the point at which the liquid-line flow was observed to become two-phase. The response then continues to rise with a shallower slope until the compressor clutch engages. We have found that this discontinuous change in slope generally serves as a good indicator that the refrigerant flow at the inlet of expansion device has changed from a subcooled flow to a two-phase flow. When the compressor clutch engages, the inlet refrigerant temperature rises very sharply until the liquid line becomes flooded. The temperature then pulls down to -11 °F as the suction pressure lowers. The outlet refrigerant temperature is seen to remain steady and superheated by 60 °F or more throughout the entire response—this despite the fact that the evaporator outlet sight tube exhibited a lightly misted refrigerant flow for the first 20–25 s of each ON cycle. In light of the large amount of superheat, one may be tempted to conclude that the observed refrigerant mist was actually oil. However, such a conclusion is most likely false; the mist had a cloudy white color consistent with more definitive two-phase misted refrigerant flows, and the droplet size was extremely fine compared to that of any other oil flow we have observed to date. In fact, the visual observations prove that one cannot always rely on quantitative pressure and temperature measurements to identify the state of a transient refrigerant flow, particularly when considering the fact that the refrigerant is not always in a state of thermodynamic equilibrium when the transient measurements are taken. The sight tubes are clearly an invaluable asset to our facility.

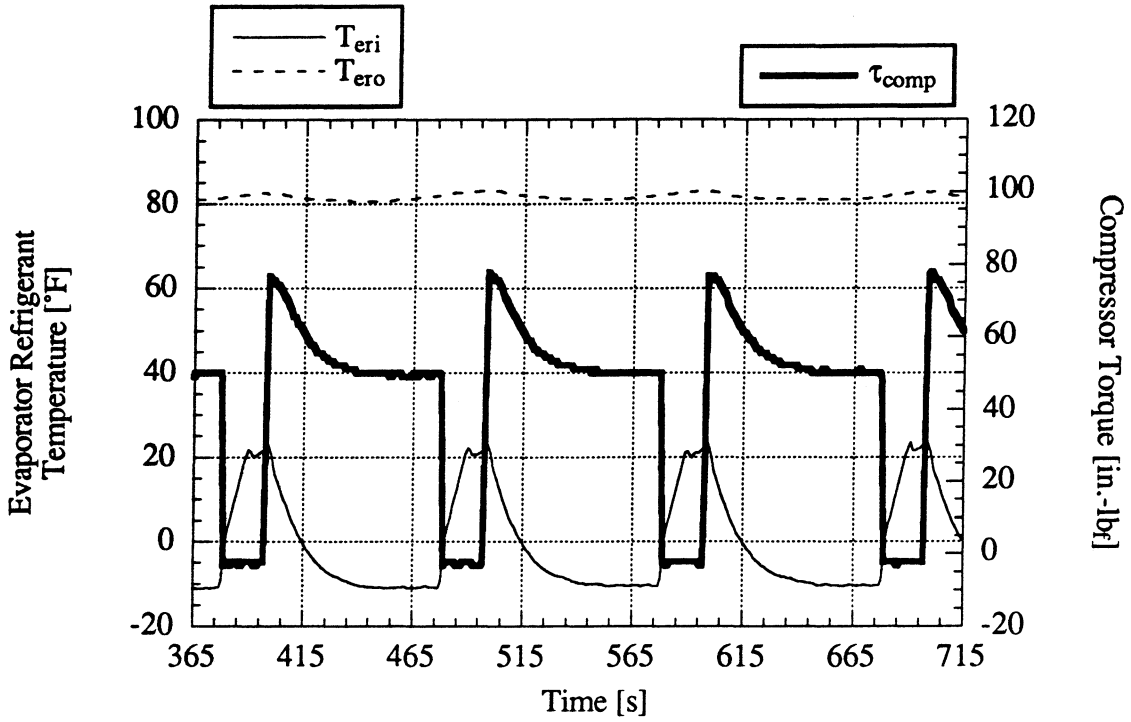


Figure 4.11 The evaporator refrigerant-side temperature responses for the 80/20 clutch cycle.

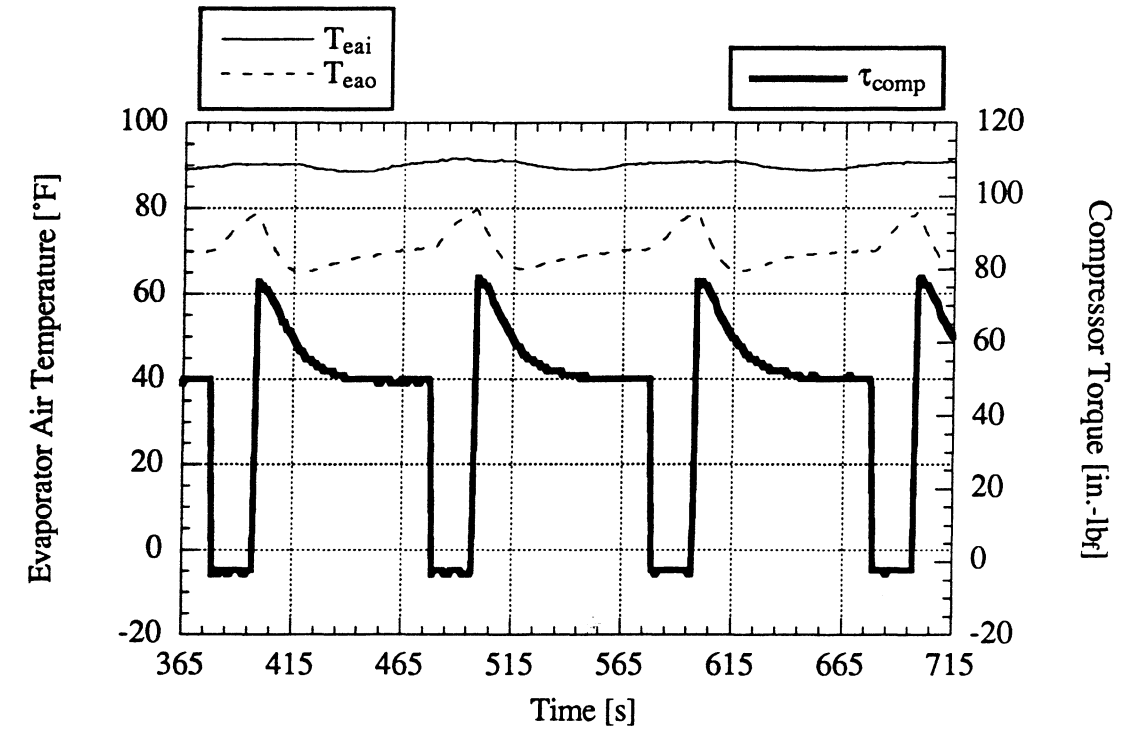


Figure 4.12 The evaporator air-side temperature responses for the 80/20 clutch cycle.

Continuing, Figure 4.12 shows a plot of the evaporator air-side temperature responses. The inlet air temperature is seen to fluctuate by ± 1.5 °F about its setpoint value of 90 °F. Although not of major concern for the case at hand, the inlet air temperature fluctuations can likely be reduced through the addition of a feedforward control action which compensates for the loop transport delay. The fluctuations cannot be completely eliminated because some of the variation is due to the natural settling time of the controller response. The outlet air temperature is seen to exhibit peak-to-peak fluctuations of 15 °F, just as in the pressure-based clutch cycling example. However, in the 80/20 case, the average outlet air temperature (70 °F) is 17 °F warmer than in the pressure-cycled case, even though the system input conditions are the same. This may be somewhat surprising at first, considering the fact that the compressor remains on for 61 s longer (and off for only 7 s longer) than in the pressure-cycled case, and that the average evaporator inlet refrigerant temperature (-1 °F) is 34 °F colder than in the pressure-cycled case. However, the evaporator operates with much more outlet superheat than in the pressure-cycled case, indicating that the evaporator is comparatively starved for refrigerant in the 80/20 case. As one may have expected, the overall cooling response is greatly affected by where the refrigerant charge is distributed throughout the cycle.

20/80 Time Cycle

To further explore the effect that the clutch cycling action has on the refrigerant charge distribution, a second test was performed in which the clutch was cycled for the inverse case of 20 s ON and 80 s OFF. During each 80-s OFF cycle, the liquid-line sight tube displayed a subcooled flow for the first 21 s. The flow then quickly became stratified. The blowdown process visibly ceased after 45–50 s had elapsed. By the end of the blowdown period, the evaporator inlet sight tube had become completely or near-completely flooded with standing liquid. Clearly, a significant redistribution of the refrigerant charge had occurred. In fact, each time the compressor clutch engaged, the needle of the dial-type pressure gage installed at the evaporator inlet would pull down with the suction pressure as usual, but would intermittently pulse to higher values as large quantities of liquid slugged their way into the evaporator. The response sensed by the inlet pressure transducer indicated the same phenomena. This latter response is plotted in Figure 4.13. The liquid-line sight tube became flooded within the first 1.5 s of each ON cycle and remained flooded into the next OFF cycle. The evaporator outlet sight tube immediately showed a heavily misted refrigerant flow upon the engagement of the clutch. The misting steadily decreased over 17–18 s. For the last 2–3 s of each ON cycle, the evaporator outlet sight tube displayed a superheated vapor flow with entrained droplets of oil. The accumulator outlet sight tube also initially showed a heavily misted flow. The misting

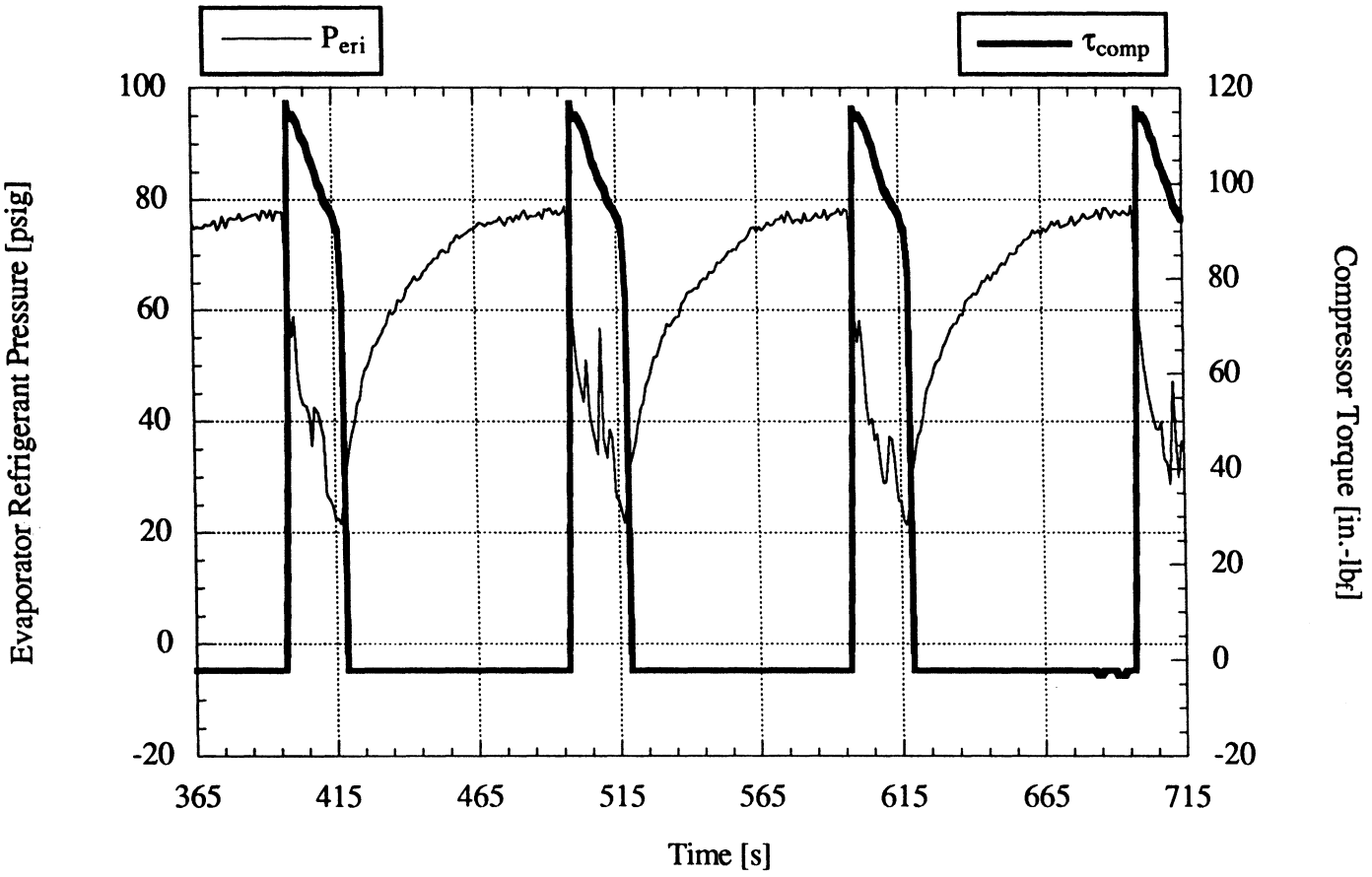


Figure 4.13 The evaporator inlet refrigerant pressure for the 20/80 clutch cycle.

decreased over 10–11 s. Thereafter, this tube also displayed a superheated vapor flow with entrained droplets of oil.

Figure 4.14 shows a plot of the evaporator refrigerant-side temperature responses. During each OFF cycle, the inlet refrigerant temperature rises with a steep slope until the liquid-line flow becomes stratified. The slope then jogs to a shallower value, just as in the 80/20 case. The inlet refrigerant temperature continues to rise until the blowdown process completes, after which the temperature begins to fall. Upon the engagement of the clutch, the inlet refrigerant temperature rises very sharply until the liquid line becomes flooded, again displaying the same behavior as in the 80/20 case. The temperature then falls rapidly to 23 °F. The outlet refrigerant temperature spikes downward toward the saturated inlet refrigerant temperature as the heavily misted saturated flow passes through the outlet. The outlet refrigerant temperature then rises away from the inlet saturation temperature as the flow becomes less misted. Once again, the sight tube observations play an important role in identifying the state of the transient flow. Without knowledge these observations, one may have been falsely led to believe that the evaporator outlet flow was superheated throughout the 20-s ON cycle because the outlet refrigerant temperature always lies above the inlet refrigerant temperature in the plot.

Figure 4.15 shows a plot of the evaporator air-side temperature responses. The outlet air temperature response achieves an average value of 74 °F, which is only 4 °F warmer than in the 80/20 case. This result comes despite the fact that the average evaporator inlet refrigerant temperature (51 °F) is 52 °F warmer than in the 80/20 case. In addition, the outlet air temperature cools by a full 28 °F during the 20-s ON cycle of the 20/80 case, whereas the outlet air temperature cools by a maximum of only 15 °F during the 80-s ON cycle of the 80/20 case. Hence, a more efficient evaporator-side heat transfer occurs in the 20/80 case, most likely because the majority of the evaporator coil remains flooded with saturated refrigerant throughout each ON cycle (superheated refrigerant has a relatively poor heat transfer coefficient). The penalty of running the coil in the flooded state is a higher compressor startup torque. Recall that the accumulator did not prevent the heavily misted flow from entering the compressor at the start of each ON cycle. As a result, the compressor startup torque is 33 % higher than in the 80/20 case. As a final note, because the oscillations in the outlet air temperature are much larger than in the 80/20 case, the fluctuations in the controlled inlet air temperature increase to ± 3 °F, and the need for a feedforward control action becomes more apparent.

8/2 Time Cycle

To explore the effects of varying the total duration of the cycle period, a third test was performed in which the clutch was cycled for 8 s ON and 2 s OFF. That is, the ON/OFF time ratio was kept the same as in the 80/20 case, but the overall period was reduced from 100 s to

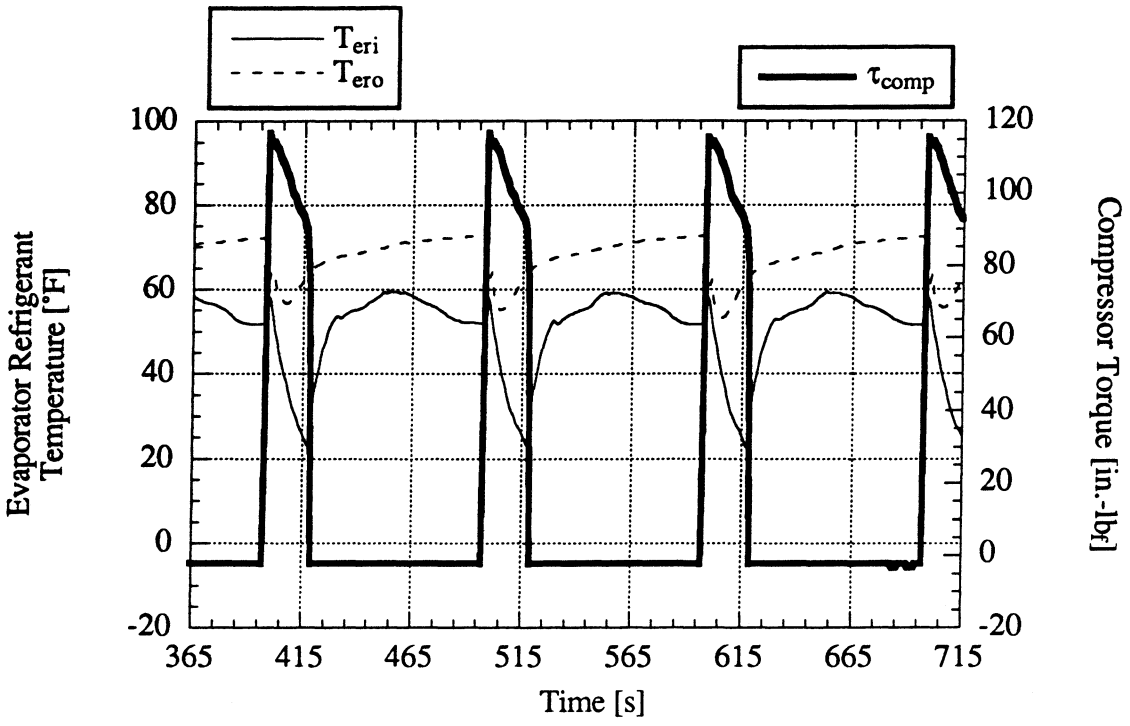


Figure 4.14 The evaporator refrigerant-side temperature responses for the 20/80 clutch cycle.

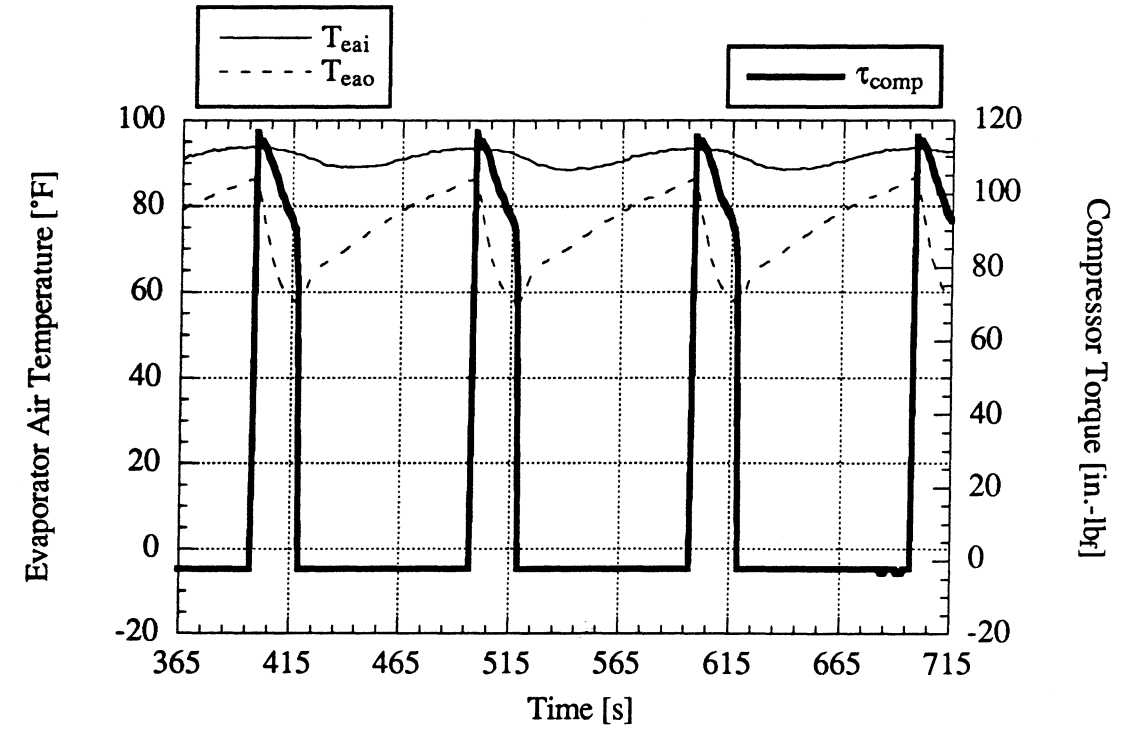


Figure 4.15 The evaporator air-side temperature responses for the 20/80 clutch cycle.

10 s. During the 8/2 test, the liquid-line sight tube exhibited a subcooled liquid flow throughout the entire 10-s period. During each ON cycle, the evaporator outlet sight tube and the accumulator outlet sight tube both displayed a superheated vapor flow with entrained droplets of oil. During each OFF cycle, the oil droplets immediately stopped flowing and gripped the walls of the tubes. The oil remained clinging to walls of the tubes until the clutch re-engaged. This behavior was also observed in the 80/20 and 20/80 cases, but not in the next example.

Figure 4.16 shows a plot of the evaporator refrigerant-side temperature responses. The inlet refrigerant temperature fluctuates by less than 8 °F, and the outlet refrigerant temperature is seen to be smooth and superheated at all times. Figure 4.17 shows a plot of the evaporator air-side temperature responses. The outlet air temperature is seen to be extremely steady and much colder than in the 80/20 case, even though the refrigerant stream always enters the evaporator at a warmer temperature than in the 80/20 case. The startup torque is seen to be very similar to that of the 80/20 case. In short, the 8/2 case makes much better use of the evaporator by running with less outlet superheat, but still maintains enough superheat to prevent excessive startup torques.

2/8 Time Cycle

For the last example, the clutch was cycled for the inverse short-period case of 2 s ON and 8 s OFF. During each OFF cycle, a wave of subcooled liquid refrigerant sloshed toward the expansion device and backfilled the pipe, causing the liquid-line sight tube to become flooded for approximately 2 s. After 2 s, the flow became a plug or stratified flow. During each ON cycle, the liquid-line sight tube continued to show a plug or stratified flow, while both the evaporator and accumulator outlet sight tubes showed a very heavily misted flow. Each time the clutch disengaged, the flow in the latter two tubes immediately stopped, and a thick, viscous coating of oil and liquid refrigerant remained on the walls. The liquid mixture then seeped down the walls and formed a standing river at bottom of each tube. When the clutch re-engaged, the surge of heavily misted flow swept the standing liquid into the accumulator and compressor. This flow pattern was much different than the flow patterns observed in any of the previous cases.

Figure 4.18 shows a plot of the evaporator refrigerant-side temperature responses. The inlet and outlet temperatures are seen to coincide at all times, indicating the complete absence of superheat throughout the entire cycle period. The startup torque is seen to be similar to the 20/80 case, in which a heavily misted flow was also observed to enter the compressor. Figure 4.19 shows a plot of the evaporator air-side temperature responses. The outlet air temperature is seen to be smoother and (on the average) colder than in the 80/20 and 20/80 cases, even though the evaporator inlet refrigerant temperature is always warmer than in those cases. The results of the 8/2 and 2/8 cases indicate that pulsing the clutch over a short time period is perhaps a viable method of obtaining a cool, stable outlet air temperature response through efficient use of the

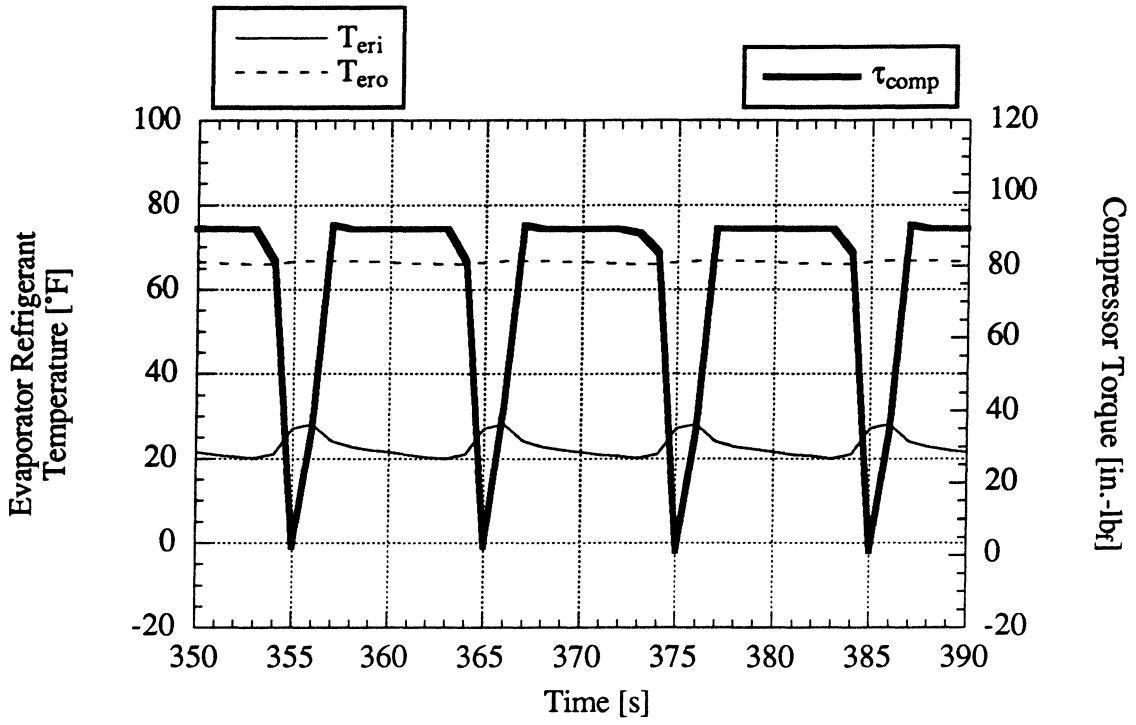


Figure 4.16 The evaporator refrigerant-side temperature responses for the 8/2 clutch cycle.

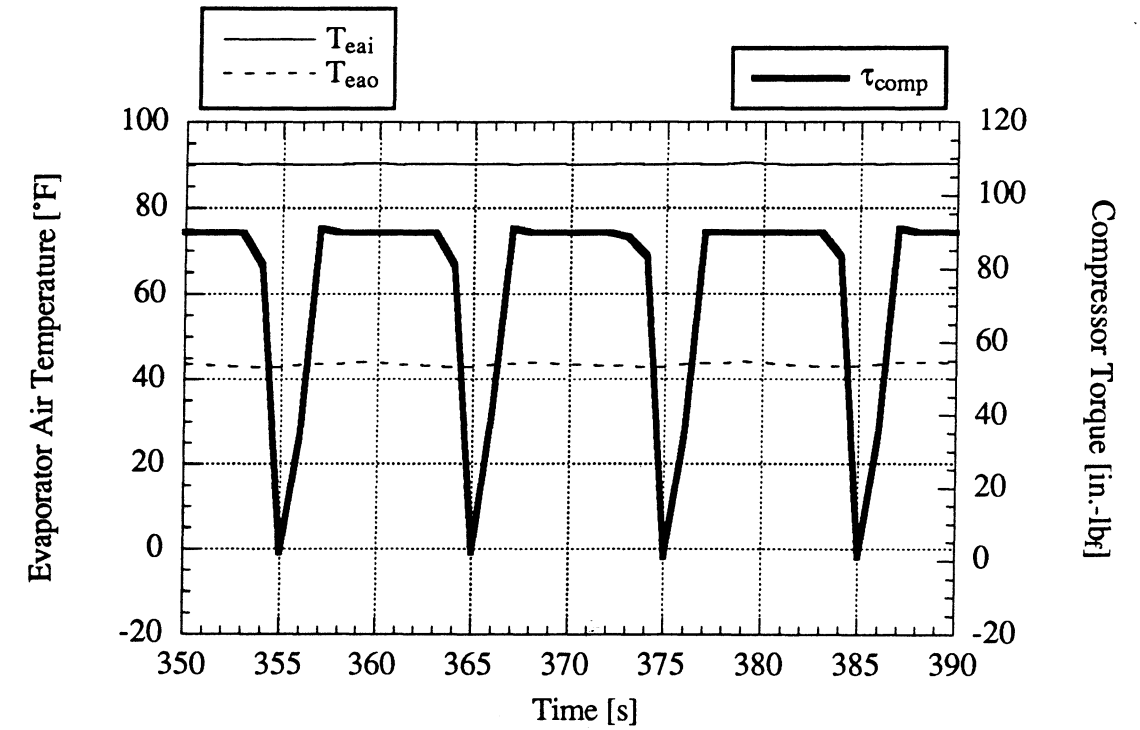


Figure 4.17 The evaporator air-side temperature responses for the 8/2 clutch cycle.

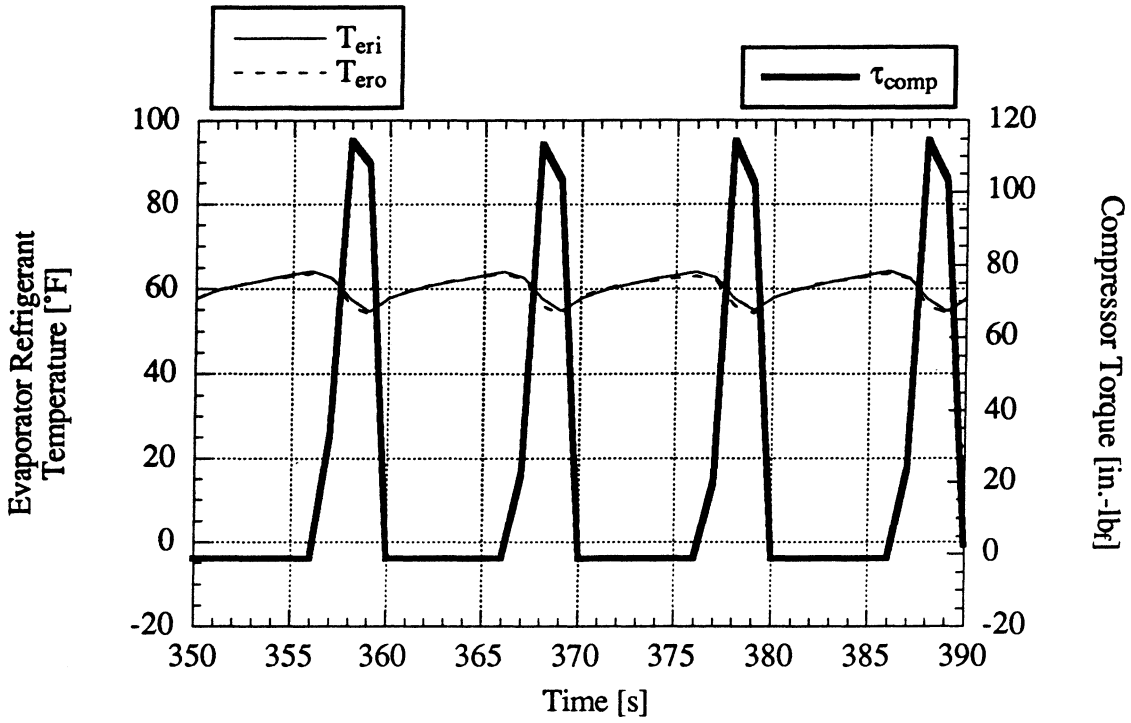


Figure 4.18 The evaporator refrigerant-side temperature responses for the 2/8 clutch cycle.

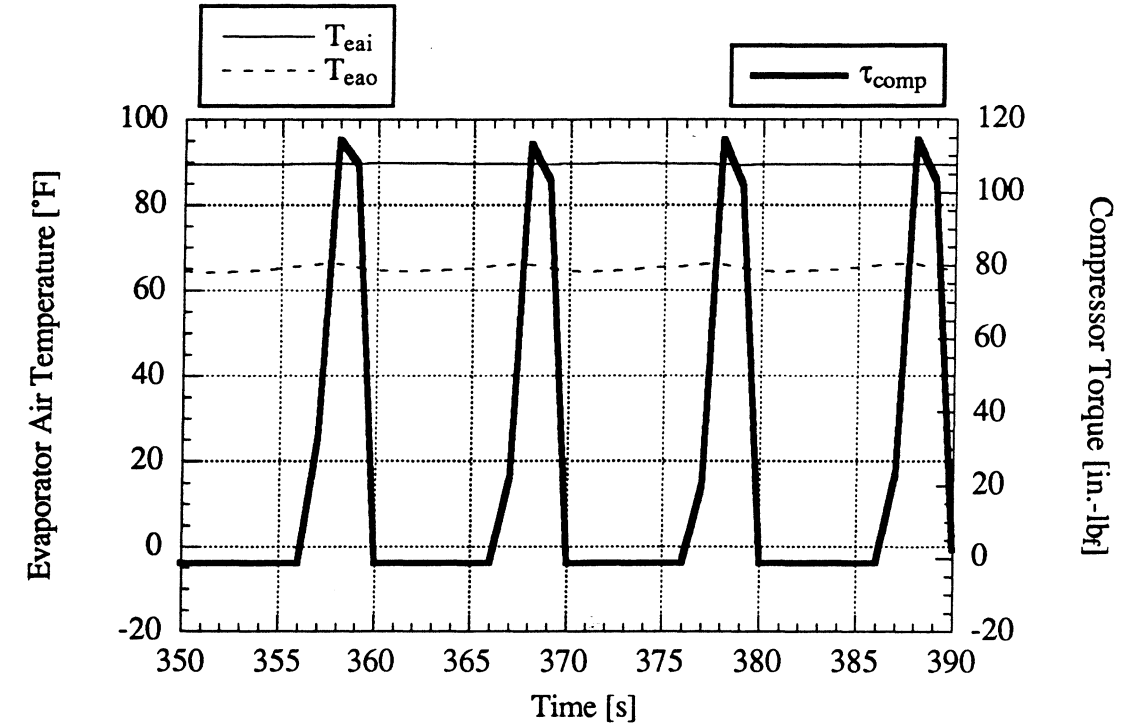


Figure 4.19 The evaporator air-side temperature responses for the 2/8 clutch cycle.

evaporator. In actual practice, the frequent pulsing action would probably cause excessive clutch wear and noticeable surges in the vehicle engine load, particularly if the refrigerant distribution promoted a high compressor startup torque such as in the 2/8 case. At any rate, our facility has been shown to be a valuable tool for generating both the qualitative and quantitative data necessary to evaluate such an operating scheme.

### 4.2.3 Simulated Driving Cycles

The term "driving cycle" refers to any random or deterministic sequence of changes in the operating speed of a vehicle (e.g., the random speed changes which occur when driving in stop-and-go traffic, or the relatively repetitive speed changes which occur when driving between a series of stoplights). The vehicle speed has a significant impact upon the performance of the a/c system because the a/c compressor is driven by a belt from the vehicle's engine. Hence, the compressor speed changes whenever the vehicle operator accelerates, brakes, or shifts gears throughout the driving cycle. The condenser air flow rate also changes throughout the driving cycle because the amount of air forced through the condenser (i.e., the "ram-air" supply) varies in proportion with the speed of the vehicle. To simulate a driving cycle in our lab, we wired the remote-setpoint input terminals of the compressor motor speed controller and the condenser blower speed controller to a 5-VDC digital output of the DAS. The square wave generator routine built into the WorkBench software was used to drive the output. The parameters of each speed controller were set such that the 0- and 5-VDC plateaus of the square wave corresponded to drive frequencies which represented idling and running conditions, respectively. Table 4.7 lists these conditions along with the values of the other system inputs. The durations of the low and high segments of the wave were selected in the DAS software to be 30 s and 135 s, respectively. The acceleration time and acceleration pattern parameters of each speed controller were set such that the motors linearly accelerated from the idling condition to the running condition in 15 s when the input signal changed from 0 VDC to 5 VDC. The deceleration parameters were set such that the motors linearly decelerated from the running condition to the idling condition in 10 s when the input signal changed from 5 VDC to 0 VDC.

Figure 4.20 shows a plot of the measured responses of the compressor speed and the condenser air flow rate. The driving cycle emulates a case in which a vehicle idles at a stop sign for 20 s, accelerates to a running condition in 15 s, runs for 120 s, and then decelerates to another stop sign in 10 s. The cycle then repeats. Two examples were performed using the driving-cycle input of Figure 4.20: one with clutch cycling, and the other without. Prior to beginning each test, evaporator air stream was heated to the desired inlet air temperature with the compressor clutch disengaged, and the initial state of the system was recorded for 2 min. Then, at time t = 0, the driving-cycle input signal was activated starting from the beginning of the idling period, and

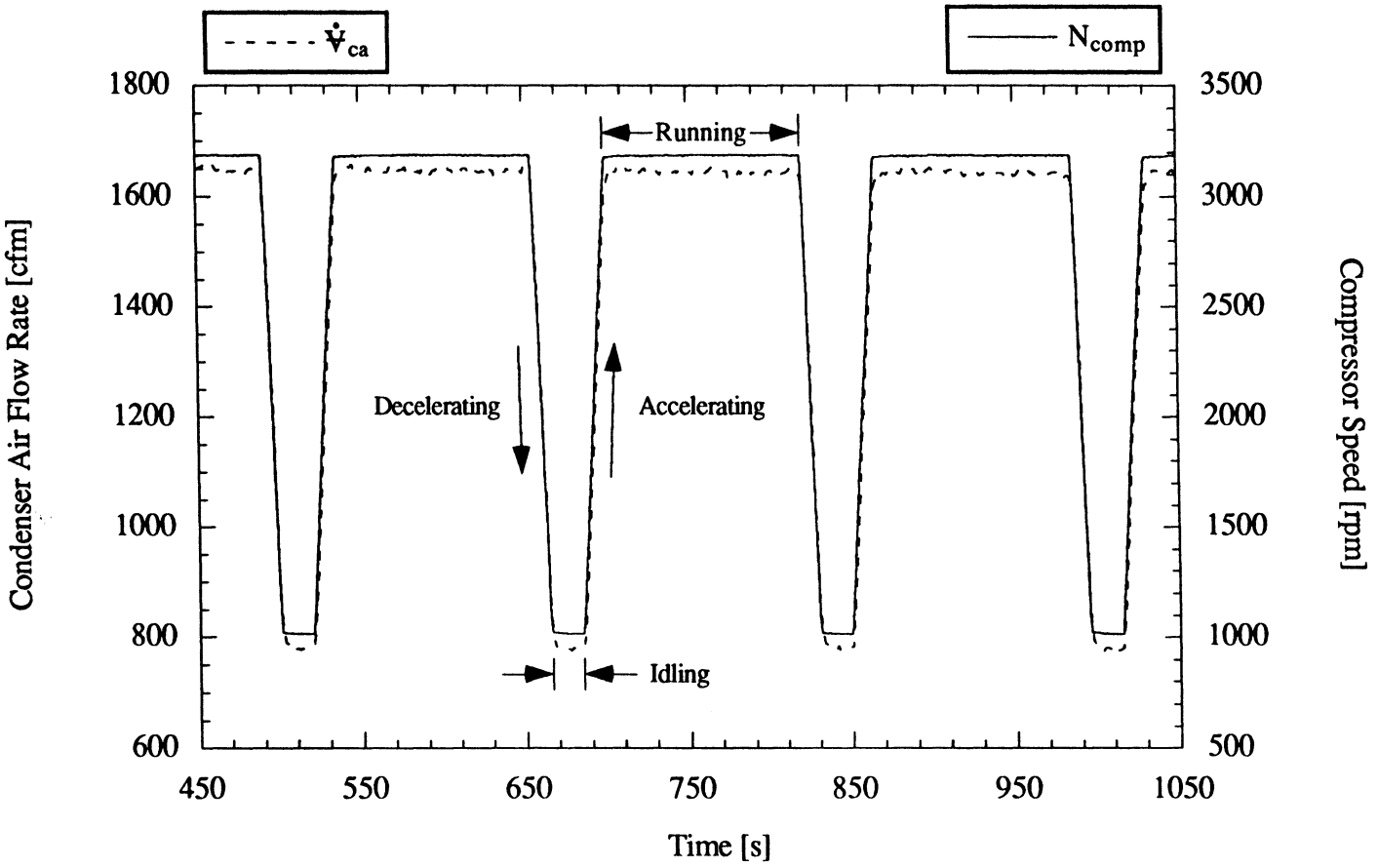


Figure 4.20 The input patterns of the simulated driving cycle.

the compressor clutch was either engaged manually or placed under computer control. The system response was then recorded for approximately 20 min. In each case, the data were sampled at a rate of 1 Hz.

Table 4.7 The system input conditions for the driving cycle tests.

| System Input Parameter | Value |
|---|---|
| Compressor Speed | Idling: 1015 rpm<br>Running: 3185 rpm |
| Condenser Air Flow Rate | Idling: 780 cfm<br>Running: 1645 cfm |
| Evaporator Air Flow Rate | 215 cfm |
| Condenser Inlet Air Temperature | 70 °F (ambient) |
| Evaporator Inlet Air Temperature | 90 °F |
| Metering Valve Position | 4.50 turns open |
| Refrigerant Charge | 2.9965 $lb_m$ |

4.2.3.1 Simulated Driving Cycle without Clutch Cycling

For the first example, the compressor clutch was kept continuously engaged throughout the simulated driving cycle. The system reached a quasi-steady state after three driving-cycle periods had elapsed. Figure 4.21 shows a plot of the condenser refrigerant-side temperature and pressure responses for a few cycles during the quasi-steady state. The condenser outlet pressure response has the same shape and phasing as the inlet pressure response and is not plotted in the figure so as to maintain the readability of the plot. The compressor speed response is overlaid on the graph so that the reader can identify the various segments of the driving cycle. The reader should keep in mind that the condenser air flow rate is simultaneously changing in the same pattern. As is shown in Figure 4.21, when the compressor decelerates from the running condition to the idling condition, the condenser inlet refrigerant temperature decreases, which is a natural result of the fact that the compressor performs less work on the refrigerant per unit time at the lower speed. The condenser outlet refrigerant temperature rises by approximately 5 °F during the idling period due to the decrease in the condenser air flow rate (i.e., due to the decrease in the rate at which heat is removed from the refrigerant stream). Despite the decrease in the heat transfer rate, the condenser outlet flow was observed to remain subcooled throughout the entire cycle period. The condenser inlet and outlet pressures remain at the approximately the same values as during the running period, indicating that with regard to pressure, the decrease in compressor speed (which generally causes a decrease in the condenser-side pressures) is counterbalanced by the decrease in the heat transfer rate. Consequently, the liquid-line flow rate

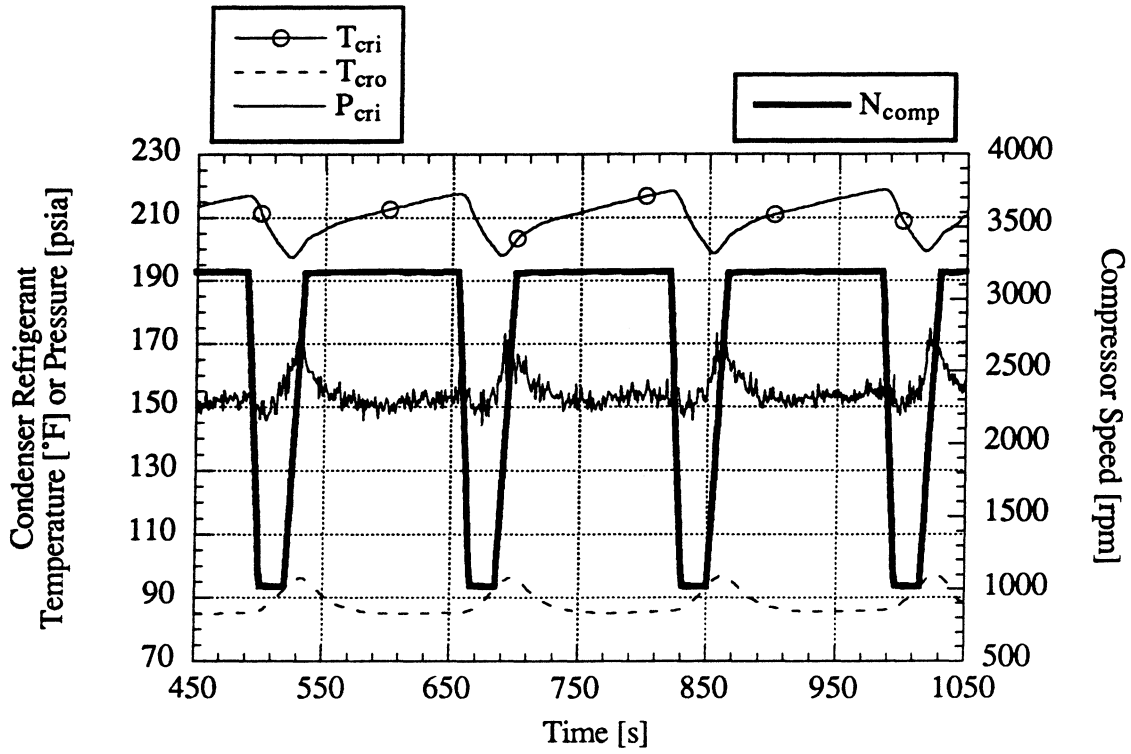


Figure 4.21 The condenser refrigerant-side temperature and pressure responses for the simulated driving cycle performed without clutch cycling.

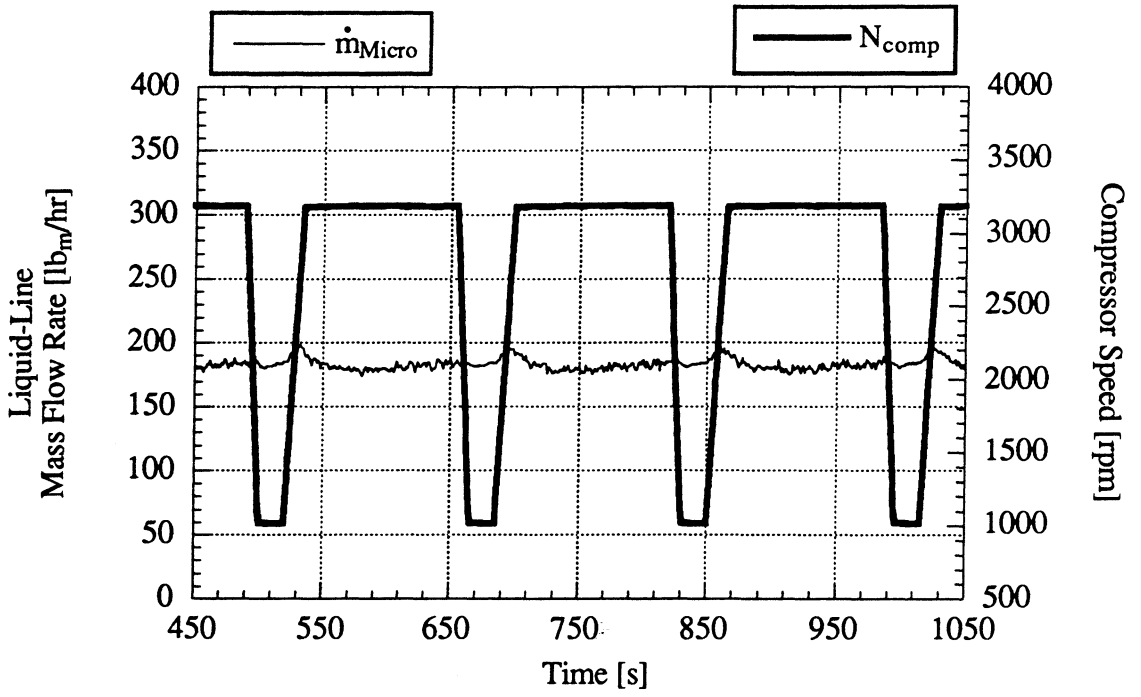


Figure 4.22 The liquid-line mass flow rate for the simulated driving cycle performed without clutch cycling.

remains the same as during the running period because the metering valve remains choked at the same inlet pressure. The liquid-line flow rate (as given by the Micro Motion flow meter) is plotted in Figure 4.22. When the compressor speed and the condenser air flow rate accelerate from the idling condition to the running condition, the compressor work rate increases, and this effect initially dominates over the effect of the increase in the condenser air flow rate. As a result, the condenser-side refrigerant temperatures and pressures rise during the acceleration period, and the liquid-line flow rate rises in accordance with the increase in pressure at the inlet of the metering valve. The variables settle back to their former values as the effect of the increased condenser-side heat transfer rate becomes more predominant.

Figure 4.23 shows a plot of the evaporator refrigerant-side temperature responses. The evaporator refrigerant-side pressure responses have the same shape and phasing as the inlet refrigerant temperature response plotted in the figure. When the compressor decelerates from the running condition to the idling condition, the suction-line flow rate naturally decreases, thereby causing the evaporator volume to flood with refrigerant (recall that the evaporator inlet flow rate (i.e., the liquid-line flow rate) does not decrease along with the compressor speed in this case). As the evaporator volume fills, the pressure and temperature of the saturated evaporator inlet refrigerant stream correspondingly increase, thereby decreasing the potential for heat transfer between the hot inlet air stream and the now warmer refrigerant stream. Hence, during the idling period, the evaporator outlet refrigerant temperature plummets from a superheated temperature down to the inlet saturation temperature, and a low-quality two-phase flow forms at the evaporator outlet. The temperature of the saturated, two-phase outlet refrigerant flow pulls down with the suction pressure during the acceleration period, but the flow returns to a superheated state during the running period as the heat transfer potential is restored. Figure 4.24 shows plot of the evaporator air-side temperature responses. The outlet air temperature rises by 7 °F during the idling period but quickly returns to the main operating value of 27 °F at the onset of the running period.

#### 4.2.3.2 Simulated Driving Cycle with Clutch Cycling

For the second example, the pressure-based clutch cycling scheme discussed earlier in this chapter was used to regulate the compressor clutch throughout the simulated driving cycle. Figure 4.25 shows a plot of the evaporator refrigerant-side temperature responses. The clutch cycling action dominates the dynamics of the responses and induces large fluctuations in the evaporator refrigerant temperatures. The clutch cycling action also induces small fluctuations in the compressor speed response because each time the clutch engages, the sharp increase in operating torque generates excess slip between the rotor and the stator of the drive motor. The

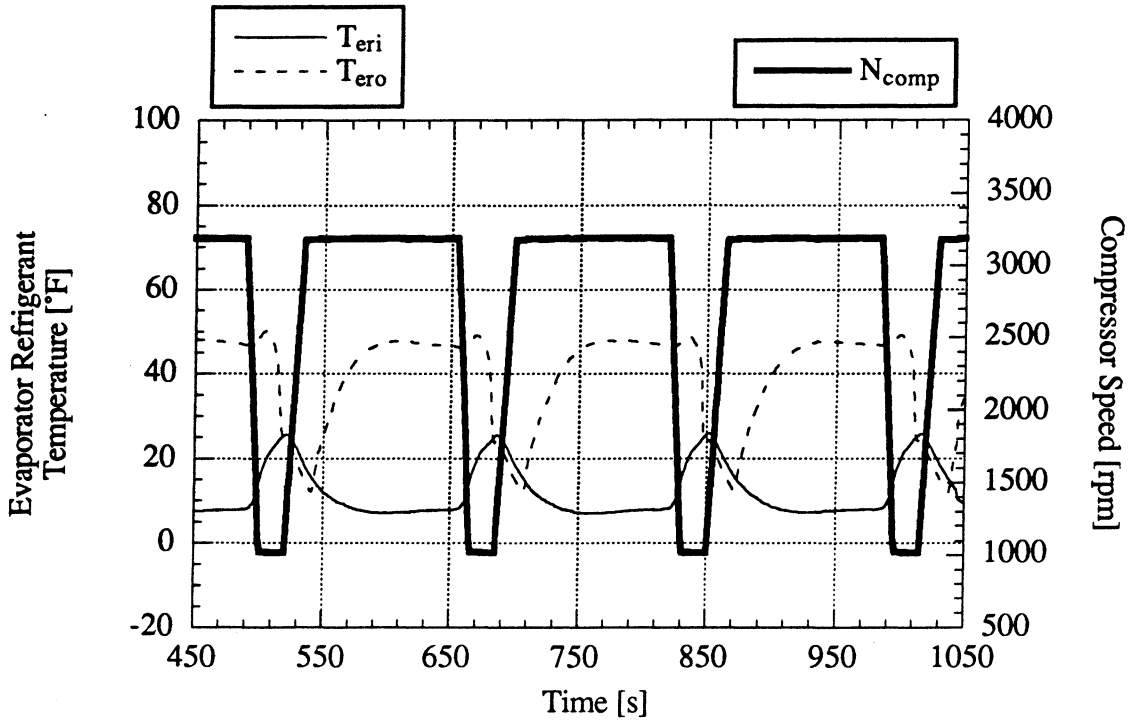


Figure 4.23 The evaporator refrigerant-side temperature responses for the simulated driving cycle performed without clutch cycling.

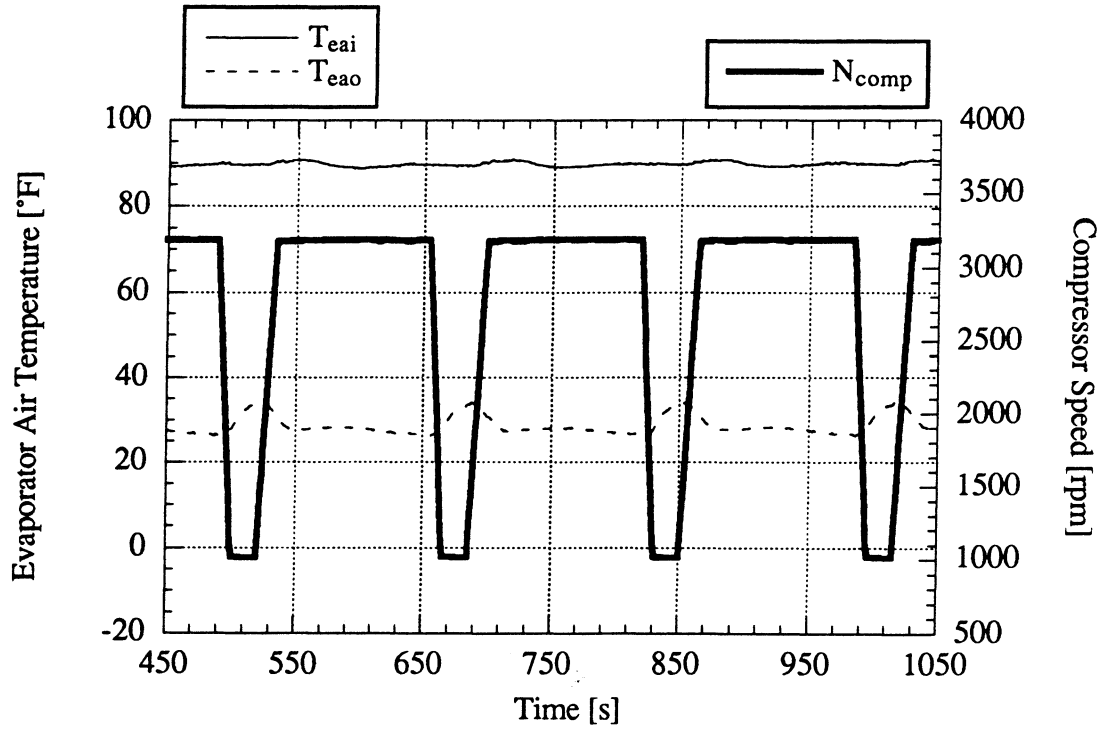


Figure 4.24 The evaporator air-side temperature responses for the simulated driving cycle performed without clutch cycling.

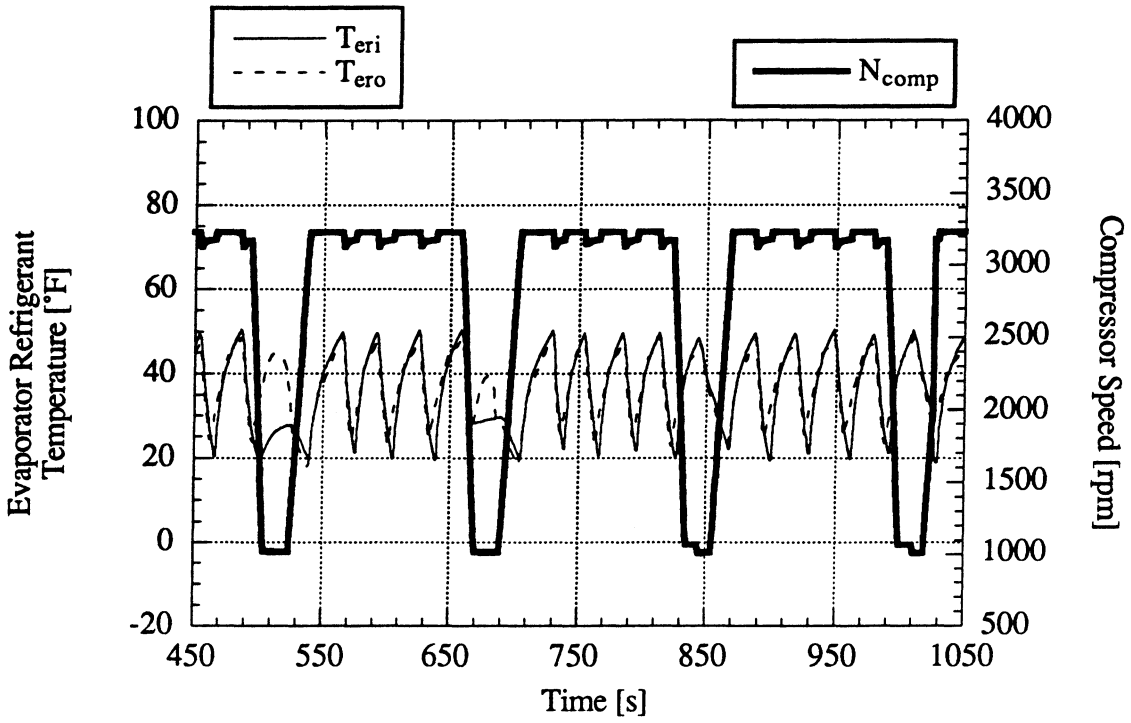


Figure 4.25 The evaporator refrigerant-side temperature responses for the simulated driving cycle performed with pressure-based clutch cycling.

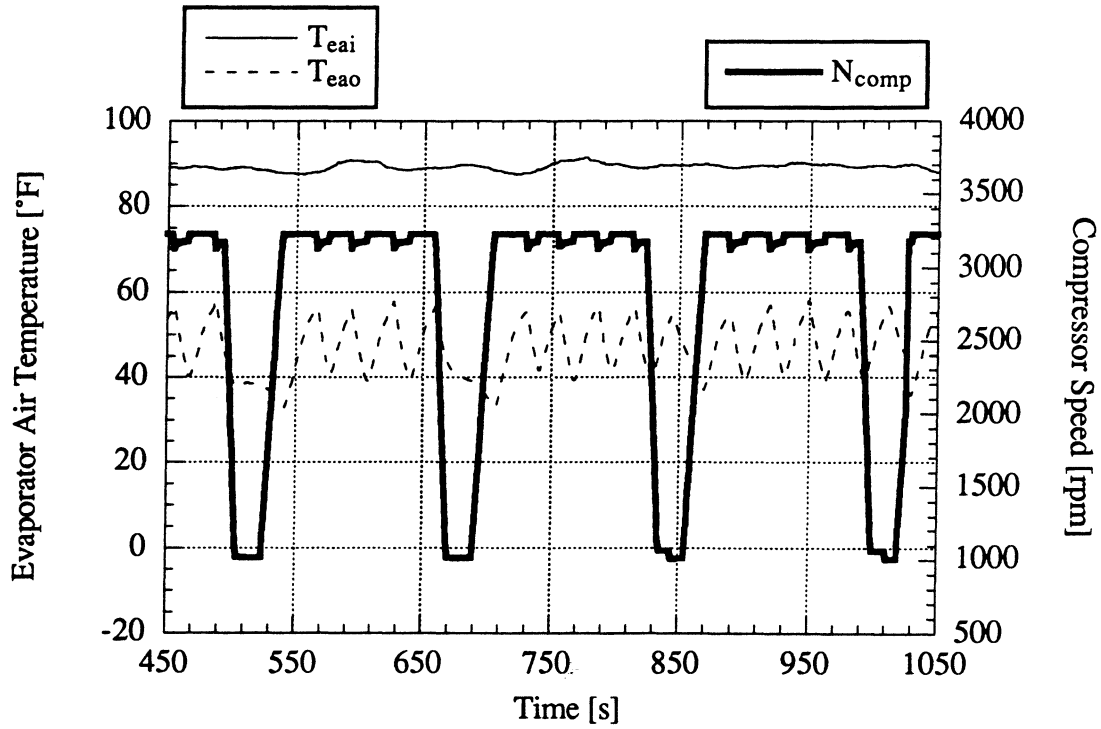


Figure 4.26 The evaporator air-side temperature responses for the simulated driving cycle performed with pressure-based clutch cycling.

compressor speed fluctuations can be reduced in the future by adding a tachometer feedback loop to the drive setup.

Figure 4.26 shows a plot of the evaporator air-side temperature responses. The outlet air temperature fluctuates by up to 20 °F and is always warmer than in the uncycled-clutch example. Recall that the purpose of the pressure-based clutch cycling scheme is to prevent frost from accumulating on the surface of the evaporator. The smoother, colder outlet air temperature response achieved in the uncycled-clutch example is obviously more desirable from a customer-perceived performance standpoint, but the evaporator would be greatly susceptible to frost formation under high-humidity conditions. By installing a humidity addition and control scheme in our evaporator air loop in the future, we will be able to better simulate the full dynamic behavior of actual operating scenarios.

# 5. CONCLUSIONS AND RECOMMENDATIONS

## 5.1 Conclusions

A versatile experimental facility has been designed for testing the transient behavior of mobile air conditioning systems. The air- and refrigerant-side loops of the facility are thoroughly instrumented and can accommodate the components of nearly any stock mobile a/c system. The design makes extensive use of sight tubes, electronic transducers, and controlled input devices which allow the researcher to generate and record a wide range of qualitative and quantitative data. However, steady-state validation tests revealed that the evaporator- and condenser-side energy balances are consistently in error by 11.5 % and 16.6 %, respectively, indicating that systematic errors exist in the data which must be identified and corrected in future work. Some possible sources of error were discussed in Chapter 4, and an extensive list of improvements to reduce these and other errors is given below. Transient demonstration tests proved that the facility is capable of generating a vast array of useful transient data and can simulate many of the transient operating scenarios encountered by mobile a/c systems in the field. Once the environment controller is installed and operating along with an evaporator-side humidity addition and control scheme, our facility will be a powerful and flexible tool for accurately simulating a wide variety of real-world conditions.

## 5.2 Recommendations

Present and future users of the test facility may find the following list of recommendations helpful in reducing the energy balance errors and improving the general quality of the data and the facility as a whole. Many of the suggestions given below are reiterated from previous discussions.

### 5.2.1 Temperature Measurements

- Calibrate all of the thermocouple circuits to account for installation effects and manufacturer variability in the compositions of the wires.
- Configure the DAS to log the output voltages of the thermocouple circuits as opposed to the present practice of logging the screen display temperatures calculated from the reduced-order versions of Equations 3.26 and 3.31. Use the higher-order NIST polynomials (or, when available, in-house calibration polynomials) to compute the temperatures from the logged voltages in all off-line data reduction calculations.
- Shield the thermocouple wires and probes to prevent pickup of non-60 Hz noise signals generated by the motor speed controllers. The integrating A/D converter of the STI DAS cannot attenuate noise frequencies which are not multiples of 60 Hz.

- Replace the single thermocouple at the inlet of each heat exchanger with, say, a nine-point bath-referenced thermopile of the series or parallel type so as to measure a spatially averaged inlet air temperature as opposed to a single-point temperature. Ultimately, in each air loop, a section of mixing vanes (e.g., an array of small muffin fan blades, such as those used to cool computer power supplies and circuit boards) should be added to the entrance section to reduce or eliminate stratification at the heat exchanger inlet. Recall that if a mixing section is added, a section of flow straightening devices (e.g., a bank of straws or a sheet of honeycomb material) must be installed downstream of the mixing equipment to prevent swirl from destroying the uniformity of the heat exchanger inlet velocity profile. Be aware that the added pressure drops of the mixing equipment and the flow straightening devices will decrease the maximum flow rate obtainable from the blower. Hopefully, the blowers have been oversized enough to allow the addition of such equipment.
- Replace the nine-point thermopile at the outlet of each heat exchanger with, say, a 50-point bath-referenced thermopile of the series or parallel type to give a more accurate reading of the average outlet air temperature. Ultimately, each grid of outlet junctions should be preceded by an insulated section of mixing vanes to reduce stratification in the outlet air temperature profile. Again, each mixing section must be followed by a section of flow straightening devices to prevent swirl from degrading the performance of the downstream blower.
- Install a fine-mesh polypropylene screen upstream of the outlet air temperature grid of each heat exchanger to flatten the velocity profile entering each grid. On the evaporator side, the addition of such a screen would also help keep condensed moisture from spitting off the evaporator surface onto the thermocouples of the grid. On the condenser side, such a screen would help shield the thermocouples from condenser surface radiation.
- Install an array of probe ports at the outlet of each heat exchanger so that the outlet air temperature and velocity profiles can be traversed.
- Use silicone oil in the thermocouple reference bath instead of water. Silicone oil has a higher thermal conductivity than water (i.e., it better attenuates temperature gradients) and does not evaporate over time (i.e., it does not require maintenance).
- Calibrate the RTD's, and program the RTD resistance measurement algorithm into the data reduction code so as to eliminate the present practice of using the STI WorkBench routine. Use the in-house calibration equations (or, pending the calibrations, Equation 3.47) to convert the calculated RTD resistances to temperatures.
- Add a thermocouple to the evaporator drain pan to measure the temperature of the escaping condensate. This will yield a more accurate value for the enthalpy of the condensate ($h_w$).

- Use Teflon compression ferrules when installing refrigerant-side thermocouple probes in the future. Brass ferrules permanently crimp to the probe and cannot be removed, making it difficult to reuse the probe at a different immersion length (thermocouple probes are no small expense and should be reused whenever possible).

### 5.2.2 Pressure Measurements

- Return the four Setra Model 228-1 pressure transducers used in the refrigerant loop to the manufacturer for inspection and repair. Specifically, the internal Viton O-ring of each transducer should be replaced with a Buna-N O-ring to ensure compatibility with R-134a. The sensors also use external Viton O-rings which seal the transducer bleed screws. These latter O-rings were replaced in-house and do not require service.
- Recalibrate the 4–20 mA pressure transducers with the shunt loads intact. Recall that for all future tests conducted with the STI DAS, the 2.5-Ω shunts should be replaced with 25-Ω shunts to minimize the uncertainties in the measurements.
- Install low-pass filters across the outputs of the ΔP transducers of the refrigerant-side VFT's to prevent high-frequency pressure pulsations from being aliased into the data. Each filter should have a stable DC gain of 0 dB, and each filter should be wired through a bypass switch so that the researcher can easily exclude the filter from the circuit to measure the natural dynamics of the response.
- Determine if the refrigerant-side pressure measurements are affected by the presence of compressor oil. For example, it may be necessary to replace the 1/8-in. O.D. (0.065-in. I.D.) pressure transmission lines with larger diameter lines to avoid pressure measurement errors caused by oil surface tension effects within the lines.
- Replace all of the needle valves used in the air- and refrigerant-side transducer lines with ball valves or plug valves. The seats of the needle valves tend to wear excessively after being repeatedly opened and closed, especially if overtightened when closed. The needle valves were installed on a temporary basis because they were very inexpensive and readily available.
- Procure and install a sensor to measure the air-side pressure drop across the evaporator. Such a sensor may help to indicate the degree of evaporator frosting during wet-coil tests because a heavily frosted coil is likely to generate an unusually high air-side pressure drop.

### 5.2.3 Compressor Speed and Torque Measurements

- Check the operation of the jackshaft speed sensor. The output of the sensor did not agree with measurements obtained from two different strobe tachometers obtained from the ME

equipment loan pool, but the strobe tachometers themselves may have been in need of calibration.

### 5.2.4 Humidity Measurements

- Calibrate the humidity probes.
- Move the condenser-side humidity probe to a location upstream of the condenser, such as in the entrance section duct. The probe gives a more accurate reading when used at the lower condenser inlet temperatures because, for a given humidity ratio $\omega$, the relative humidity $\phi$ reads much higher when T is lower. The air stream is also less stratified at the condenser inlet.
- Move the evaporator outlet humidity probe to a location where the outlet air stream is better mixed, such as in the blower exit pipe. Ideally, the probe should be located after an outlet mixing section and before the evaporator duct heater because the air temperature is lower (i.e., $\phi$ will read higher) at such a location.

### 5.2.5 Mass Flow Measurements

- Calibrate the refrigerant-side VFT's.
- Add flow straighteners upstream of each air-side VFT, and increase the inlet pipe lengths as much as possible. Be sure to leave a sufficient length of straight pipe between the inlet of the flow straightening section and the outlet of the elbow located at the end of the blower outlet pipe. If the flow straightener is located too close to the elbow, it may preserve the nonuniformities generated by the elbow (Halmi, 1972).
- Compressibly calibrate the gas-metering VFT's to determine the proper function(s) for Y.
- Insulate the body of each VFT to minimize heat transfer with the ambient environment and thereby help ensure that the adiabatic assumption of the VFT flow analysis is met.
- Insulate the inlet pipe of each VFT to minimize the temperature changes which may occur as the fluid travels between the upstream temperature probe and the inlet of the VFT.
- Determine if the refrigerant-side VFT measurements are affected by the presence of compressor oil. For example, oil may coat the throat of the discharge-line VFT and effectively change the operating beta ratio.
- Install a static pressure tap upstream of each VFT to sense the true static inlet pressure $P_1$. Static inlet pressure measurements yield more accurate values for the inlet density $\rho_1$.
- Temporarily install a differential pressure transducer across the Micro Motion flow meter to quantify the pressure drop across the meter during two-phase flow modes, particularly those which occur during startup and shutdown transients. If the pressure drop is found to be uncharacteristic of actual mobile a/c system operation, then install the meter on a bypass

line so that it can be excluded from the loop to more accurately simulate real-world operating conditions.

- Replace the 2.5-Ω shunt installed across the 4–20 mA output leads of the Micro Motion flow meter with a 25-Ω shunt to minimize the uncertainty in the current/flow measurement.

### 5.2.6 Refrigerant Loop

- Insulate the length of line between the outlet of the expansion device and the inlet of the evaporator. At present, the cold refrigerant stream exiting the expansion device gains an unknown amount of heat from the warmer ambient environment when traveling to the inlet of the evaporator, thereby causing the true value of the evaporator inlet refrigerant enthalpy $h_{eri}$ to be larger than the value derived from the measurements taken at the inlet of the expansion device. As a result, the difference between the measured evaporator inlet and outlet refrigerant enthalpies reads larger than the true difference, and the data reduction program overestimates the refrigerant-side heat transfer rate. Note that correction of this problem (if, in fact, it is a problem) would make the present evaporator-side energy balance errors slightly worse.
- Install mufflers at the inlet and outlet of the compressor to dampen pressure pulsations in the refrigerant lines so that smooth, unaliased refrigerant-side pressure measurements can be obtained. Mufflers can usually be obtained from the stock refrigerant lines.
- Finish developing the oil concentration sensor. After the sensor has been calibrated and is operating properly, remove the mixture sampling assembly from the refrigerant loop, or place the assembly on a bypass.
- Establish a set of rules for determining the proper charges of refrigerant and oil for any given system installation. The charge levels specified for the stock system may not truly apply to the facility installation due to differences in line lengths. In addition, it is likely that additional oil must be added to the system to make up for the amounts which remain settled in the pressure transducer lines of the facility.

### 5.2.7 Evaporator and Condenser Air Loops

- Install a fine-mesh screen upstream of the evaporator-side heater to provide a more uniform velocity profile at the heater inlet. At present, the evaporator outlet flow does not adequately expand to the full duct area at the heater inlet, thereby causing the coils nearest to the duct walls to run exceedingly hot and trip the heater's ARTC.
- Insulate all of the ductwork between the exit of evaporator-side heater and the entrance of the evaporator-side plenum to prevent heat loss to the ambient environment and thereby improve the inlet air temperature control capability.

- Resize the condenser-side blower to permit proper testing of heavy-equipment systems. Unfortunately, this will not only require the purchase of a new blower, but also a new VFT with a larger flow capacity and a new speed controller with a larger power capacity.
- Determine why the present condenser-side blower does not produce its rated flow.
- Select and install better recirculation dampers in the condenser air loop. The present dampers leak when closed and often move away from their set positions when open.
- Install a controlled heater in the entrance section of the condenser air loop to refine the condenser inlet air temperature control capability. Note that the recirculation scheme cannot be used to set above-ambient initial temperature conditions because the condenser must be operating in order to produce the hot air to be recirculated. In addition, the recirculation scheme cannot be used to maintain a constant inlet air temperature during a transient test because the temperature of the condenser outlet air stream varies throughout such a test. The installation of a controlled heater not only alleviates the above problems, but also allows the researcher to input programmable inlet temperature patterns to the condenser to generate a wide range of dynamic system responses for modeling and control purposes. Recall that a section of mixing vanes must be installed downstream of the condenser-side heater to prevent stratification at the condenser inlet, and that a fine-mesh screen must be located upstream of the heater to ensure a well-developed velocity profile at the heater inlet. A 240-VAC, 3-phase, 40-A power hookup has already been installed in the lab to accommodate the heater. A PID process controller (CAPP/USA Model No. 535-44120B0S01) has also been installed. The controller is a duplicate of the model used to regulate the evaporator-side heater.
- Add an air filter to the intake port of the condenser-side plenum to prevent fine dust particles from entering the loop and clogging the fine-mesh polypropylene screens.
- Verify the uniformity of the velocity profiles at the inlets and outlets of the heat exchangers. Add screens and flow straightening devices to each air loop as necessary.
- Add viewing windows upstream and downstream of the evaporator to permit visual identification of wet- and frosted-coil conditions.

### 5.2.8 Control Systems

- Install the environment controller.
- Add a tachometer feedback loop to compressor drive setup to compensate for motor slip.
- Install a humidity addition and control scheme in the evaporator air loop. The removal of moisture from the air stream by the evaporator and the associated effects of evaporator frosting are important aspects of real-world mobile a/c system operation which cannot be neglected.

- Add a feedforward control action to the evaporator heater control loop to compensate for the air loop transport delay. The feedforward action can be implemented by adjusting the MANUAL RESET parameter of the PID controller via serial communication commands sent from the environment controller. As an alternative solution, the heater could be moved back to its original location in the entrance section to altogether eliminate the delay. However, doing so would require the installation of a good mixing scheme downstream of the heater to prevent temperature stratification at the evaporator inlet.
- Add control loops to the air-side blowers to improve the researcher's ability to hold the air-side volumetric flow rates (or mass flow rates) constant from test to test. Recall that each air-side blower does not always generate the exact same flow rate each time its drive motor is run at a given frequency because the performance of the blower/system combination is dependent upon the density of the air stream.

### 5.2.9 Data Reduction

- Account for the presence of compressor oil in all refrigerant-side property calculations.
- Replace the EES data reduction program with a C or FORTRAN program which uses standardized refrigerant property routines and can reduce large transient data sets in addition to steady-state data sets.

### 5.2.10 Test Facility Enhancements

- Install cooling coils in the evaporator and condenser air loops to facilitate testing of winter defrosting conditions and diagnostic routines which predict faults associated with cold-weather a/c system operation.
- Install a second test section tunnel in the evaporator air loop to facilitate testing of two-evaporator systems.
- Monitor the sight tubes with video cameras whose images are time-stamped in synchronization with the data sampling process. Observations recorded from the sight tubes are often invaluable in clarifying the events of a transient response, and the video tapes would provide a visual record which could be passed on to the project sponsors and future members of the research team.
- Equip the refrigerant loop with devices which serve to simulate the hot environment of a vehicle engine compartment (e.g., wrap heating tape around the walls of the accumulator canister and the refrigerant lines, and install a heated enclosure around the compressor to raise the ambient temperature around the compressor shell).

# REFERENCES


AMCA. 1988. *Fans and Systems.* AMCA Publication No. 201. Air Movement and Control Association, Arlington Heights, IL. p. 22.

ASME. 1971. *ASME Fluid Meters.* 6th ed. American Society of Mechanical Engineers, New York.

ASHRAE. 1985. *Laboratory Methods of Testing Fans for Rating.* ANSI/ASHRAE Standard 51-1985. The American Society of Heating, Refrigerating, and Air-Conditioning Engineers, Atlanta, GA.

ASHRAE. 1989. *1989 Fundamentals Handbook (SI Edition).* The American Society of Heating, Refrigerating, and Air-Conditioning Engineers, Atlanta, GA. pp. 32.1–32.39.

Baker, D.H., E.A. Ryder, and N.H. Baker. 1975. *Temperature Measurement in Engineering.* OMEGA Press, Stamford, CT. Vol. 1, p. 59.

Benedict, R.P. 1977. *Fundamentals of Pressure, Temperature, and Flow Measurements.* 2nd ed. John Wiley & Sons, New York.

Burns, G.W., *et al.* 1975. *Thermocouple Reference Tables Based on the IPTS-68.* National Bureau of Standards Monograph 125.

Burns, G.W., *et al.* 1993. *Temperature-Electromotive Force Reference Functions and Tables for the Letter-Designated Thermocouple Types Based on the ITS-90.* National Institute of Standards and Technology (U.S.) Monograph 175.

CRC. 1994. *CRC Handbook of Chemistry and Physics.* 75th ed. D.R. Lide and H.P.R. Frederikse, ed. CRC Press.

DuPont Chemicals. 1993. *DuPont HFC-134a: Properties, Uses, Storage and Handling.* DuPont Publication P134a. Stock No. H-45945-1. DuPont Chemicals Fluorochemicals Customer Service Center, Wilmington, DE.

Farell, C., V. Saxena, and S. Youseff. 1993. "Experiments on Turbulence Management Using Screens and Honeycombs." *Devices for Flow Measurement and Control.* ASME FED-Vol. 159, pp. 1–10.

Gavin, P.M. 1983. *A Theoretical and Experimental Investigation of Evaporation from Drops Containing Nonvolatile Solutes.* University of Illinois at Urbana-Champaign. Ph.D. Thesis. pp. 72–73.

Halmi, D. 1972. "Practical Guide to the Evaluation of the Performance of Differential Producers." ASME Paper No. 72-WA/FM-2.

Halmi, D. 1973. "Metering Performance Investigation and Substantiation of the 'Universal Venturi Tube' (UVT)." ASME Paper Nos. 73-WA/FM-3 and 73-WA/FM-4.

Halmi, D. 1974. "'C' Evaluation—Differences Between 'Mathematical' and 'Physical' Possibilities." ASME Paper No. 74-WA/FM-2.

Horowitz, P., and W. Hill. 1989. *The Art of Electronics*. 2nd ed. Cambridge University Press, Cambridge, MA. pp. 52–53 and 413–414.

Knobloch, L.A. 1992. *Dynamic Modeling of a Mobile Air Conditioning Compressor and Condenser From Actual Performance Data.* University of Illinois at Urbana-Champaign. M.S. Thesis.

Laws, E.M., and A. Chesnoy. 1993. "The Design and Development of Flow Conditioning Devices." *Devices for Flow Measurement and Control.* ASME FED-Vol. 159, pp. 11-17.

Lenk, J.D. 1967. *A B C's of Thermocouples*. 1st ed. Howard W. Sams & Co., Inc., Indianapolis, IN. pp. 17–18.

Meyer, J.J., and Saiz J.M. Jabardo. 1994. "An Ultrasonic Device for Measuring the Oil Concentration in Flowing Liquid Refrigerant." *International Journal of Refrigeration.* Vol. 17, No. 7.

Michael, T.A. 1989. *Design of an Automotive Air Conditioning Test Stand for Screening and Transient Studies*. University of Illinois at Urbana-Champaign. M.S. Thesis. pp. 15–16.

Moffat, R.J. 1988. "Describing the Uncertainties in Experimental Results." *Experimental Thermal and Fluid Science.* Vol. 1, pp. 3–17.

OMEGA. 1992. *OMEGA Complete Temperature Measurement Handbook and Encyclopedia.* OMEGA Engineering, Inc. OMEGA Press, Stamford, CT. Vol. 28.

PRINCO. 1992. *Instruction Booklet for use with PRINCO Fortin Type Mercurial Barometers (English Language Edition).* PRINCO Instruments, Inc., Southhampton, PA. pp. 10–11.

SDI. 1986. *Platinum Resistance Temperature Detectors.* Sensing Devices, Inc., Lancaster, PA.

Sears, F.W., M.W. Zemansky, and H.D. Young 1987. *University Physics.* 7th ed. Addison-Wesley Publishing Co., Inc. pp. 347–349.

Stoecker, W.F., and J.W. Jones. 1982. *Refrigeration and Air Conditioning*. 2nd ed. McGraw-Hill, Inc. Chapter 6, pp. 103–129.

Weston, P.G. 1996. *Design and Construction of a Mobile Air Conditioning Test Facility for Transient Studies*, University of Illinois at Urbana-Champaign. M.S. Thesis.